

1 **Alpacas in Space - An Autobiography**
2

3 By
4

5 JOSEPH LEVINE
6 DISSERTATION
7

8 Submitted in partial satisfaction of the requirements for the degree of
9
10 DOCTOR OF PHILOSOPHY

11 in
12

13 Physics
14

15 in the
16

17 OFFICE OF GRADUATE STUDIES
18
19 of the
20

21 UNIVERSITY OF CALIFORNIA
22

23 DAVIS
24

25 Approved:
26

27 J. Anthony Tyson, Chair
28

30 S. Mani Tripathi
31

33 Brian Kolner
34

36 Committee in Charge
37

38 2025

39

Abstract

40 comment: This is my qual write up and is here only as a place holder. Don't edit this
41 yet It is believed that a large majority of the mass in the universe comes from an as yet
42 undetermined source. This claim stems originally from work performed in 1933 by Fritz
43 Zwicky who noticed a discrepancy between measured velocities of galaxies within the Coma
44 Cluster and velocities predicted by applying the virial theorem. He wrote

45 *If this [experimental result] would be confirmed we would get the surprising result
46 that dark matter is present in much greater amount than luminous matter [1].*

47 Vera Rubin furthered this work by measuring velocities of stars rotating in the M31 galaxy
48 and concluded there must be additional non-luminous mass (originally published in [2],
49 and shown in Fig.0.1). Studies of other phenomena, such as lensing (see [**lensing2**]) have
50 confirmed the existence of this dark matter, and it is currently one of the major mysteries
51 in modern physics.

52 Since the 1980's, the leading theories have consisted of an unknown species of elementary
53 particle. The search for weakly interacting massive particles (WIMPs) have dominated
54 the budgets and schedules of the dark matter search effort but have yet to provide any
55 experimental evidence.

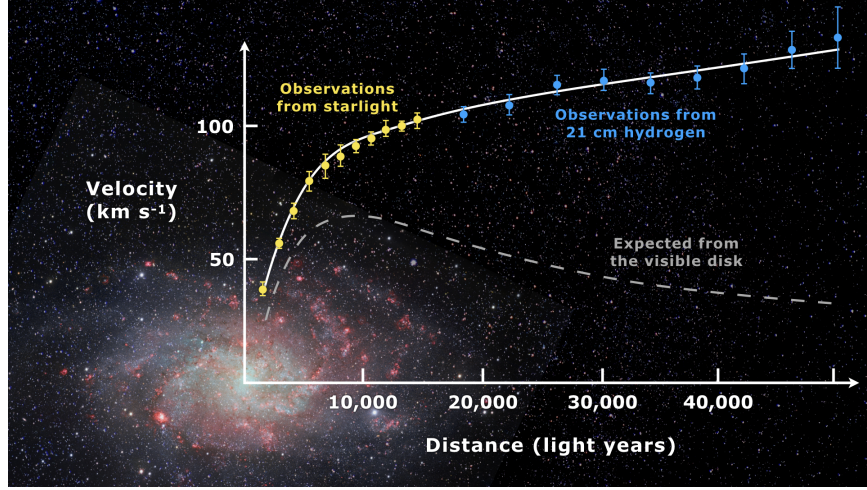


Figure 0.1: Expected vs observed velocity distributions of M33

56 In light of this, the 2017 community report on dark matter [3] highlights a need for a multi-
 57 experiment program in which many small scale experiments (< \$10M) split up to cover the
 58 vast landscape of potential dark matter candidates (see Fig. 0.2). Since very little is known
 59 about the dark matter, it is a playground for theoretical physicists to invent candidates.

60 This overwhelming search should be narrowed down.

61 The enormous mass range splits nicely into two regimes; waves and particles. At a mass of
 62 order 1eV the inter-particle spacing \approx wavelength. Lighter than this it is more convenient
 63 to think of dark matter as a wave. Alternatively, dark matter candidates heavier than this
 64 are more conveniently modeled as exhibiting particle-like behavior. The Dark E-Field Radio
 65 experiment searches for dark photons in the nano- to milli-eV mass range where dark matter
 66 is best described as a wave. This property means one would search for a dark photon using
 67 wave-like detectors, e.g. antennas.

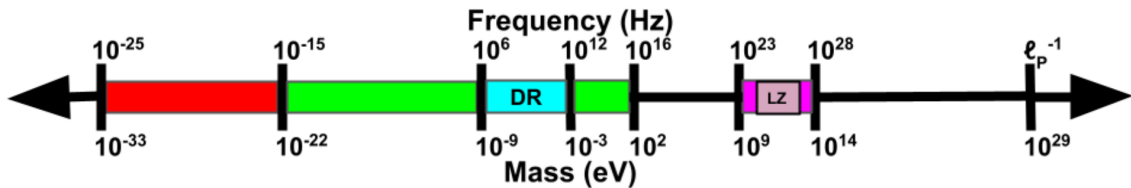


Figure 0.2: Cartoon depicting the mass scales over which dark matter may be found. Corresponding frequencies shown above. At heavy mass scales $> \mathcal{O}(1\text{ eV})$ the dark matter would behave like a particle, while on the lighter end it would behave like a wave. The Dark Radio Experiment searches at radio/microwave frequencies (blue) for a hidden photon using an antenna and spectrum analyzer. LUX-ZEPLIN Experiment (LZ) also shown.

68 comment: Discussion from paper. Good to pull from

69 This experiment extends the earlier results of our pilot experiment [4], which was designed to
 70 demonstrate feasibility of the Dark E-field Radio technique. The pilot experiment was run
 71 over the same frequency range as the experiment reported here, but did not make use of the
 72 calibration techniques to approximate statistical uniformity, nor did it fully account for the
 73 resonant enhancement of the cavity. In this paper we describe how we randomize antenna
 74 positions by moving it many times during the run. In addition, we detail EM simulations
 75 which give the average relation between the E-field at the antenna and the voltage into
 76 the LNA, accounting for resonant enhancement of the cavity. A 2^{24} -point FFT produces a
 77 spectrum dominated by background thermal noise which varies gradually with frequency.

78 We then searched over the full 50-300 MHz frequency span for any narrow-band dark photon
 79 signal of at least 5% global significance. Optimally filtering the resulting spectrum, we detect
 80 a single candidate which we are able to identify as interference, likely from our electronics.

81 Rejecting this candidate, we obtain a null result for any signal which could be attributed
82 to the dark photon in our frequency range. The resulting 95% exclusion limit for the dark
83 photon kinetic coupling ϵ is then obtained over this mass range of 0.2-1.2 μeV . Our null result
84 is a factor of ≈ 100 more sensitive than current astrophysical limits.

85 Ultimately, we can apply this detection technique at higher frequencies, ultimately going up
86 to the sub-THz band. This will require new antennas and microwave electronics. Cryogenic
87 cavities and LNAs could improve our sensitivity by an order of magnitude.

88 **Contents**

89	Contents	vi
90	List of Figures	x
91	List of Tables	xiv
92	1 The Dark Matter Story	1
93	1.1 The History of Dark Matter	2
94	1.1.1 Early ideas in dark matter	2
95	1.1.2 Into the modern era	3
96	1.1.2.1 Galactic rotation curves	7
97	1.1.3 Local dark matter density measurements	7
98	1.2 From “History” to “Current Events”	7
99	1.2.1 Modern evidence and observations of dark matter	8
100	1.2.1.1 The cosmic microwave background	8
101	1.2.1.2 Gravitational lensing	8
102	1.2.1.3 MOND and the bullet cluster	8
103	1.3 MACHOs, WIMPs and WISPs, oh my!	9
104	1.3.1 WISPs	9
105	1.3.1.1 Axions	9
106	1.4 Dark Photon Physics	9
107	1.5 Detection Strategy: a Resource Allocation Problem	10
108	2 Experiment Overview and Design	11
109	2.1 Sources of Power in Measured Spectrum	14
110	2.1.1 Thermal Noise	14
111	2.1.1.1 Blackbody Electric Field Density	14
112	2.1.1.2 Antenna Noise	17
113	2.1.1.3 Dicke radiometer equation	20
114	2.1.2 Dark Photon Signal	25
115	2.1.3 Radio Frequency Interference	27
116	2.1.4 Amplifier Chain Noise	28
117	2.1.5 ADC effects	32

118	2.1.5.1	Spurious signals	33
119	2.1.5.2	ADC noise	33
120	2.2	Toy Analysis	34
121	2.2.1	Signal significance	36
122	2.2.1.1	Computing an exclusion limit	38
123	2.2.2	Predicted time to detection	42
124	2.3	Thermal Noise in A Cavity: Thermal Wiggles	44
125	2.3.1	Theory of thermal radiation in a cavity	44
126	2.3.2	Inspection of thermal noise spectra	48
127	2.3.3	A simple resonator: shorted coax cable	49
128	2.3.3.1	RF circulators	52
129	2.3.4	A simpler resonator: shorted coax cable and circulator	55
130	2.3.5	A more complex resonator: antenna in room	57
131	2.3.6	Effective temperature of amplifier	59
132	2.3.7	Intentional breaking of thermal equilibrium	62
133	2.3.8	Relation of antenna S_{11} to thermal noise without a circulator	69
134	2.3.9	Discussion of Thermal Wiggles	72
135	2.4	Reverberation Chambers and Statistical Uniformity	73
136	2.4.1	Deterministic solutions to electromagnetic waves in cavities	75
137	2.4.2	Statistical approach to electromagnetic waves in cavities	79
138	2.5	System Design	80
139	2.5.1	Shielded room	83
140	2.5.2	Antenna	84
141	2.5.3	Terminator and fiber-optic switch control	88
142	2.5.4	Signal conditioning	88
143	2.5.4.1	Low noise amplifier	89
144	2.5.4.2	Secondary amplifier	89
145	2.5.4.3	Band pass filter	90
146	2.5.4.4	Putting together a signal conditioning chain	91
147	2.5.5	Veto antenna	94
148	2.5.6	12 V power system	95
149	2.5.7	GPU-Based Real-Time Spectrum Analyzer	98
150	3	System Characterization and Data Acquisition System	102
151	3.1	Measurement of Amplifier Chain Performance	103
152	3.1.1	Y-factor method	103
153	3.1.2	Confirming gain with tracking generator measurement	111
154	3.1.3	System stability over a run period	112
155	3.2	Measurement of shielding effectiveness and radio frequency interference	116
156	3.3	Spectrum Analyzer Characterization	122
157	3.3.1	Spectrum analyzer calibration	122
158	3.3.2	Spurious signal performance of the ADC	123
159	3.3.3	ADC clock performance	125

160	3.3.4 Real-time data collection efficiency	126
161	4 Data Acquisition, Data Analysis and Calibration	128
162	4.1 Data Acquisition	130
163	4.1.1 Raw data, S_o	131
164	4.2 Data Analysis	134
165	4.2.1 Fit background, $\hat{B}(\nu)$	136
166	4.2.2 Normalized spectrum, S_o^{norm}	138
167	4.2.3 Signal-matched filter	139
168	4.2.4 Monte Carlo: pseudo experiments	142
169	4.2.5 Rejection of a single candidate	147
170	4.3 Calibration	148
171	4.3.1 Average effective aperture, $\langle A_e(\nu) \rangle$	149
172	4.3.2 Simulation of $\langle \tilde{Q} A_e \rangle$	150
173	4.3.3 Correction and uncertainty of $\langle \tilde{Q} A_e \rangle$	153
174	4.4 Hardware Injection Test	156
175	4.4.1 Injection test prerequisites	157
176	4.4.1.1 Determination of required injected power	157
177	4.4.1.2 Proxy dark photon signal injection	160
178	4.4.2 Performing the injection test	162
179	4.4.3 Inspection of Data	166
180	5 Results	170
181	5.1 Discussion of uncertainties	171
182	5.2 Exclusion Limit ¹	172
183	6 Beyond 300 MHz	175
184	6.1 A first attempt at Run 1B ²	178
185	6.1.1 Run 1B upgrades	178
186	6.1.1.1 Run 1B spectrum analyzer	178
187	6.1.1.2 Vivalid antenna stand	179
188	6.1.1.3 Mode stirrer and statistical uniformity	179
189	6.1.2 Run 1B data run and analysis	181
190	6.2 Mixer System: Run 2	185
191	6.2.1 Frequency mixing	185
192	6.2.1.1 The superheterodyne receiver	188
193	6.2.1.2 Beyond the ideal mixer	190
194	6.2.2 Design requirements	191
195	6.2.3 The Dual-conversion superheterodyne receiver	192

¹Code for this section can be found at: <https://github.com/josephmlev/darkRadio/tree/master/Computelimit>

²Code for this section can be found at: <https://github.com/josephmlev/darkRadio/tree/master/daqAnalysisAndExperiments/run1B/analysis>

196	6.2.3.1	Run 2A mixer system design	196
197	6.2.3.2	Additional considerations	197
198	6.3	Possible Future Upgrades	198
199	6.3.1	Detector design principles to maximize the signal-to-noise ratio	199
200	6.3.1.1	Maximize the signal	199
201	6.3.1.2	Reduce noise	200
202	6.3.1.3	Filtering	200
203	6.3.2	Leveraging Axion experiments for Dark Photon searches	201
204	6.3.2.1	Reanalysis of Axion data	202
205	6.3.2.2	Design and operation of Axion experiments with Dark Pho-	
206		tons in mind	202
207	A	Overview of RTSA code base	204
208	A	Tips for using the RTSA system	206
209	B	Data structure and processing	207
210	B.1	Writing data	207
211	B.2	Reading and averaging data	211
212	Bibliography		214

²¹³ List of Figures

214	0.1	Expected vs observed velocity distributions of M33	iii
215	0.2	Dark matter mass regimes	iv
216	2.1	Overview of the Dark E-field Radio experiment	13
217	2.2	Blackbody electric field spectral density from radio to UV frequencies	16
218	2.3	An antenna and matched resistor in cavities which are in thermal equilibrium.	19
219	2.4	Simulated antenna noise voltage at room temperature in the time domain	21
220	2.5	Simulated antenna noise power spectral density at room temperature in the frequency domain	22
221	2.6	Effect of averaging on simulated antenna noise power spectral density at room temperature in the frequency domain	24
222	2.7	Schematic of LNA adding input referred noise	28
223	2.8	Schematic of cascade of amplifiers and their added noise	30
224	2.9	Cascaded noise temperature for system with two amplifiers	31
225	2.10	Input-referred power spectral density from simplified simulation	36
226	2.11	Noise spectrum containing sub-detection-threshold signal	40
227	2.12	Noise spectrum containing sub-detection-threshold signal, various number of averages	41
228	2.13	Predicted time to detection for the toy analysis spectra	43
229	2.14	Two cavities in thermal equilibrium of arbitrary shape, material and physical contents contain equivalent radiation fields	45
230	2.15	A cavity with a small hole behaves like a black body as long as the probability of absorption << 1. The probability of absorption at each reflection is given by the emissivity, so the total probability of <i>reflection</i> is the emissivity raised to the power of the average number of bounces. Figure from Wikipedia.	47
231	2.16	Output-referred Vivaldi antenna and terminator spectra as measured through Run 1A amplifier chain	49
232	2.17	A coax cable with a short on the end and a matched measurement device on the other behaves like a “closed-open” resonator. Replacing the short termination with an open (not shown here) produces a similar resonator, though with a 180-degree phase shift.	51
233	2.18	Power spectrum of short and open terminations at the end of 1.85 m of RG400 coax cable	51
234	2.19	Schematic symbol of a circulator	52

247	2.20 Photo of Teledyne C-0S03A-3M RF circulator	53
248	2.21 3-port, frequency-dependent S-parameter data for Teledyne C-0S03A-3M circulator	54
249	2.22 A coax cable with a short on one end and a circulator isolating the system from the amplifier.	56
251	2.23 Power spectrum of 185 cm coax resonator as measured through circulator.	56
252	2.24 Schematic of experimental set-up using circulator to isolate antenna from ampli- fier effects	58
254	2.25 Normalized power spectrum for Vivaldi antenna in the room with and without circulator	58
256	2.26 Schematic of set-up to measure the noise emerging <i>out</i> of an amplifiers input . .	61
257	2.27 Power spectrum of noise emerging <i>out</i> of the input of an amplifier's input	61
258	2.28 Setup to create hot and cold terminator	63
259	2.29 Spectra resulting from the antenna and circulator set up at a variety of temper- atures above room temperature	65
261	2.30 Spectra resulting from the antenna and circulator set up with the terminator 210 K above and below room temperature	67
263	2.31 Sum of normalized spectra shown in Fig. 2.30	68
264	2.32 $1 - S_{11} ^2$ and the normalized antenna spectrum over plotted	70
265	2.33 Correlation of $1 - S_{11} ^2$ and the normalized antenna spectrum	71
266	2.34 Modal density for an electromagnetic cavity with dimensions of the shielding room	77
267	2.35 Pictures of conductor configurations in shielded room	78
268	2.36 Measured S_{11} with different conductors in shielded room	78
269	2.37 Schematic of the RF receiver system	81
270	2.38 Photo of dark radio lab	82
271	2.39 AB-900A biconical antenna free space effective aperture, simulated, measured and theoretical	86
273	2.40 simulated AB-900A biconical antenna free space complex input impedance, vs measured biconical data	87
275	2.41 Through gain (S_{21}) of bandpass filter	93
276	2.42 Schematic of Run 1A Amplifier chain	94
277	2.43 Schematic of Interlock board	96
278	2.44 Photo of lead-acid battery and slow turn on circuit	97
279	2.45 Real time DAQ data stream.	100
280	3.1 Cartoon showing Y-factor data	104
281	3.2 Raw output power spectra used to compute the gain and noise temperature for the Run 1.4 amplifier chain using the Y-factor method	106
283	3.3 Y-factor data from Run 1.4 amplifier chain at a single frequency (625 MHz) . .	107
284	3.4 Frequency dependent noise temperature of Run 1.4 amplifier chain, measured using the Y-factor method	108
286	3.5 Frequency-dependent gain of the Run 1.4 amplifier chain, measured using the Y-factor method	109
288	3.6 Run 1.4 terminator, input-referred power spectral density	110

289	3.7	Gain vs. frequency of Run 1.4 amplifier chain	111
290	3.8	Gain vs. LNA voltage of Run 1.4 amplifier chain	113
291	3.9	Voltage at LNA vs. time	114
292	3.10	Frequency-averaged power spectral density vs. time of the terminator from Run 293 1.4	115
294	3.11	Photo of setup to measure Shielding effectiveness of shielded room	118
295	3.12	Shielding effectiveness of shielded room, 50-300 MHz	119
296	3.13	Shielding effectiveness of shielded room, 125-3000 MHz	120
297	3.14	Spectrum from veto antenna during 300 MHz data run	121
298	3.15	Scan of terminated input of Teledyne spectrum analyzer system to measure spur 299 performance	124
300	3.16	Acquisition efficiency for GPU-based Real-time spectrum analyzer	127
301	4.1	Run 1A averaged, output-referred antenna power spectrum S_o	132
302	4.2	Logarithmic scaled Run 1A averaged, output-referred, antenna and terminator 303 power spectra	133
304	4.3	Flow chart outlining the logic of signal processing in the detection algorithm of 305 sections 4.2.1 through 4.2.3	135
306	4.4	Fitting background \hat{B} in the presence of a synthetic signal	138
307	4.5	Normalized, output-referred power spectrum S_o^{norm}	140
308	4.6	S_o^{norm} after it has been passed through a matched filter	142
309	4.7	Result of Monte Carlo pseudo experiments on signal detection	145
310	4.8	Limit on output-referred total integrated signal power, P_o^{lim}	146
311	4.9	Screenshot of COMSOL simulation GUI for two-antenna validation	152
312	4.10	Simulated vs measured $\langle S_{21} \rangle$	153
313	4.11	Corrected average effective aperture	155
314	4.12	Schematic of hardware injection test	158
315	4.13	Average S-parameters of hardware injection test	159
316	4.14	Histogram of frequencies used for hardware injection test	162
317	4.15	Output-referred power spectral density from the hardware injection test	164
318	4.16	Standard deviation of output-referred power spectral density from the hardware 319 injection test, computed with median absolute deviation	165
320	4.17	Output-referred power spectrum from hardware injection test, various levels of 321 zoom	167
322	4.18	Normalized, output-referred power spectrum from hardware injection test, various 323 levels of zoom	168
324	4.19	Matched filtered, output-referred power spectrum from hardware injection test, 325 various levels of zoom	169
326	5.1	Zoom of 95 % exclusion limit on ϵ from Dark E-field Radio run 1A	173
327	5.2	Dark photon limits of various experiments with this work shown in red	174

328	6.1	Picture of modified COMPOWER antenna stand holding Vivaldi antenna for Run 1B	179
330	6.2	Closeup picture of modified COMPOWER antenna stand holding Vivaldi antenna for Run 1B	180
332	6.3	Run 1B averaged, output-referred antenna power spectrum S_o	182
333	6.4	Run 1B S_o^{norm} after it has been passed through a matched filter.	183
334	6.5	9-day averaged veto spectrum and Run 1B S_o^{norm} after it has been passed through a matched filter	184
336	6.6	Overview of basic mixer operation in both upconversion and downconversion mode	187
337	6.7	Illustration of the problem of images in frequency mixing	188
338	6.8	Schematic of a basic superheterodyne receiver system	189
339	6.9	XXXX	190
340	6.10	Block diagram of the mixer system to be used in Run 2	192
341	6.11	Schematic of simplified dual conversion superheterodyne receiver	194
342	6.12	XXXX	194
343	6.13	XXXX	195
344	6.14	Schematic of Run 2A dual conversion superheterodyne receiver	196
345	6.15	Picture of dual-conversion mixer system	197
346	A.1	Real-time heads up window for data acquisition.	210

³⁴⁷ List of Tables

348	2.1	Statistics of simple Monte Carlo simulation for probability of signal detection in the toy analysis	42
350	2.2	Direction, coordinate, and length measurements of the shielded room in lab 314. Note that Fig. 2.38 is looking south, so x is right-left, and z is into the page. Note that these are the mean values of several measurements. The room was found to be about 5 mm out of square, so these should be interpreted as ± 5 mm.	84
354	2.3	Specifications for the Pasternack PE15A1012-E. The voltage is regulated inter- nally, so the exact voltage supplied is not critical, though there is a slight gain dependence on voltage since a higher voltage causes the amp to run warmer, see Fig 3.8.	89
358	2.4	Specifications for the Mini-Circuits ZKL-1R5+ as measured with 9.05 V bias. There is no internal regulator, so the voltage is set using an external regulator (built around a TI LM317 [64]).	90
361	2.5	Specifications for the custom, real-time spectrum analyzer used for run 1A.	99
362	4.1	Run 1.4 Details. Many specifications are related and can be computed from each other but are listed for reference. The efficiency differs from that calculated in Fig. 3.16 mainly because of switching to a terminator and brief daily pauses to move the antenna.	130
366	4.2	Threshold parameters that are part of the detection algorithm and Monte Carlo. X is the significance of the analysis. It is a parameter passed to the detection algorithm which specifies the significance threshold. The quantity $100\% - Y$ is the statistical power of the analysis. It is a parameter in the MC, which specifies a threshold on signal power where a given signal is detected in $100\% - Y$ of the MC iterations. We choose both X and Y = 5%.	144
372	6.1	Overview of future runs including hardware (antenna, LNA, mixer), status, how/if statistical uniformity will be ensured, and any comments	177
374	A.1	Example database file.	208

375

Acknowledgments

376 Thank you to: Ben

377 Dave Hemmer

378 Nathan IT

379 Monda

380 emiljia

381 Bill Tuck

382 Buchholtz/Ayars/Nelson/Kagan/Clare/Patrova/Rick Danner/pechkis

383 parents

384 janet/joel

385 baba/papa

386 Belva

387 chatGPT

388 Mr Keye

389 Bill Nye

390 pechkis

391 hepcat

392 paul

393 Self plagiarism statement <https://journals.aps.org/copyrightFAQ.html>

394 As the author of an APS-published article, may I include my article or a portion
395 of my article in my thesis or dissertation? Yes, the author has the right to use
396 the article or a portion of the article in a thesis or dissertation without requesting
397 permission from APS, provided the bibliographic citation and the APS copyright
398 credit line are given on the appropriate pages.

399 <https://grad.ucdavis.edu/preparing-filing-your-thesis-or-dissertation>

400 Published or publishing pending material may be used with permission from the
401 copyright owner, if not you, and the Graduate Chair, if you are not the first-
402 author. See the Copyright FAQ for information about permissions when using
403 published material.

404 Material you have authored, and which has been previously published or is pend-
405 ing publishing, may be used in its published format with three exceptions: 1)
406 Margins - You must maintain 1" margins on all sides throughout the paper. 2)
407 Pagination - page numbers must follow the UC Davis standards. 3) The title
408 page must follow UC Davis standards and you must include an overall abstract.

409 comment: Need to add note about github and where code comes from

⁴¹⁰ Chapter 1

⁴¹¹ The Dark Matter Story

⁴¹²

If we start making a list of things that aren't
here, we could be here all night. You know, pens
for instance. Let's stick with things we can see.

Wheatley

413 While there are many ways to begin a thesis on a dark matter search (of which many
414 hundreds are written every year), I have opted to prioritize narrative over completeness. I
415 will aim to answer the following questions:

- 416 • Why do we believe there to be some mysterious “dark matter” which we can’t even
417 see?
- 418 • Can we back up this prediction?
- 419 • What is the best way to balance answering this question with the economic reality of
420 finite money?

421 There will be a few digressions along the way, however the goal of this chapter is simply
422 to motivate what brought society to the point of paying young scientists to put antennas in
423 metal boxes and measure noise.

424 **1.1 The History of Dark Matter**

425 **1.1.1 Early ideas in dark matter**

426 The fundamental idea that things exist which can not be easily observed by human senses is
427 not a new one. Following a long history of discovery of previously unobserved phenomena,
428 the study of dark matter began to take shape around the end of the 19th century with the
429 discovery of dark regions among areas with a high density of stars [5]. It was Lord Kelvin
430 who began a dynamical study of the motions of stars in order to tease out the weight of

431 the luminiferous aether (who's "existence is a fact that can not be questioned" as stated
432 in his 1901 lecture which is transcribed on page 260 of [6]). Eventually the theory of the
433 aether would give way to special relativity, which ruled out a potential candidate for the
434 dark regions. This proposing of dark matter candidates and their rejection is a cycle that
435 continues to this day, and is the topic of this thesis.

436 1.1.2 Into the modern era

437 1905, known as Einstein's miracle year, ushered in a new era of "modern physics". The
438 aether that Lord Kelvin was trying to weigh was accepted as non-existent, but that didn't
439 answer the questions of galactic dynamics which were posed by those who believed in it.
440 Fritz Zwicky is credited with the first discovery of dark matter in 1933 [1], though it was
441 not widely accepted at this time. This lack of acceptance was in part due to his technique
442 of "morphological analysis" which is similar to arranging refrigerator magnets to arrive at
443 creative solutions¹. The many "creative" solutions are simultaneously to the benefit and
444 detriment of this technique. To quote Stephen Maurer[7],

445 *When researchers talk about neutron stars, dark matter, and gravitational lenses,*
446 *they all start the same way: "Zwicky noticed this problem in the 1930s. Back then,*
447 *nobody listened..."*.

448 It even seems if Zwicky himself didn't believe his own result[1],

¹This analogy is from a class I took from Andrew Wetzel at U.C. Davis. In researching it for this thesis, it is surprisingly accurate

449 *If this [experimental result] would be confirmed we would get the surprising result*
 450 *that dark matter is present in much greater amount than luminous matter [1].*

451 comment: Tony summarizes virial therm this in his '97 physics today article, p. 1 [8] In
 452 retrospect however, this idea is seemingly on firm theoretical footing. The viral theorem is a
 453 well known from statistical mechanics. It was formalized 1870 by Rudolf Clausius (English
 454 translation can be found here [9]). The name *virial* was coined by Clausius. Kinetic energy
 455 was, at the time, referred to as *vis viva* latin for “living force”. The plural of vis is virias,
 456 and since the theorem is concerned with many particles each with their own vis vita the
 457 name *virial* theorem was chosen. The theorem is derived briefly here (following chapter 3 of
 458 Goldstein[10]) since it is informative, however the reader can skip to Eq. 1.6 for the result
 459 as it applies to galacite dynamics.

460 The “virial” the system is defined as

$$G \equiv \sum_{i=1}^N \mathbf{r}_i \cdot \mathbf{p}_i \quad (1.1)$$

461 Where \mathbf{r}_i is the position of the ith particle and \mathbf{p}_i is it's momentum, $m_i \mathbf{v}_i$.

462 By the product rule, the time derivative of G is

$$\dot{G} = \sum_{i=1}^N (\dot{\mathbf{r}}_i \cdot \mathbf{p}_i + \mathbf{r}_i \cdot \dot{\mathbf{p}}_i) . \quad (1.2)$$

463 Since the first term is really $m_i \mathbf{v}_i \cdot \mathbf{v}_i$ it can be seen as twice the kinetic energy, $2T$. The
 464 second term can be simplified by Newton's second law, $\mathbf{F} = \dot{\mathbf{p}}$. So,

$$\dot{G} = 2T + \sum_{i=1}^N (\mathbf{r}_i \cdot \mathbf{F}_i) . \quad (1.3)$$

Solving for the time-averaged, time-derivative of G ,

$$\begin{aligned}\bar{\dot{G}} &= \frac{1}{T} \int_0^T dt \dot{G} \\ &= \frac{G(\tau) - G(0)}{\tau}\end{aligned}$$

465 Where T is the period the average is taken over, not to be confused with the Kinetic energy.

466 In the case that the system is bound together (i.e. $\mathbf{r}_i, \mathbf{p}_i > \infty$), G is finite and as τ
467 approaches ∞ , $\bar{\dot{G}}$ approaches 0

468 Returning to Eq. 1.2, we can now say

$$\overline{T} = -\frac{1}{2} \overline{\sum_{i=1}^N (\mathbf{r}_i \cdot \mathbf{F}_i)}, \quad (1.4)$$

469 A familiar statement of the virial theorem, where the term on the right hand side is
470 known as *the virial of Clausius*.

471 While incredibly general (one can pull the ideal gas law out of this in just a few steps,
472 see again Ch. 3 of Goldstein [10]), we are concerned not with a jar filled with gas in some
473 lab, but with “gas” of stars (among which all labs are contained!).

474 To specify the equation to that of galactic dynamics, recognize for a conservative central
475 force, $\mathbf{F} = -\nabla U$ and $\mathbf{r} \cdot \mathbf{F} = r F$. If U is in a power law, i.e. of the form $k r^{n+1}$, it can quickly
476 be seen that the virial of Clausius of Eq. 1.4 can be written $\frac{n+1}{2} \overline{U}$.

477 For a problem involving an inverse square force as we are concerned with, $n = -2$, and we
478 arrive at the well known result which is usually just called “the virial theorem”, though as we
479 have seen, it reaches much deeper than a simple statement of kinetic vs potential energies
480 for galaxies:

$$\overline{T} = -\frac{1}{2}\overline{U}. \quad (1.5)$$

481 Finally following Edington's 1916 paper [11] we can form a useful formula which ul-
 482 timately gave a clue to the existence of dark matter. By setting $T = 1/2M\overline{v^2}$ and $U =$
 483 $GM^2/2R$ where M is the total mass of a cluster or galaxy, v is it's velocity, and R is it's
 484 radius, we arrive at

$$M \approx \frac{2R\overline{v^2}}{G} \quad (1.6)$$

485 As pointed out by Bertone [12], one of the earliest "clean" arguments for the existence
 486 of dark matter is known as the timing argument. It was derived by Kahn and Woltjer [13].
 487 The basic idea is given the negative red-shift (i.e. blue-shift) of the Andromeda galaxy, they
 488 are approaching (at 125 km/s), an indication that they are bound system. Given that the
 489 period of this system must be less than the age of the universe (assumed to be 10^{10} yr), a
 490 lower bound can be set on the reduced mass of the system (since orbital period T is inversely
 491 proportional to the reduced mass).

492 In the years following these arguments, WWII brought unprecedeted destruction, the
 493 reconstruction of which slowed the progress of all science that was not essential to the war
 494 effort, especially in Europe. The focus of astronomy and astrophysics largely shifted to
 495 stellar structure and evolution, in large part due to the work and understanding of nuclear
 496 reactions around this time. The war also brought with it advances in radar technology. At
 497 the end of the war, the German occupation forces left large amounts of radar equipment

498 strewn about Europe. This included a large number of 7.5 m Würzburg antennas designed
499 to 54 cm aircraft radar, but were also sensitive to the famous Hydrogen 21[cm] line [14]. This
500 would play a major role in what was to come.

501 **1.1.2.1 Galactic rotation curves**

502 **1.1.3 Local dark matter density measurements**

503 **comment: Add plots of local dark matter density estimate.**

504 Good figure 2 of historical DM density through 2014 by Read [15]. Also Figure 1 explains
505 the difference between local and global density of DM

506 Read is also an author on [16], which has a nice figure 1 showing a continuation of this
507 out to 2021

508 This is questionable (not peer-reviewed, 2 citations) but has a good overview of Gaia,
509 and gets DM density using data release 3 [17]

510 **1.2 From “History” to “Current Events”**

511 As pointed out by Trimble, “Practicing scientists will normally put the cut between history
512 and current events at the time when they started reading the literature for themselves,
513 probably early in graduate school.” [18]. While that puts my personal cut-off around 2020,
514 the cut-off of the Dark E-field Radio group is closer to the mid-1960’s, a fruitful time for
515 research into dark matter.

516 A characteristic shift in the dark matter problem occurs in this era of current events.
517 Instead of asking “is there dark matter (and if so how much)”, we ask “what is this stuff?!”.
518 To be sure, the first question is still relevant today and the ever more precise answer was
519 outlined in Sec. 1.1.3. This section is concerned with more modern evidence for dark matter,
520 which tend to point to the modern non-baryonic particle models, which the Dark E-Field
521 Radio Experiment is searching for.

522 **1.2.1 Modern evidence and observations of dark matter**

523 **1.2.1.1 The cosmic microwave background**

524 Billy and Ben’s thesis

525 **1.2.1.2 Gravitational lensing**

526 -ben thesis

527 -tony 92 article// -J. A. Tyson, G. P. Kochanski, and I. P. Dell’Antonio, Detailed mass map
528 of CL0024+1654 from strong lensing

529 **1.2.1.3 MOND and the bullet cluster**

530 -history of dark matter bertone

531 - billy and ben

532 - D. Clowe, M. Bradac, A. H. Gonzalez, M. Markevitch, S. W. Randall, et al., A direct
533 empirical proof of the existence of dark matter,

534 **1.3 MACHOs, WIMPs and WISPs, oh my!**

535 -Billy thesis sec 1.2

536 - G. Bertone, D. Hooper, and J. Silk, Particle dark matter: Evidence, candidates and con-
537 straints

538 **1.3.1 WISPs**

539 **1.3.1.1 Axions**

540 **1.4 Dark Photon Physics**

541 - Ben's thesis

542

$$|\mathbf{E}_{\text{ant}}| \approx \epsilon \sqrt{\frac{2}{\varepsilon_0} \rho_{\text{DM}}}, \quad (1.7)$$

543 Tony says 9/23/25– Production mechanisms: fluctuation occurs early in inflation or mis-
544 alignment mechanism.

545

546 two scales cross, peter graham Point out that DP doesn't have a thermal origin like a
547 WIMP does

⁵⁴⁸ **1.5 Detection Strategy: a Resource Allocation**

⁵⁴⁹ **Problem**

⁵⁵⁰ - US Cosmic Visions 2017

⁵⁵¹

⁵⁵² Chapter 2

⁵⁵³ Experiment Overview and Design

554

A month in the laboratory can often save an hour in the library.

Frank Westheimer

555 Veljko Radeka said of detectors, “One would imagine that in each particular case the
556 best solution is arrived at by 1) the detector design to maximize the significant signal, 2)
557 reduction of noise at its physical source, and 3) optimum filtering of signal and noise.” [19].
558 While he was referring to position-sensitive particle detectors, the same three principles
559 apply to this experiment. Put more directly, the goal is to maximize the signal-to-noise
560 ratio. The detector, in this case, is a low-noise, wide-band radio receiver system searching
561 not for discrete instances of particle-like interactions but for coherent waves that are constant
562 over long periods. The signal is a small RF-power excess received by an antenna in a cavity.
563 The dominant noise is due to the thermal background of the 300 K cavity walls. This noise
564 is nearly white, with small variations. See Sec. 2.1.1 for an overview and Sec. 2.3 for more
565 detail. An overview of the entire experiment is shown in Fig. 2.1.

566 This chapter begins with Sec. 2.1, devoted to exploring the sources of power in the mea-
567 sured spectrum. It walks through several back-of-the-envelope calculations to follow the
568 signals and noises as they progress from fields in free space through a simplified detector.
569 Section 2.2 takes the next step. It simulates these signals and noises and shows a framework
570 for statistical data analysis. These two sections serve to build up intuition about the experi-
571 ment which will explain design choices discussed in later chapters. Furthermore, this section
572 is useful because the actual experiment will report a null result, i.e. a lack of detection of a
573 signal. By following a signal *forward* through the system and toy data analysis, it will be
574 clearer how to infer an exclusion limit from a power spectrum and working *backward* through
575 the experiment. In the following two sections, 2.3 and 2.4, effects will be introduced that
576 were not apparent from the simplistic analysis of the first section. The final section, 2.5,

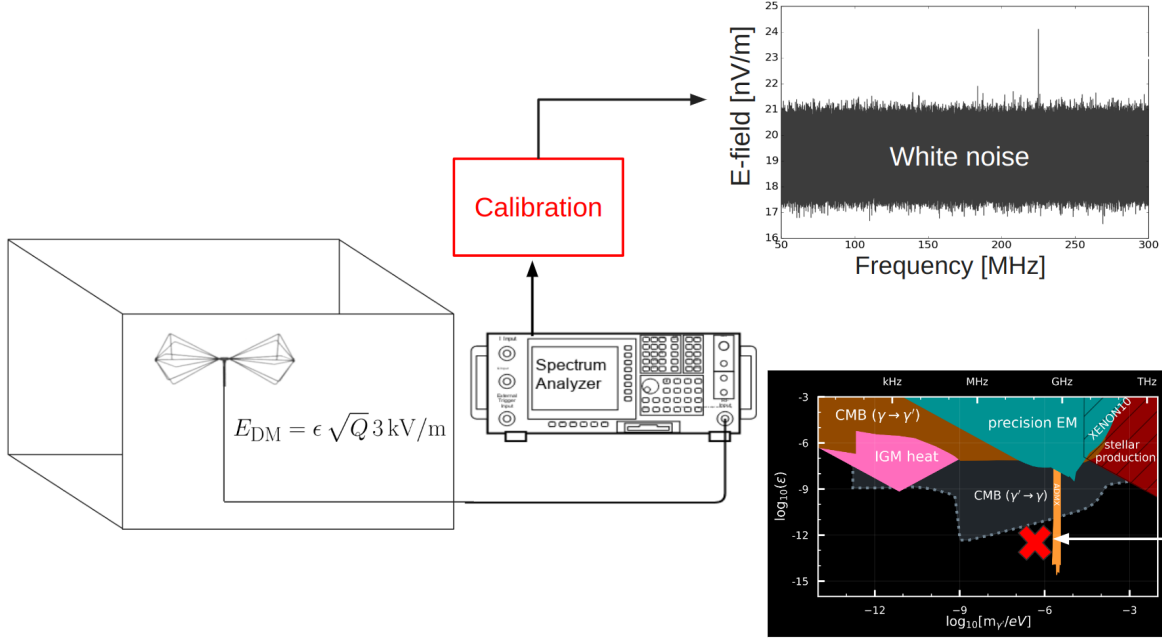


Figure 2.1: Overview of Dark E-field Radio experiment. The free space electric field strength was calculated in Sec. 1.4, and will be modified to include the Q of the cavity in Sec. 2.1.2. The design of the system is outlined in this chapter, while its performance is measured in Ch. 3. The use of the system, its calibration, and setting a limit are all discussed in Ch. 4. **comment: Remake this. Change E_{DM} to E_{ant} , 3kV to 4.5kV, change limit plot. Image from google slide called "schematic"**

577 details each piece of the system. Measurements of system performance are put off until Ch.
 578 3).

579 A note on experiment “run numbers”. Run 1A is the 50-300 MHz run. There have been
 580 four attempts at collecting run 1A data. The final, published data run was collected between
 581 May 10 and May 19, 2023, and is called run 1.4 or run 1p4 throughout my power points and
 582 file names. I will refer to this run interchangeably as run 1A or run 1.4. Strictly speaking,
 583 it should be run 1A.4, but if I change it now it will be inconsistent with file names.

584 **2.1 Sources of Power in Measured Spectrum**

585 This section will break down each term in the following equation for the input-referred power

$$P_i = \text{Thermal Noise} + \text{Dark Photon Signal} + \text{RFI} + \text{Amp Chain Noise} + \text{ADC Effects}/G, \quad (2.1)$$

586 where G is a gain factor. While convenient, this word equation is not rigorous and relies

587 on the following subsections 2.1.1 - 2.1.5 for definition.

588 **2.1.1 Thermal Noise**

589 **2.1.1.1 Blackbody Electric Field Density**

590 This subsection estimates the noise-like¹ electric field in free space due to black body ra-
591 diation. It assumes to be in *some* enclosure in that the ambient temperature is known to
592 be 300 K and not, for example, the 3.6 K of the sky. The enclosure considered is assumed
593 to be "black" in that all radiation impinging on its surface is absorbed. This assumption is
594 introduced in Sec. 2.1.1.2 and investigated further in Sec. 2.3.

595 Planck's law gives the black body spectral energy density as

$$u_\nu(\nu, T) d\nu = \frac{8\pi h\nu^3}{c^3} \frac{1}{e^{h\nu/kT} - 1} d\nu \quad \left[\frac{J}{m^3} \right]. \quad (2.2)$$

596 This is frequently written in terms of spectral radiance,

¹"Noise-like" simply means that the power contained in a signal is proportional to the bandwidth measured. Noise-like signals are more conveniently described as a power spectral density (PSD) which we will describe with the symbol S . As we will see, coherent signals that have finite width in frequency space $\Delta\nu_{\text{sig}}$ can share this property if the measurement bandwidth $\Delta\nu_{\text{RF}} \lesssim \Delta\nu_{\text{sig}}$, even though one wouldn't think of a coherent signal as being "noise-like"

$$B_\nu(\nu, T) d\nu = \frac{2h\nu^3}{c^2} \frac{1}{e^{h\nu/kT} - 1} d\nu d\Omega \quad \left[\frac{W}{m^2} \right]. \quad (2.3)$$

597 Integrating this isotropic radiance over a solid angle 4π sr as well as a small frequency
 598 band $\Delta\nu$ gives the flux density $|\mathbf{S}|$ (AKA, the magnitude of the Poynting vector),

$$\begin{aligned} |\mathbf{S}| &= \int_0^{4\pi} \int_\nu^{\nu+\Delta\nu} B_\nu(\nu, T) d\nu d\Omega \\ &= \int_0^{4\pi} \int_\nu^{\nu+\Delta\nu} \frac{2h\nu^3}{c^2} \frac{1}{e^{h\nu/kT} - 1} d\nu d\Omega \quad \left[\frac{W}{m^2} \right]. \\ &\approx \frac{8\pi h\nu^3}{c^2} \frac{1}{e^{h\nu/kT} - 1} \Delta\nu \end{aligned} \quad (2.4)$$

599 Poynting's theorem relates this flux density to the RMS electric field

$$|\mathbf{S}| = \frac{|E_{rms}|^2}{\eta} \quad \left[\frac{W}{m^2} \right], \quad (2.5)$$

600 where η is the impedance of free space. Equating Eqs. 2.4 and 2.5 and solving for the
 601 electric field gives

$$\frac{|E_{rms}|}{\sqrt{\Delta\nu}} = \sqrt{\eta \frac{8\pi h\nu^3}{c^2} \frac{1}{e^{h\nu/kT} - 1}} \quad \left[\frac{V}{m \cdot \sqrt{Hz}} \right], \quad (2.6)$$

602 and is plotted in Fig. 2.2.

603 Eq. 2.6 breaks up nicely into two regimes,

$$\frac{|E_{rms}|}{\sqrt{\Delta\nu}} = \begin{cases} \sqrt{\eta \frac{8\pi kT\nu^2}{c^2}} & \text{Rayleigh-Jeans regime } (h\nu \ll kT) \\ \sqrt{\eta \frac{8\pi h\nu^3}{c^2} e^{-h\nu/kT}} & \text{Wien approximation } (h\nu \gg kT) \end{cases} \quad \left[\frac{V}{m \cdot \sqrt{Hz}} \right]. \quad (2.7)$$

604 At frequencies and temperatures where the experiment is operated (< 300 MHz and
 605 300 K), $h\nu/kT \lesssim 5 \times 10^{-5}$ suggesting the Rayleigh-Jeans approximation is valid. At 300 K,

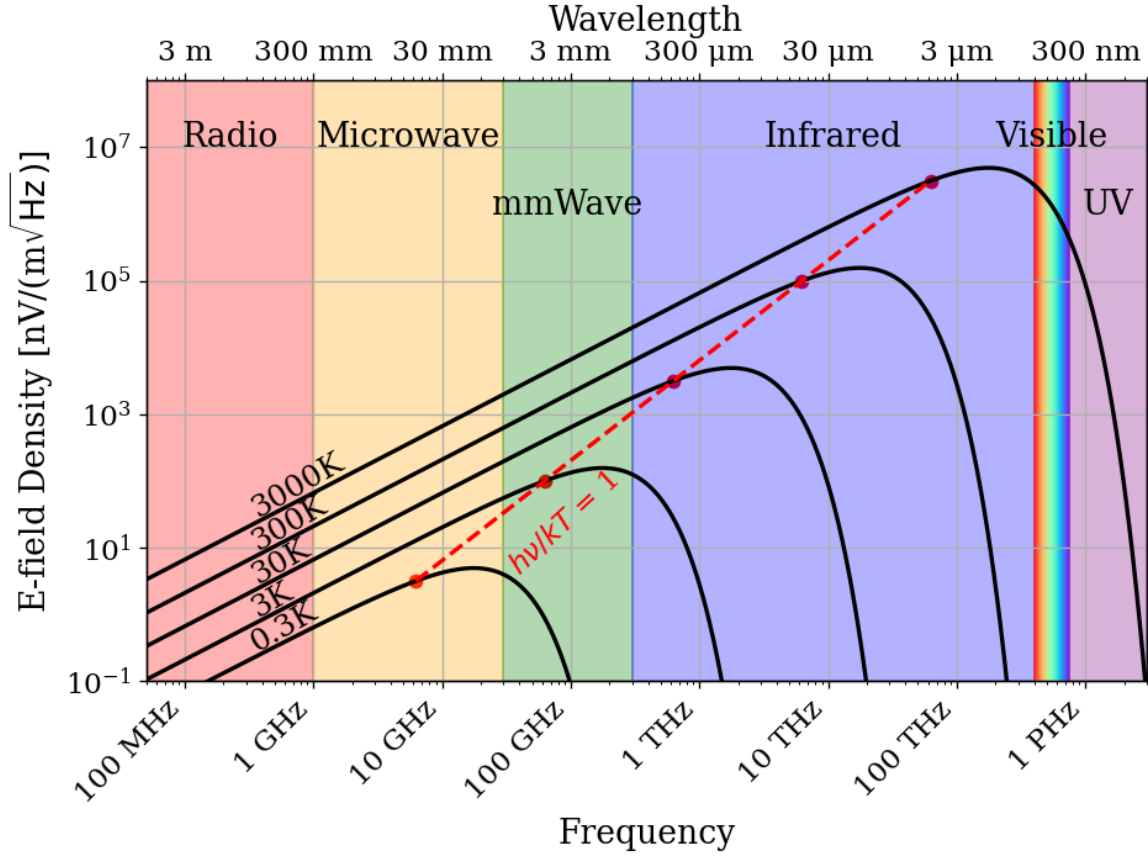


Figure 2.2: Blackbody electric field spectral density from radio to UV frequencies. A variety of temperatures are shown in black. The dashed red curve and red points indicate where along the black curves $h\nu = kT$, i.e. where Eq. 2.7 breaks up between the Rayleigh-Jeans regime to the Wien approximation. Note that these points are only a function of ν and T ; their vertical placement is chosen to lie on their respective curve but has no physical significance. The dark radio experiment is firmly in the Rayleigh-Jeans regime.

606 this yields electric field spectral densities of 1 and 6 nV/(m $\sqrt{\text{Hz}}$) at 50 and 300 MHz respec-

607 tively.

608 It is interesting to note, however, that for cryogenic experiments operating at a few GHz

609 and in the sub K range (A common technique; see, for example, [20–22]), $h\nu/kT \approx 1$ and

610 the full form of Eq. 2.6 must be used. This is shown at frequencies and temperatures to the

611 right of the red dashed line in Fig. 2.2.

612 2.1.1.2 Antenna Noise

613 An antenna's effective aperture, A_e [m^2], represents the effective area that it has to collect
614 power density or irradiance [W/m^2] from an incident Poynting vector,

$$P_A = |\mathbf{S}|A_e, \quad (2.8)$$

615 Where $|\mathbf{S}|$ is the magnitude of the incident Poynting vector, and P_r is the power received at
616 the antenna, which is available at its terminals.

617 A_e is a directional quantity that varies with the antenna's directivity $D(\Omega)$, where Ω
618 represents the solid angle around the antenna. It varies with frequency ν , though it is
619 generally discussed in terms of wavelength λ . Three matching parameters are introduced to
620 describe how much actual power the antenna is able to deliver to a transmission line; p the
621 polarization match of the wave to the antenna, m the impedance match of the antenna to
622 the transmission line and η_a the efficiency of the antenna which represents how much power
623 is absorbed compared to that lost to Joule heating of the antenna. p , m and η_a are all real,
624 dimensionless and vary between 0 and 1.

$$A_e \equiv \frac{\lambda^2}{4\pi} D(\Omega) p m \eta_a. \quad (2.9)$$

625 This definition follows [23], though some authors do not include p in the definition [24,
626 25].

627 A simple derivation of the direction-averaged effective aperture based on thermodynamics
 628 will provide intuition. An isotropic antenna placed in a cavity at temperature T will be
 629 illuminated by randomly polarized, isotropic radiation of the form given by the Rayleigh-
 630 Jeans limit of Eq. 2.4, $|\mathbf{S}| = 8\pi kT\Delta\nu\nu^2/c^2$. The power received by the antenna can be found
 631 by Eq. 2.8,

$$\begin{aligned}
 P_A &= \langle A_e \rangle \frac{1}{2} |\mathbf{S}| \\
 &= \langle A_e \rangle \frac{4\pi kT\nu^2}{c^2} \Delta\nu,
 \end{aligned} \tag{2.10}$$

632 Where the factor of 1/2 is introduced to account for the random polarization and the $\langle \rangle$
 633 indicate an average aperture over all angles around the antenna. If a resistor is placed in a
 634 second cavity, also at temperature T, it will deliver its Johnson-Nyquist noise power [26, 27]

$$P_R = kT\Delta\nu \tag{2.11}$$

635 into a matched transmission line. This is shown in Fig. 2.3. The second law of thermo-
 636 dynamics makes a very powerful statement here: the net power flow between the antenna
 637 and terminator must equal 0 if the two temperatures are indeed equivalent. This means
 638 $P_R = P_A$ or Eq. 2.10 = Eq. 2.12,

$$\langle A_e \rangle \frac{4\pi kT\nu^2}{c^2} \Delta\nu = kT\Delta\nu \tag{2.12}$$

639 or,

$$\begin{aligned}
 \langle A_e \rangle &= \frac{c^2}{4\pi\nu^2} \quad [\text{m}^2] \\
 &= \frac{\lambda^2}{4\pi}
 \end{aligned} \tag{2.13}$$

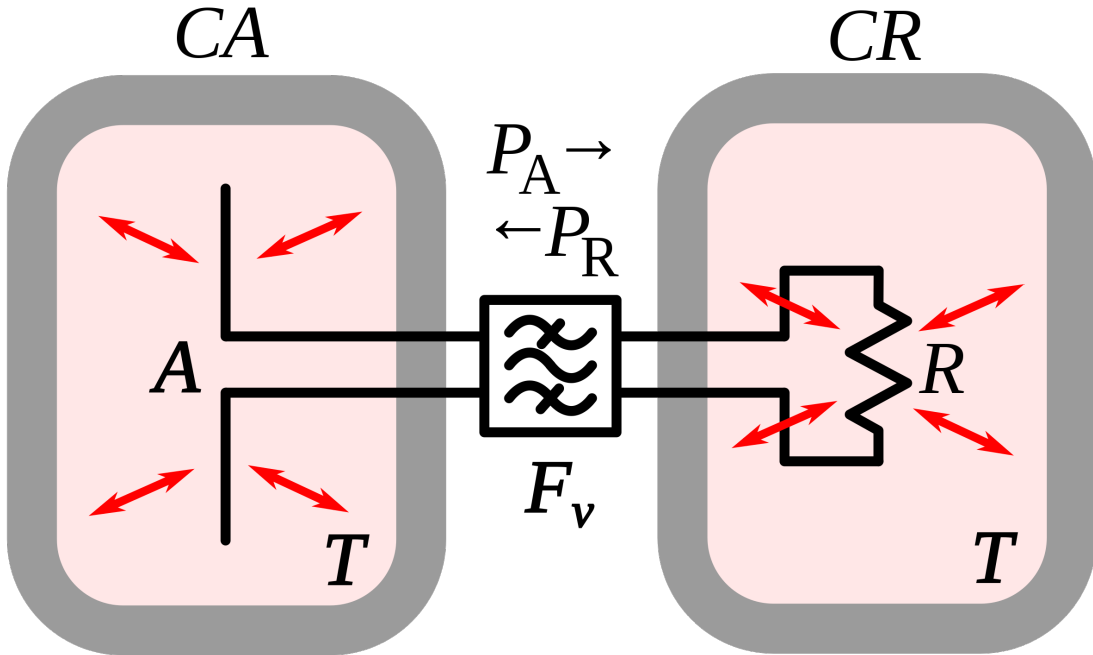


Figure 2.3: An antenna and matched resistor in cavities that are in thermal equilibrium. They are connected by a narrow filter permitting a narrow frequency band $\Delta\nu$. Image from Wikipedia, and is similar to the thought experiment proposed by Dicke [28].

640 This allows us to conclude that the power spectral density S_{ant} received by an antenna
 641 surrounded by an isotropic temperature is simply $kT\Delta\nu$ in the Rayleigh-Jeans limit of room
 642 temperatures and standard electronic frequencies. This result is independent of frequency,
 643 which can be understood by the reciprocal frequency dependence of the blackbody radiation
 644 (Eq. 2.4) and the average effective aperture (Eq. 2.13). The result is an antenna power which
 645 is equivalent to the well-known result for a resistor at 290 K,

$$S_{\text{ant}} = 3.9 \times 10^{-22} [\text{W}/\text{Hz}] = -174 [\text{dBm}/\text{Hz}]. \quad (2.14)$$

646 Note that S_{ant} indicates power spectral density and should not be confused with S which

647 indicates a Poynting vector.

648 **2.1.1.3 Dicke radiometer equation**

649 Equation 2.14 gave the mean of a power spectrum that is inherently noisy. We will now
650 show the origin of this spectrum.

651 An enclosure whose electrically-lossy walls contain free charge carriers at a finite tem-
652 perature will radiate incoherently by the fluctuation-dissipation theorem. This theorem is
653 the underlying principle of phenomena such as Brownian motion [29] and Johnson-Nyquist
654 noise [26, 27], but was not generally proven until 1951 by Callen and Welton [30]. The
655 random thermal fluctuation of the charge carriers will radiate a black-body spectrum. Ob-
656 serving the electric field in the time domain, one can imagine the radiation arriving at a
657 detector at a wide variety of random frequencies and phases. This is incoherent noise in that
658 at each time domain sample is independent of the one proceeding it ². The detector will
659 produce a voltage that can be modeled as Gaussian with zero mean and standard deviation
660 $\sigma = \sqrt{S_{\text{ant}} \Delta \nu_{\text{RF}} |Z|}$ where Z is the system impedance (here 50Ω). This is shown for a room
661 temperature antenna (or equivalently a room temperature resistor, see Fig. 2.3) in Fig. 2.4.

²The hidden assumption here is that blackbody radiation is totally incoherent. It actually has a coherence time $\tau_c \approx 2 \times 10^{-14} \text{ s}$ at 300 K [31]. For this statement to hold, the sample time $\tau_s \gg \tau_c$. For run 1A, $\tau_s = 1/800 \text{ MHz} = 1.25^{-9} \text{ s}$, 5 orders of magnitude more than τ_c

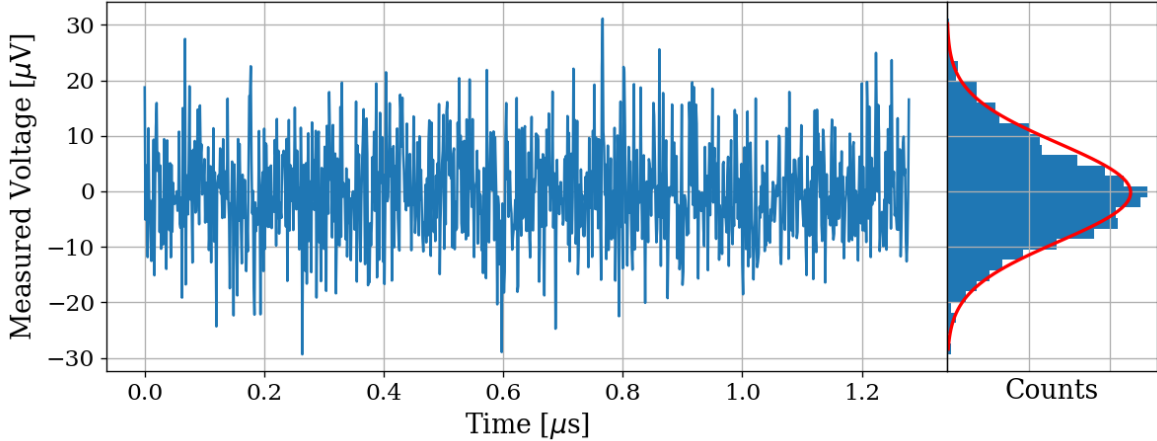


Figure 2.4: Simulated antenna noise voltage at room temperature in the time domain. Sample rate $\nu_s = 800\text{MHz}$ and number of samples $N = 2^{10} = 1024$. Bin width $\Delta\nu_{\text{RF}} = \nu_s/N \approx 800\text{ kHz}$. Data are binned and plotted as a histogram to the right. The best fit Gaussian is shown on the histogram in red with $\mu = -0.199\text{ }\mu\text{V}$ and $\sigma = 8.86\text{ }\mu\text{V}$. Counts have been normalized such that the bins add up to unity.

662 The next step is converting this time-domain voltage signal to a frequency-domain power
 663 spectral density (PSD). The first step is taking a discrete Fourier transform. This is usually
 664 implemented with an algorithm known as a fast Fourier transform (FFT), so that $\tilde{V} =$
 665 $\text{FFT}(V)$. In order to convert to a power spectrum, a non-trivial normalization prefactor
 666 must be included;

$$S = \frac{2}{N^2 |Z|} |\Re(\tilde{V})[:N//2]|^2, \quad (2.15)$$

667 where N is the number of samples, Z is the system impedance, and [:N//2] is Python notation
 668 for the second half of the samples contained in the \tilde{V} array. Performing this operation on
 669 the data in Fig. 2.4 yields the data in Fig. 2.5

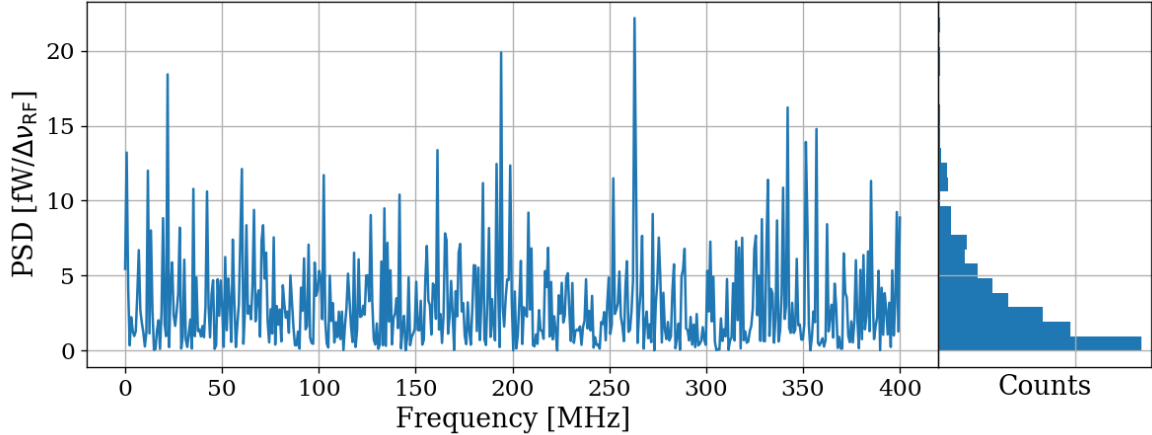


Figure 2.5: Simulated antenna noise power spectral density (PSD) at room temperature in the frequency domain. Sample rate $\nu_s = 800\text{MHz}$ and number of samples $N = 2^{10} = 1024$. Bin width $\Delta\nu_{\text{RF}} = \nu_s/N \approx 800\text{ kHz}$. Data are binned and plotted as a histogram to the right. Counts have been normalized such that the bins add up to unity.

670 The peculiar PDF of the histogram shown in Fig. 2.5 is known as a χ^2 distribution with
 671 1 degree of freedom and comes about because power is a positive-definite quantity and the
 672 standard deviation of the PSD is greater than it's mean.

673 However, by averaging many of these power spectra together, the central limit theorem
 674 dictates that we can expect the resulting PDF to be Gaussian. The transition from χ^2 to
 675 Gaussian distributed spectra is shown in Fig. 2.6.

676 Finally, this averaged power spectrum can be modeled with the Dicke radiometer equa-
 677 tion. The measured power (assuming only thermal noise) is given by

$$P_{\text{ant}} = kT\Delta\nu \left(1 \pm \frac{1}{\sqrt{\Delta\nu\tau}} \right) \quad [\text{W}]. \quad (2.16)$$

678 Here τ is the total acquisition time, and so $\Delta\nu\tau$ is equivalent to the number of spectra

679 that are averaged together. This can be nondimensionalized and written

$$\frac{P_{\text{ant}}}{kT\Delta\nu_{\text{RF}}} = 1 \pm \frac{1}{\sqrt{N}} \quad [\text{None}], \quad (2.17)$$

680 which will become important during data analysis which is the topic of Sec. 4.2.

681 For the remainder of this thesis, unless otherwise stated, it will be assumed enough
682 spectra have been averaged together that a PSD is Gaussian and scales with the square root
683 of total acquisition time according to Eq. 2.16.

684 Thus far the analysis has focused only on thermal noise, however there are other sources
685 of noise and interfering signals which must be considered, not to mention the actual dark
686 photon signal.

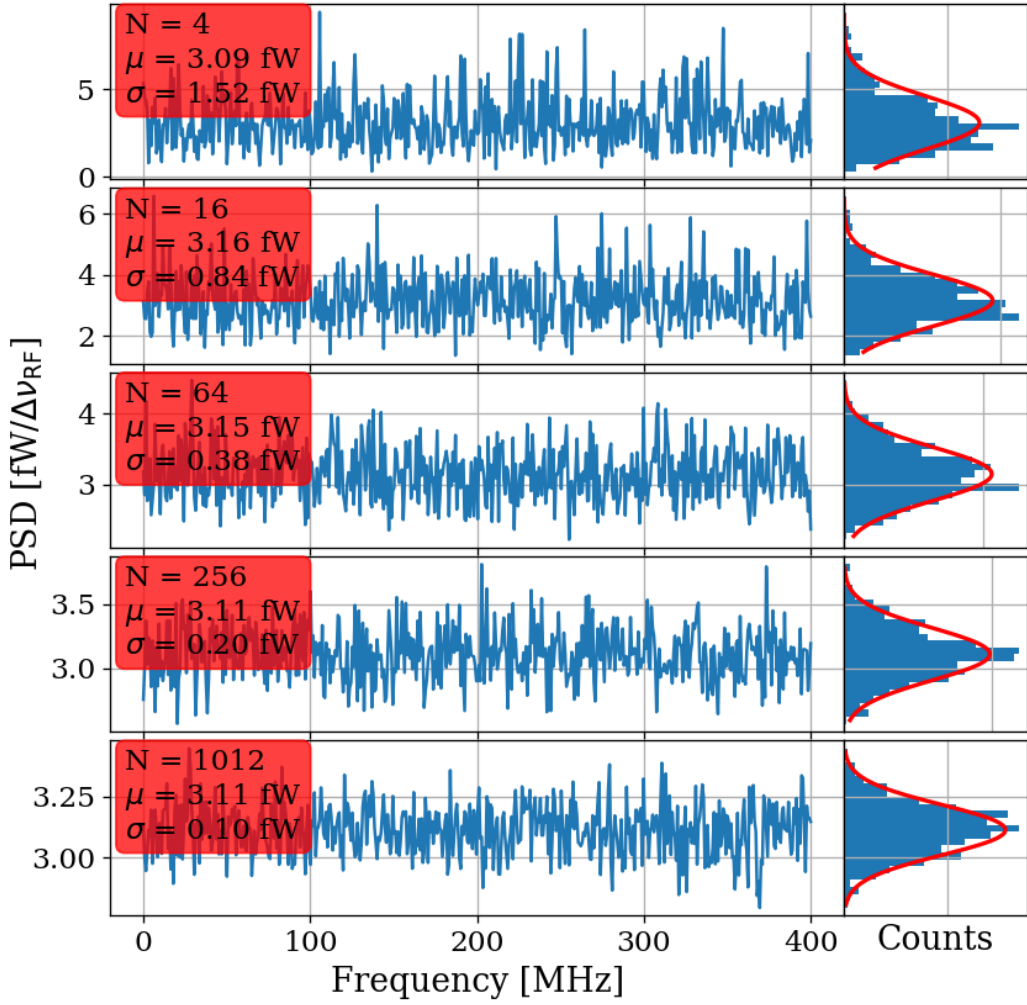


Figure 2.6: Effect of averaging on simulated antenna noise power spectral density (PSD) at room temperature in the frequency domain. Subplots show different numbers of averaged power spectra from $N = 4$ to 1024. Each subplot shows a factor of 4 times more averaging than the previous one. The Dicke radiometer equation predicts the standard deviation σ will scale like $N^{-1/2}$ once a large number of averages have been taken such that $\sigma \ll \mu$. Sample rate $\nu_s = 800\text{MHz}$ and number of samples $N = 2^{10} = 1024$. Bin width $\Delta\nu_{\text{RF}} = \nu_s/N \approx 800 \text{ kHz}$. Data are binned and plotted as a histogram to the right with a best-fit Gaussian shown in red. Counts have been normalized such that the bins add up to unity. Note that the Y-axis scale changes between subplots to show the improvement of the Gaussian fit. The standard deviation is indeed decreasing between plots.

687 **2.1.2 Dark Photon Signal**

688 The electric field of a kinetically mixed dark photon in free space $\mathbf{E}_{\text{ant}}^{\text{free space}}$ was shown in
689 Eq. 1.7. In a cavity, the E-field will be enhanced by the quality factor Q of the cavity. This
690 Q must be measured or simulated, but for this toy analysis, we will assume it to be known
691 ³. The E-field inside the cavity then is

$$\mathbf{E}_{\text{ant}} = \mathbf{E}_{\text{ant}}^{\text{free space}} \sqrt{Q}, \quad (2.18)$$

692 since Q is proportional to power, i.e. \mathbf{E}^2 . This E-field will then need to be converted from
693 a wave in the cavity to a wave in a 50Ω transmission line by an antenna. Similar to the
694 thermal noise of the previous section, this electric field will be converted via the effective
695 aperture of the antenna. Similar to Q , the aperture will be assumed to be known.

696 The total received power from a coherent signal inside the room then is

$$P = \frac{\mathbf{E}_{\text{ant}}^{\text{free space}^2}}{\eta} Q < A_e >, \quad (2.19)$$

697 where η is the impedance of free space.

698 The observed spread of the frequencies of the dark photon is an important effect that
699 determines system design. In the following paragraphs of this section, several sections of
700 Gramolin et al. [33] are summarized. Also note that the original calculation for the predicted
701 line shape appears to be Michael Turner in 1990 [34].

702 A simple model of the dark photon line assumes it is monochromatic, i.e. its line shape
703 is a delta function in the frequency-domain,

$$\nu_{\text{obs}} = \delta(\nu - \nu_{\text{DP}}). \quad (2.20)$$

³Typical values are in the ballpark of 100. Some experiments have ultra-high Q cavities $\approx 10^{10}$ [32]

704 This is consistent with its production add reference: misalignment mechanism/ch 1.

705 However, when observed in a frame other than its rest frame, the frequency of a (single)

706 dark photon will shift by an amount proportional to its kinetic energy

$$\nu_{\text{obs}} = \left(1 + \frac{v_n^2}{2c^2}\right) \nu_{\text{DP}}, \quad (2.21)$$

707 where ν_{obs} is the observed frequency of the n th dark photon, v_n is its velocity, c is the speed

708 of light, and ν_{DP} is its rest frequency. The end result will be a signal that has some spread

709 in frequency, $\nu_{\text{DP}}/(\Delta\nu) \equiv Q_{\text{DP}} \approx 10^6$, with a line shape given by 2.24.

710 By summing over an infinity of dark photons of random phases and velocities (sampled

711 from the relative velocity of the dark matter halo), each with a frequency given by Eq. 2.21,

712 one can construct a PSD of the dark photon signal as measured on earth, S [W/Hz].

713 When performing a measurement, one records the voltage V emerging from a detector

714 for a period of time greater than the coherence of the dark photon $\tau_{\text{FFT}} \gg \tau_c$. The Fourier

715 transform of $V(t)$ is denoted $\tilde{V}(\nu)$

716 The signal will have a total power

$$P_0 = \frac{1}{\tau_{\text{FFT}}} \int_0^{\tau_{\text{FFT}}} \frac{V(t)^2}{|Z|} dt = \int_0^{1/\tau_{\text{FFT}}} S(\nu)^2 d\nu, \quad (2.22)$$

717 which is a statement of Parseval's theorem.

718 The normalized line shape is defined by dividing by P_0 ; $\lambda(\nu) \equiv S(\nu)/P_0$. This has the

719 property of being normalized to unity,

$$\int_0^\infty \lambda(\nu) d\nu = 1. \quad (2.23)$$

720 Finally, the result for this normalized line shape is

$$\lambda(\nu) = \frac{2 c^2}{\sqrt{\pi} v_0 v_{\text{lab}} \nu_{\text{DP}}} \exp \left(-\frac{\beta^2 v_0^2}{4 v_{\text{lab}}^2} - \frac{v_{\text{lab}}^2}{v_0^2} \right) \sinh \beta \quad \left[\frac{1}{\text{Hz}} \right], \quad (2.24)$$

721 where $|v_0| \approx 220$ km/s is the circular rotation speed of the Galaxy at the radius of the sun

722 (approximately 8 kpc), $v_{\text{lab}} \approx 233$ km/s is the relative velocity of the Sun to the rest frame

723 of the Galaxy and

$$\beta \equiv \frac{2 c v_{\text{lab}}}{v_0^2} \sqrt{\frac{2 (\nu - \nu_{\text{DP}})}{\nu_{\text{DP}}}}.$$

724 Equation 2.24 is used to generate Fig. 4.14. Note the quality factor $Q_{\text{DP}} \approx 10^6$ as

725 mentioned above.

726 2.1.3 Radio Frequency Interference

727 Radio Frequency Interference (RFI) includes any coherent interfering signals which can be

728 detected by the experiment. While noise is better described as a power spectral *density*

729 [W/Hz] or electric field *density* [V/(m $\sqrt{\text{Hz}}$)], RFI is made up of more narrow lines and is

730 discussed in terms of power [W] or electric field [V/m]. In this experiment, RFI is mitigated

731 through the shielding effectiveness (SE) of the cavity. SE measurements and more details

732 about local RFI are discussed further in Sec. 2.5.1 and Sec. 3.2, and a plot of the local RFI

733 spectrum is shown in Fig. 3.14.

734 The peak RFI spike is at 186 MHz and approximately 100 $\mu\text{V}/\text{m}$, an energy density

735 of roughly 10^{-11} W/m². This will be reduced by the SE of the room (roughly 120 dB at

736 200MHz, see Fig. 3.11), but just like a coherent dark photon, it will be enhanced by the

737 Q/effective aperture. This will be right on the edge of detection, but in the actual data run,
 738 it was not detected.

739 **2.1.4 Amplifier Chain Noise⁴**

740 Any amplifier will have some noise which it adds to an incoming signal which will degrade
 741 the signal-to-noise ratio (SNR) of the measurement ⁵. A low noise amplifier (LNA) is an
 742 amplifier that has been specifically designed to minimize the noise contribution. This process
 743 is shown schematically in Fig. 2.7.

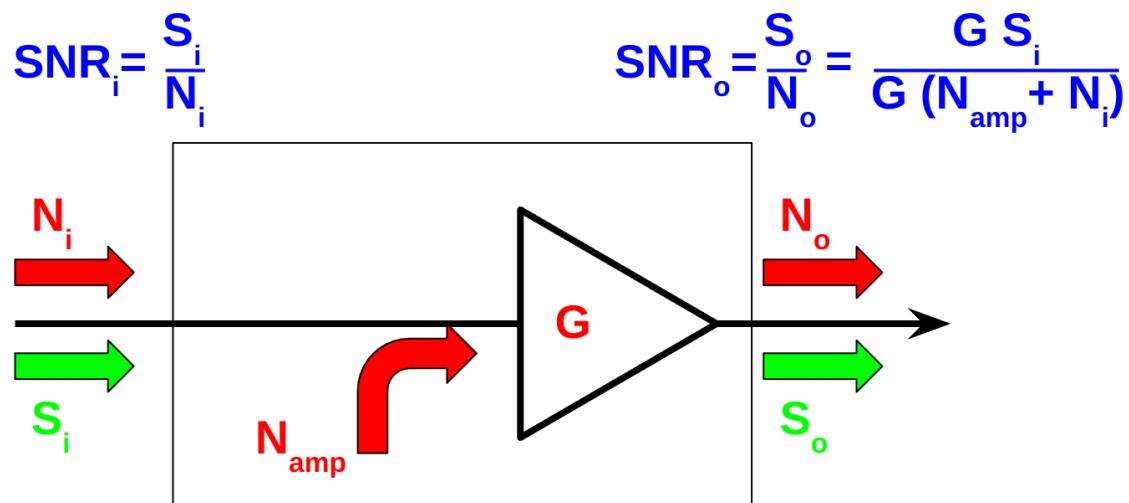


Figure 2.7: Schematic of LNA (with power gain G) adding input referred noise N_{amp} . Since N_{amp} is referred to the input, it can be directly added to the input noise which is itself input-referred. The ideal, noiseless amplifier is represented by the triangle, while the physical amplifier, including noise, is contained in the rectangle.

⁴Code for this section can be found at: <https://github.com/josephmlev/darkRadio/tree/master/thesis/ch2/CH2.ipynb>

⁵A great lecture on the subject by Prof. Greg Durgin can be found at [35]

744 The performance of an LNA is generally evaluated by its noise factor (F). F is defined
 745 to be the ratio of the SNR at the input of an LNA to that at its output.

$$\begin{aligned}
 F &\equiv \frac{\text{SNR}_i}{\text{SNR}_o} \\
 &= \frac{S/N}{[S G]/[(N + N_{\text{amp}})G]} \\
 &= \frac{1}{1/[1 + N_{\text{amp}}/N]} \\
 &= 1 + \frac{N_{\text{amp}}}{N},
 \end{aligned} \tag{2.25}$$

746 where S and N are the signal and noise [W] presented to the LNA respectively, N_{amp} is
 747 the input-referred noise added by the LNA, and G is the power gain. By factoring out the
 748 implicit $k \Delta\nu$ from $N = kT\Delta\nu$, we find

$$F = 1 + \frac{T_e}{T_0}, \tag{2.26}$$

749 where T_e is the noise temperature of a device and T_0 is the temperature of the system
 750 being measured by the LNA.

751 Note that following the same derivation as Eq. 2.25, it is simple to show that the noise
 752 figure of an attenuator at temperature T with loss L is given by

$$F_{\text{att}} = 1 + \frac{(L - 1)T}{T_0}, \tag{2.27}$$

753 where T_0 is the reference temperature defined above. If $T = T_0$, Eq. 2.27 simplifies to
 754 $F_{\text{att}} = L$

755 In order to standardize device specifications for across system applications, it is common
 756 to choose a reference temperature T_0 of 290K. If not specified, it is generally safe to assume
 757 this has been done.

758 Noise factor is simply defined in terms of noise figure,

$$\text{NF} \equiv 10\log_{10}(F). \quad (2.28)$$

759 When working with LNAs, all three measurements (T_e , F and NF) are frequently used,
 760 and one must use Eqs. 2.26 and 2.28 to convert between them.

761 One important generalization is that of a cascaded series of amplifiers, shown schemati-
 762 cally in Fig. 2.8.

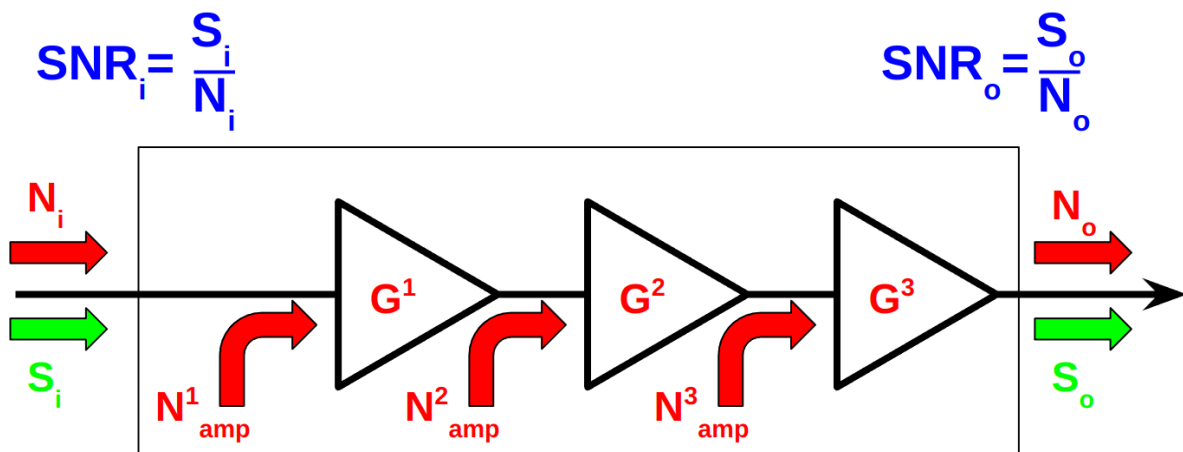


Figure 2.8: Schematic of cascade of $n = 3$ amplifiers and their added noise N_{amp}^n . Each amplifier has a gain of G^n . The SNR at the output is derived in Eq. 2.29. Note that superscripts in the figure and caption refer to the index of each component and are not exponents.

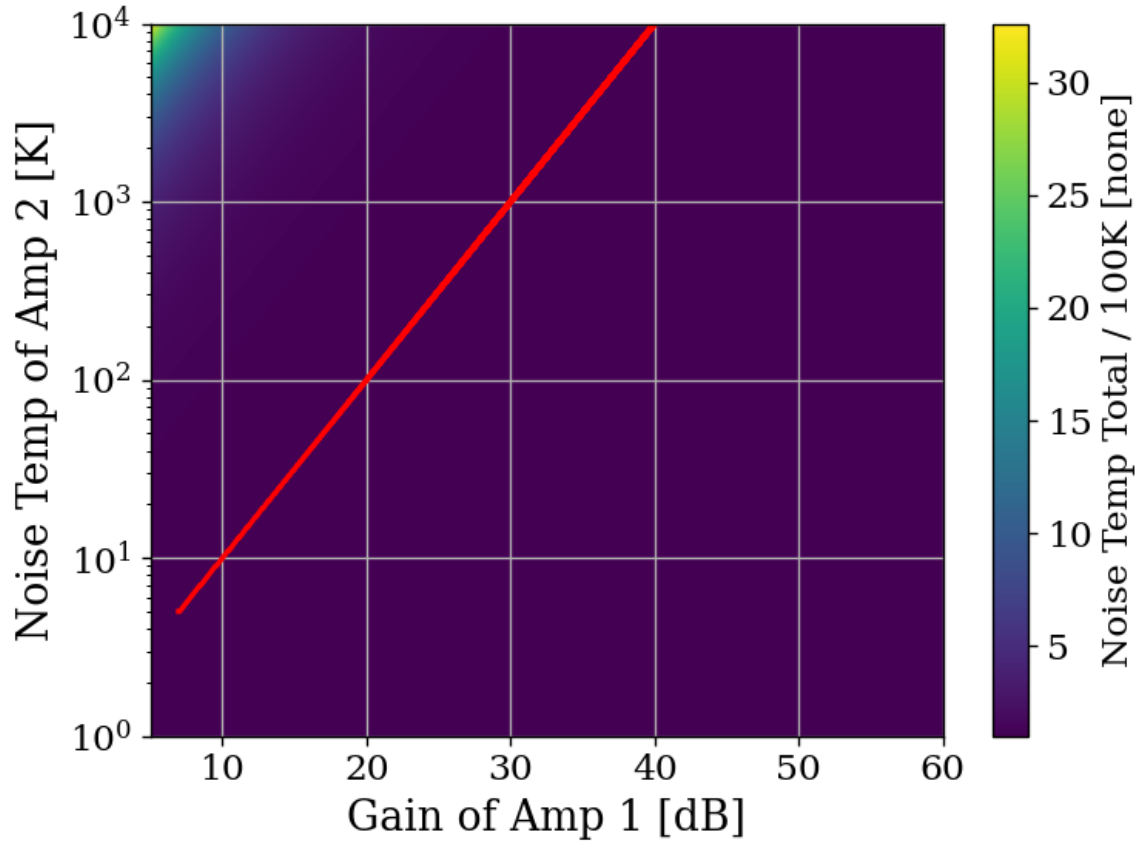


Figure 2.9: Cascaded noise temperature for a system with $n = 2$ amplifiers, normalized to noise temperature of amplifier 1 (the so-called LNA) = 100 K. Shown schematically (for $n = 3$) in Fig. 2.8. The first amplifier's noise temperature and gain (40 dB and 100 K, respectively) are roughly equivalent to the LNA used in phase 1A of the experiment[36]. The red curve shows where the system's noise temperature is 1% higher than LNA noise temperature. This shows that for a 40 dB, 100 K LNA, in order to change the system noise temperature by 1 K, a second-stage amplifier with a noise temperature of 10^4 would be required. Secondary amplifiers with noise temperatures closer to 500 K are realistic and inexpensive. Note that the red curve should continue but is cut off as a plotting artifact.

763 Here the total noise figure of n amplifiers can be shown to be

$$F_{\text{total}} = F_1 + \frac{F_2 - 1}{G_1} + \frac{F_3 - 1}{G_1 G_2} + \cdots + \frac{F_n - 1}{G_1 G_2 \cdots G_{n-1}}, \quad (2.29)$$

764 following the same derivation as Eq. 2.25. Since the noise temperature of a system depends

765 on the noise temperature a given amplifier divided by he gain which precedes it, a front-end
766 LNA with modest gain ensures the total noise figure of the the system is equal to it's noise
767 figure to very good approximation. This is shown in Fig. 2.9. We will use this approximation
768 and assert

$$\text{Amp Chain Noise} = \text{LNA Noise}, \quad (2.30)$$

769 Where LNA here is taken to mean the first gain stage in the amplifier chain
770 Noise figures are typically frequency dependent, though they vary slowly over frequency
771 and can be approximated as constant over narrow frequency bands. Noise figures are typically
772 given on the data sheet of the LNA [36], but can also be measured. Measurement of LNA
773 noise is covered in Sec. 3.1.1 and is shown in Fig. 3.4 (which is in good agreement with the
774 LNA's data sheet [36]).

775 The power contributed by the LNA's noise is simply given by

$$P_{\text{LNA}} = kT_e\Delta\nu \quad (2.31)$$

776 This is again the mean of a fluctuating power, just as 2.16.

777 2.1.5 ADC effects

778 “ADC effects” is a catch-all term that refers to power introduced by an analog-to-digital
779 converter. It contains are a three components, listed in order of importance;

$$\text{ADC Effects} = \text{Spurious Signals} + \text{ADC Noise Floor} \quad (2.32)$$

780 Equation 2.29 shows that (power) gain G introduced before a noisy element in the RF
781 chain will reduce the relative contribution of that noise (power) by a factor of G . The same
782 idea applies to ADC effects, though one must be careful with the language used to describe
783 this; spurious *signals* are not noise, and the experiment's output *is* mostly noise.

784 **2.1.5.1 Spurious signals**

785 Spurious signals (also known as spurs) are coherent signals that are introduced into the signal
786 path at the ADC⁶. They are likely caused by candidates caused by RFI due to various clocks
787 in the PC in close proximity to the ADC. The coherence of spurs means they will pop up
788 above the noise with more averaging. Spurs don't degrade the SNR of the experiment in
789 the same way a noisy amplifier chain would; instead, they produce false positive candidates,
790 which must be excluded, similar to RFI discussed in Sec. 2.1.3. Similar to ADC noise,
791 they can be measured easily by terminating the input of the ADC and scanning. They are
792 investigated in Sec. 3.3.2 and shown in Fig. 3.15, where they are shown to be nearly negligible,
793 having been mitigated by the gain of the system. There is a single spur detected after a few
794 days (see Sec. 4.2.5), but for this simple analysis, we will assume spurs are negligible.

795 **2.1.5.2 ADC noise**

796 ADC noise can simply be measured by terminating the input and taking a scan. This is the
797 same procedure used to measure spurs and can be seen in Fig. 3.15. The result is that ADC

⁶Note that these spurs described here are not the same as the spurs that are described by the ADC specification *spur free dynamic range* (SFDR). SFDR is measured in dBc, i.e. *relative* to a carrier. Since our "carrier" is broadband noise, each bin produces some spurs, which are -66 dBc [37] relative to itself. The aggregate of these spurs is also broadband and averages down with the experiment's noise. The SFDR spurs are negligible for an experiment that looks at a noise-like background.

798 noise is $\approx -130\text{dBm}/47.7\text{Hz}$; a factor of 10^5 lower than the thermal noise of the experiment
 799 $\approx -81\text{dBm}/47.7\text{Hz}$, both output-referred⁷, which agrees with the ADC's data sheet [37].
 800 Since ADC noise follows the same scaling as the experiment's thermal noise (Eq. 2.16), this
 801 factor of 10^5 is independent of averaging, and ADC noise is totally negligible.

802 **2.2 Toy Analysis**⁸

803 With each of the terms of Eq. 2.1 defined in the previous section, we will now perform and
 804 view several simulations of a simplified dark photon signal on a simplified background. This
 805 section should provide intuition about the process of detecting a weak, narrow signal on a
 806 background PSD of thermal noise. It is assumed the noise has been averaged a sufficient
 807 number of times such that its PDF is Gaussian (discussed in Sec. 2.1.1.3). Furthermore,
 808 following the discussion of Sec. 2.1, Eq. 2.1 can be simplified by setting RFI and ADC
 809 Effects to zero and combining Thermal Noise (300 K) with Amp Chain Noise (100 K) into a
 810 single term which represents the total of the noise in the whole system, $S_{\text{sys}} = P_{\text{sys}}/\Delta\nu_{\text{RF}} =$
 811 $k(T_{\text{ant}} + T_{\text{LNA}})$. With these simplifications, the input-referred measured power of Eq. 2.1
 812 reduces to

$$P_i = P_{\text{DP}} + kT_{\text{sys}}\Delta\nu_{\text{RF}} \left[1 \pm \frac{1}{\sqrt{N}} \right], \quad (2.33)$$

813 where $T_{\text{sys}} \equiv 400$ K, realistic for the experiment that is being simulated. Also, note that this
 814 equation assumes the dark photon's line shape is much more narrow than $\Delta\nu_{\text{RF}}$ such that the

⁷Technically it doesn't matter where they are referred since they are taken in ratio. As long as they are referred to the same point!

⁸Code for this section can be found at: <https://github.com/josephmlev/darkRadio/tree/master/thesis/ch2/toyAnalysis.ipynb>

measured input-referred dark photon power is independent of $\Delta\nu_{\text{RF}}$. In the simulations, the line shape will be modeled as a delta function as in Eq. 2.20. The signal will be introduced simply by adding some power in a single bin to a Gaussian background in the frequency-domain. Performing an FFT on a perfect (discretized) sine wave can cause it's power to be split among adjacent bins depending on the ratio of the sample rate to the sine wave's frequency. This can be minimized by windowing the time-domain data as is discussed in Ch. 2 Sec. 2 of Ben Godfrey's thesis [38]. This effect is avoided by working in the frequency domain and adding power to a single bin which is the method used here. A reminder that throughout this thesis, code is available at github and is linked in the footnote of each section title.

With a simple simulation framework in place, we can now begin to generate signal-containing-spectra. Figure 2.10 qualitatively shows the 400 K system noise (input-referred antenna plus LNA) averaging down, leaving a small signal visible. Further subsections in this section will quantify this.

With a basic conceptual framework in place, it is now simpler to quantify signal detection and the uncertainty on how many averages are required to detect a signal and have that detection be significant in that it isn't a random fluctuation (false positive).

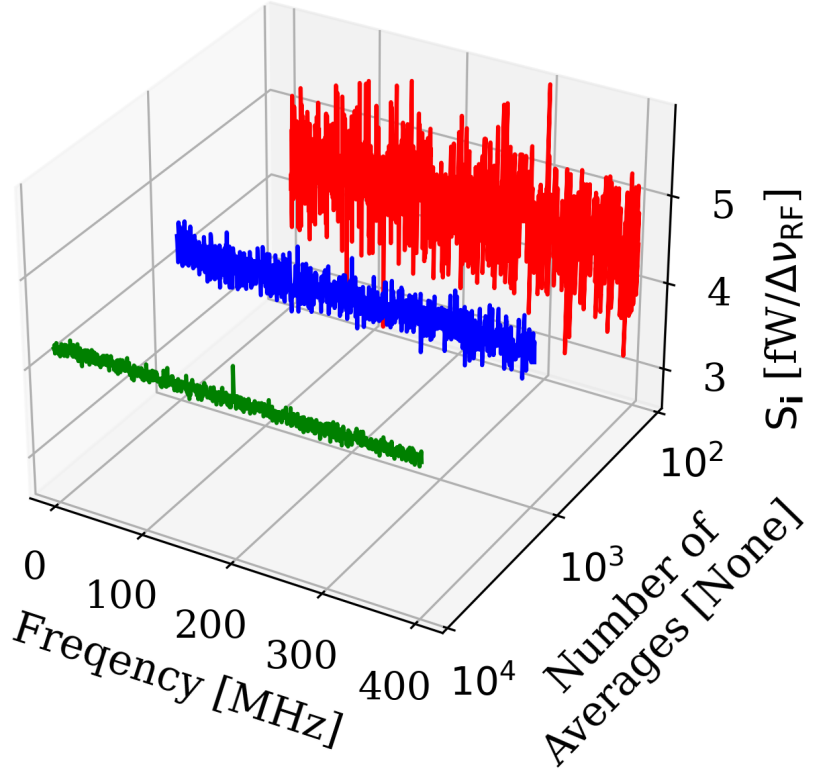


Figure 2.10: Input-referred power spectral density from simplified simulation illustrating noise averaging down to reveal a persistent, software-injected, dark photon proxy signal. The red, blue and green spectra represent 100, 1,000 and 10,000 averages, respectively. The power of the signal P_{DP} is set to 0.4 fW and it only occupies a single bin. The mean of the noise is $\approx 4.3 \text{ fW}/\Delta\nu_{RF}$ where $\Delta\nu_{RF} \approx 0.78 \text{ MHz}$. The standard deviation ranges between $0.41 \text{ fW}/\Delta\nu_{RF}$ and $0.041 \text{ fW}/\Delta\nu_{RF}$ for 100 and 10,000 averages respectively. Note that this factor of 10 reduction in noise is predicted by the Dicke radiometer equation Eq. 2.16 for a factor of 100 times more averaging, as is shown in the red and green curves. Noise represents a 300 K antenna into a 100 K LNA for a total system temperature of 400 K. Signal is in a single bin at 200 MHz with a delta function line shape, defined in Eq. 2.20.

832 2.2.1 Signal significance

833 The problem of the extraction of signal from noise is fundamentally a statistical one since,
 834 in general, both the signal and noise are random variables. A method for computing a

835 *significance threshold* (ST) must be established, such that any bin containing more power
836 than this threshold is X % significant. In this way, it is possible to have some known
837 confidence a given signal was not just a random fluctuation.

838 The probability that all N bins are less than z standard deviations $z\sigma$ for a standard
839 Gaussian distribution is given by

$$P(\max < z\sigma) = \left\{ \frac{1}{2} \left[1 + \operatorname{erf} \left(\frac{z}{\sqrt{2}} \right) \right] \right\}^N, \quad (2.34)$$

840 where P is the probability, $\operatorname{erf}(z)$ is the standard error function and z is real. Setting
841 this equal to 100%–X (where X is the *significance* or the desired probability a fluctua-
842 tion crosses the $z\sigma$ threshold assuming no signal), and inverting $\operatorname{erf}(z)$ yields a significance
843 threshold (ST). A convenient significance that was used in [39] is X = 5% corresponding to
844 a 5% probability that an observed fluctuation above this ST is due to chance rather than a
845 significant effect (i.e., a signal). A 5% ST for $2^{10}/2 = 512$ frequency bins⁹ works out to 3.9σ .

846 It should be noted that it is common in physics to discuss “ 5σ significance”. This means
847 that a given experiment has a $1 - \operatorname{erf}(5/\sqrt{2})$ probability (about 1 in 3×10^6) of a false positive.
848 The analysis of these normal spectra involves testing many independent frequency bins to see
849 if any one of them exceeds some threshold. It is helpful to view these bins as “independent
850 experiments”, each involving a random draw from the same parent Gaussian distribution.
851 In this context, we discuss global significance (all of the bins) in contrast to local significance
852 (a single bin). Setting a global 5% significance threshold is equivalent to setting a local

⁹Note that a real FFT produces half the number of frequency bins as an output compared to the time domain sample it received, hence the factor of 2 established in Fig. 2.4

853 threshold of 3.9σ given 512 bins.

854 One concept that can assist in choosing the significance is known as the *cost* of a decision.

855 If an experiment requires a facility that charges by the hour and where the schedule is

856 set years in advance, a false positive is quite expensive since it will lead to publicity and,

857 ultimately, humiliation. A follow-up experiment will have to take out more expensive time

858 to verify the results, and until that happens, theorists will spend their time rewriting physics

859 to explain the result of a random fluctuation. In this case, the global significance should

860 be quite low to avoid these high-cost outcomes, hence the 5σ discussed in the previous

861 paragraph.

862 In the case of the dark radio experiment, a false positive is quite inexpensive. If a signal

863 is detected, just repeat the experiment. For run 1A, this is 9 days of averaging which is

864 mostly passive and is little more than an annoyance. If a signal is detected at the same

865 frequency, things become interesting. This concept of cost is discussed formally in Appendix

866 1 of Extraction of Signals From Noise by Wainstein and Zubakov [40].

867 For this reason, a significance of 5 % (i.e. 5 % chance of a false positive) is acceptable

868 for this experiment, where it is certainly not acceptable at the LHC.

869 **2.2.1.1 Computing an exclusion limit**

870 With the significance threshold (ST) defined for a spectrum containing a signal in the previ-

871 ous subsection, we turn briefly to the concept of an exclusion limit. In the actual experiment,

872 no signals were detected. In this case, the null result must be translated into an exclusion

873 limit, as in Fig. 5.2. While this section on toy analysis looks at small signals riding on noise

874 spectra, it can be easy to lose sight of the fact that no signal was observed.

875 It is tempting to draw a line above the spectrum, claim no signals were observed above
876 it, and cite that as the exclusion limit. This is the red dashed line in Fig. 2.11. However,
877 this line is riding on the thermal background and is actually significantly higher than the
878 true exclusion limit, which is shown in dashed green. The mean μ must be subtracted from
879 this upper (red) line to compute the exclusion limit. In Fig. 2.12, the exclusion limit is
880 pushed down with additional averaging, resulting in the detection of a small signal shown as
881 an orange dot. The frequency-dependent exclusion limit from the actual run 1A data run is
882 shown in Fig. 4.8.

883 With the derivation of the significance threshold complete, the next subsection will focus
884 on predicting the amount of time.

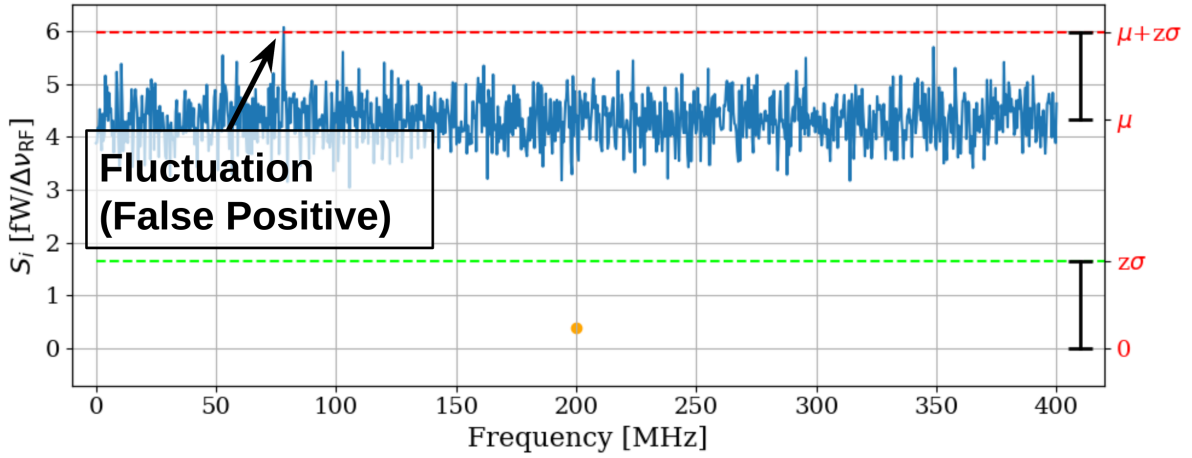


Figure 2.11: Simulated, input-referred noise spectrum containing small signal at 200MHz. The signal power = 0.4 fW, system temperature = 400 K and $N_{avg} = 100$; the same as is shown in the red spectrum of Fig. 2.10. The 0.4 fW signal is shown as an orange point. This power is added to the random background, so the measured power in the bin at 200 MHz is a Gaussian random variable given by Eq. 2.33; the mean is shifted up by the power contained in the signal. The dashed red line shows $\mu + z\sigma$, where z was derived in section 2.2.1. The detection threshold (dashed green line) is the red line minus the mean, $(\mu + z\sigma) - \mu = z\sigma$. This shows that the detection threshold is set by *fluctuations* of the measured power spectrum and not its mean. Note the detection at approximately 75 MHz; this is a random fluctuation and is expected to occur in 5 out of 100 simulations of these spectra since the significance used to calculate the ST was set at 5%.

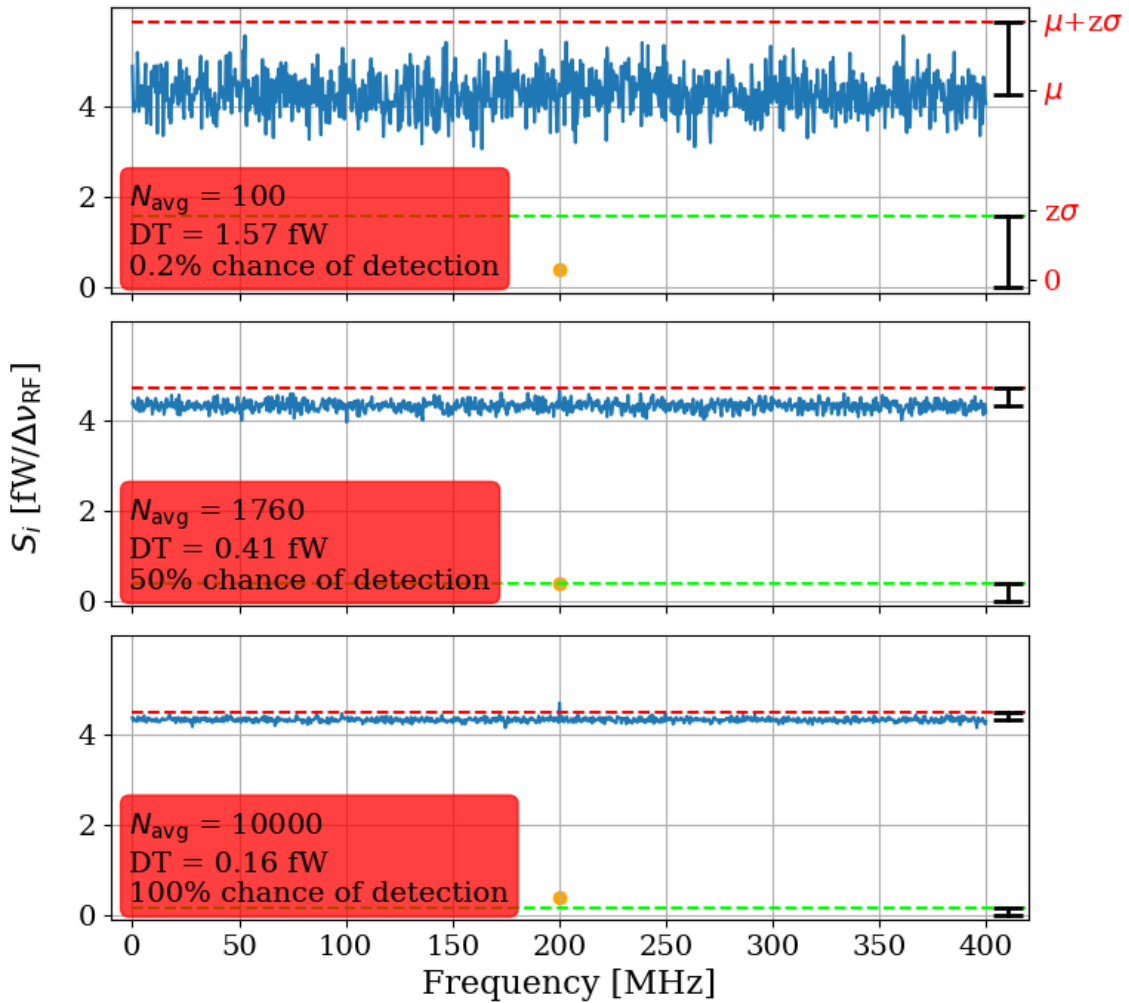


Figure 2.12: Simulated, input-referred noise spectrum containing small signal at 200MHz. The signal power = 0.4 fW, system temperature = 400 K and N_{avg} = 100, 1,760 and 10,000; the first and last are shown as the red and green spectra respectively in Fig. 2.10. The 0.4 fW signal is shown as an orange point. The chance of detection is computed via a simple Montie Carlo where 100,000 similar spectra containing noise and signal are generated, and the number of times the measured power at 200 MHz is greater than $\mu + z\sigma$ (red dashed line). The full set of statistics from this Montie Carlo is shown in Table 2.1. The detection threshold (DT, dashed green line) is $(\mu + z\sigma) - \mu = z\sigma$. Note that red labels on the right Y-axis are suppressed for the second and third subplots to prevent clutter, but they are the same as the first subplot

885 **2.2.2 Predicted time to detection**

886 To conclude this subsection, Fig. 2.13 fills in the gaps between the three sub-plots shown
887 in Fig. 2.12. The continuous detection threshold is shown to decrease following $1/\sqrt{N}$
888 shape given by Eq. 2.16. The intersections with this curve and the $1-\sigma$ uncertainty of the
889 background give the $1-\sigma$ uncertainty on the number of averages required for a known signal
890 and background. Table 2.1 summarizes the statistics for the probability of detection for a
891 few numbers of averages.

Number of Averages	True Pos. [%]	False Neg. [%]	False Pos. [%]	True Neg. [%]
100	0.2	99.8	5.7	94.3
971	16.3	83.7	5.5	94.5
1,760	49.8	50.2	5.7	94.3
2,782	83.8	16.2	5.7	94.3
10,000	100.0	0.0	5.6	94.4

Table 2.1: Statistics of simple Monte Carlo simulation for the probability of signal detection in the toy analysis. Number of averages chosen based on Fig. 2.13. 100 and 10,000 averages show extreme cases, 1760 is a 50% chance of detection, and the two remaining values show the $\pm 1\sigma$ uncertainty band (shaded red region in Fig. 2.13).

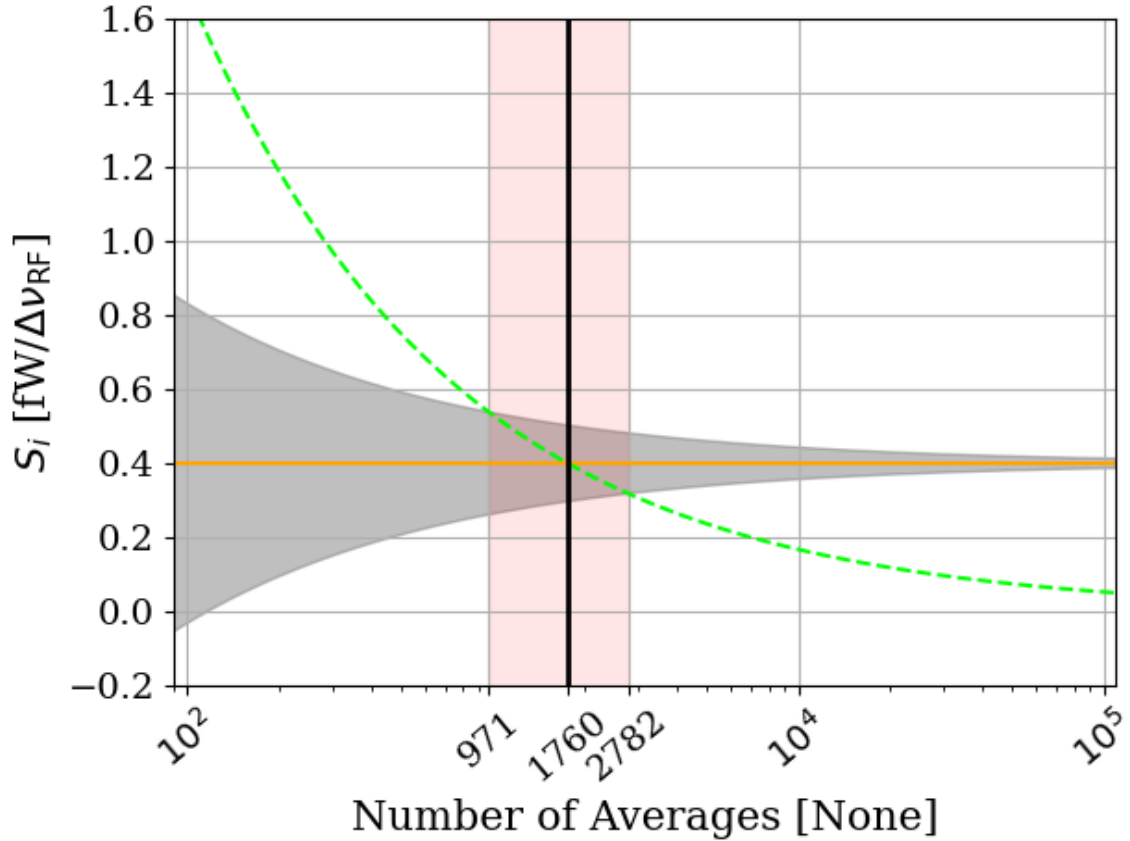


Figure 2.13: Predicted time to detection for the toy analysis spectra shown throughout this section. This is a companion to Fig. 2.12 and shows all numbers of averages between the three subplots shown in that figure, though only at a single frequency bin; 200 MHz in the case of the previous figures in this section. Orange line represents the known, injected signal, shown as orange points in Fig. 2.12. Gray shaded region shows the standard deviation of the noise σ , which is equivalent to the uncertainty on the measured power. It is given by Eq. 2.16, and scales with the square root of time. Dashed green curve is the exclusion limit defined in Sec. 2.2.1.1. It is also shown as a dashed green line in Fig. 2.12. Finally, the red shaded region shows the intersection of the exclusion limit (dashed green) with measurement uncertainty (shaded gray), which gives the $\pm 1\sigma$ uncertainty on the number of averages required to detect the signal. The detection statistics from a simple Monte Carlo simulation at a few points from this plot are shown in Tab. 2.1. This figure is a recreation of Fig. 3 in [4].

892 **2.3 Thermal Noise in a Cavity: Thermal Wiggles**

893 This section is concerned with the topic of variations of thermal noise emerging from a cavity;
894 “Thermal Wiggles”. Throughout this experiment, this was a challenging concept since the
895 theory outlined in Sec. 2.3 predicts the experiment will measure a frequency-independent
896 noise spectrum, and it doesn’t. This theory will be expanded upon, the data that seem
897 not to conform to this theory will be presented, the reasons for this disagreement will be
898 discussed, and finally, an experiment that tests this understanding will be presented.

899 **2.3.1 Theory of thermal radiation in a cavity**

900 In his 1946 paper The Measurement of Thermal Radiation at Microwave Frequencies [28],
901 Robert Dickie presented a thought experiment to derive the aperture of a matched antenna
902 from thermodynamic arguments. This was previously discussed in Sec. 2.1.1.2.

903 To recap the argument; if an antenna (in a black cavity) and matched load are matched
904 to a transmission line and in thermal equilibrium (the situation presented in Fig. 2.3), the
905 net power flow in the line must be zero by the second law of thermodynamics. If there was
906 a power flow, one of the environments would warm up, resulting in spontaneous pumping of
907 heat. An interesting way to model this situation is by treating the antenna as an aperture
908 in the cavity, as pointed out in [41].

909 A simpler model removes the antenna and load altogether. Although removal of the
910 antenna also removes the ability to perform the measurement, this is a useful thought exper-
911 iment. In Fundamentals of Statistical and Thermal Physics [42], F. Reif uses four examples

912 to explore the radiation field $f_\alpha(\kappa, \mathbf{r})$ (wave vector κ at position \mathbf{r} with polarization α)
 913 within cavities connected by an aperture (see Fig. 2.14). All cavities and materiel contained
 914 within them are presumed to be in thermal equilibrium. As we shall see, this function is
 915 independent of position, direction, polarization and specifics of the cavity. It can be written
 916 simply as $f(|\kappa|)$, where the dependence on wave number is simply given by Eq. 2.6.

$$f_\alpha^{(1)}(\kappa) = f_\alpha^{(2)}(\kappa)$$

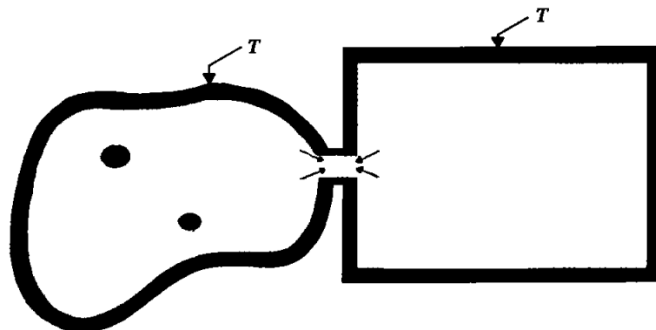


Figure 2.14: Two cavities in thermal equilibrium of arbitrary shape, material and physical contents contain equivalent radiation fields $f_\alpha(\kappa, \mathbf{r})$. Figure from Reif [42].

- 917 1. **Independence of Position:** The radiation field inside an enclosure is homogeneous,
 918 meaning $f_\alpha(\kappa, \mathbf{r}) = f_\alpha(\kappa)$, independent of position \mathbf{r} . If the radiation field depended
 919 on position, two identical bodies at temperature T placed at different points in the
 920 enclosure would absorb different amounts of radiation, leading to a temperature dif-
 921 ference.
 922 2. **Independence of Direction:** The radiation field is isotropic, meaning it depends
 923 only on $|\kappa|$ and not its direction. If this were not true, then bodies placed in the
 924 enclosure would absorb different amounts of energy based on orientation.

925 3. **Independence of Polarization:** The radiation field is unpolarized, meaning $f(|\kappa|)$
926 is independent of the polarization index α . If it depended on polarization, bodies
927 surrounded by polarizing filters would absorb different amounts of radiation depending
928 on the orientation, leading to temperature differences.

929 4. **Independence of Enclosure Shape and Contents:** The function $f(|\kappa|)$ is inde-
930 pendent of the shape, volume, and material of the enclosure, as well as the bodies
931 contained within. The argument is that if $f^{(1)}(|\kappa|)$ and $f^{(2)}(|\kappa|)$ were different for two
932 enclosures at the same temperature T , then connecting them would result in unequal
933 radiation transfer. Therefore, $f(|\kappa|)$ must be the same across different enclosures.

934 To further flush out argument four, picture a photon entering a metallic cavity (emissivity
935 < 1) through a small hole as in Fig. 2.15. At each bounce, the photon has a probability of
936 absorption given by the emissivity (a photon hitting a perfect black body has a 100% chance
937 of being absorbed). As long as the geometries of the cavity and aperture allow a photon to
938 bounce many times before it escapes, even a highly reflective cavity will behave like a black
939 body. This is because when a photon enters, it is likely to be absorbed and a new photon will
940 be emitted with a random wavelength drawn from the blackbody spectrum corresponding
941 to the temperature of the walls. (Fig. 2.2).

942 The conclusion is rather surprising; a cavity with a small aperture will behave as a
943 black body, and the spectrum emanating from a black body is a universal function that is
944 independent of the cavity and its modes. Therefore, **a well-matched antenna in a cavity**
945 **will not measure the modal structure of the cavity.** This seems to defy intuition.

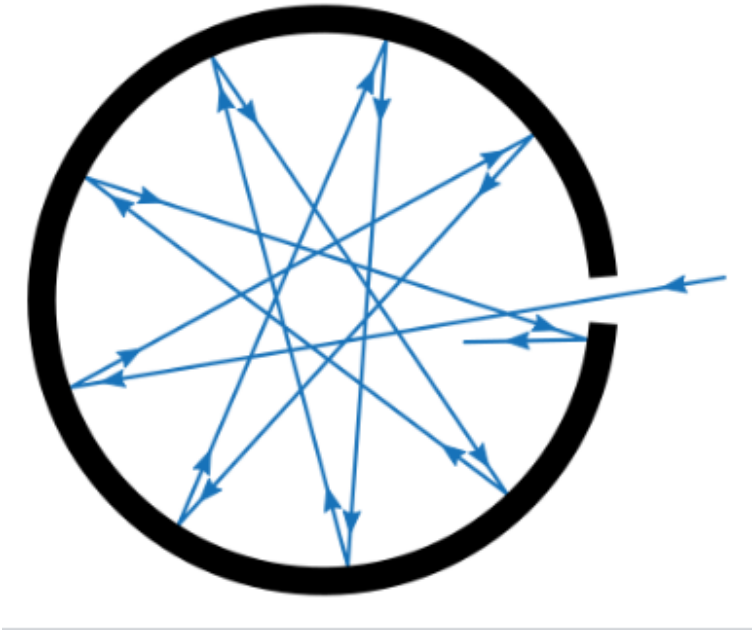


Figure 2.15: A cavity with a small hole behaves like a black body as long as the probability of absorption $\ll 1$. The probability of absorption at each reflection is given by the emissivity, so the total probability of *reflection* is the emissivity raised to the power of the average number of bounces. Figure from Wikipedia.

946 Cavities are resonators, and resonators... resonate?

947 The resolution to the seeming discrepancy is that this intuition only holds outside of
948 equilibrium, a situation that is nearly ubiquitous in engineering contexts. A resonant cavity
949 has the resonance it does because photons are being pumped in faster than they can be
950 absorbed by the walls and remitted with a thermal distribution. In this out-of-equilibrium
951 case, the photons interfere in such a way as to excite cavity modes. Turn the amplitude of the
952 source down to $\approx kT$ and the modes vanish. This case, among others, will be investigated
953 in the following subsections.

954 **2.3.2 Inspection of thermal noise spectra**¹⁰

955 The theory outlined above predicts the (input-referred) spectrum of an antenna in a cavity
956 should not vary with frequency if there is thermal equilibrium between the cavity and the
957 receiver system¹¹. A real measurement will take place after an amplifier (in other words,
958 will be output-referred), and will vary due to the gain and noise figure of the amplifier. A
959 simple way to correct for the amplifier is to compare the spectrum between an antenna and
960 a terminator since both will have identical gain and amplifier noise contributions. Since we
961 are more focused on the qualitative *shape* of the spectrum and not absolute input referred
962 power, this method is acceptable. A comparison of antenna and terminator data from an
963 identical amplifier chain is shown in Fig. 2.16.

964 The variations are unexpected in light of the theory presented in the previous subsection.

965 In the following subsection, the thermal spectrum emerging from a simple resonator will be
966 presented.

¹⁰Code for this section can be found at: https://github.com/josephmlev/darkRadio/tree/master/daqAnalysisAndExperiments/run1p4/thermalNoiseVsH/thermalWiggles_writeup.ipynb

¹¹this assumes $h\nu \ll kT$ (Rayleigh-Jeans limit), an ideal antenna aperture $\propto \lambda^2$, and an impedance match between the antenna and amplifier. The final assumption will be relaxed in Sec. 2.3.8.

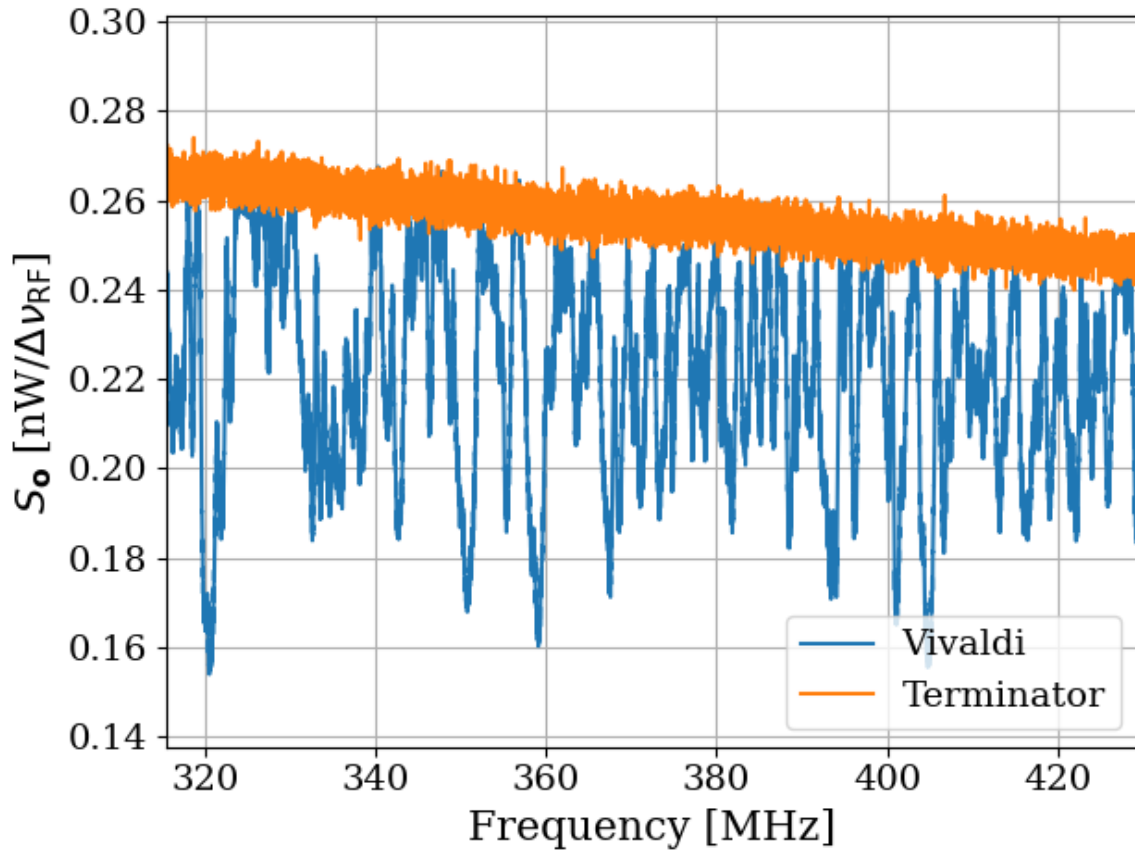


Figure 2.16: Output-referred Vivaldi antenna and terminator thermal spectra as measured through an amplifier chain ($G \sim 68$ dB, noise temperature ~ 120 K). The Vivaldi is inside the shielded room. Both spectra represent about 1 second of data, with $\Delta\nu_{\text{RF}} = 9.5$ kHz. The Vivaldi antenna is in a single position throughout all averaging, in contrast to the technique where it moves, outlined in later chapters.

967 2.3.3 A simple resonator: shorted coax cable

968 A coax cable that is shorted on one end and matched to a measurement device ¹² on the other
 969 is a simple resonator. The short provides a boundary condition demanding the voltage goes
 970 to zero¹³ while the measurement device, being matched, absorbs the wave. A “closed-open”

¹²In the entirety of this section, a Pasternack PE15A-1012 will be used as the front end amplifier.

¹³Similarly, an open termination will force the *current* to zero, resulting in a similar resonator, though with a 180-degree phase shift.

971 resonator such as this will resonate with frequency

$$\nu = \frac{v(2n - 1)}{4L}, \quad (2.35)$$

972 for integer $n > 0$, where v is the wave speed in the cable and L is the length. For a

973 185 cm cable with velocity factor = 69.5% (i.e. $v = 0.695 c$), this works out to a first mode

974 at 28.2 MHz and following modes every 56.4 MHz. A schematic of the setup is shown in

975 Fig. 2.17, and the output power spectrum is shown in ratio to a terminator in Fig. 2.18.

976 Also shown in Fig. 2.18 is an open termination at the end of the cable in place of the short.

977 Fitting the peaks ¹⁴ reveals the average spacing between peaks is 55.2 ± 2.4 MHz, in good

978 agreement with the prediction of 56.4 MHz of Eq. 2.35.

979 By the fluctuation-dissipation theorem, the loss of the cable will dissipate some thermal

980 noise into the system, which can excite the cable. As discussed in Sec 2.3.1, if the resonator

981 (cable) is in thermal equilibrium with the measurement device, a frequency-independent

982 power spectrum is expected. The deviation from this expectation is surprising because the

983 data seem to be in contradiction with thermodynamics. Now, a cable is not a particularly

984 good resonator ($Q \lesssim 10$), so the effects are rather small here, but the simplicity of the system

985 makes it one that is worth exploring.

986 One assumption which is critical to the above logic is that of equilibrium. The amplifier

987 is a likely culprit for breaking this equilibrium, so a test that can remove the amplifier's

988 ability to interact with the resonator is worth pursuing. Fortunately, such a test is quite

989 simple to implement using a circulator ¹⁵.

¹⁴Code for this section can be found at: https://github.com/josephmlev/darkRadio/tree/master/daqAnalysisAndExperiments/run1p4/thermalNoiseVsH/thermalWiggles_writeup.ipynb

¹⁵I got one for \$36 on Ebay!



Figure 2.17: A coax cable with a short on the end and a matched measurement device on the other behaves like a “closed-open” resonator. Replacing the short termination with an open (not shown here) produces a similar resonator, though with a 180-degree phase shift.

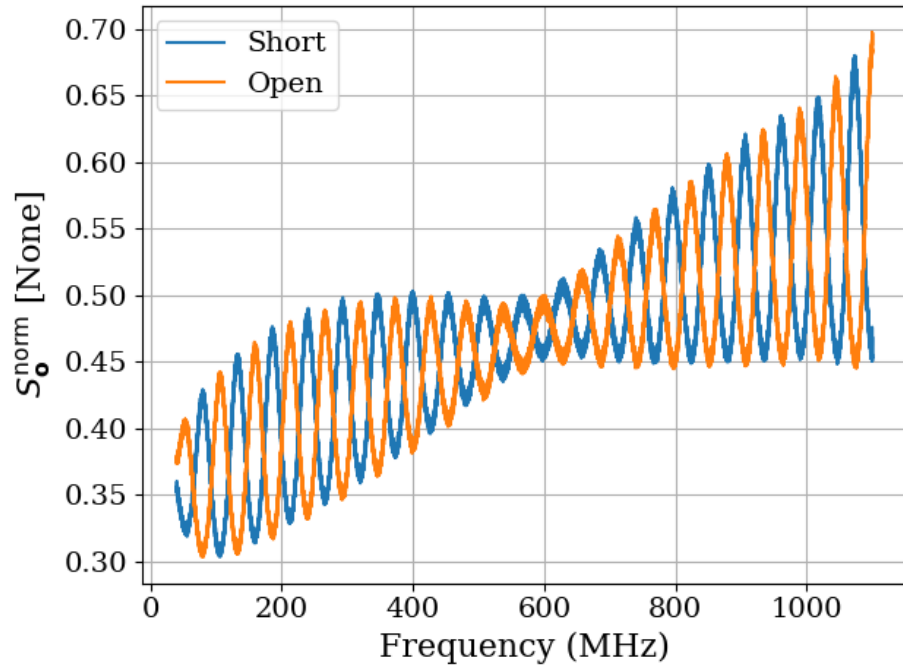


Figure 2.18: Power spectra of short (blue) and open (orange) terminations at the end of 1.85 m of RG400 coax cable (velocity factor = 69.5%). Schematic of this set-up is shown in Fig. 2.17. These spectra are normalized to the spectrum of a terminator, which was measured through the same amplifier chain. For example, when $S_o^{\text{norm}} = 0.5$, the power measured in this setup is half of the power measured by a terminator through the same amplifier chain. The average spacing between peaks is 55.2 ± 2.4 MHz, in good agreement with the prediction of 56.4 MHz of Eq. 2.35.

990 **2.3.3.1 RF circulators**¹⁶

991 A circulator is a three-port, non-reciprocal device that allows power to flow only in specific

992 ways between its ports¹⁷. A schematic symbol is shown in Fig. 2.19.

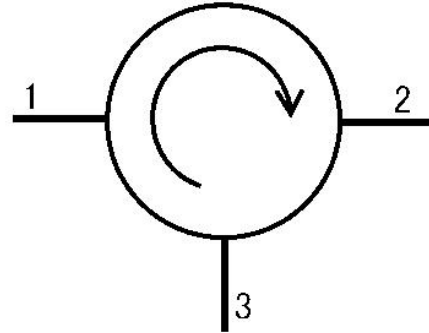


Figure 2.19: Schematic symbol of a circulator. Power can only flow from ports 1 to 2, 2 to 3 and 3 to 1. Image from Wikipedia.

993 The (linear) S-parameters [43, 44] of an ideal circulator are given by the matrix

$$S = \begin{pmatrix} 0 & 0 & 1 \\ 1 & 0 & 0 \\ 0 & 1 & 0 \end{pmatrix}. \quad (2.36)$$

994 In other words, in an ideal circulator, $S_{12} = 0$, so power can not flow from port 2 to port

995 1, while $S_{21} = 1$, so power can flow from 1 to 2. Also of note, the diagonal elements $S_{ii} = 0$,

996 meaning ports do not reflect power.

997 A Teledyne C-0S03A-3M RF circulator has an approximate bandwidth from 490-510 MHz

998 and was available inexpensively on eBay, so it is used for testing. A photo of it is shown in

¹⁶Code for this section can be found at: https://github.com/josephmlev/darkRadio/tree/master/thesis/ch2/circulatorData/SParameter_circulator/calc3portSPParam.ipynb

¹⁷See Ch. 9 of Pozar's *Microwave Engineering* for a detailed reference.

999 Fig. 2.20, and its S-parameter data are shown in Fig. 2.21. Note that a circulator with one
1000 port terminated is sometimes known as an “isolator”, but I will refrain from using this term.



Figure 2.20: Photo of Teledyne C-0S03A-3M RF circulator. Lines in the background are collage-ruled lined paper (\approx 7mm spacing) for scale.

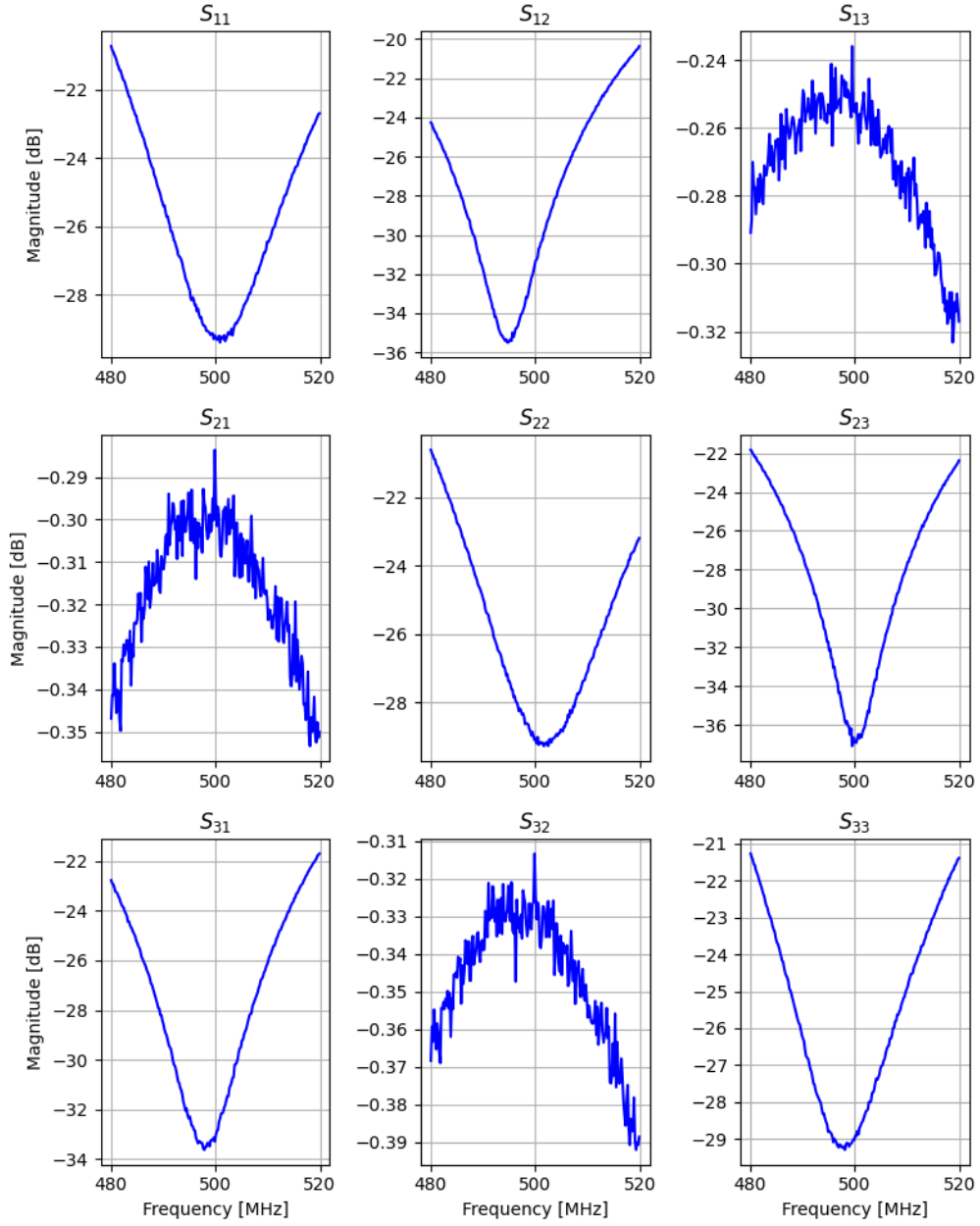


Figure 2.21: 3-port, frequency-dependent S-parameter data for Teledyne C-0S03A-3M circulator. Data taken by Ben Godfrey and Andrea Lopez Arguello with 2-port VNA with the circulator's unused port terminated. Circulator is rated for use between 490 and 510 MHz. These data show good agreement with Eq. 2.36. Note that magnitude is in dB, so these data are proportional to power, i.e. the square of linear S-parameters.

1001 **2.3.4 A simpler resonator: shorted coax cable and circulator**

1002 In light of the variations observed in Fig. 2.18, a similar measurement was made using
1003 a circulator in order to isolate the coax resonator from any effects of the amplifier. The
1004 schematic of this setup is shown in Fig. 2.22, and resulting the spectrum is shown in Fig. 2.23.
1005 This is an interesting measurement because any net power flow from the amplifier will be
1006 absorbed by the terminator on port three since it presents a good impedance match. This
1007 net power flow has the potential to cause a temperature change in the terminator; however,
1008 it is in a thermally-conductive metal can that is exposed to the air, which serves as a heat
1009 bath and holds it very close to room temperature. The coax resonator will just see the
1010 Johnson noise of the room temperature terminator in equilibrium with the Johnson noise
1011 caused by its internal loss. The overall effect is a resonator that is in thermal equilibrium
1012 yet is able to be measured by an extremely sensitive spectrum analyzer.

1013 The result of introducing the circulator and matched load on port 3 is the removal of the
1014 variations that were seen without the circulator (Fig. 2.23).

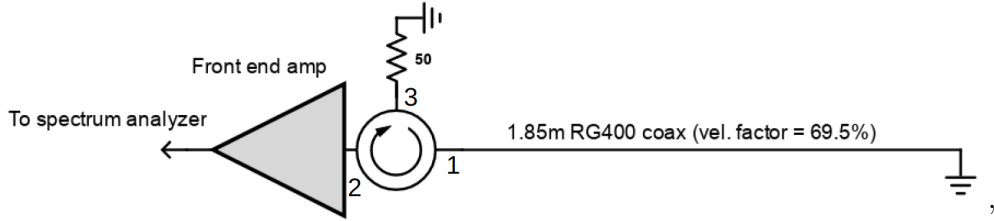


Figure 2.22: A coax cable with a short on one end and a circulator isolating the system from the amplifier.

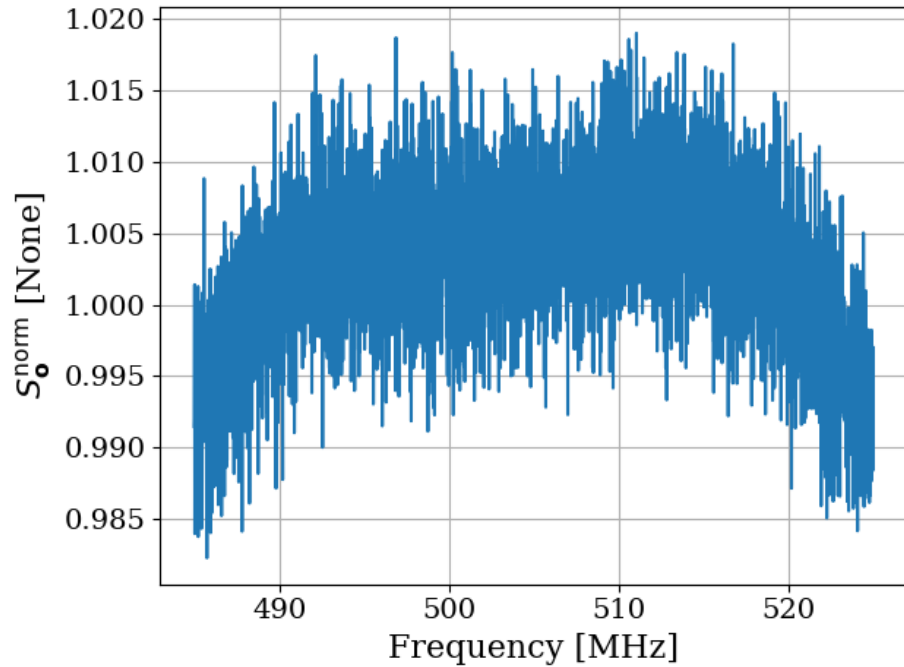


Figure 2.23: Power spectrum of 185 cm coax resonator as measured through a circulator. Short termination at the end of the cable as depicted in Fig. 2.22. The amplitude of the variations in this spectrum is on the order of half a percent and hardly visible under the noise. They are much smaller than those at the $\sim 15\%$ level without a circulator (Fig. 2.18). Also, note this spectrum is normalized to a terminator through the same amplifier chain and very close to 1. The normalized spectrum without the circulator shown in Fig. 2.18 was significantly lower, around 0.5. Note that the peak-to-peak frequency variations of the cable without a circulator (Fig. 2.18) are $\approx 55\text{ MHz}$, and would be visible in the $\approx 30\text{ MHz}$ span shown here. This span is limited by the circulator.

1015 **2.3.5 A more complex resonator: antenna in room**

1016 Similar to the coax resonator shown in Fig. 2.17, the antenna data presented in Fig. 2.16
1017 are of a resonator (antenna-room system) which is being measured by an amplifier. The
1018 experiment in the previous section suggests that the amplifier seems to have an effect on
1019 the delicate thermal equilibrium, which can be mitigated by including a circulator. The
1020 experimental set-up for the antenna in the room is shown in Fig. 2.24, and the data from
1021 this setup is shown in Fig. 2.25.

1022 The result is striking. The theory outlined early in the chapter predicted the noise
1023 power spectrum of an antenna in a cavity will look the same as a matched terminator;
1024 -174 dBm/Hz, independent of frequency. The Dark E-Field Radio Experiment measures
1025 just such a spectrum, but comparing a terminator and antenna in Fig. 2.16, they are remark-
1026 ably different; the Vivaldi has large variations. However, introducing a circulator to the set
1027 up such as in Fig. 2.24 removes these variations. Compare blue/orange curves in Fig. 2.25.

1028 A nice test case would be to measure the thermal noise of an extremely high Q cavity
1029 after carefully ensuring the radiation that is allowed to enter has a black body spectrum of
1030 the same temperature of the cavity. This is nicely demonstrated in a few places, notably by
1031 Cervantes et. al with a cavity of $Q = 10^{10}$ (!!!) [32]. When care is taken to create equilibrium
1032 here, the resulting spectrum is flat, even on a frequency span that includes the resonance
1033 (Fig. 2). When this equilibrium condition is broken, the cavity resonance becomes visible
1034 (Fig. 10).

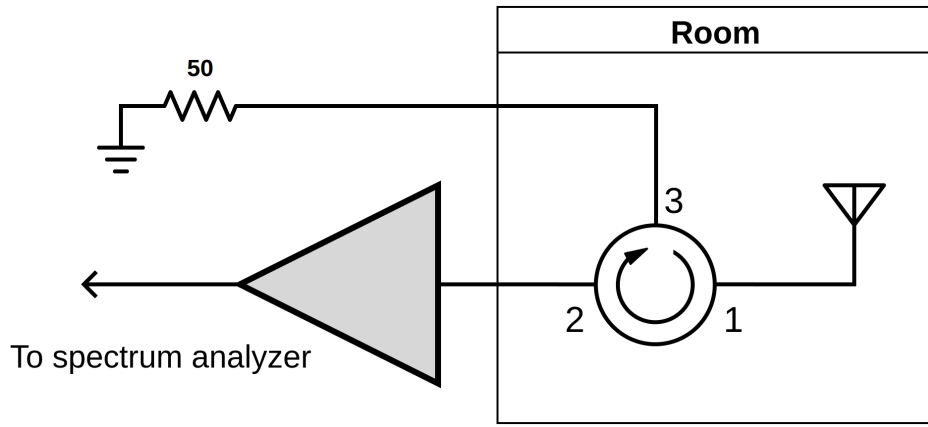


Figure 2.24: Schematic of experimental set-up using circulator to isolate the antenna from amplifier effects.

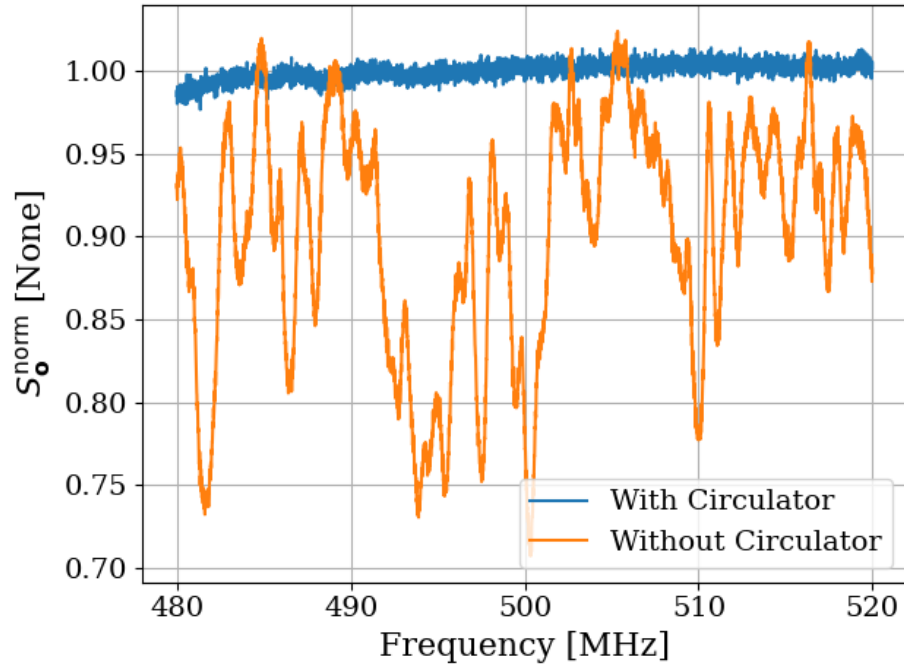


Figure 2.25: Normalized power spectrum for Vivaldi antenna in the room with/without circulator (blue/orange). This setup is shown schematically in Fig. 2.24. The normalized spectrum of the same antenna in the same position is shown with the circulator removed in orange for reference. This orange spectrum is the same as that shown in Fig. 2.16, but here it has been normalized to a terminator measured through the same amplifier chain. The terminator's spectrum is also shown in Fig. 2.16.

1035 2.3.6 Effective temperature of amplifier

1036 At this point, the seemingly obvious explanation is that the amplifier, being warm, is sourcing
1037 more power than it's absorbing. To test this theory, two amplifiers can be placed input-to-
1038 input as shown in Fig. 2.26. The noise power emerging *out* of the amp-under-test's input will
1039 be measured by the front-end amplifier. This amplifier has a noise temperature $\sim 100\text{ K}$, so
1040 it should be sensitive to very small variations in power. The data from the set-up is shown
1041 in Fig. 2.27. Also shown in this figure are the spectra of the amp-under-test replaced by
1042 both short and open terminations for reference.

1043 An important number to keep in mind is the noise floor of this detector and what it looks
1044 like in the dimensionless units shown. This is set by the noise temperature of the front end
1045 amp, $\sim 100\text{ K}$. If the load-under-test were at 0 K , the power measured $S_{0\text{K}}^{\text{meas}}$ would be only
1046 that of the front end amp. Taken in ratio to a 300 K matched terminator measured by the
1047 same amp chain,

$$\frac{S_{0\text{K}}^{\text{meas}}}{S_{300\text{K}}^{\text{meas}}} \approx \frac{0 + 100\text{ K}}{300 + 100\text{ K}} \quad (2.37)$$

$$= 0.25, \quad (2.38)$$

1048 where the factors of Boltzman's constant k and the measurement bandwidth $\Delta\nu_{\text{RF}}$ were
1049 suppressed since they cancel immediately.

1050 Thus, anything with an apparent noise temperature $\ll 100\text{ K}$ will appear with a dimen-
1051 sionless power spectral density of ~ 0.25 in Fig. 2.27.

1052 This phenomenon actually has been discussed in the literature[19].¹⁸, which I will provide
1053 a brief summary of.

1054 In this case, two amplifiers are placed back to back on either side of a transmission
1055 line. When a particle interacts with the transmission line, a pulse is detected at each of the
1056 amplifiers, and the difference in time provides a means to work out the position the particle
1057 came in along the line. It is advantageous in this case to minimize the noise emanating out
1058 of the inputs of these amplifiers. By tuning the reactance of the input of these amplifiers,
1059 they can absorb a net power, putting them at an “effective temperature” lower than their
1060 physical temperature.

1061 In the case of off-the-shelf Pasternack RF amplifiers, this was likely not an intentional
1062 effect. However, the data presented here seem to agree with the idea that the amplifiers have
1063 an effective temperature $\ll 100\text{ K}$.

1064 In the next subsection, I will demonstrate that by changing the temperature of the
1065 matched load outside the shielded room (shown in Fig. 2.24), the amplitude of the thermal
1066 wiggles can be controlled.

¹⁸I am very grateful to Greg Wright for pointing this out.

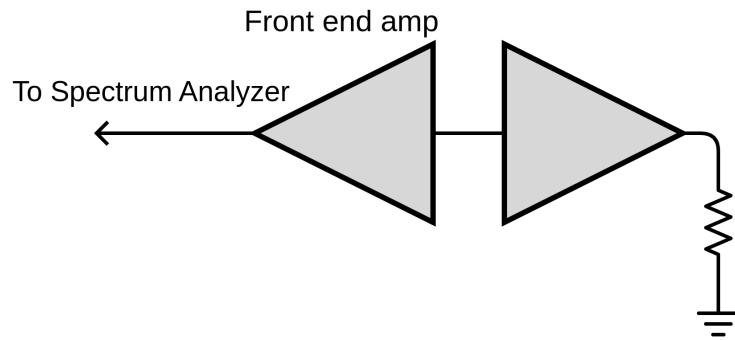


Figure 2.26: Schematic of set-up to measure the noise emerging *out* of an amplifier's input.

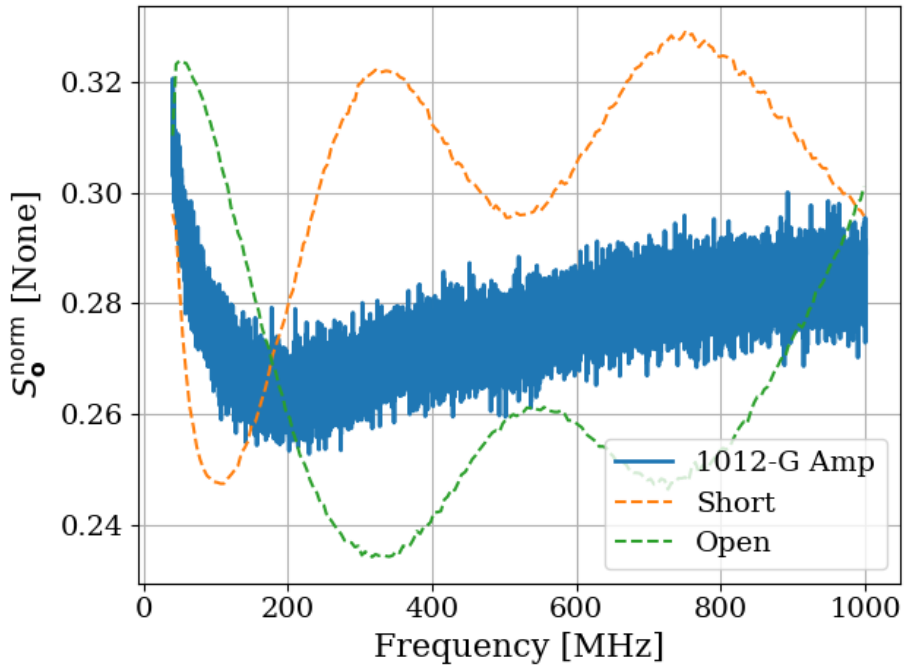


Figure 2.27: Power spectrum of noise emerging *out* of the input of an amplifier's (Paster-nack PE15A-1012-G) input, see Fig. 2.26. Normalized to a matched 50Ω terminator. Also shown as dashed curves are the spectra of a short and open termination. These spectra have a median fit applied to reduce visual clutter. Low-frequency behavior is due to the high noise figure of the amplifier at these frequencies; see Eq. 2.37.

1067 2.3.7 Intentional breaking of thermal equilibrium

1068 At this point, it has been demonstrated that an amplifier absorbs more thermal noise than
1069 it emits, likely due to the electronic cooling effect described by Radeka [19]. This causes the
1070 spectrum of a resonator, which is measured with such an amplifier, to exhibit wiggles, which
1071 disappear when a circulator is used to isolate the system from the amplifier. An interesting
1072 question naturally arises; what happens when the the thermal equilibrium is disturbed by
1073 varying the temperature of the 50Ω terminator on port 3 of the circulator (Fig. 2.24)? Since
1074 the terminator is outside the room, it is simple to conduct a highly controlled experiment
1075 where the terminator's temperature is varied without entering the room and disturbing
1076 sensitive boundary conditions.

1077 The hot terminator is created by using a noise source (red device in the left panel of
1078 Fig. 2.28). The noise source has an effective noise ratio (ENR) of approximately 16.1 dB
1079 according to its calibration sheet. Noise temperature is related to ENR by the formula[45]

$$T_n = (10^{\text{ENR}/10} \times 290 K) + 290 K, \quad (2.39)$$

1080 where ENR is measured in dB and a reference temperature of 290 K has been assumed.
1081 Therefore, the noise source has a noise temperature of around 12,100 K ¹⁹.
1082 The cold terminator is a standard Pasternack 50Ω (with the blue rubber case removed),
1083 and the cable is semi-rigid and rated for cryogenic temperatures. This assembly is shown
1084 immersed in liquid nitrogen in the right panel of Fig. 2.28.

¹⁹This testing was performed before the Y-factor measurements of Sec. 3.1.1. The noise source worked correctly here but failed before the Y-factor measurements.

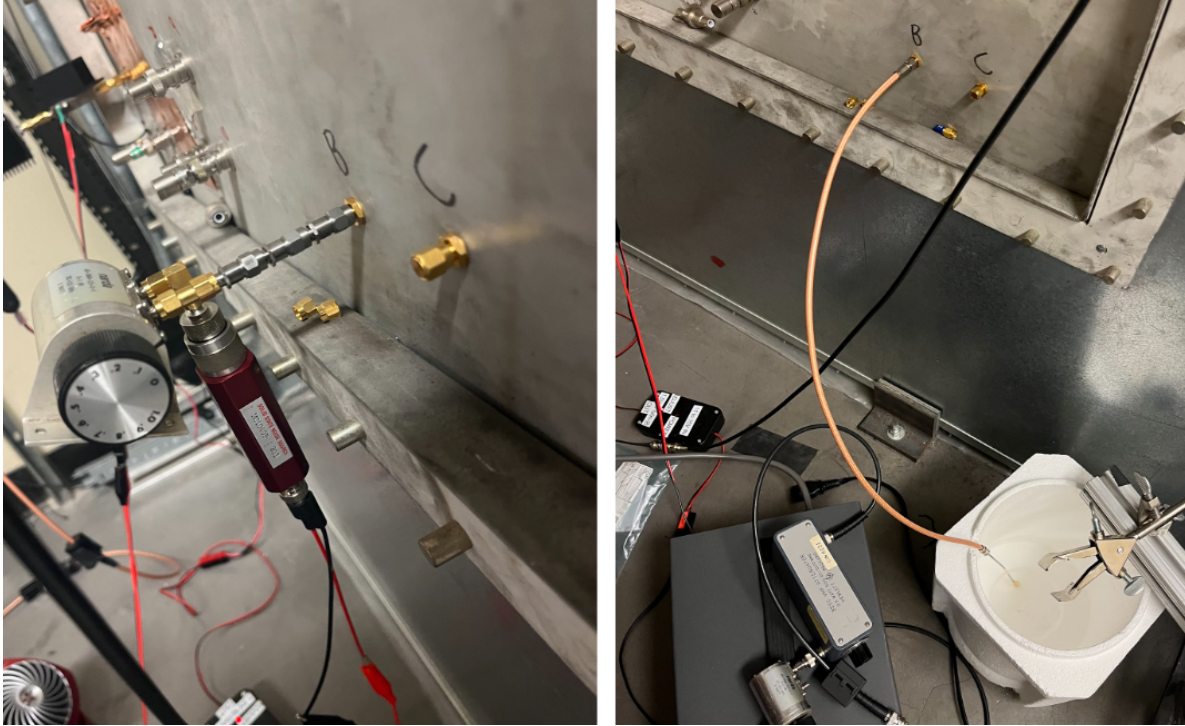


Figure 2.28: Setup to create hot and cold terminator. The hot/cold load is connected to port 3 of the circulator (as shown in Fig. 2.24). The circulator is in the room and not visible in this photo. The left panel shows the noise source ($16.1 \text{ dB ENR} \approx 12,000 \text{ K}$ noise temperature) and attenuators allowing the specific control of the hot temperature, see Eq. 2.40. Course attenuation is controlled by adding fixed attenuators, while fine control (0.1 dB steps) is provided by the step attenuator. Right panel shows the semi-rigid cryogenic-capable cable in liquid nitrogen to create a cold load.

1085 In both the hot and cold measurements, the loads were shown to have a good impedance
 1086 match to the 50Ω line using a VNA. The noise source is designed to have a good match,
 1087 but the terminator is not rated for cryogenic temperatures, so this is an important test.
 1088 The cryogenic test load (semi-rigid cable plus terminator) was measured to have $S_{11} <$
 1089 -35 dB at both room temperature and at 77 K (by submerging in liquid nitrogen), confirming
 1090 performance at cryogenic temperatures.

1091 The noise source looks like a terminator, which is a factor of ~ 40 times hotter than room

1092 temperature, while the cryogenic terminator is a factor of ~ 4 colder than room tempera-
1093 ture. To account for this, room temperature attenuators can be added to bring the effective
1094 temperature of the noise source down closer to room temperature. Therefore, the total noise
1095 temperature T_{out} of a terminator at physical temperature T_{in} in series with an attenuator at
1096 physical temperature T_{att} with (linear) loss L is a useful quantity. For brevity, the derivation
1097 outlined in the white paper by Whitham D. Reeve [46] is skipped, and the result is provided;

$$T_{\text{out}} = \frac{T_{\text{in}}}{L} + T_{\text{att}}\left(1 - \frac{1}{L}\right). \quad (2.40)$$

1098 Returning to the set-up in Fig. 2.24, replacing the terminator on port 3 with either a
1099 noise source (including an attenuator chain) or a terminator in liquid nitrogen provides a
1100 means to break thermal equilibrium in both the hot and cold direction by applying a matched
1101 load at a very precise temperature to port 3 of the circulator. Equation 2.40 converts the
1102 attenuation and noise source temperature into an output temperature.

1103 Figure 2.29 shows the resulting spectra from the set-up shown in Fig. 2.24 using a noise
1104 source/attenuator chain shown in the left panel of Fig. 2.28. The two panels show the spectra
1105 from the same set-up, but for different ranges and resolutions of T_{out} as defined by Eq. 2.40.

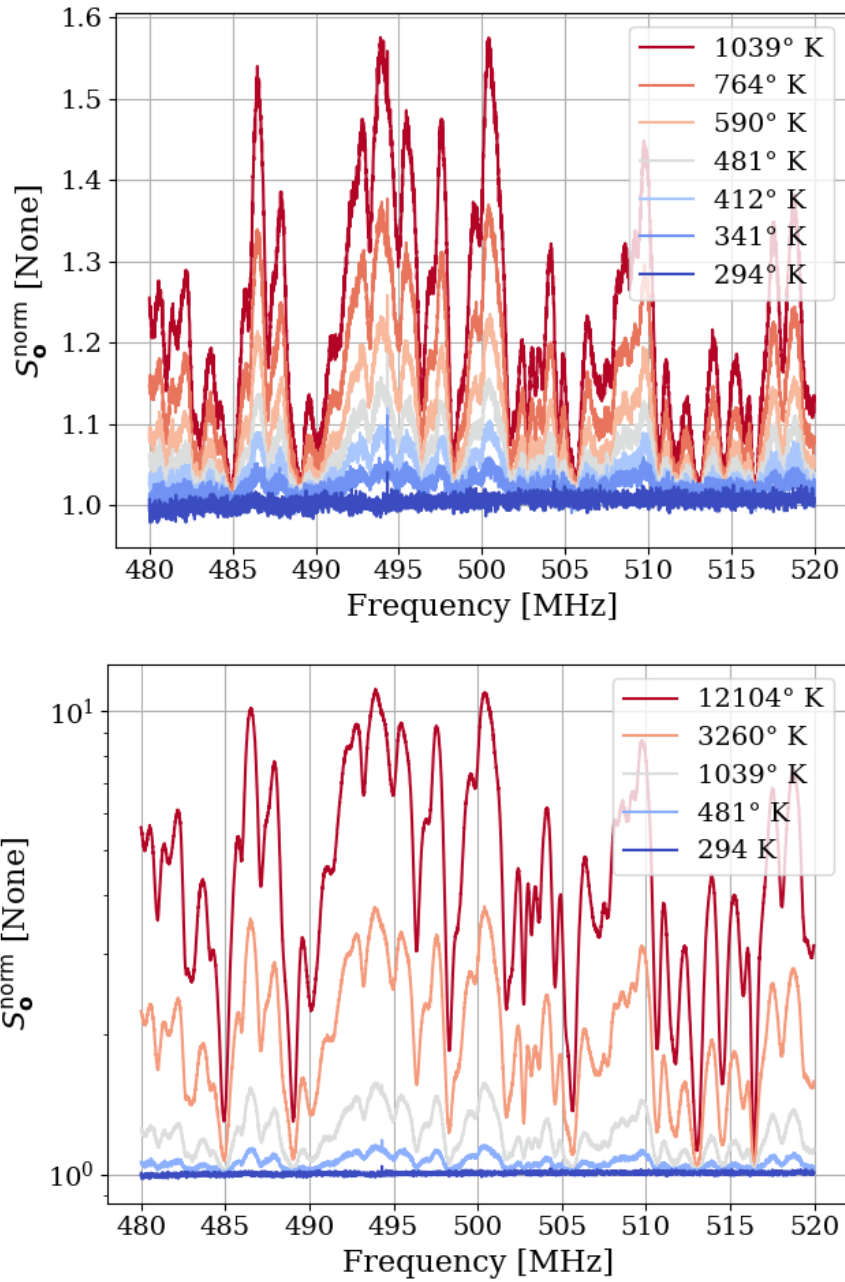


Figure 2.29: Spectra resulting from the antenna and circulator set up of Fig. 2.24 with the terminator on port 3 of the circulator at a variety of temperatures, as calculated by Eq. 2.40. Spectra are all normalized to a terminator through the same amplifier chain. The two panels show different ranges and resolutions of temperatures for clarity, but are the same setup.

1106 Figure 2.29 showed spectra from the set-up shown in Fig. 2.24 for a hot terminator, but
1107 a cold terminator can also be used by dunking a terminator into liquid nitrogen (Fig. 2.28).
1108 Neglecting the small attenuation of the cable, the noise temperature is simply 77 K. An
1109 interesting test case is to set the hot temperature such room temperature is halfway between
1110 T_{hot} and T_{cold} . In other words, let

$$T_{\text{hot}} = (T_{\text{room}} - T_{\text{cold}}) + T_{\text{room}} \quad (2.41)$$

$$\approx 511 \text{ K}. \quad (2.42)$$

1111 For $T_{\text{hot}} = 12,100 \text{ K}$, $T_{\text{att}} = 294 \text{ K}$ and $T_{\text{out}} = 511 \text{ K}$, inverting Eq. 2.40 we expect L to
1112 be ~ 54.4 or 17.4 dB .

1113 The two spectra with the terminator at 504 K (the closest temperature accessible with the
1114 0.1dB step attenuator) and 77 K are shown in Fig. 2.30. Again, they have been normalized
1115 to the spectrum of a room-temperature terminator.

1116 The two spectra shown in Fig. 2.30 appear to be mirrored about $S_0^{\text{norm}} = 1$. In a test of
1117 this reflection, these spectra are added, and the resulting sum spectrum is flat to about 1%
1118 with another 1.5% offset from the expected value of 2. This is shown in Fig. 2.31. The offset
1119 is likely due to the amplifier gain or ambient temperature drift between measurements.

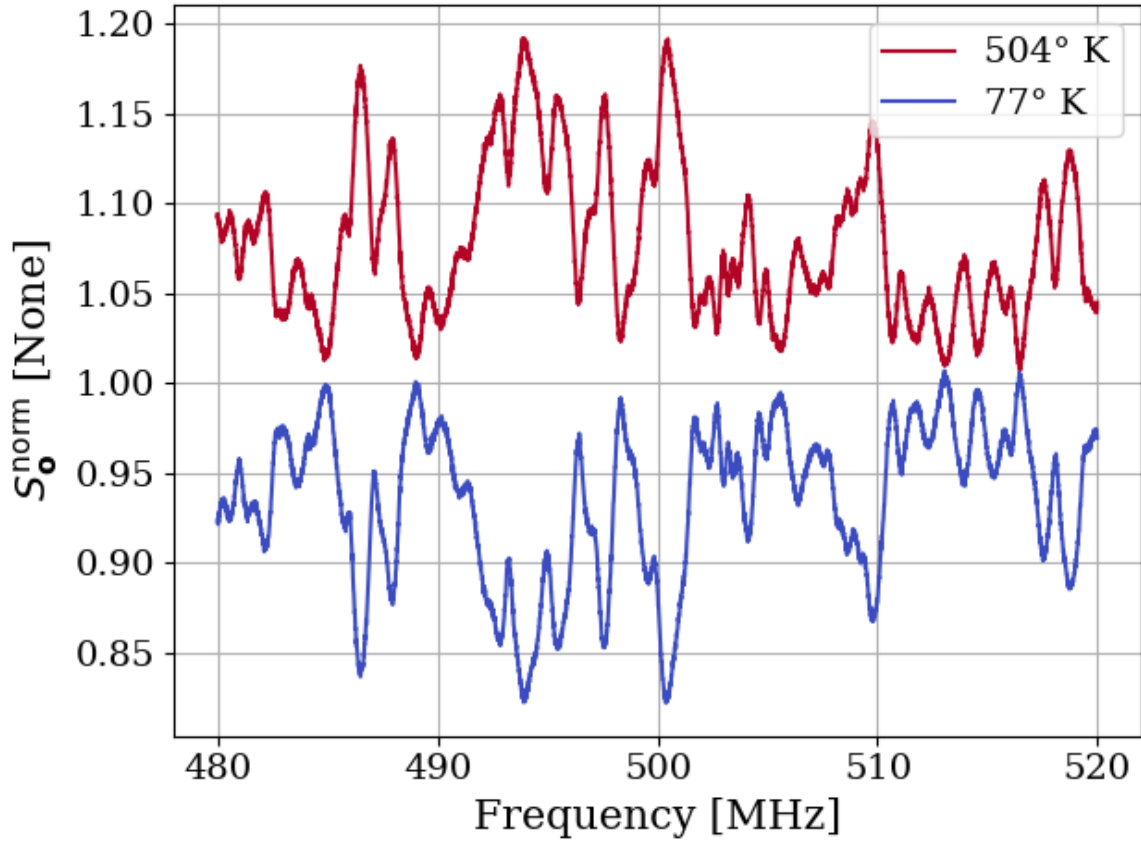


Figure 2.30: Spectra resulting from the antenna and circulator set up of Fig. 2.24 with the terminator on port 3 of the circulator $\approx 210\text{ K}$ above and below room temperature, as calculated by Eq. 2.40. Spectra are both normalized to a terminator through the same amplifier chain.

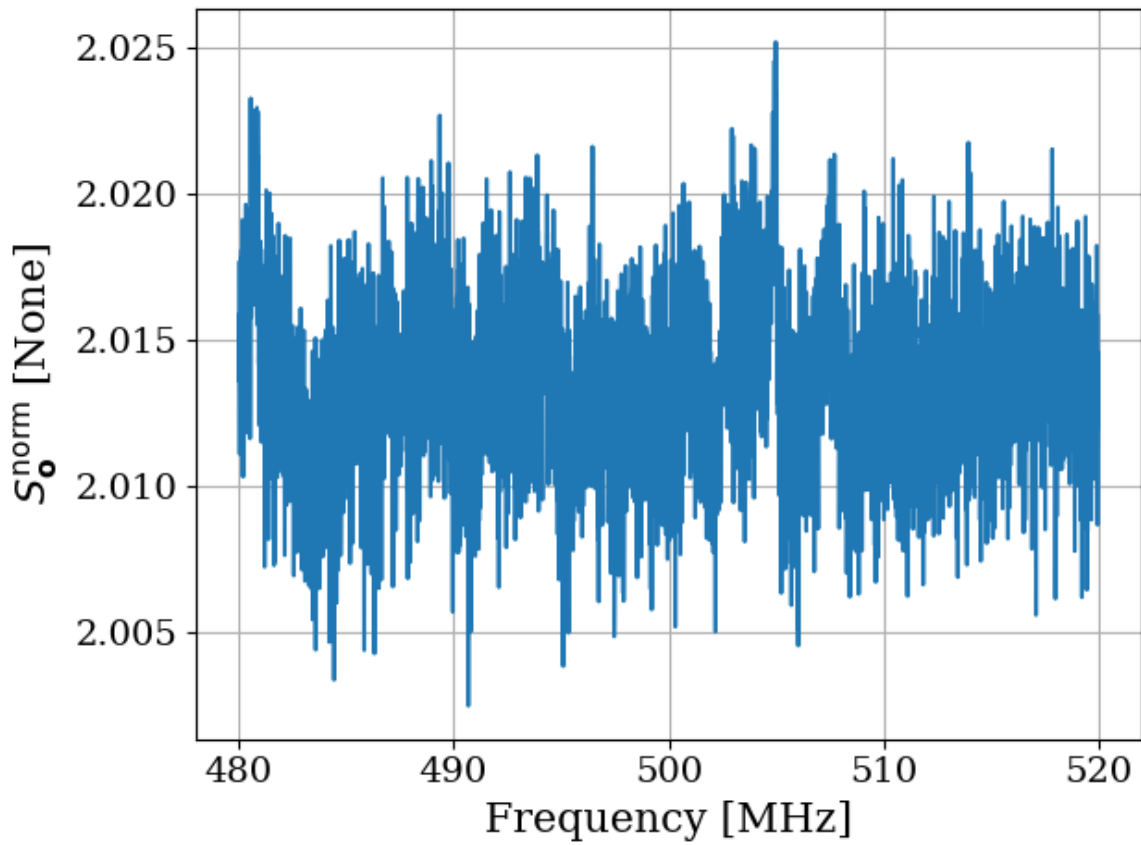


Figure 2.31: Sum of normalized spectra shown in Fig. 2.30. If the two normalized spectra in that figure were perfect reflections about 1, their sum would be a constant 2 in this figure. That is close to what is observed.

1120 **2.3.8 Relation of antenna S_{11} to thermal noise without a**

1121 **circulator**

1122 As pointed out in [41], the antenna impedance determines how much power is transferred

1123 from the cavity's electric field noise into the transmission line, and therefore what is mea-

1124 sured by the amplifier²⁰. Indeed, impedance is a useful tool in understanding the situation

1125 outside equilibrium. However, viewing from this perspective misses a subtle point when con-

1126 sidering equilibrium; while an impedance mismatch will prevent the antenna's noise power

1127 from entering the transmission line, it will also prevent the noise in the line from leaving!

1128 This power will reflect off of the mismatch at the antenna and be absorbed by the matched

1129 amplifier, resulting in a flat spectrum. This can be seen in the coax resonator when mea-

1130 sured with the circulator in Sec. 2.3.4, specifically Figs. 2.22 and 2.23. Figure 2.32 shows a

1131 comparison of $1 - |S_{11}|^2$ and the noise spectrum of an antenna measured with a Pasternack

1132 low noise amplifier (LNA). There is no circulator in the setup, so variations are observed.

1133 Figure 2.33 shows the strong correlation between the curves in Fig. 2.32.

²⁰The amplifier has a small impedance mismatch as well ($S_{11} \lesssim -15$ dB), but this is a small effect and is neglected.

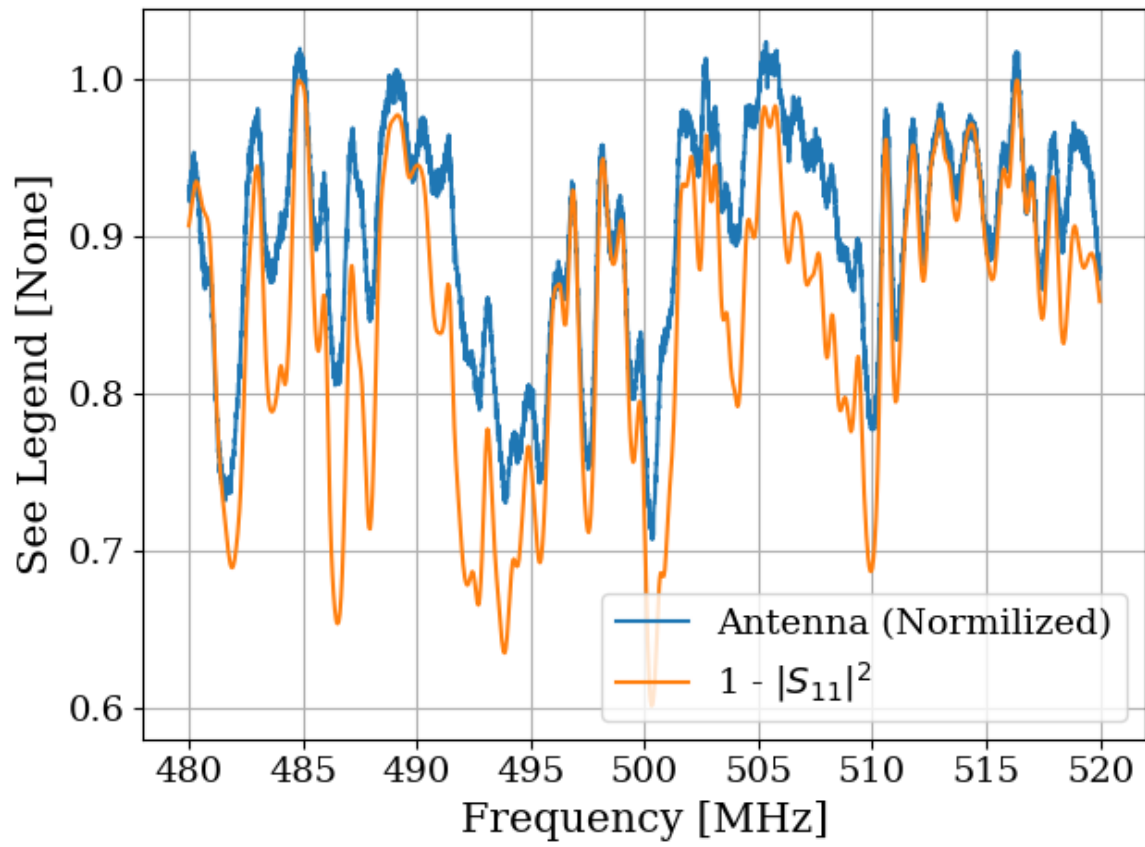


Figure 2.32: $1 - |S_{11}|^2$ and the normalized antenna spectrum without circulator. Shown at significant zoom to show detail. A much wider span is used to generate the correlation shown in Fig. 2.33.

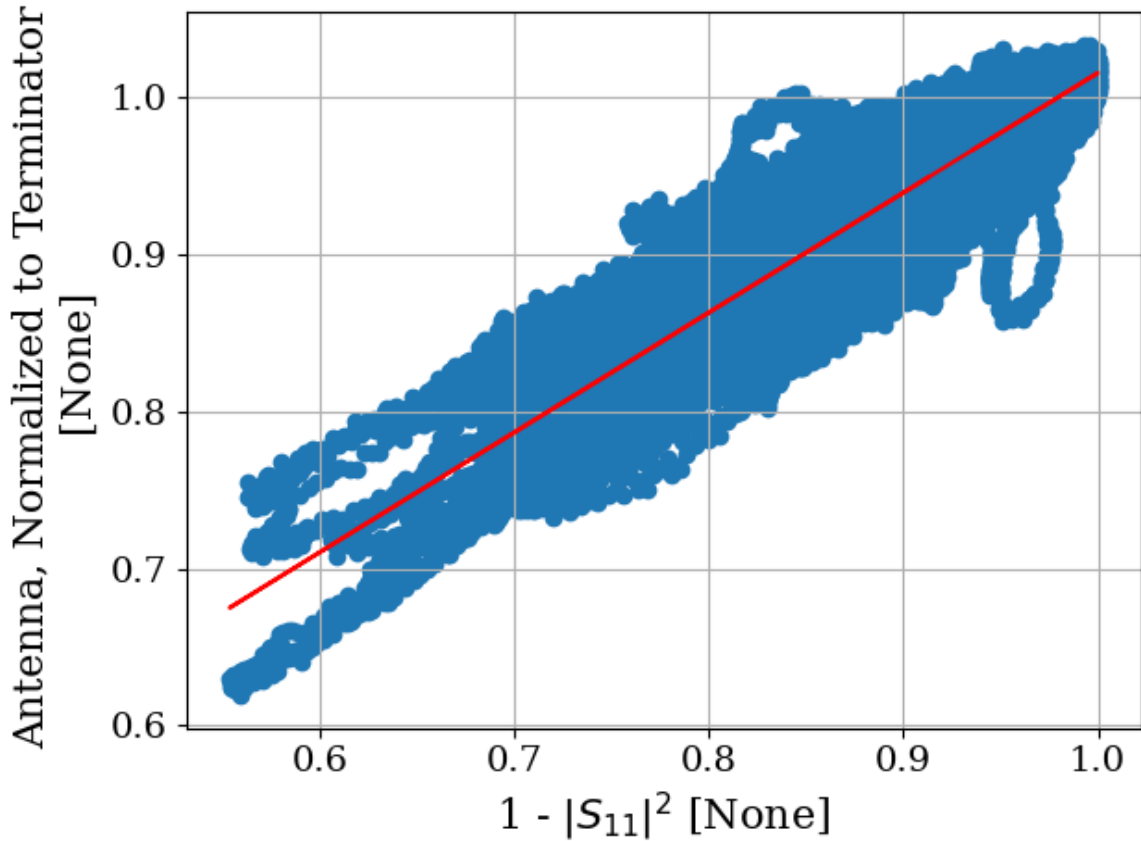


Figure 2.33: Correlation of $1 - |S_{11}|^2$ and the normalized antenna spectrum without the circulator. The data are taken between 300 and 800 MHz, a much wider span than shown in Fig. 2.32. The antenna is connected directly to the low noise amplifier (LNA), i.e. with the circulator shown in Fig. 2.19 removed. The line of best fit is shown in red. The Pearson correlation coefficient is 0.92.

1134 2.3.9 Discussion of Thermal Wiggles

1135 Inspection of the output of the experiment (S_o , Fig. 2.16) reveals small variations in PSD
1136 (power spectral density) over spans of tens of kHz. Given an antenna in a cavity in thermal
1137 equilibrium with the input of an LNA, whose input is assumed to be real and matched,
1138 one would expect an output PSD which is constant with respect to frequency (up to small
1139 variations in system gain and noise temperature). The theory for this is outlined in Sec 2.3.1.
1140 These observed variations are not noise; for a given antenna position, the same shape is
1141 repeatedly measured (though the noise riding on these variations *is* random). The origin of
1142 the observed small variations lies in the effective temperature difference between the room
1143 and the LNA, causing a net power flow from the antenna into the LNA (Fig. 2.26). This
1144 effective temperature difference partially excites modes of the antenna/cavity system, causing
1145 the observed variations. This effect likely originates from a small reactive component of the
1146 LNA's input causing the electronic cooling described originally by Radeka [19]. This effect
1147 can be eliminated by adding a circulator between the antenna and LNA [47, 48] though for
1148 this experiment, it is impractical to get an isolator that covers such a wide band at relatively
1149 low frequency. Furthermore, the relatively wide (tens of kHz) variations can be handled by
1150 fitting to them, which is discussed in Sec. 4.2. Finally, a topic which was not described here
1151 but may be fruitful for future inquiry into this topic is the analysis of noise waves. See [49]
1152 or Sec. 9.12 of [50].

1153 **2.4 Reverberation Chambers and Statistical**

1154 **Uniformity**

1155 The Dark E-Field Radio experiment consists of an antenna in a cavity. An averaged noise
1156 power spectrum is measured and an exclusion limit is set on the amount of power excess
1157 that would have been detected if it were there. In order to convert this limit on power into
1158 a limit on kinetic mixing ϵ , the antenna/cavity detector system must be calibrated.

1159 In many situations, an electromagnetic cavity can be treated with a "spherical cow"
1160 approach; they contain one mode with a few simple properties that can be analytically
1161 computed. This works well enough for a smooth, empty cavity that resonates near its
1162 first mode, but for complex cavities, this treatment turns out to be insufficient. At high
1163 frequencies (where the wavelength is much smaller than the cavity), many modes, each with
1164 a finite spread in frequency, overlap. Each of these modes depends on very specific boundary
1165 conditions of the cavity and everything within it. The configuration of the cavity and its
1166 contents simply cannot be known to a level of precision that would allow for an analytic or
1167 simulated solution. Qualitatively, placing a small conducting object²¹ in a cavity greatly
1168 impacts the cavity's resonances as measured by its S-parameters (Fig. 2.36).

²¹This is a point made by Hill [51], with the example of placing a soda can in a reverb chamber. Ben Godfrey and I independently discovered this by measuring S_{21} of an antenna in our shielding room with and without a small SMA terminator on the ground with surprisingly different results.

1169 The problem is summarized nicely by Price et al. [52];

1170 The solution cannot depend in detail on such things as whether a small metallic
1171 can has been set down somewhere inside the test article, or the position of the
1172 pilot's arms, or whether some mechanical widget has moved from position A
1173 to position B, changing the mode structure. If the answer did depend on those
1174 things, all of the measurements would be useless, defeated by the minutiae present
1175 in all systems.

1176 The answer to this dilemma is found in the study of mode-stirred reverberation chambers,
1177 such as those studied by Price, whose quote appears directly above. These are electromag-
1178 netic or acoustic cavities in which a large volume is occupied by an object that is highly
1179 reflective and designed to move, a so-called *mode stirrer*. Making the geometry more com-
1180 plex seems counter-intuitive. However, the payoff is in the transition from a deterministic
1181 theory to a statistical one. The fields in the cavity at any given configuration are complex
1182 and are not known, but the statistics of the fields subject to the stirring can be rather simple.

1183 This section provides a mostly qualitative overview of the subject. The de facto reference
1184 is David Hill's 2009 book [51] which consolidates his many papers spanning his ~ 30 -year
1185 career. There is little I can do to explain the theory of electromagnetic reverberation cham-
1186 bers, which is not in this book, so I will focus on their application to the experiment and
1187 cite Hill where appropriate. The reader is encouraged to consult this book and its references
1188 for a more detailed exploration of the subject.

1189 2.4.1 Deterministic solutions to electromagnetic waves in cavities

1190 The electromagnetic fields within a cavity can be modeled by applying Maxwell's equations
1191 with the appropriate boundary conditions. In principle, with enough knowledge about the
1192 contents of the cavity, this treatment could calculate fields in any cavity. Unfortunately,
1193 it quickly becomes untenable for all but the simplest cases. Therefore, we will restrict
1194 ourselves to an empty cavity with perfectly conducting surfaces. The resulting fields have
1195 simple analytic solutions which vary sinusoidally in both space and time. They are derived
1196 in many places. See for example [51, 53]. While this treatment will not solve the problem
1197 at hand, it is a good starting point and will illustrate important features leading to the
1198 statistical treatment in the following subsection.

1199 For a rectangular cavity of linear dimensions a , b and d , the frequencies of resonance are
1200 given by

$$\nu_{mnp} = \frac{c}{2} \sqrt{\left(\frac{m}{a}\right)^2 + \left(\frac{n}{b}\right)^2 + \left(\frac{p}{d}\right)^2}, \quad (2.43)$$

1201 for integer mode numbers m , n and $p \geq 0$ and wave speed c . The lowest frequency of
1202 resonance requires at least two non-zero mode numbers. Thus, for $a < b < d$ the lowest
1203 frequency is at TE_{011} . For an ideal cavity with dimensions equal to that of the shielded
1204 room in this experiment ($8 \times 10 \times 12$ feet), the lowest mode is 63.6 MHz. An important
1205 consideration is the degeneracy of electric and magnetic fields for any mode where all three
1206 mode numbers are non-zero. For example, TE_{111} and TM_{111} occur at the same frequency,
1207 and both of these modes must be counted in the following section. See page 28 of Hill [51]
1208 for a discussion.

1209 A quantity of interest is the functional form of the cumulative number of modes at
 1210 frequencies below a given frequency $N(\nu)$. This is rather simple by brute force computer
 1211 counting²², though an analytic solution can be computed by looking at the volume enclosed
 1212 in a sphere of k -space [54], where k is the wave vector²³. This analytic form is given by

$$N_s = \frac{8\pi}{3} abd \frac{\nu^3}{c^3} - (a + b + d) \frac{\nu}{c} + \frac{1}{2}. \quad (2.44)$$

1213 Differentiation of Eq. 2.44 results in a functional form for the mode density, i.e. the
 1214 number of modes contained in a frequency band,

$$\frac{dN_s}{d\nu} = 8\pi abd \frac{\nu^2}{c^3} - \frac{a + b + d}{c}. \quad (2.45)$$

1215 Equations 2.44 and 2.45 are plotted in Fig. 2.34

1216 This is useful because as the mode density becomes high, modes in a cavity of finite
 1217 conductivity begin to overlap. The modification of modal structure by conductors is demon-
 1218 strated in Figs. 2.35 and 2.36 by placing different conductors in the room and measuring
 1219 S_{11} .

1220 From these measurements it can be seen that modes can be pulled around, even by
 1221 conductors occupying a small percentage of room volume. This is especially true for high
 1222 frequencies. However, by using a large volume of conductors such as a mode-stirrer (sim-
 1223 ulated here with scrap metal), high-frequency modes are pulled around so much that they
 1224 overlap. This is the intuition behind reverb chambers and the idea of statistical uniformity.

²²As long as you don't forget the degeneracy!

²³This whole business of mode counting is directly analogous to the calculation of density of states in statistical mechanics. It shouldn't come as a surprise that the calculation is carried out in the same way.

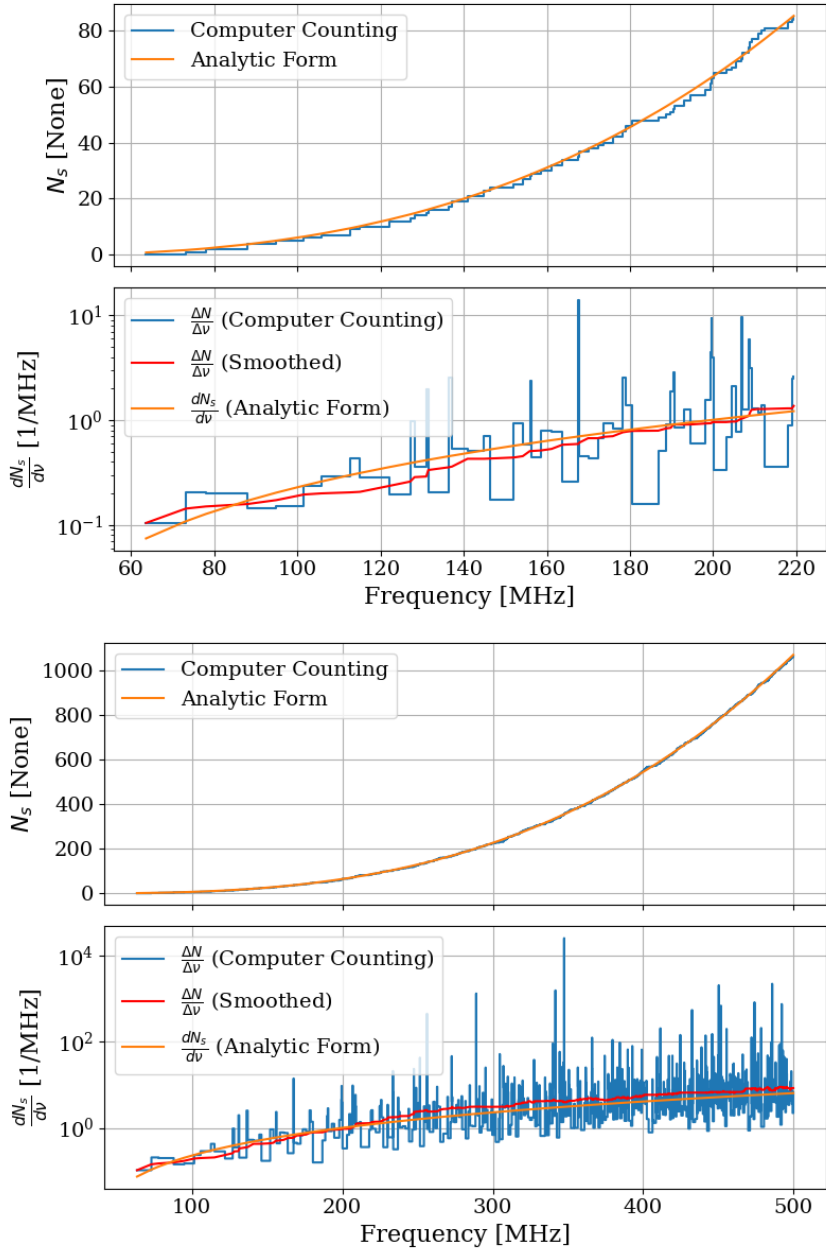


Figure 2.34: Modal density for an electromagnetic cavity with dimensions of the shielding room (nominally $8 \times 10 \times 12$ ft, see table 2.2). The upper sub-plot shows $N_s(\nu)$, the cumulative number of modes below a given frequency. The lower sub-plot shows the derivative of $N_s(\nu)$. The upper and lower panels show the same data at two different frequency spans. These plots are a recreation of Figs. 3, 4 and 5 from [54] for a cavity with dimensions of the shielding room. Note that large spikes in $\Delta N/\Delta\nu$ should be interpreted as binning artifacts and are only shown for reference. The analytic derivative is more useful.



Figure 2.35: Pictures of conductor configurations in the shielded room. The antenna is in the same position between photos. The left panel shows a tin foil hat, and the right shows a random placement of scrap metal. Hat and scrap metal courtesy of Tyler Erjavec.

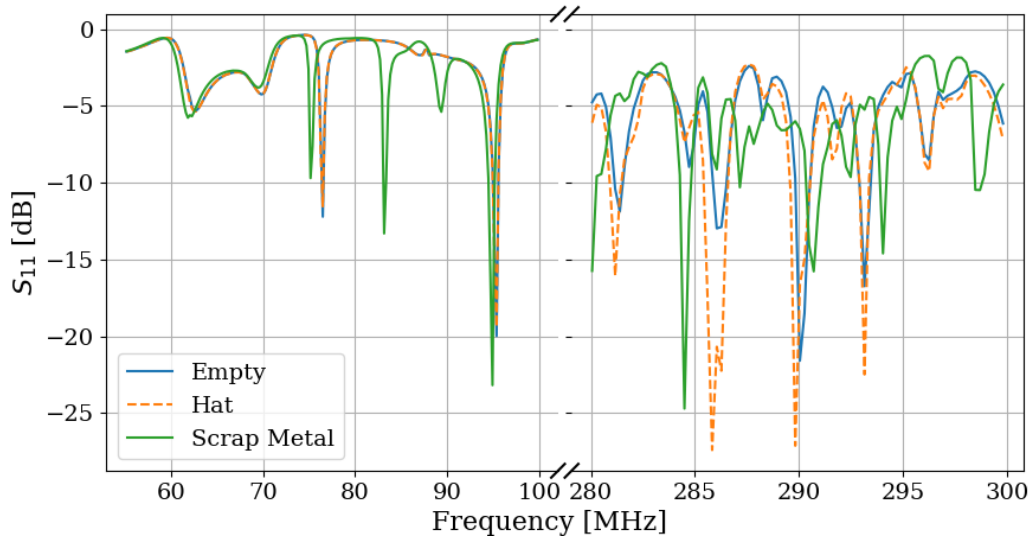


Figure 2.36: Measured S_{11} with different conductors in shielded room, as pictured in Fig. 2.35. Modes visible at low frequency agree nicely with the predictions of Eq. 2.43, though they are pulled around by the scrap metal. Note, the scale changes slightly after the X-axis break.

1225 2.4.2 Statistical approach to electromagnetic waves in cavities

1226 By using a mode stirrer, modes are intentionally pulled around in frequency, and the average
1227 response of the cavity begins to converge to be relatively flat. The regime where this occurs is
1228 known as being well-stirred. It requires the stirrer to be large enough and obey some design
1229 principles and that the frequency to be above a threshold. This lowest usable frequency
1230 (LUF) is determined by a minimum modal density since the modes must be close enough
1231 together in order to overlap. For a room-sized reverberation chamber with a lowest resonance
1232 of around 60 MHz (~ 3 or 4 meters per side), the rule of thumb cited by Hill, among others,
1233 is the LUF is close to where the modal density is about 1 mode/MHz. Therefore, according
1234 to Fig. 2.34, the LUF of our shielded room is about 200 MHz.

1235 A simple alternative to using a purpose-built mode stirrer is moving a receive antenna
1236 around in the room. Instead of moving the spatial structure of the modes around the antenna,
1237 the antenna is moved through the modes. While not as effective, it is simpler to implement,
1238 so this was the method used in Run 1A. Note that Run 1A does not rely on statistical
1239 uniformity. Simulations provide a means to calibrate the system as discussed in Sec. 4.3.
1240 However, using these statistical ideas provides a much more stable simulation with a much
1241 better agreement with measurement.

1242 One final remark that is relevant to the experiment is the concept of composite Q . This
1243 parameter represents a resonant enhancement factor that corresponds to the antenna/room
1244 system's tendency to “ring up” in the same way any resonator will. It is referred to as *com-*
1245 *posite Q* and represented as \tilde{Q} . It is analogous to the standard quality factor of a resonator

1246 with one important modification; the experiment is operated across a wide frequency range,
1247 so \tilde{Q} is defined across the continuum of these resonances, not only on classical eigenmodes
1248 of the system.

1249 **2.5 System Design**

1250 This section outlines the subsystems which make up the experiment. While specifics and
1251 basic calculations are provided as they apply to design choices of subsystems, testing and
1252 characterization of the system as a whole is left to Ch. 3. A simplified schematic of the
1253 entire experiment is shown in Fig. 2.37 and a photo of the lab is shown in Fig. 2.38.

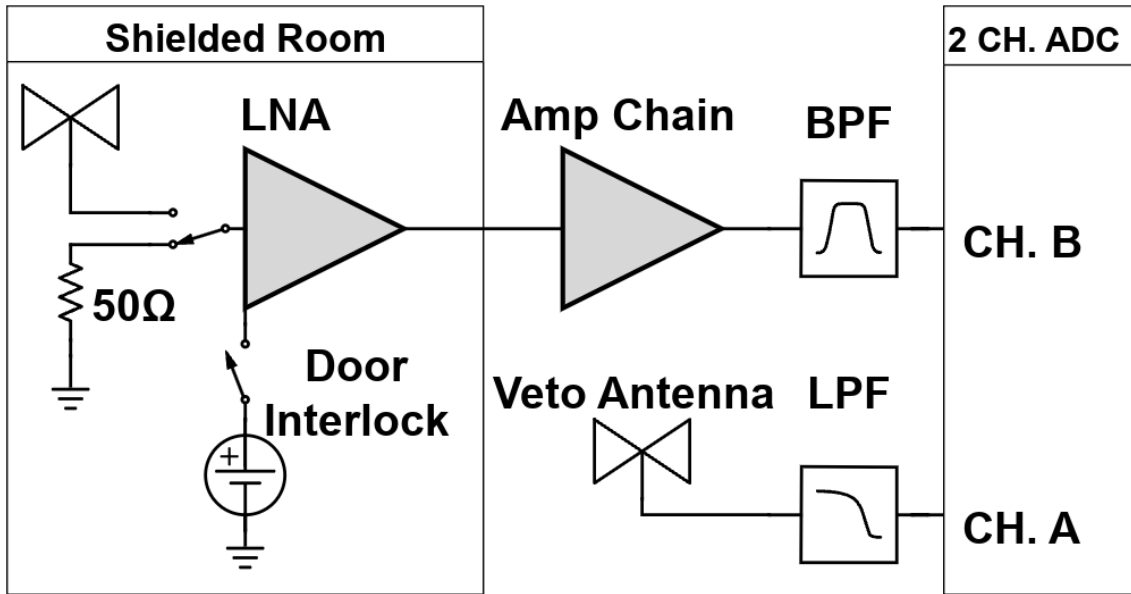


Figure 2.37: Schematic of the RF receiver system. An RF coax switch allows the PC to control the source (antenna or terminator). The amplifier chain is shown with more detail in Fig. 2.42. The switch is controlled by optical fiber to maintain the isolation of the room. The LNA (Pasternack PE15A1012) has a nominal gain and noise temperature of 40dB and 100K (measurements shown in Sec. 3.1.1). It is interlocked (Fig. 2.43) to the door to protect amp B and the ADC from large signals when the door is open. The secondary amplifier is a Mini-Circuits (MC) ZKL-1R5+ and has a nominal gain of 38dB. Not pictured after this amplifier is a fixed 4dB of attenuation. The band pass filter (BPF) defines the experiment's bandwidth, $-3 \text{ dB} \approx 40 - 320 \text{ MHz}$ and is discussed in Sec. 2.5.4. The veto antenna is outside of the room and interference is not reduced by the $\approx 100 \text{ dB}$ SE of the room, so no gain is required. The low pass filter (LPF) on the veto is for anti-aliasing.



Figure 2.38: Photo of dark radio lab. The shielded room contains the main antenna as well as the LNA and power supply (not visible). The veto antenna can be seen hanging outside of the shielded room. Photo taken looking south.

1254 **2.5.1 Shielded room**

1255 The shielding room [55] serves two purposes. The first is straightforward; to shield the
1256 antenna, keeping radio frequency interference (RFI) *out*. The second purpose is a bit more
1257 subtle; to keep any converted dark photons *in*. This second point is addressed further as an
1258 aspect of system calibration in Ch. 4, but roughly can be described by the loaded quality
1259 factor [56–58] of the antenna/room system. Namely, a more resonant system will be more
1260 sensitive to coherent signals. This subsection will focus on the first point, keeping RFI out.

1261 Shielding effectiveness SE is a measurement of a shielding enclosure's ability to attenuate
1262 electromagnetic waves from entering,

$$\text{SE} \equiv 10 \log_{10} \left(\frac{P_{\text{open}}}{P_{\text{closed}}} \right) = P_{\text{open}, \text{dB}} - P_{\text{closed}, \text{dB}} \quad (2.46)$$

1263 where $P_{\text{open}}/P_{\text{closed}}$ are powers received with the door open/closed. The ratio of powers
1264 allows all the specifics of antenna matching to cancel, allowing for a very simple differential
1265 measurement. The results of this are described in Sec. 3.2.

1266 Another important measurement are the dimensions, shown in table 2.2. I carefully
1267 measured the room with a laser range finder. I checked the rangefinder against a measuring
1268 tape, and it gives good agreement to 1 mm²⁴. The room is out of square by a few mm,
1269 especially the height measured in the south-west corner compared to the height measured
1270 everywhere else. This is the most extreme deviation and is about 5 mm.

²⁴After a year, I dropped it and it now gives crazy readings which jump around by 10s of cm. Be careful!

Direction	Coordinate	Nominal Length [ft]	Measured Length [m]
West-East	x	10	3.070
Vertical	y	8	2.457
North-South	z	12	3.684

Table 2.2: Direction, coordinate, and length measurements of the shielded room in lab 314. Note that Fig. 2.38 is looking south, so x is right-left, and z is into the page. Note that these are the mean values of several measurements. The room was found to be about 5 mm out of square, so these should be interpreted as \pm 5 mm.

2.5.2 Antenna

The antenna plays an important role in the experiment as the matching device between electromagnetic waves in the cavity and the 50Ω receiver system. For a broadband search such as the 50-300 MHz run (a 6:1 bandwidth), a broadband antenna must be used. The chosen antenna must provide a good impedance match and high efficiency since an inefficient antenna would convert a substantial amount of the converted dark photon's power into heat within the antenna's structure. The antenna is connected to the RF switch via a low loss (0.45dB at 300 MHz) 21 ft. LMR400 cable. This contributes about 31.6 K to the ≈ 400 K antenna noise, see Eq. 2.27. Note that the final limit on epsilon scales with the square root of system temperature, so this is only a few percent degradation in the final limit after a 9 day run.

For the 50-300 MHz run, a ≈ 131 cm biconical antenna (bicon) was chosen. The selected model is manufactured by COMPOWER, model AB-900A [59]. In a phone call with the manufacturer as well as testing of the isolated balun, it was determined that the balun used in the antenna was 1:1. This allows for simple simulation of a free-space aperture which

1286 agrees remarkably well with manufacturer data, Fig. 2.39. In COMSOL [60], the lumped
1287 port option allows for a balanced drive of an antenna. A match to a 50Ω transmission line
1288 through a 1:1 balun is simply modeled as a lumped port, a very simple object in COMSOL
1289 featured in nearly all of the antenna tutorials²⁵. Additionally, there is good agreement
1290 between simulated and measured antenna impedance. See the Smith Chart in Fig. 2.40.

²⁵See for example the dipole antenna tutorial, available at <https://www.comsol.com/model/dipole-antenna-8715>

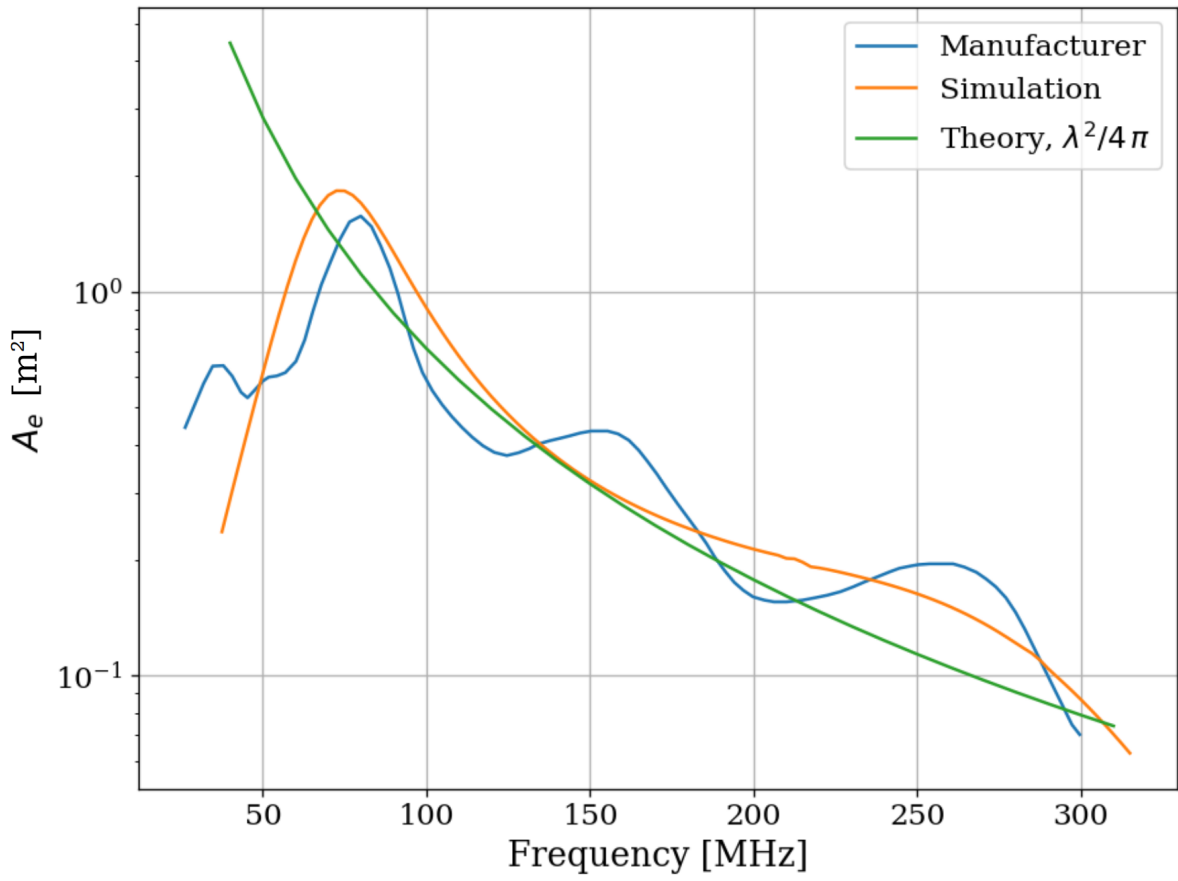


Figure 2.39: AB-900A biconical antenna effective aperture, simulated, measured and theoretical in free space. Simulation performed in COMSOL [60]. The measurement was provided by manufacture [59] as an antenna factor and was converted to aperture. Variations observed in the manufacturer's measured data are the result of testing over a ground plane and are a known discrepancy between simulations and measurements of “free space” antenna factor. See for example [61]

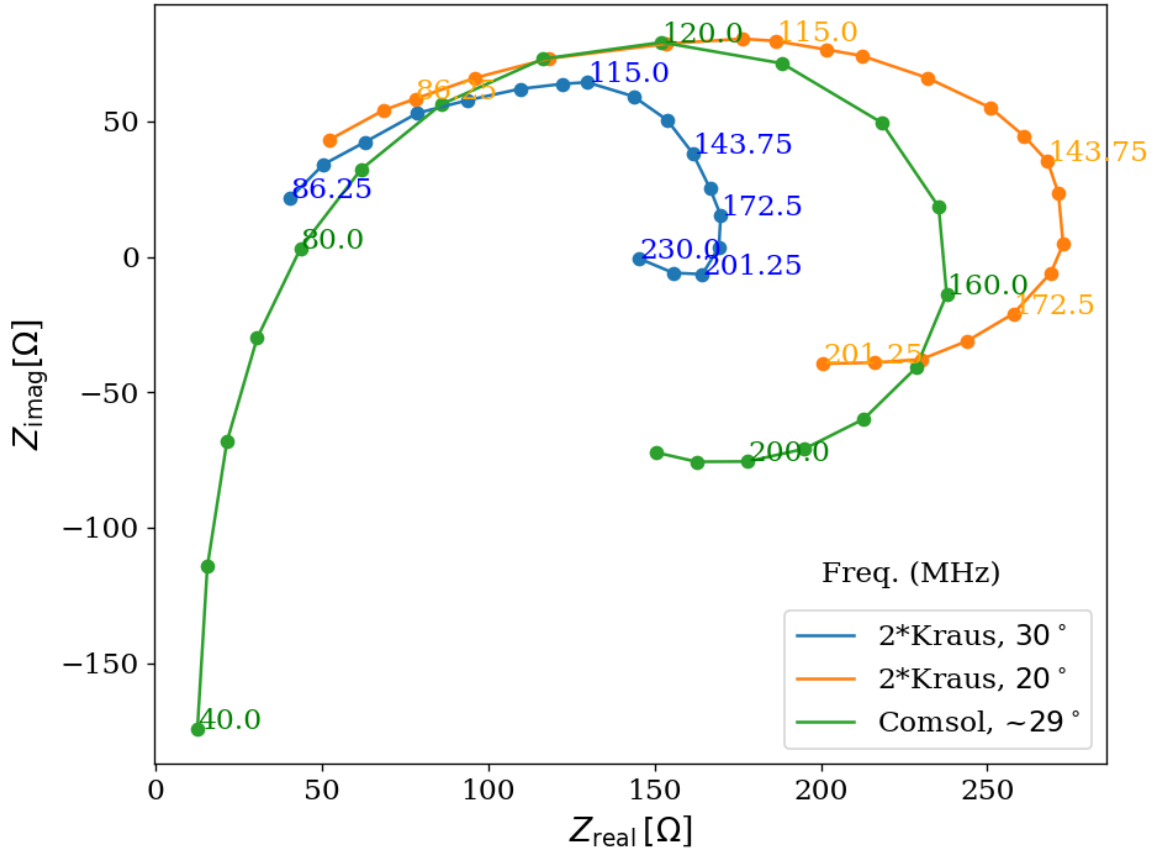


Figure 2.40: Simulated AB-900A biconical antenna free space complex input impedance shown in blue. The simulation was performed in COMSOL. The measurement is from Kraus' Antennas, second edition, Fig 8-13 [62]. Measured data is for a monoconical antenna and must be multiplied by 2 to compare to a biconical antenna, as discussed in Kraus. Numbers along the curve indicate the frequency in MHz.

1291 **2.5.3 Terminator and fiber-optic switch control**

1292 Experience has shown that it is advantageous to have a stable noise reference at the begin-
1293 ning of the signal chain to monitor system performance. One may think the antenna can
1294 provide this following Sec. 2.1.1.2, but in practice, the antenna is not that stable, Sec. 2.3.
1295 Furthermore, while RFI was not significant in the actual run, it very well could have been,
1296 introducing some uncontrolled, coherent power into the spectrum, which would have had
1297 an unknown origin. A terminator will give a very constant noise power density $S_{\text{term}} = kT$
1298 regardless of RFI and antenna position. For this reason, one is included. It is at the same
1299 temperature as the walls and is a nice passive solution. The RF switch shown in Fig. 2.37
1300 is actuated periodically during the run to measure the terminator's noise power through the
1301 same amplifier chain as the antenna. The terminator is connected to the switch via a 21-foot
1302 cable (LMR 400) that is identical to the antenna's cable. The switch is controlled via a
1303 fiber-optic link in order to reduce RFI. The fiber optic is an extremely important feature
1304 that was overlooked for several years at the beginning of the experiment, leading to lots of
1305 RFI.

1306 **2.5.4 Signal conditioning**

1307 As discussed in Sec. 2.1.5, the ADC has internal signals that are mitigated by introducing
1308 gain before the ADC. The amount of gain must be carefully chosen since too much will
1309 cause the ADC to clip. Additionally, high frequencies must be limited before digitizing to
1310 prevent aliasing. To accomplish this, several RF components must be selected to condition

1311 the analog signal: an LNA, a secondary amplifier, band-pass filter and several attenuators.

1312 **2.5.4.1 Low noise amplifier**

1313 The important concepts of the LNA have been introduced in Sec. 2.1.4. The key takeaway

1314 is that low noise gain helps to mitigate signal-to-noise degradation that occurs later in the

1315 signal path. Relevant specifications for the Pasternack PE15A1012 [36] are summarized in

1316 table 2.3.

Specification	Value	Uncertainty (50-300MHz)	Units
Frequency Range	50-1,000	-	MHz
Gain	40	± 1	dB
Noise Temperature	110	± 10	K
Input Return Loss	< -15	-	dB
Output Return Loss	< -15	-	dB
Price	500	-	USD
Voltage	9-15		V
Current	100	10	mA

Table 2.3: Specifications for the Pasternack PE15A1012-E. The voltage is regulated internally, so the exact voltage supplied is not critical, though there is a slight gain dependence on voltage since a higher voltage causes the amp to run warmer, see Fig 3.8.

1317 We have several identical amplifiers which are labeled with letters. At the time of writing,

1318 amplifiers A-D are out of commission. Amplifier E was used for run 1.4.

1319 **2.5.4.2 Secondary amplifier**

1320 As discussed in 2.1.4, the noise temperature of a secondary amplifier has negligible impact

1321 on the total system noise temperature. For this reason, a cheaper secondary amplifier is

1322 used. The specifications for the Mini-Circuits ZKL-1R5+ [63] are outlined in Table 2.4.

1323 This amplifier has no internal regulator, so gain and noise temperature depend strongly on
 1324 the bias voltage. Voltage was set to 9.05 V for run 1.4 using an external regulator (built
 1325 around a TI LM317 [64]).

Specification	Value	Uncertainty (50-300MHz)	Units
Frequency Range	50-1,000	-	MHz
Gain	40.5	.3	dB
Noise Temperature	275	15	K
Input VSWR	<1.14	-	dB
Output VSWR	<1.37	-	dB
Price	235	-	USD
Voltage	9-15	-	V

Table 2.4: Specifications for the Mini-Circuits ZKL-1R5+ as measured with 9.05 V bias.
 There is no internal regulator, so the voltage is set using an external regulator (built
 around a TI LM317 [64]).

1326 2.5.4.3 Band pass filter

1327 The band-pass filter has two purposes. The first purpose is to minimize the bandwidth
 1328 entering the ADC. This allows for introducing as much gain as possible without wasting
 1329 power amplifying frequencies where the antenna doesn't offer a good match. This will be
 1330 computed below in Sec. 2.5.4.4. The second purpose is to prevent aliasing²⁶. Aliasing occurs
 1331 when the analog signal contains frequency components at frequencies greater than half the
 1332 sample rate, in other words, when the signal and ADC don't obey a condition called the
 1333 Nyquist criterion, $\nu_s/2 \geq \nu$, where ν_s is the sampling frequency and ν is the frequency of
 1334 the analog signal.

²⁶Aliasing is a rather complex topic that is greatly simplified here. Wikipedia's aliasing page is an excellent reference. For a more rigorous treatment, see Ch. 7 Sec. 3 of the second edition of Signals and Systems by Oppenheim et. al [65]

1335 When this criterion is not met, higher frequencies are mapped back down to a lower
1336 frequency, described by the aliasing formula:

$$\nu_{\text{alias}} = |\nu_{\text{signal}} - n \times \nu_s|, \quad (2.47)$$

1337 where ν_{alias} is the aliased frequency, ν_{signal} is the original signal frequency, ν_s is the
1338 sampling rate, and n is an integer which specifies the Nyquist zone. In the simple case
1339 with bandpass filters that roll off well within the first Nyquist zone, only $n = 1$ must be
1340 considered.

1341 As an example, a $\nu_{\text{signal}} = 500$ MHz signal sampled at $\nu_s = 800$ MHz (the run 1.4 sample
1342 rate), it would alias to $\nu_{\text{alias}} = 300$ MHz. This also means that 1,300 MHz (residing in the
1343 second Nyquist zone) would alias down to 300 MHz, but again this and higher frequencies
1344 won't be considered. This means that by choosing only to analyze frequencies less than 300
1345 MHz, only frequencies greater than 500 MHz will alias into this analysis span.

1346 The Mini-Circuits ZX75LP-288-S+ low pass filter[66] serves as the anti-aliasing filter in
1347 run 1.4. It has an insertion loss of 68 dB at 500 MHz, while being flat to within 2dB from
1348 50 to 300 MHz. Additionally, the Mini-Circuits SHP-50+ [67] is used as the high pass filter.
1349 When connected in series, these two filters constitute the band-pass filter shown in Fig. 2.37.

1350 2.5.4.4 Putting together a signal conditioning chain

1351 The total gain required can be estimated by setting the output referred power of bandlimited,
1352 400 K noise source times the gain equal to the maximum power the ADC can handle,

1353 $V_{\text{RMS}}^2/Z = 0.63 \text{ mW}$ for $Z = 50 \Omega$. Assuming a perfect filter from 50-300MHz (a 250 MHz
1354 bandwidth), the gain required is

$$G = \frac{0.63 \text{ mW}}{k 400\text{K} 250 \text{ MHz}} = 4.5 \times 10^8 = 87\text{dB}. \quad (2.48)$$

1355 Noise is a Gaussian random process, however. This much gain ensures 1σ of the time-
1356 domain samples are below clipping. Since many samples are collected ($2^{24} \approx 1.6 \times 10^7$ in
1357 run 1.4), and each has a probability of about 16% of clipping, many samples will clip with
1358 87 dB of gain. However, it gives a good estimation for what to expect.

1359 The band-pass filter is not a brick wall from 50 - 300 MHz as was assumed in 2.48. The
1360 effective bandwidth of a filter is defined here as the integral of the square magnitude of its
1361 through gain,

$$B_{\text{eff}} \equiv \int_{-\infty}^{\infty} d\nu 10^{S_{21}/10}. \quad (2.49)$$

1362 Where S_{21} is measured in dB, and we are interested in integrating a quantity that is
1363 proportional to linear power, so it is divided by 10 rather than 20. The linear S-parameters of
1364 components connected in series multiply [43], but since dB are logarithmic, this is equivalent
1365 to adding their S-parameters (in dB). Also note that $S_{21} \equiv \text{IL}$, the insertion loss. Insertion
1366 loss is frequently given on data sheets.

1367 With all this in mind, we can compute $B_{\text{eff}} = 237.06 \text{ Hz}$ for the actual filters (Mini-
1368 Circuits SLP-50+ high pass filter and Mini-Circutis ZX75LP-288-S+ low pass filter) from
1369 their data sheets. Curves of S_{21} for the real band pass filter and an ideal brick wall filter are

1370 shown in Fig. 2.41. Note that it is actually slightly less than the ideal 250 MHz bandwidth
1371 since there is some loss in band.

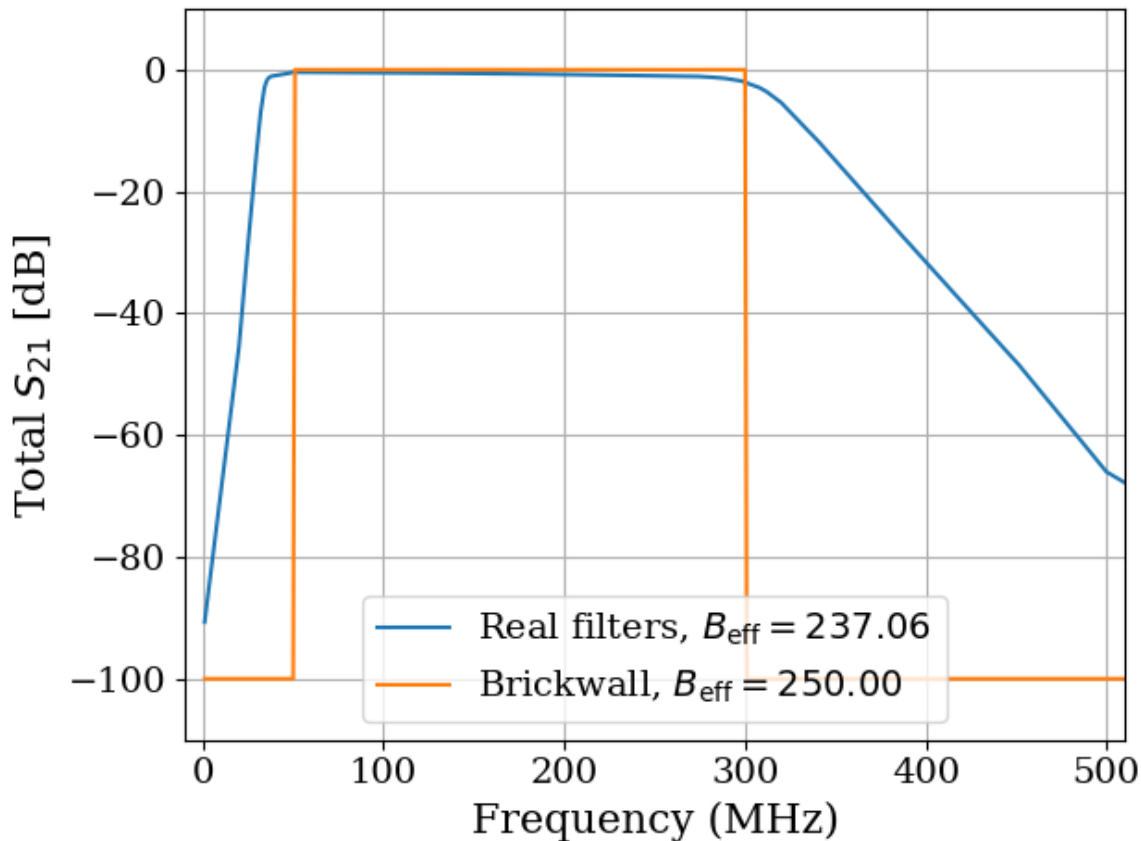


Figure 2.41: Through gain (S_{21}) of bandpass filter. Shown in dB, however B_{eff} is computed with linear S_{21} as in Eq. 2.49. Ideal brickwall filter shown for reference.
comment: Add Hz in legend

1372 Setting the gain is ultimately done by trial and error; taking a scan, adding some atten-
1373 uation if it clips, taking a scan, etc. Experience and preliminary simulations have shown
1374 that a few dB of clipping for a noise-dominated signal actually doesn't matter much, but
1375 this was not fully explored. If future runs are to scan for longer, they may have significant
1376 contamination from ADC spurs (see Sec. 2.1.5.1), so additional gain driving into clipping

1377 may be fruitfully explored. Every dB of gain added allows for $10^{1dB/5} \approx 44\%$ more averaging
 1378 before ADC effects are at the same relative level²⁷, so a little extra gain goes a long way.

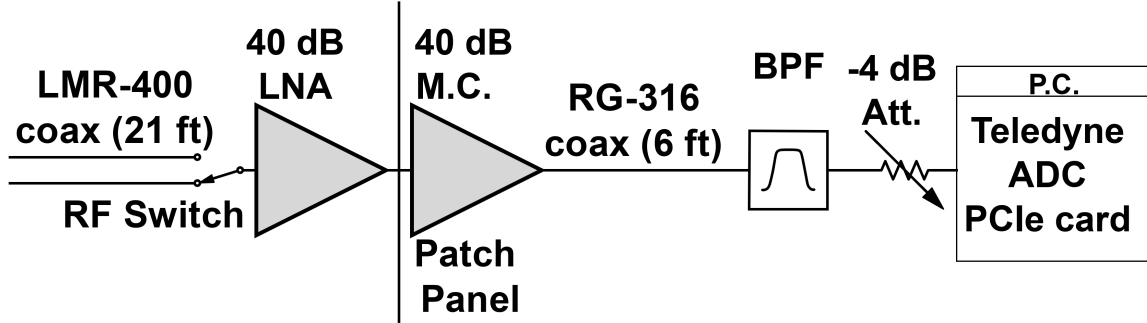


Figure 2.42: Schematic of Run 1A amplifier chain. Antenna (Sec. 2.5.2) and terminator (Sec. 2.5.3) are not part of the amplifier chain and, therefore, are not shown, but they would be at the far left of the schematic. All RF connectors are SMA, except the connection between the bicon antenna and its cable which is N type (though that cable has SMA on the switch-side). RF switch is Teledyne CR-33S8D-T. 40 dB LNA is Pasternack PE15A1012-E (Table 2.3). The patch panel uses an SMA bulkhead connector labeled “A” (far left-hand side when standing outside the shielding room, as shown in Fig. 2.38). 40 dB Mini-Circuits (M.C.) is Mini-Circuits ZKL-1R5+ (Table 2.4). Band-pass filter (BPF) is made up of Mini-Circuits SLP-50+ high pass filter and Mini-Circutis ZX75LP-288-S+ low pass filter. Note that filters and attenuator are directly connected to the SMA port of the Teledyne ADC (Sec. 2.5.7) to mitigate RFI received in the RG-316 cable run.

1379 2.5.5 Veto antenna

1380 The veto antenna is an identical Compower AB900 bicon antenna [68] as is used in the
 1381 shielded room. It is connected to channel A of the ADC with no amplification. However, it
 1382 has a Mini-Circuits ZX75LP-288-S+ low pass filter [66] to prevent aliasing. This is the same
 1383 model low pass filter that is used for the main channel. The antenna is hung a few feet in

²⁷Calculations in dB like this are handy once they are understood, but can seemingly come out of nowhere. This can be worked out by a careful reading of section 2.2, using properties of logarithms and definition of the dB.

1384 front of the door from some pipes on the ceiling. The proximity to these pipes likely gives
1385 the antenna a strange response, but its purpose is simply to look for large RFI signals, so
1386 this isn't that important.

1387 **2.5.6 12 V power system**

1388 The LNA and switch are active components that require power to operate. The experiment
1389 is incredibly sensitive to RFI, so while there is 120 VAC in the room, it is simpler to provide
1390 the power from a 12 V battery than to use an AC/DC regulator. Originally a 12 V lithium-
1391 ion (LiFePO4) battery was used. Lithium-ion batteries contain several cells and a controller
1392 to regulate charge/discharge between the cells. In order to remove the possibility of this
1393 controller emitting RFI in the room (which would create candidates that would be extremely
1394 difficult to veto), the lithium-ion was replaced with a 12 V lead acid golf cart battery ²⁸.

1395 The LNA is interlocked to the door such that power is cut when the door is opened.
1396 This prevents the large radio signals from being amplified once they enter the room and
1397 protects the ADC. The circuit that controls this is shown in Fig. 2.43. Note that it takes a
1398 few seconds for the slow turn on circuit to discharge, so the door should be opened slowly

²⁸This was done between run 1.2 and 1.3 due to interference resulting in many candidate detections. Most of these were likely external RFI, which were eliminated by cleaning the door (discussed in Sec. 3.2). Two variables were changed (cleaning of the door and replacement of the battery) so it's unclear if a lead acid is necessary. It works, however, and if it ain't broke, don't fix it.

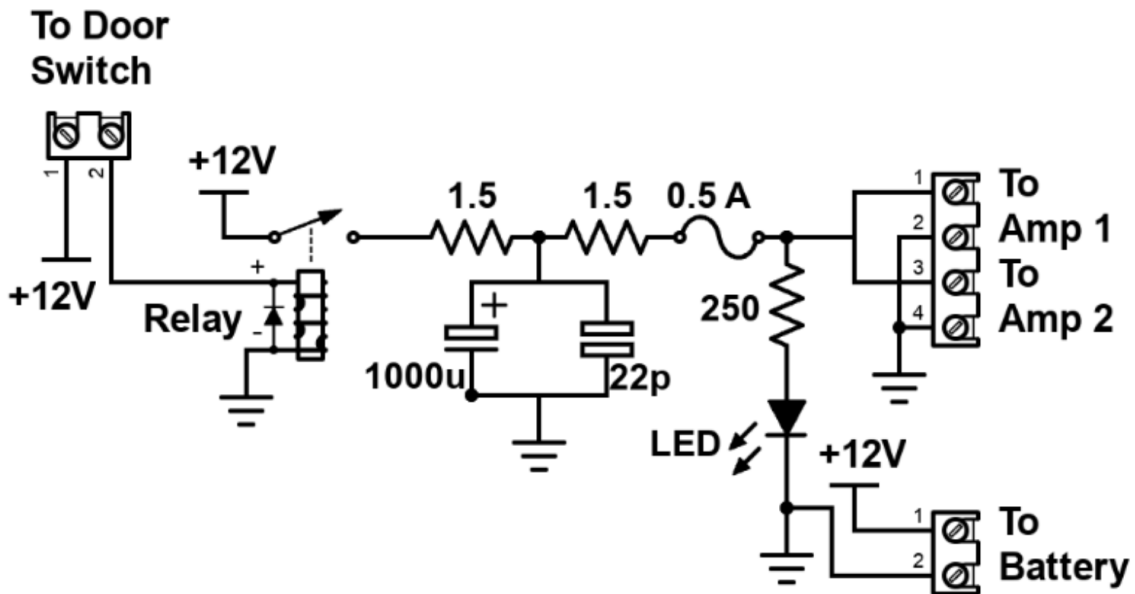


Figure 2.43: Schematic of Interlock board. No voltage regulation is provided because it is designed to work with amplifiers containing internal regulation (Pasternack PE15A1012 [36]). Not shown is a simple “slow turn on circuit” consisting of a 0.68 F capacitor and an $8\ \Omega$, 10 W resistor (time constant = 5.4 seconds) which was installed to protect the amplifier from transient voltages when the door is closed. This circuit can be seen in Fig. 2.44. Experience has shown the liberal use of fuses to be prudent when working with car batteries in a metal room.

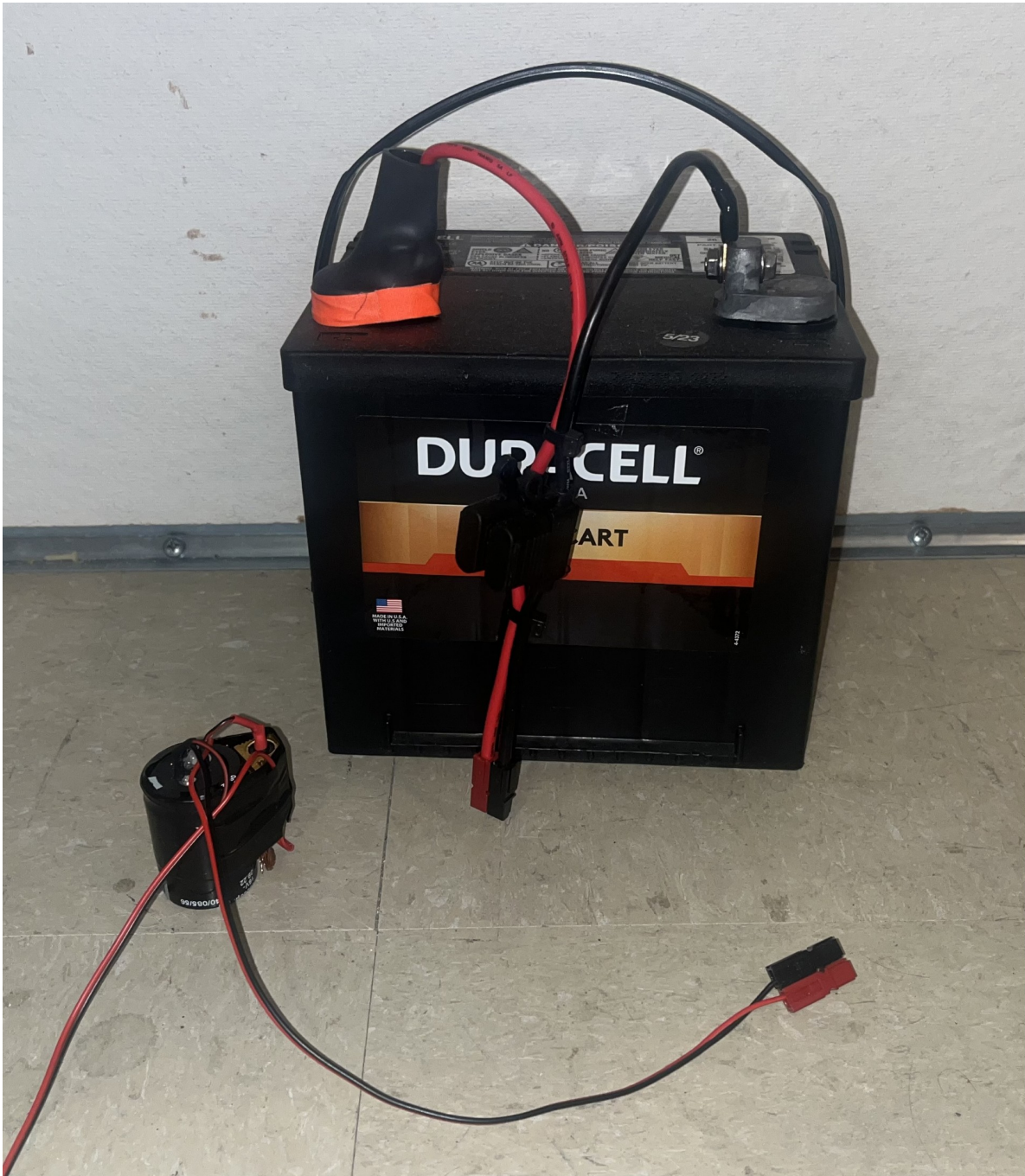


Figure 2.44: Photo of 12 V lead-acid battery and slow turn-on circuit. Both connect directly to the interlock board shown in Fig. 2.43. The slow turn-on circuit is connected between the interlock board and amplifier. The battery includes a 2A fast fuse installed in a commercial Anderson power pole assembly.

1399 **2.5.7 GPU-Based Real-Time Spectrum Analyzer**²⁹

1400 The use of commercial Spectrum Analyzers (SAs) that feature so-called real-time spectrum
1401 analyzer (RTSA) mode comes with several restrictions that limit the efficiency with which
1402 they are able to perform wide-band scans with narrow frequency resolution, as pointed out
1403 the dark radio pilot run [4]. The number of frequency bins output by a real discrete Fourier
1404 transform (DFT) is equal to half of the number of time domain samples, while the bandwidth
1405 is given by half of the sample rate. Furthermore, the ability to acquire data in real-time
1406 requires a DFT algorithm (generally implemented as a fast Fourier transform, FFT) and
1407 computational resources that can operate on time domain data at least as fast as it is
1408 acquired. In practice, real-time DFTs with high-frequency resolution and wide bandwidth
1409 require modest memory, transfer rates and processing resources. Commercial “real-time
1410 spectrum analyzers” tend to cheat a bit to reduce hardware requirements. Frequency mixers
1411 reduce the required sample rate (and therefore span), limits on FFT lengths reduce either
1412 span or resolution, and limits on the rate of scans make it so that these SAs aren’t real-time
1413 (at least in the sense that we require them to be).

1414 For this reason, I have constructed a custom SA based on the Teledyne ADQ32 PCIE
1415 digitizer[37], which is wide-bandwidth (up to 1.25 GHz frequency span), high resolution
1416 (2^{24} point FFT), and nearly 100% real-time (see Fig. 3.16). I have been unable to find a
1417 commercial SA with comparable capabilities. Specifications are shown in table 2.5.

²⁹Code for this section can be found at: <https://github.com/josephmlev/darkRadio/tree/master/daqAnalysisAndExperiments/teledyne>

Bit depth	12 bits
Sample rate	800MHz
DFT input length	2^{24} samples
FFT compute time	2 ms
Channel count	2
Efficiency	99.765%

Table 2.5: Specifications for the custom, real-time spectrum analyzer used for run 1A.

1418 After passing through an amplifier and filter chain outlined in Sec. 2.5.4, both the main
 1419 and veto antenna's RF signals are digitized by the ADQ32's two independent ADCs. This
 1420 raw, digitized time series is sampled at the digitizer's clock rate. Since the discrete Fourier
 1421 transform (DFT) of a perfect sinusoid sampled by an unstable clock will have a finite spectral
 1422 width, clock stability must be better than the expected spectral width of candidate signals,
 1423 which in our case is set by the expected $Q_{DP} \approx 10^6$. To achieve the required stability, we
 1424 synchronize the sample clock (Valon 5009 RF synthesizer) of our ADC to a 10 MHz rubidium
 1425 frequency standard (Stanford Research Systems FS725), which is further steered by the
 1426 one pulse-per-second (PPS) signal from a GPS receiver. Clock performance is discussed in
 1427 Sec. 3.3.3.

1428 This system utilizes a GPU direct write in order to minimize CPU-GPU copies tends to
 1429 be significantly slower than the FFT itself. This GPU direct write is implemented by the digi-
 1430 tizer's C++ API which is called from python. This happens in the `teledyneTemplate/drDaq.py`
 1431 script (within the directory linked as a footnote at the beginning of this subsection). The
 1432 GPU is a Nvidia A5000. The process is shown graphically in Fig. 2.45

1433 First, several buffers are allocated in GPU memory. A record is acquired (2^{24} time domain

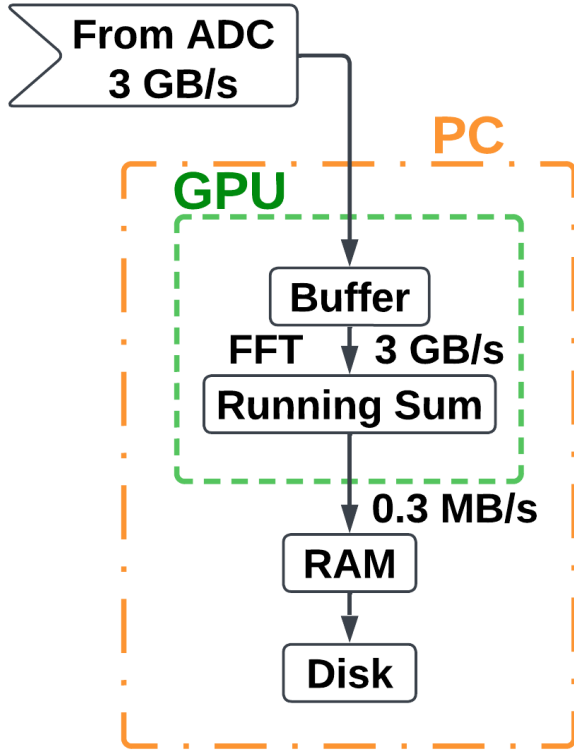


Figure 2.45: Real time DAQ data stream. Approximately 10^4 time series records (about 3 minutes of real-time data) are written from the ADC directly to GPU buffers. FFTs are performed on these records, resulting in a pre-averaged spectrum that can be saved to disk. This setup is duplicated for channels A and B, though the data rates indicate the sum of both channels.

samples for run 1.4). This record is written to a pre-allocated, time-domain buffer in the GPU's memory. Next, an FFT is performed using Pytorch, which I found to be the fastest algorithm, at least on a Nvidia GPU. 8,600 FFTs are performed and added to a cumulative sum on the GPU (representing about 3 minutes of real-time data). Dividing by the number of FFTs provides an averaged spectrum that is saved for offline processing. This *pre-averaging* reduces the raw $\approx 1.5 \text{ GB/s}/\text{channel}$ data stream to $\approx 0.15 \text{ MB/s}/\text{channel}$, which greatly reduces storage requirements. However, this comes at the cost of temporal resolution of

1441 transient candidates. Since we are interested in constant (or at least very slowly varying)
1442 signals, this is not a problem, but in other radio astronomy applications, this step should be
1443 avoided. Pre-averaging is set using the NOF_BUFFERS_TO_RECEIVE variable, see Appendix A .

¹⁴⁴⁴ **Chapter 3**

¹⁴⁴⁵ **System Characterization and Data**

¹⁴⁴⁶ **Acquisition System**

¹⁴⁴⁷

“When you can measure what you are speaking about and express it in numbers you know something about it; but when you cannot measure it, when you cannot express it in numbers your knowledge is of meagre and unsatisfactory kind; it may be the beginning of knowledge but you have scarcely progressed in your thoughts to the stage of science whatever the matter may be.”

Lord Kelvin

1448 This chapter covers the characterization of the system as a whole, including the shielded
1449 room (Introduced in Sec. 2.5.1), amplifier chain (Sec. 2.5.4) and real-time spectrum analyzer
1450 system (RTSA, Sec. 2.5.7). This section provides data and information about how they
1451 were collected from tests that were performed, but that distract from the narratives of the
1452 preceding and following chapters. This chapter can be skimmed and referenced with further
1453 care during the reading of Ch. 4.

1454 **3.1 Measurement of Amplifier Chain Performance**

1455 The amplifier chain conditions the analog signal (described in Sec. 2.5.4). The following data
1456 show some measurements that are useful in confirming the system is operating as expected.
1457 Similar data should be collected and inspected before, during and after a new data run so
1458 that any performance degradation can be monitored. At the very least, one should take
1459 note of the power spectrum from a room temperature terminator (Fig. 3.10) and monitor it
1460 throughout the run for any changes. The heads-up display (Fig. A.1) makes this very easy.

1461 **3.1.1 Y-factor method¹**

1462 The Y-factor method [69] [70] is a common technique for measuring the gain and noise
1463 temperature of an amplifier chain (details in Sec. 2.1.4). A matched terminator is placed at
1464 the end of a transmission line, which is connected to the input of an amplifier chain under
1465 test. The output of the amplifier chain is measured with the terminator at two different

¹Code for this section can be found at: <https://github.com/josephmlev/darkRadio/tree/master/daqAnalysisAndExperiments/run1p4/yFactorTest/yFactorTest.ipynb>

1466 temperatures². These temperatures must be known, and the larger the difference the better
1467 the measurement because it is easier to extrapolate the slope and intercept from these data
1468 (see Fig. 3.1).

1469 There are a few different ways to handle the algebra, but the simplest is to fit a line of
1470 the form

$$T_{\text{out}}(\nu) = G T_{\text{term}} + B, \quad (3.1)$$

1471 where all terms are dependent on frequency. The x-intercept (and therefore the negative
1472 amplifier temperature) is simply G/B . This is shown as a cartoon for a single frequency in
1473 Fig. 3.1.

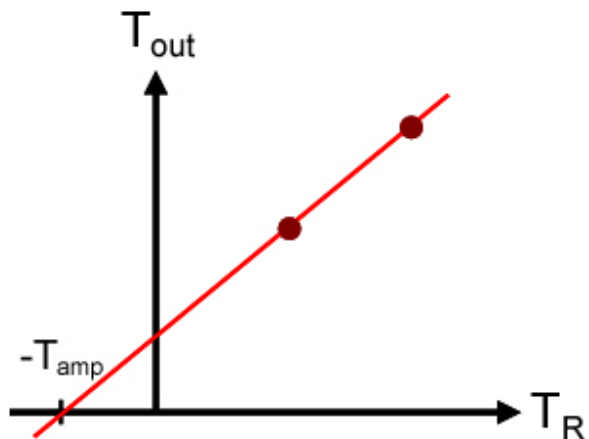


Figure 3.1: Cartoon showing Y-factor data. The (negative of) amplifier temperature is read off of the x-intercept. The gain is given by the slope. Figure from Wikipedia [71].

1474 To make this measurement, I wanted to use liquid nitrogen for the cold temperature

²Alternatively, a calibrated noise source can be used to simulate a very hot terminator, usually thousands of degrees Kelvin.

1475 (77 K) and a calibrated noise source for the hot temperature (\sim 12,000 K). The test was
1476 conducted using the noise source and a 30 dB attenuator placed directly before the ADC.
1477 This attenuation was later accounted for, yielding a calibrated measurement. However,
1478 while the test was set up to use this noise source, it gave unreliable results. I was able
1479 to confirm it became uncalibrated using a spectrum analyzer so I did not use that data
1480 point. Additionally, I made the measurements with a much wider band-pass filter (0-1 GHz)
1481 compared to the span of this Run 1.4 (0-0.3 GHz) so that the same data would also give the
1482 gain and noise temperature up to 1 GHz (though this is not shown in this thesis). Both the
1483 30 dB attenuator and the 0-1 GHz band-pass filter will be calibrated out. As a check this
1484 is done correctly, the gain was measured again using a tracking generator with the actual
1485 setup, avoiding corrections. This is shown in Fig 3.7. The two gain curves agree quite well.

1486 The test setup is nearly identical to the Run 1A amplifier chain (see Fig. 2.42). The
1487 differences are the 30 dB attenuator and band-pass filter (discussed above) and the short,
1488 semi-rigid, cryogenic-capable cable between the terminator and LMR 400 cable. The cryo-
1489 genic setup is the same as shown in the right panel of Fig. 2.28. The raw data (including
1490 only liquid nitrogen and room temperature) are shown in Fig. 3.2.

1491 The spectra of Fig. 3.2 contain hot and cold measurements at 2^{18} frequency points. At
1492 each point, a fit is performed according to Eq. 3.1. To demonstrate, this is shown for a single
1493 frequency (625 MHz) in Fig. 3.3.

1494 Finally, fitting the raw spectra shown in Fig. 3.2 with Eq. 3.1 at each of the frequency
1495 points, the frequency-dependent gain and noise temperature of the amplifier chain is ex-
1496 tracted. These are shown (after correcting for the 30 dB attenuator) in Figs. 3.4 and 3.5.

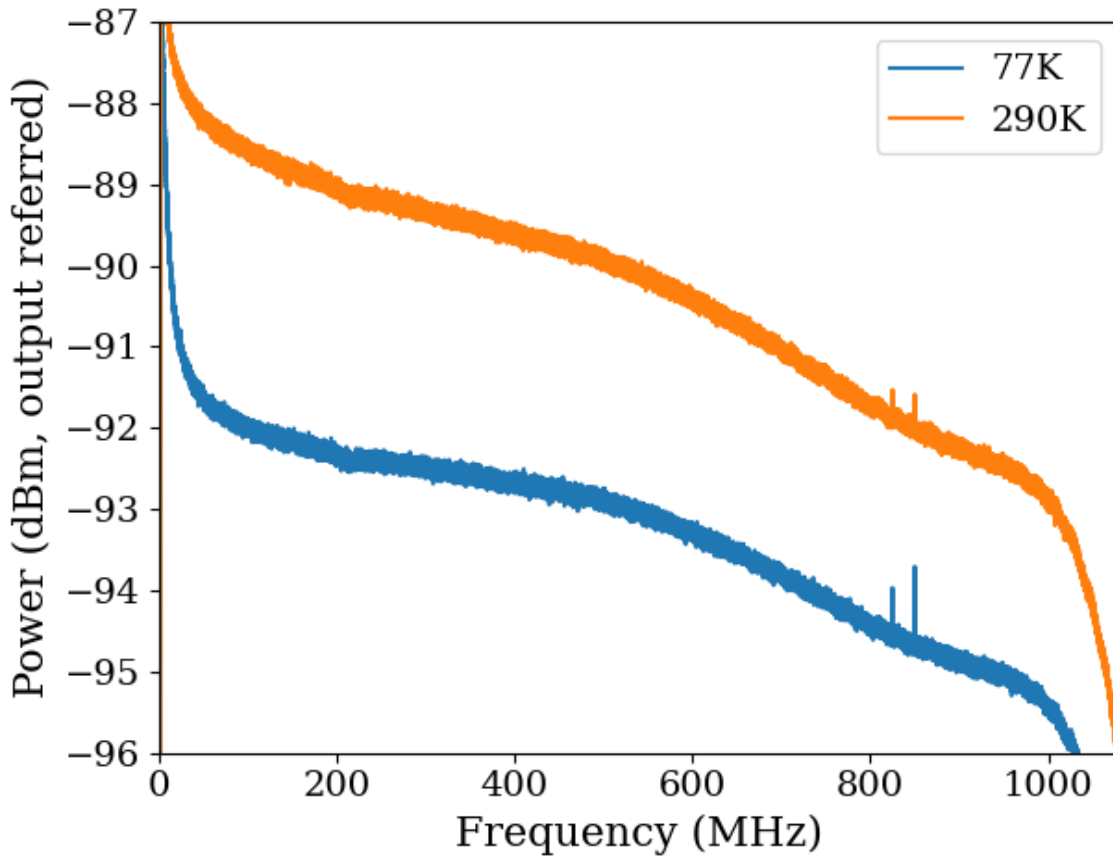


Figure 3.2: Raw output power spectra used to compute the gain and noise temperature for the Run 1.4 amplifier chain using the Y-factor method. $\Delta\nu_{\text{RF}} \approx 9.5 \text{ kHz}$, and 10,000 averages were taken. These data are only used to characterize the system between 50 and 300 MHz, so the low frequency ADC effects and RFI around 800 MHz do not affect the calculation. Note that the amplifier chain under test has a 30 dB attenuator directly before the ADC which is discussed in the text. This had an impact on the measured gain, and it is corrected for in the following analysis. It has negligible impact on the noise figure however, as shown in Eq. 2.29.

1497 As a final check, I took the Run 1.4 terminator data and corrected it for the gain and noise
 1498 figure found using the Y-factor method of this section, expecting to recover the -174 dBm/Hz
 1499 as predicted by Johnson's formula for a terminator at room temperature. The agreement is
 1500 quite good as shown in Fig. 3.6.

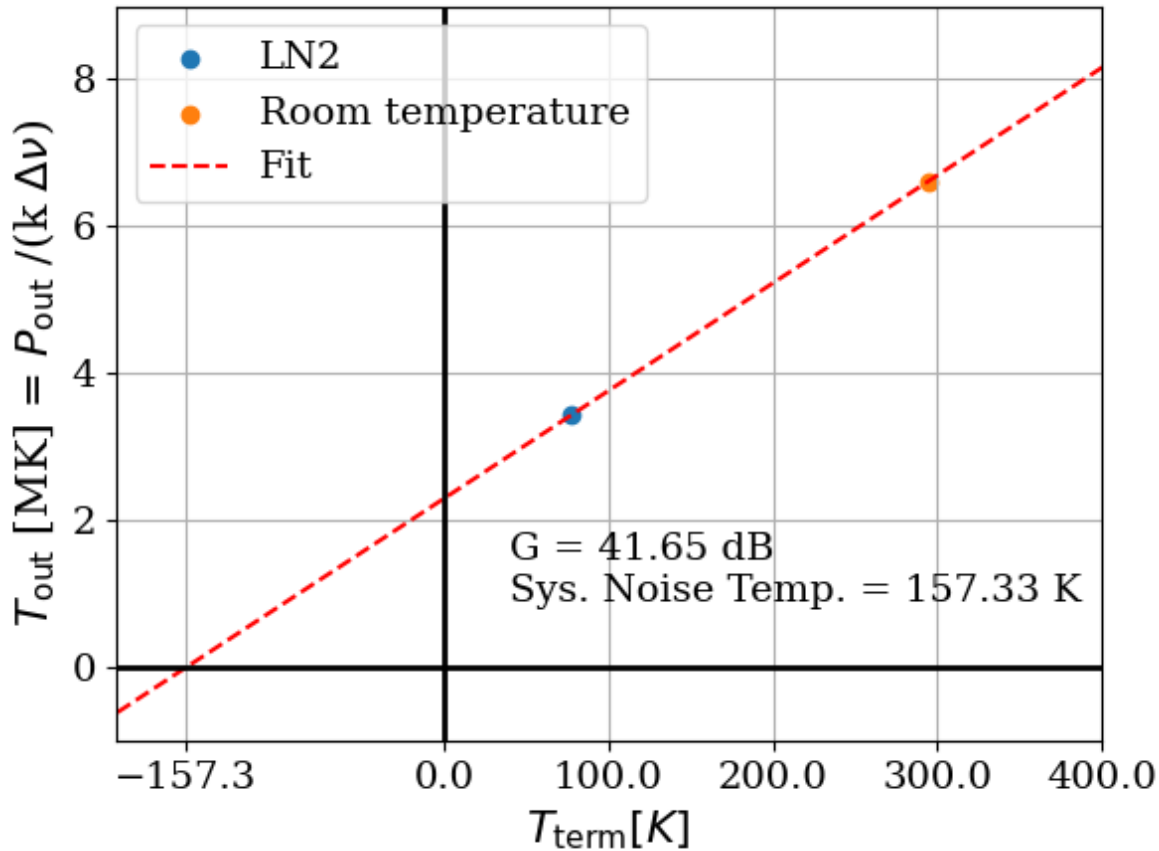


Figure 3.3: Y-factor data from Run 1.4 amplifier chain at a single frequency (625 MHz). Note that T_{out} is in MK or millions of degrees Kelvin. This is expected since there is approximately 41 dB of gain on an input temperature of a few hundred Kelvin. Reminder, there is a 30 dB attenuator which has not yet been corrected for.

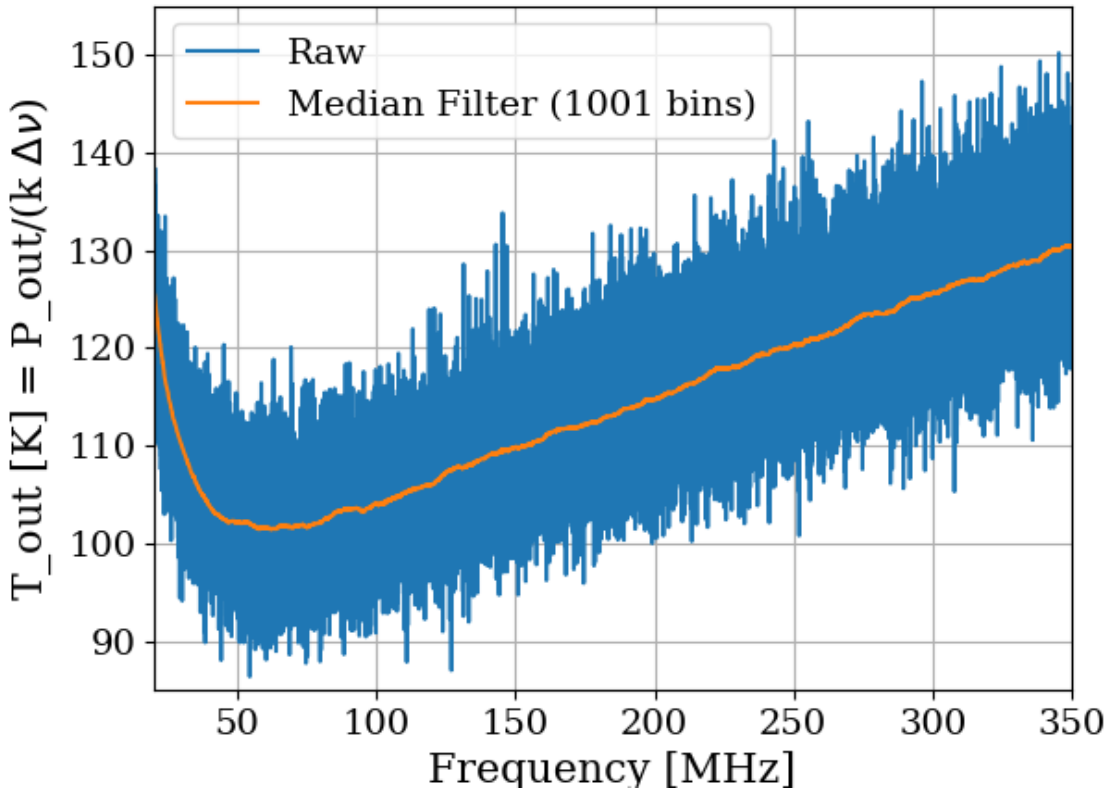


Figure 3.4: Frequency-dependent noise temperature of the Run 1.4 amplifier chain, measured using the Y-factor method. Low-frequency behavior is consistent with the data sheet of the LNA [36]. The increase at high frequency is due to the attenuation of the cable before the LNA. Future runs may place the LNA directly on the antenna to minimize this issue, though other complications will be introduced. The median filter is a simple rolling median to smooth out the noisy measurements.

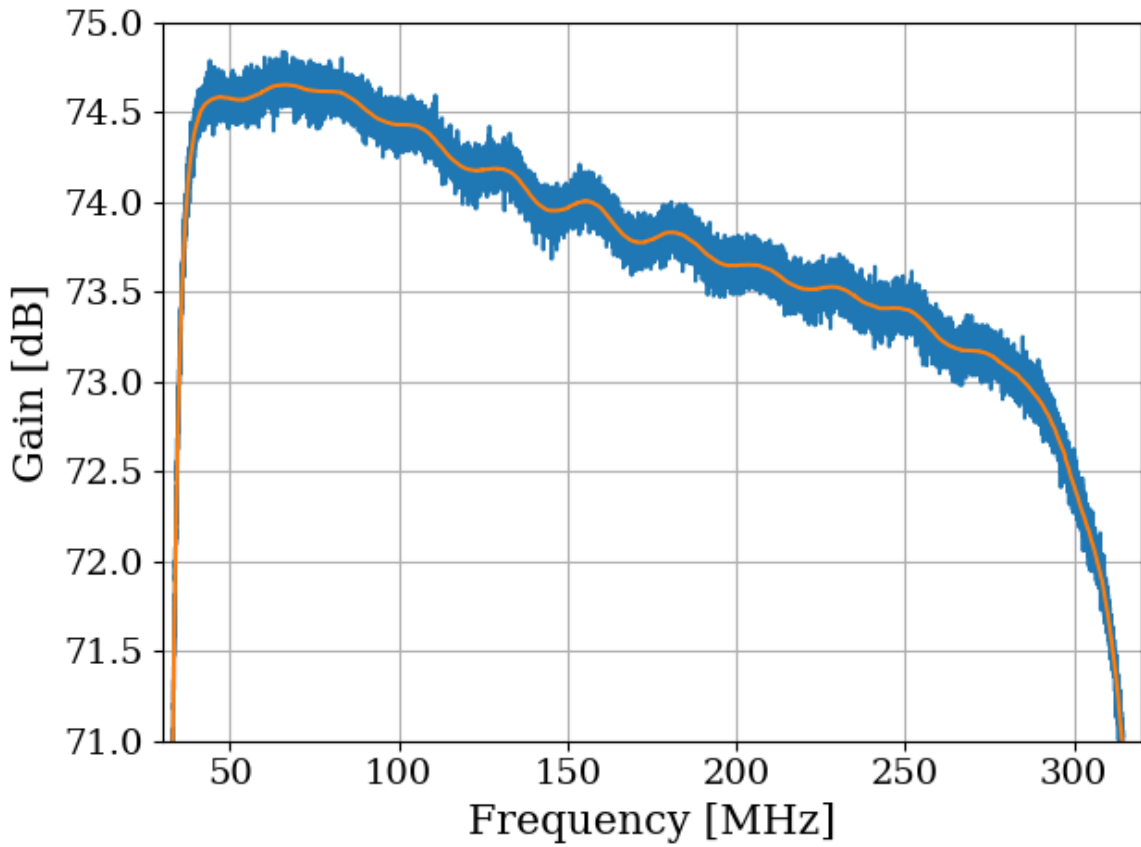


Figure 3.5: Frequency-dependant gain of the Run 1.4 amplifier chain, measured using the Y-factor method. The 30 dB attenuator and band-pass filter have been corrected for in this plot. The slow decrease of gain with frequency is consistent with the data sheets for the LNA [36] and secondary amplifier [63]. Roll-off at high and low frequencies is due to the band-pass filter (see 2.5.4.3). Bumpy behavior is due to the small impedance mismatch of the terminator to the 50Ω system.

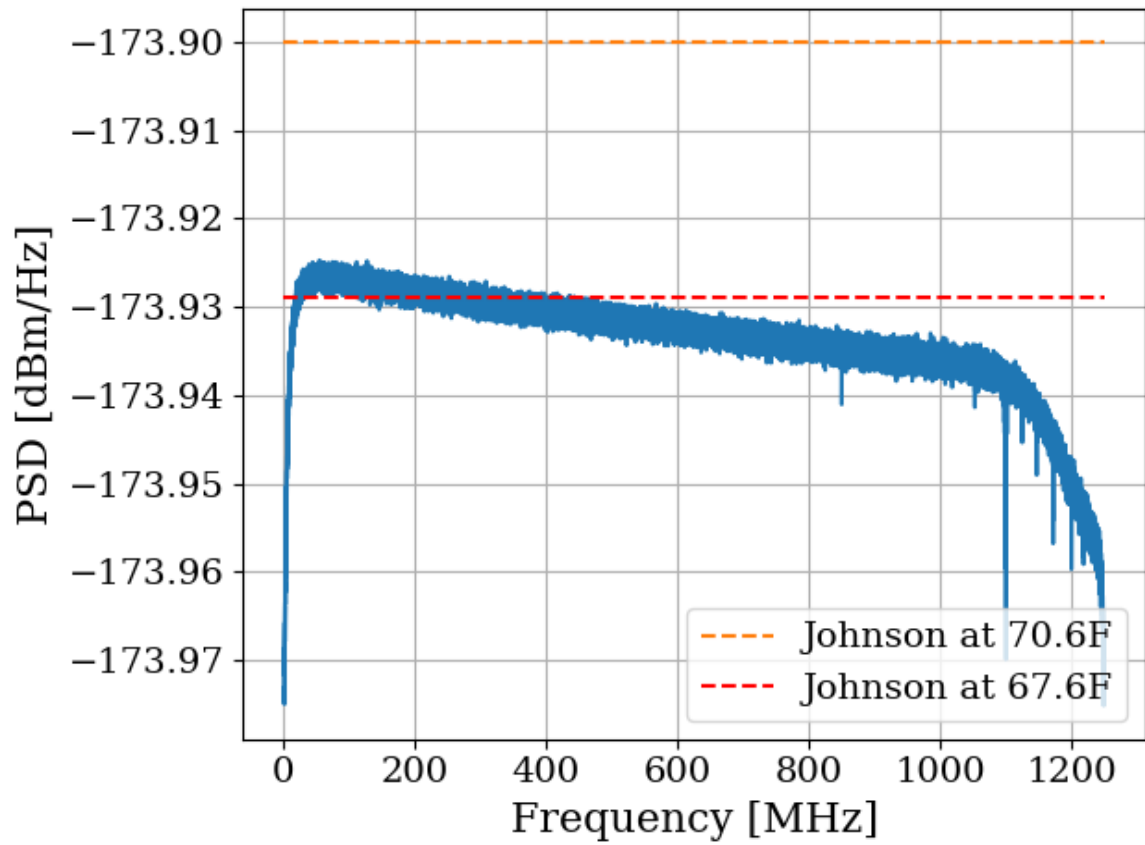


Figure 3.6: Run 1.4 terminator, input-referred power spectral density. Excellent agreement with the predicted value from the formula for Johnson noise at room temperature. Two reference temperatures are given with the dashed lines.

1501 3.1.2 Confirming gain with tracking generator measurement

1502 As a sanity check for the Y-factor method, the system gain was measured again using the
1503 tracking generator on the Rigol RSA-5065-TG [72], with good agreement. This measurement
1504 was useful since there were some corrections involved in the Y-factor measurement (the 30 dB
1505 attenuator and band-pass filter).

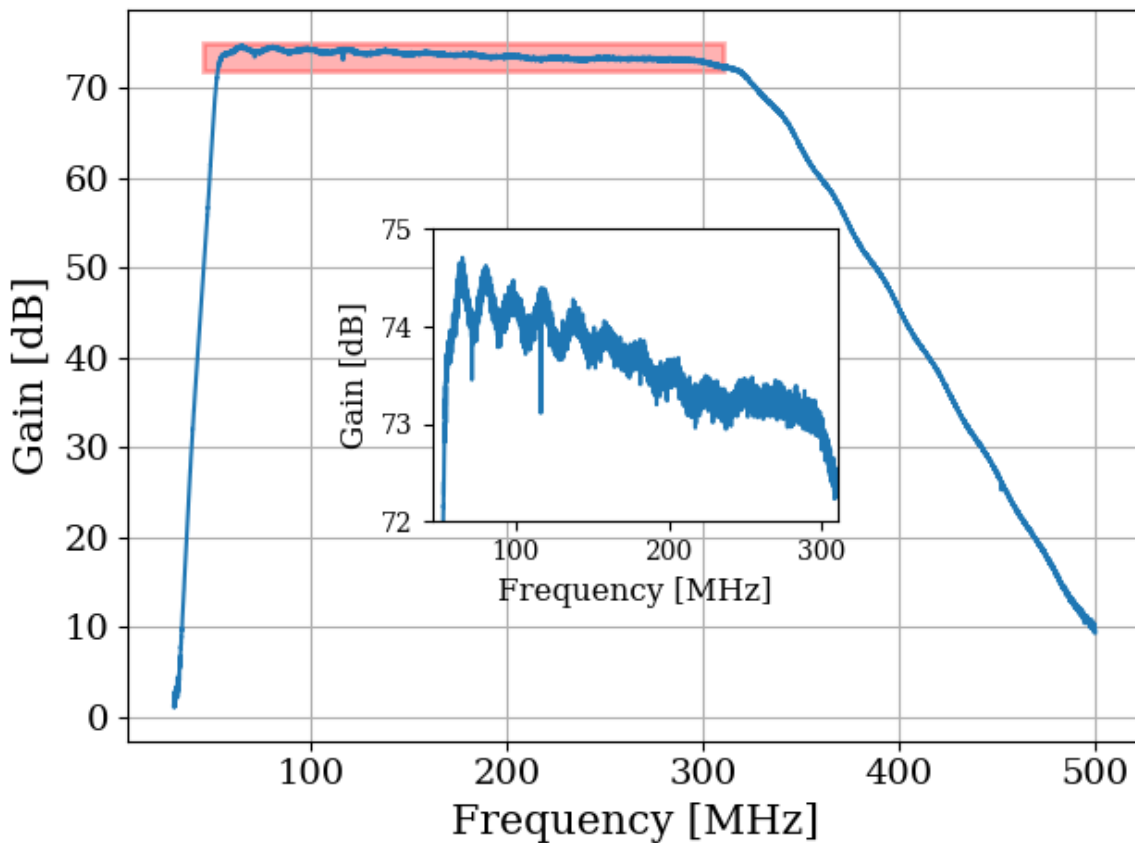


Figure 3.7: Gain vs. frequency of Run 1.4 amplifier chain, including LNA, secondary amplifier, band-pass filter and attenuators. Inset shows zoom of region enclosed in red box. This was measured using the tracking generator on Rigol RSA-5065-TG [72]. Wiggles visible in inset are a known artifact due to an impedance mismatch between the Rigol's tracking generator and the system under test. Gain was confirmed by comparing to Y-factor method (Sec. 3.1.1)

1506 **3.1.3 System stability over a run period**³

1507 The system's gain will vary slightly over the course of a run. An obvious culprit is the
1508 battery voltage decreasing with time⁴. At first glance, one may conclude that since the
1509 LNA is equipped with an internal voltage regulator, it is insensitive to the battery voltage
1510 as long as it is above some minimum value. However, at higher voltage, the regulator must
1511 dissipate more power which will make the LNA warmer. Temperature does have an effect
1512 on the gain of the LNA. Tests of gain vs. LNA voltage show that this is a minor issue. This
1513 is shown in Fig. 3.8.

1514 Knowing the gain vs voltage is only useful if it is understood how the battery voltage
1515 will behave over the course of the run. These data are shown in Fig. 3.9.

1516 As a final check of system performance during the run, Fig. 3.10 shows the output-referred
1517 power (averaged from 50-300 MHz) over the course of the 9-day Run 1.4. The gain varies by
1518 about 0.7%, an insignificant amount given the other uncertainties involved (especially that
1519 of simulation and calibration, Sec. 4.3).

³Code for this section can be found at: [https://github.com/josephmlev/darkRadio/tree/master/daqAnalysisAndExperiments/run1p4/run1p4_timeDependence.ipynb](https://github.com/josephmlev/darkRadio/tree/master/daqAnalysisAndExperiments/run1p4/run1p4_analysis/run1p4_timeDependence.ipynb)
https://github.com/josephmlev/darkRadio/tree/master/daqAnalysisAndExperiments/run1p4/gainAndNf/gainAndNF_analysis.ipynb

⁴The LNA is powered by a battery. The secondary amplifier is outside of the room and powered with a voltage regulator.

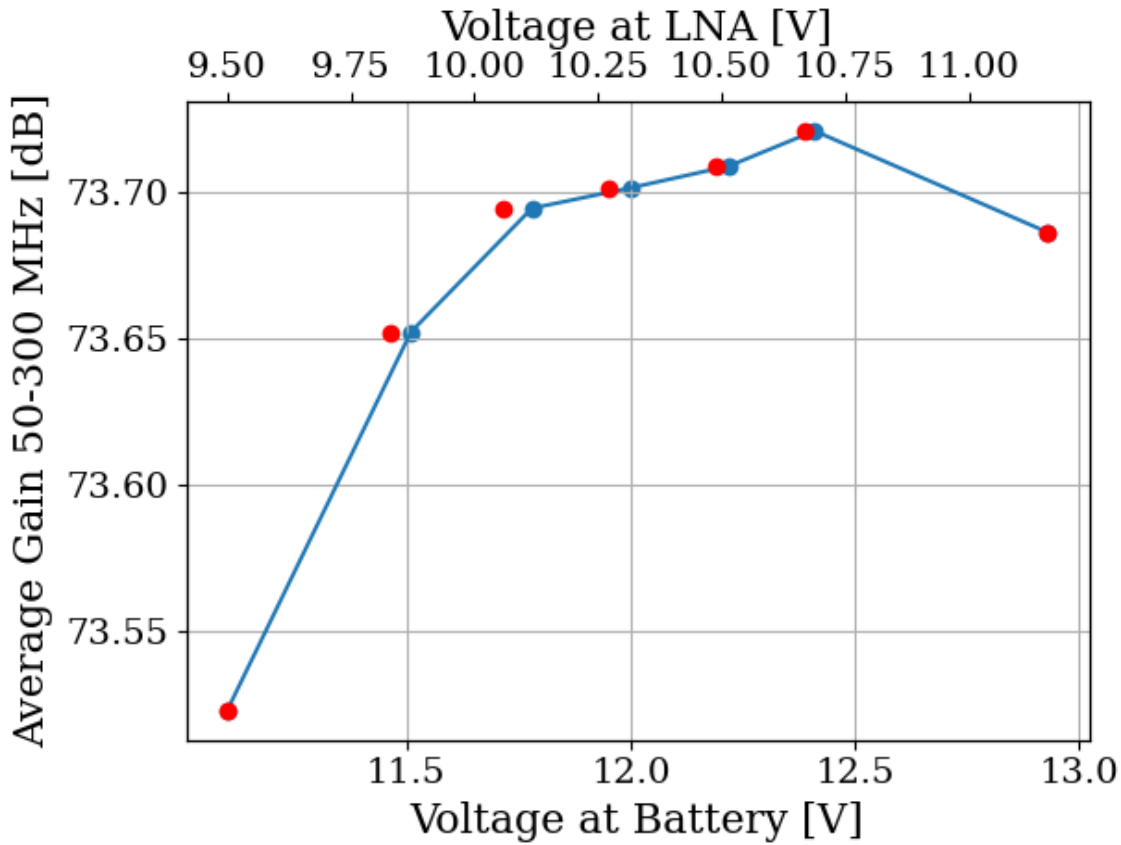


Figure 3.8: Gain vs. LNA voltage of Run 1.4 amplifier chain, including LNA, secondary amplifier, band-pass filter and attenuators. This was measured using the tracking generator on Rigol RSA 5065TG [72]. Gain is frequency dependent; its average value between 50 and 300 MHz is shown here. Voltage at the amplifier was measured directly at its terminals, after significant voltage drop due to interlock and slow turn-on circuits (described in Sec. 2.5.6). Gain is in good agreement with the previous two subsections, 3.1.1 and 3.1.2. The operating voltage range specified on LNA data sheet [36] is 10-15 V. The voltage at the LNA (red) does not exactly line up with voltage at battery (blue), so there is a slight offset. The scale of the x-axes scale has been set so that the maximum and minimum voltages line up.

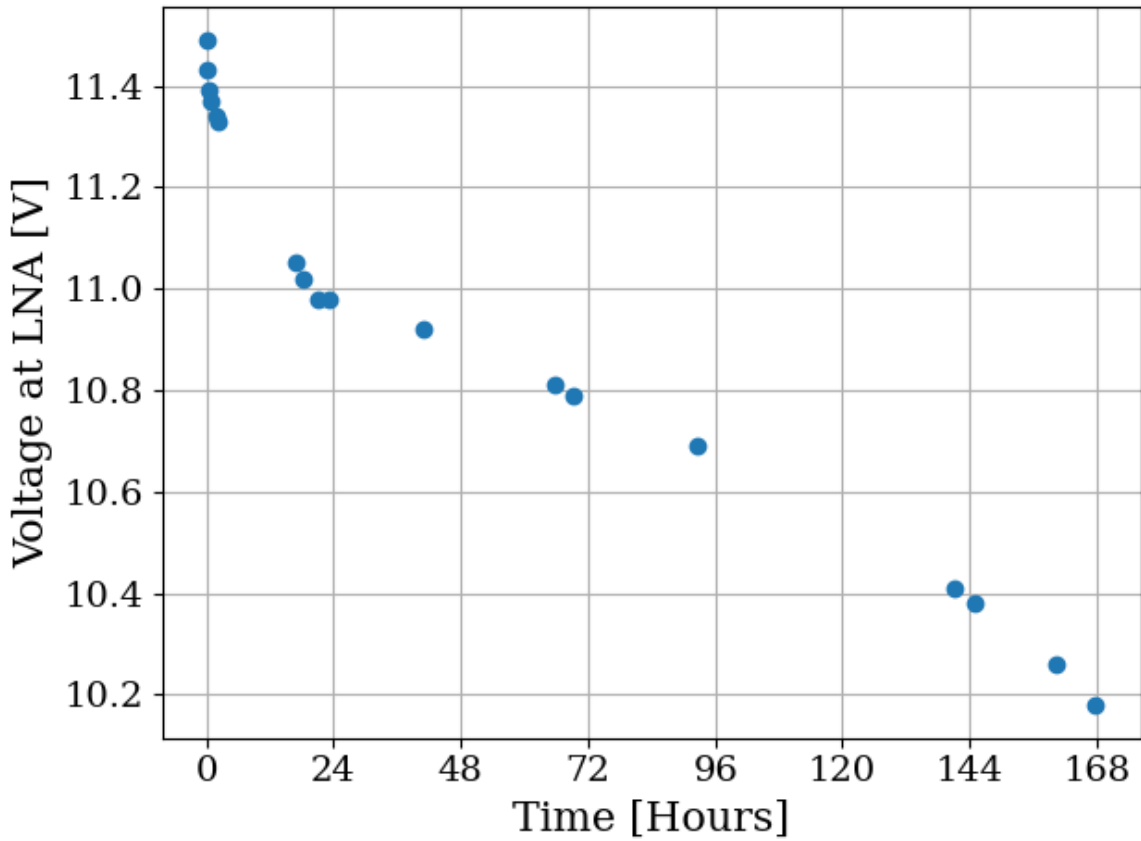


Figure 3.9: Voltage at LNA vs. time. Data were acquired 7/15/2024 through 7/22/2024 using battery number 2 immediately after being charged. The system was set up as it was for Run 1.4, including the switching cycle (on for 3 minutes, off for 45 minutes). The battery supplies 177 mA when the switch is off, and 370 mA when the switch is on. There is an additional data point (not shown) around 196 hours where the voltage has dropped to 6.2 V, well below the minimum required voltage. The battery had approximately 20 charge/recharge cycles at the time of this test and was about 14 months old. A repeat of this test may be required to use the battery for longer periods between charges.

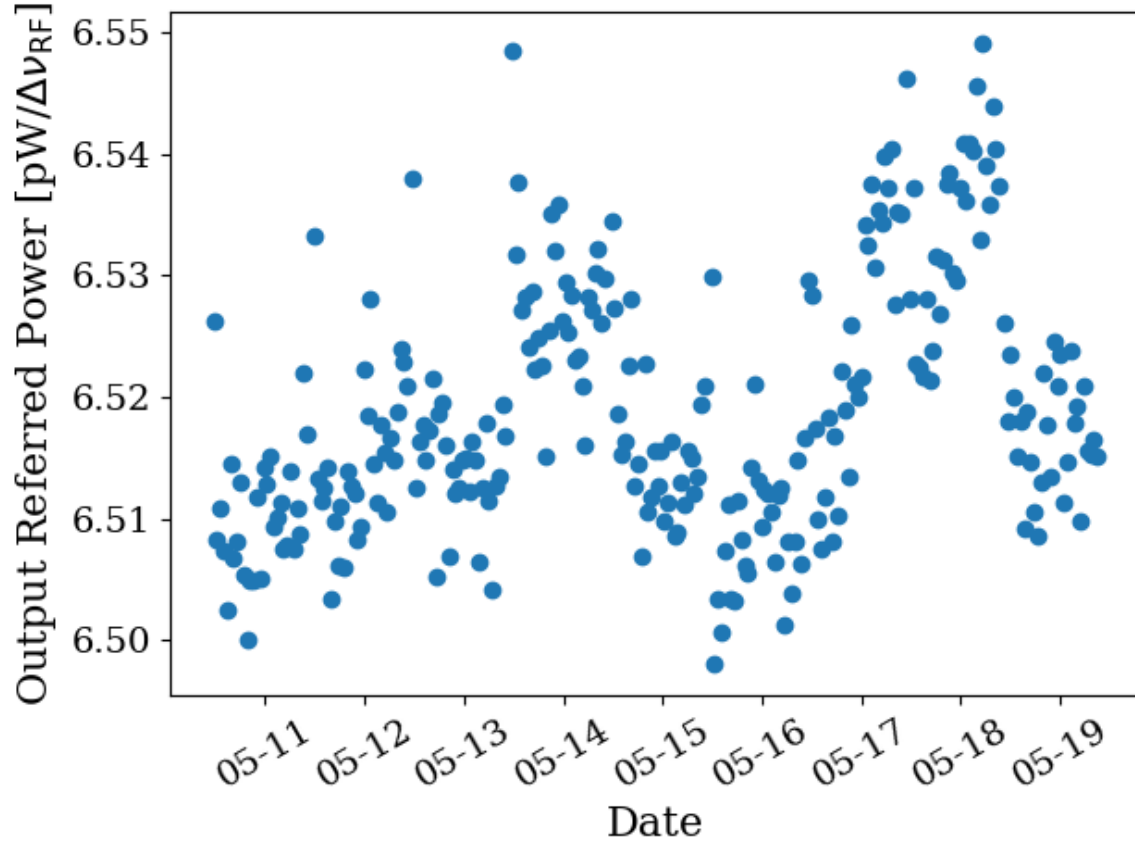


Figure 3.10: Frequency-averaged power spectral density vs. time of the terminator from Run 1.4 (schematically shown in Fig. 2.37). Each data point represents the mean power between 50 and 300 MHz of the terminator. In Run 1.4, a \sim 3 minute long scan of the terminator took place after \sim 45 minutes of antenna scans. Dates shown are all May 2023 (month-day format, year suppressed), and x-axis ticks are shown at midnight.

1520 **3.2 Measurement of shielding effectiveness and radio**
1521 **frequency interference**

1522 Shielding effectiveness (SE) and radio frequency interference (RFI) were introduced in Secs.
1523 2.1.3 and 2.5.1. Their measurement is introduced here.

1524 Similar to the warning given in the previous section, SE should be measured before
1525 starting a data run or after entering a new frequency range/modifying anything on the
1526 patch panel. In addition, it is best practice to clean the door's RF seal before beginning a
1527 run (the procedure is described in the text of this section).

1528 Due to reciprocity between antennas, measuring the shielded room's ability to keep radi-
1529 ation *out* is equivalent to measuring how well the room can keep it *in*. The latter method is
1530 simpler and was performed. The IEEE standard prescribing a very detailed SE measurement
1531 procedure [73] was used as a rough guideline, but the simple results presented here should
1532 be viewed as an estimate. While simplified, the results do tend to agree with predictions of
1533 when RFI should become detectable, based on comparisons to the veto antenna spectrum ⁵.

1534 The SE was measured by placing a Rigol DSG830 signal generator and 25 Watt RF power
1535 amplifier inside the room, both powered by the filtered 120 VAC Edison outlets inside the
1536 room, shown in Fig. 3.11. An antenna was connected to the signal generator. Outside of
1537 the room, an identical antenna was connected to a Rigol RSA-5065-TG spectrum analyzer
1538 [72]. The spectrum is scanned to find a frequency without local interference which would

⁵Or at least they did agree before cleaning the door. With the excellent isolation values, no RFI was detected in Run 1.4.

1539 confuse the results. The spectrum analyzer was set to attenuate its input to prevent clipping
1540 ⁶, and the signal generator was set to output a sine wave near the maximum power of the
1541 RF amplifier ($20\text{ W} = 43\text{ dBm}$). The power measured on the spectrum analyzer is P_{open} in
1542 Eq. 2.46. The door was closed, attenuation removed and P_{closed} was measured. In some
1543 cases the SE was so high a signal was buried below the noise floor of the spectrum analyzer.
1544 These data are shown in red in Figs. 3.12 3.13 and should be interpreted as an upper limit
1545 on isolation, since the true value is lower (better).

1546 SE can drop off to less than 80 dB if the RF gasket around the door is not clean. Previous
1547 day-long test runs detected several hundred signals that originated from RFI emitted from
1548 the PC and several local radio stations. Cleaning was performed by scrubbing the copper
1549 finger stock and steel mating surfaces with red Scotch-Brite using denatured alcohol as a
1550 lubricant ⁷. After two passes of polishing were complete, a layer of DeoxIT D100L liquid
1551 was added. Maintenance cleanings were performed using only DeoxIT D5 spray. These
1552 signals were not detected after the gasket was cleaned, which is consistent with calculations
1553 of Sec. 2.1.3

1554 The primary RFI in the 50-300 MHz span are from local radio broadcasts. The electric
1555 field of the strongest signals is $\sim 100\text{ }\mu\text{V/m}$ when measured in the lab. There are also many
1556 lower level peaks which span the entire frequency range, though are more pronounced in a
1557 few frequency bands (60-75 MHz, 130-140 MHz, and 270-290 MHz). These peaks come from

⁶The spectrum analyzer automatically calibrates the displayed spectrum to its internal attenuator and pre-amplifier. If external gain/attenuation are used, they must be accounted for manually. Since this is a relative measurement (i.e., a ratio of $P_{\text{open}}/P_{\text{closed}}$), this calibration does not matter much.

⁷Alcohol fumes are nasty. Be careful to open the hallway door and use a fan to blow in air from the hall. Take frequent breaks. Don't get dizzy while standing on a chair!



Figure 3.11: Photo showing setup to measure SE of 314. Photo taken using Vivaldi antennas for data shown in Fig. 3.13. The same setup was used with bicon antennas for the 50-300 MHz data shown in Fig. 3.12. The bicon antenna shown in the background of this photo was not used for this test.

1558 the PC which is an integral part of the spectrum analyzer system, housing the ADC, so it
1559 can not be removed. Before the door was cleaned, many of these signals were detectable
1560 after a few hours of integration, but cleaning the door resulted in a clean spectrum for the
1561 9-day data Run 1.4. The spectrum from the veto antenna (discussed in Sec. 2.5.5) is shown
1562 in Fig. 3.14

314 Shielding Effectiveness

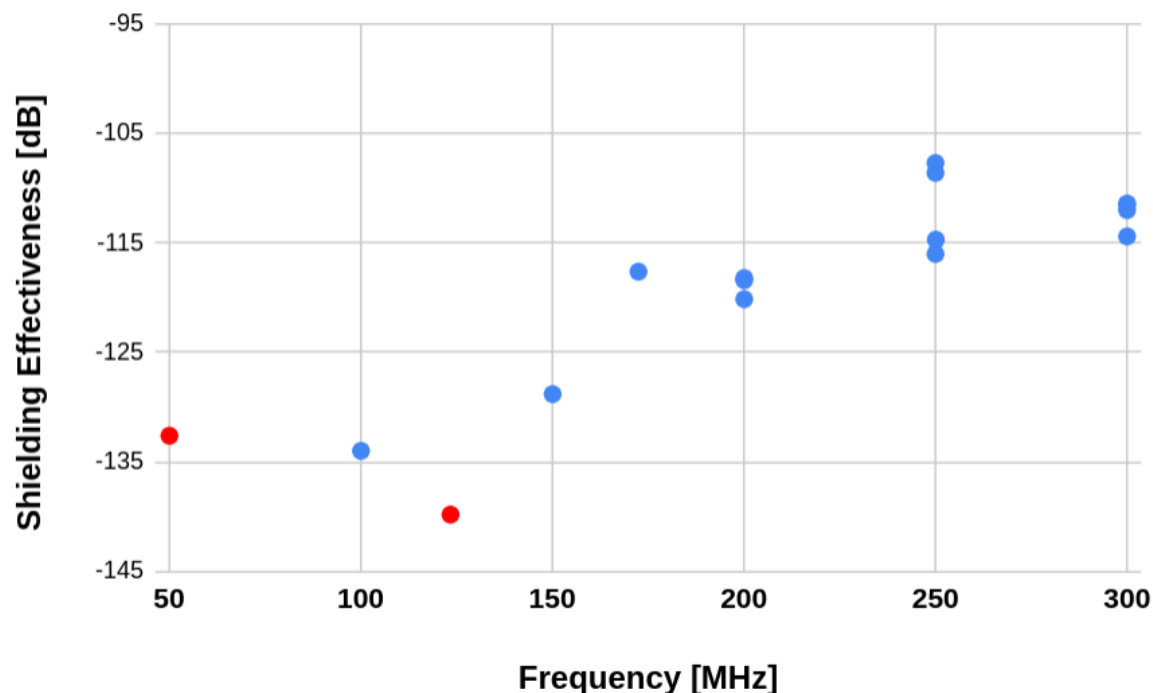


Figure 3.12: Shielding effectiveness of shielded room measured with bicon antenna. Red points indicate measurements limited by the noise floor of the spectrum analyzer located outside the shielded room and are an upper limit. The true SE is lower (better). To get the true SE for these points, measurement would require a higher gain amplifier inside the room. SE measurements are all better than required for Run 1.4, and no RFI candidates were detected. At a few frequencies, the antenna inside the room was moved to get a sense of the uncertainty of the measurement.

314 Shielding Effectiveness

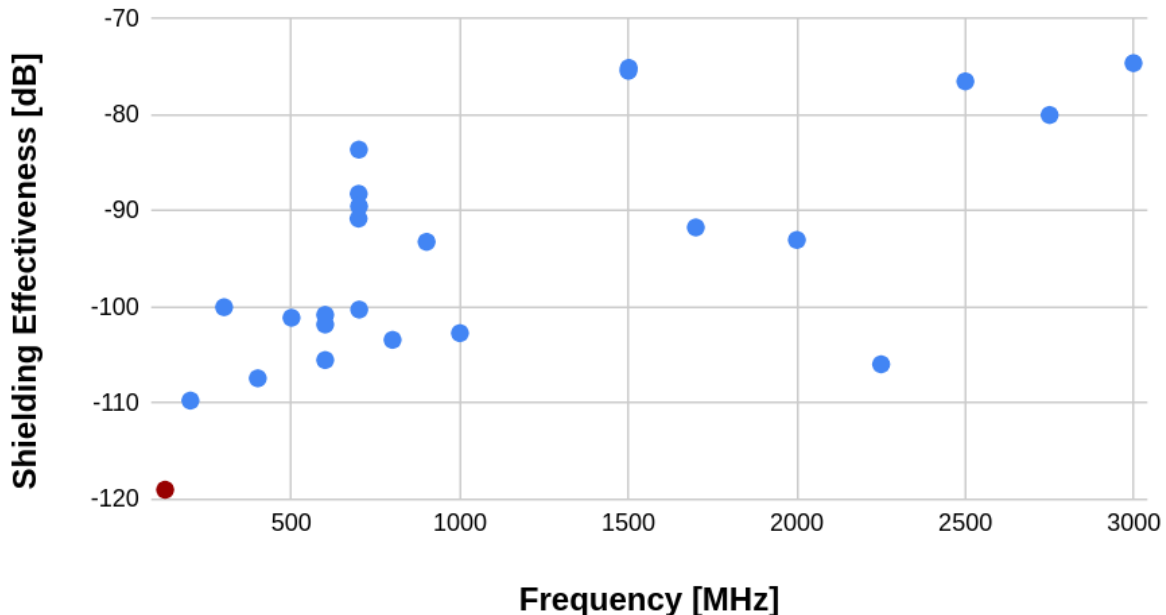


Figure 3.13: Shielding effectiveness of shielded room measured with Vivaldi antenna. Red points indicate measurements limited by the noise floor of the spectrum analyzer located outside and are an upper limit; true SE is lower (better). Measurement would require a higher gain amplifier inside the room. At a few frequencies, the antenna inside the room was moved to get a sense of the uncertainty of the measurement.

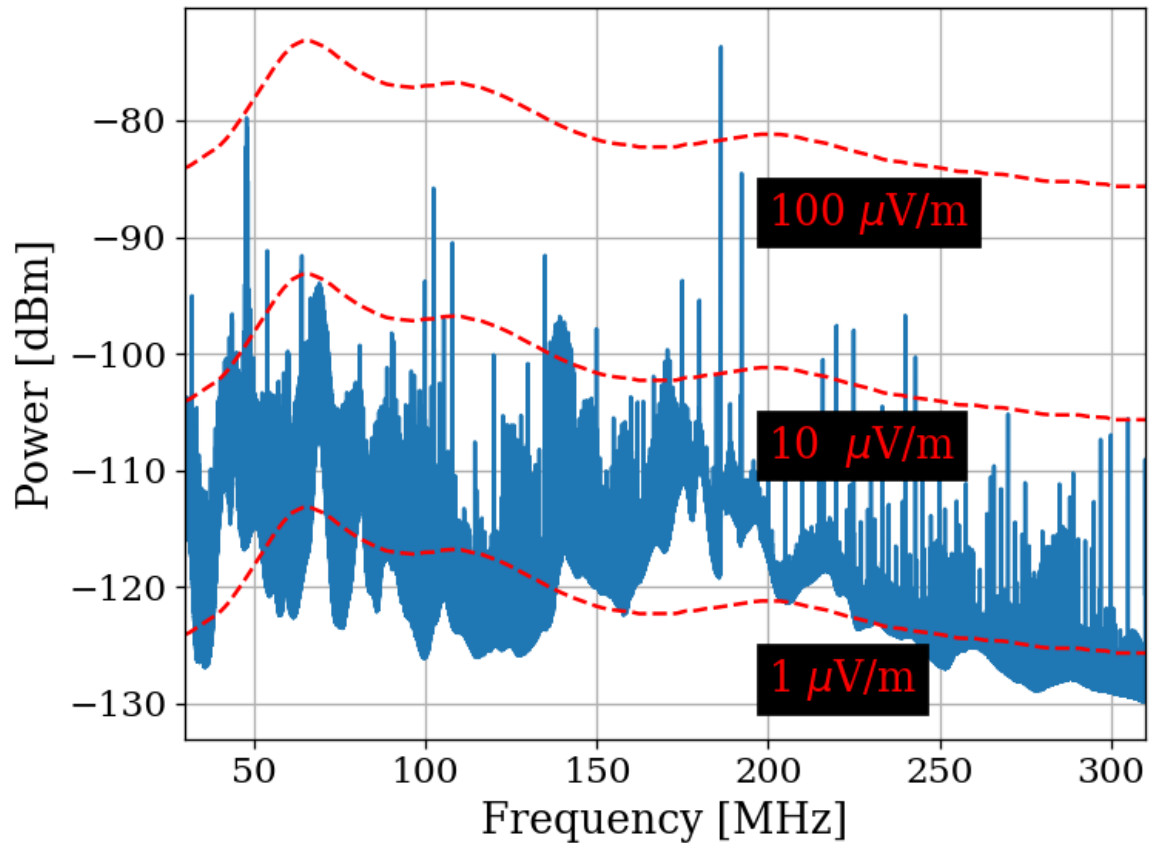


Figure 3.14: Spectrum from veto antenna during the 300 MHz data run. Spectrum plotted as measured power in dBm. Red curves indicate the equivalent field strength. These curves track the free-space antenna factor with frequency for the Com-Power AB900 [59] bicon. Two identical AB900-A antennas are used, one to search for dark photons in the shielded room, and a second to monitor the local RFI background.

1563 3.3 Spectrum Analyzer Characterization

1564 This section outlines several tests performed to ensure the GPU-based real-time spectrum
1565 analyzer (RTSA) system performs as expected. Background information that relates to
1566 this system is described in Sec. 2.5.7.

1567 3.3.1 Spectrum analyzer calibration

1568 The first step in determining if the RTSA system is working adequately is to make sure
1569 it is able to correctly identify known, injected signals and noise. This calibration step is
1570 important since the FFT is normalized manually (see Eq. 2.15), and it is rather easy to
1571 mess up. The test signals were generated with a Rigol DSG830 signal generator. The time-
1572 domain peak-to-peak voltage measured by the RTSA system agreed with the injected voltage
1573 to about 2 %. The signal generator's output frequency and power were verified in both the
1574 frequency and time domain using a separate oscilloscope and spectrum analyzer. This is an
1575 important step since cable losses are significant at this level of precision. They can be taken
1576 into account by consulting the data sheet for the cable⁸.

1577 Next, it is important to understand how the system handles noise spectra, since this is the
1578 primary use of the system. This is tested by amplifying the Johnson noise of a terminator (see
1579 Sec. 2.1.1.2) and measuring the power spectral density. Knowing the gain and noise figure
1580 of the amplifier chain allows for calibration using the procedure outlined in detail earlier in
1581 this chapter, see Sec. 3.1, specifically Fig. 3.6. These results were confirmed several times

⁸There are several cheap black SMA cables which are great for testing, but not for calibration. They have more than 5 dB of loss above 1 GHz. Use a nice cable for these tests, and blow out the SMA connector with compressed air while you are at it.

1582 preceding the data run. Note that due to windowing, other spectrum analyzers will disagree
1583 with the theoretical calculation by a few dB if the equivalent noise bandwidth (ENBW) of
1584 the window function is not included. Also remember to take cable effects into account as
1585 discussed in the previous paragraph.

1586 3.3.2 Spurious signal performance of the ADC

1587 Any practical spectrum analyzer will have small, coherent, signals that sneak into the analog
1588 signal path and, after being digitized and Fourier transformed, manifesting as spurious signals
1589 or *spurs* (see Sec. 2.1.5.1). These spurs likely come from clock signals within the same
1590 enclosure as the ADC. They can also come from local oscillators bleeding through mixers in
1591 a mixed, high-frequency system such as the Rigol RSA 5065TG [72] or the future, upgraded
1592 dark radio system discussed in Ch. 6.

1593 Regardless of their origin, the spurs must be characterized such that if a known spur is
1594 detected it can be classified as such and rejected quickly. Ideally, the system has enough
1595 gain that any spurs are subdominant to the amplified thermal noise, as discussed in Eq. 2.1.
1596 However, since there is a maximum amount of gain that can be added before clipping the
1597 ADC (see Sec. 2.5.4.3), this is not always possible.

1598 Experience with the Teledyne RTSA system has shown that spurs are rather simple to
1599 classify because they do not change much with time in either frequency or amplitude. Their
1600 frequency drifts by $\sim 1 \text{ kHz}$ and their amplitude changes by a few dB.

1601 To classify them, the input of the Teledyne is terminated and a scan is performed few

1602 minutes using the exact same system configuration as for the run (with the possible exception
 1603 of the number of averages). See Appendix A for details. The averaged spectra of the
 1604 terminated inputs are shown in Fig. 3.15.

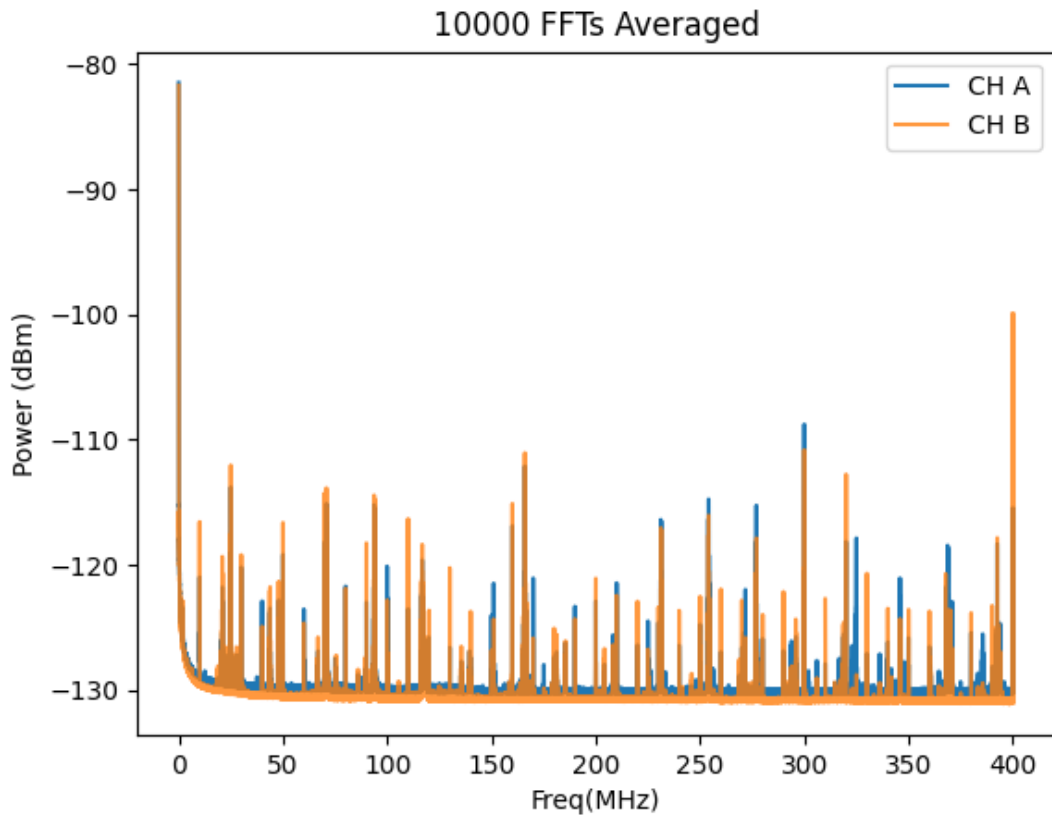


Figure 3.15: Scan of terminated input of Teledyne spectrum analyzer system to measure spur performance. The spectra were acquired with run 1A parameters ($\Delta\nu_{RF} = 47.7$ Hz) with 10,000 averages (~ 3.5 minutes). This plot is taken directly from test mode of the system (not post-processed in any way). The largest spur in the 50-300 MHz range is at 299.97 MHz and is also the single significant signal in Run 1.4 (see Sec. 4.2.5).

1605 Once a test scan is acquired, comparing the largest spurs (≈ -110 dB) to the expected
 1606 output-referred background ([Johnson noise + LNA noise] * Gain ≈ -81 dBm/ $\Delta\nu_{RF}$) allows
 1607 the calculation of the number of averages which are required before the spurs are significant.

1608 Working this out is a good test of understanding of Sec. 2.2. This spur should be detectable
1609 with 95% confidence after about 4 days, which is exactly what happened in Run 1.4. The
1610 false positive candidate is described in Sec. 4.2.5.

1611 **3.3.3 ADC clock performance**

1612 Any ADC requires a clock that dictates the precise time at which a sample should be ac-
1613 quired. This subsection deals with the evaluation of the performance of that clock.

1614 Determining the performance of a clock generally relies on having a better (read: more
1615 expensive) clock known as a *standard* and measuring the clock under test against the stan-
1616 dard. The Valon 5009 RF synthesizer was tested against a rubidium frequency standard and
1617 was found to be just on the threshold of stable enough to work (this threshold is explained in
1618 Sec. 2.5.7). To ensure the measurement is not limited by clock instability, the sample clock
1619 of the ADC is synchronized to a 10 MHz rubidium frequency standard (Stanford Research
1620 Systems FS725) which is further steered by the one pulse-per-second (pps) signal from a
1621 GPS receiver. This system has medium and long term fractional frequency stability (Allan
1622 deviation [74, 75]) of $\sigma_y(\tau) < 3 \times 10^{-12}$ (where τ is the averaging time) and phase noise of
1623 less than -65 dBc/Hz at offset frequencies > 50 Hz from the carrier [76]. This means that
1624 over the course of a single acquisition, the power contained in a bin will spread to an adjacent
1625 bin by less than 1 part in 10^6 which is more than sufficient for our experiment.

1626 This is a rare example of something in this experiment where we trust the data sheet.
1627 We do not have access to a clock which is better than this, so confirming its performance

1628 is difficult. Furthermore, even if the specs are an order of magnitude worse than advertised
1629 there is still more than enough stability for the experiment. This statement holds at higher
1630 frequencies. Since the Q of the signal is fixed, higher frequencies have wider bins so the
1631 relevant offset frequency at which the phase noise is measured increases with frequency. The
1632 dimensionless Allan deviation is also not affected.

1633 3.3.4 Real-time data collection efficiency

1634 As a final test, one would like to know how efficiently data scans can be acquired and
1635 averaged. We call a 100 % efficient system *real-time* as described in Sec. 2.5.7. Figure 3.16
1636 illustrates this efficiency. For Run 1.4, it is $\sim 99.765\%$. However, in practice run logistics
1637 such as moving the antenna prevent the full efficiency of the system from being realized.

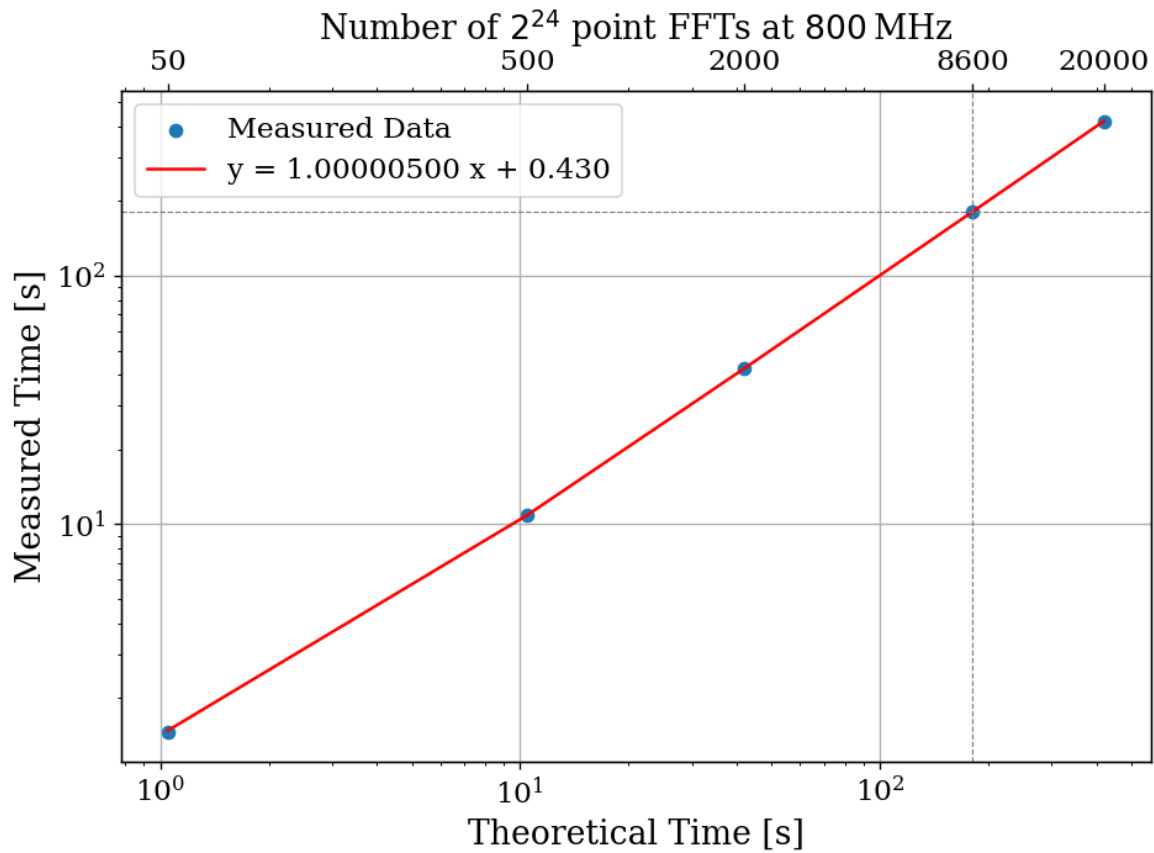


Figure 3.16: Acquisition efficiency for GPU-based real-time spectrum analyzer computed from measured vs. theoretical times. The constant offset of 0.43 s corresponds to a small set-up period when starting an acquisition containing, in the case of run 1A, 8600 FFTs. In the limit of an infinite length acquisition, the system's efficiency may be read off from the slope and is 99.9995%. The more realistic efficiency is a function of the number of FFTs per acquisition and for Run 1.4 = $180.3551 \text{ [s]} / 180.7782 \text{ [s]} = 99.765\%$.

1638 Chapter 4

1639 Data Acquisition, Data Analysis and
1640 Calibration

1641 Thus far this thesis has focused on building up a background on the dark radio technique
1642 as well as the design and testing of the experiment and its sub-systems. This chapter outlines
1643 the process of acquiring actual data, analyzing that data to search for a small power excess,
1644 and, in the absence of that excess, converting the null result into an exclusion limit on the
1645 dark photon mass/ ϵ parameter space. Section 4.4 describes an injection test that detects a
1646 realistic, hardware-injected, dark photon proxy-signal. This chapter borrows heavily from
1647 my paper, *New Limit on Dark Photon Kinetic Mixing in the 0.2-1.2 μeV Mass Range From*
1648 *the Dark E-Field Radio Experiment*[39], which was published in August 2024.

1649 The cleanest way to model the contents of this chapter is by compartmentalizing the
1650 steps outlined above. For this reason, the chapter is organized as follows. In Sec. 4.1, the
1651 procedure for a 9-day data run is outlined. Where appropriate, references to previous sections
1652 are provided which are helpful in understanding how different procedures were developed.
1653 This section concludes with the frequency-dependent, output-referred power spectral density
1654 S_o , which must be searched for a power excess. We call this search *analysis*, and it is covered
1655 in Sec. 4.2. The task of analysis is to extract a dark photon signal from this spectrum if
1656 it is present. Otherwise, in its absence, we set a limit on the amount of output-referred
1657 power that would have been detectable *most of the time* were a narrow signal to be present
1658 in this averaged dataset. We quantify the meaning of “most of the time” by conducting a
1659 series of Monte Carlo *pseudo-experiments* on artificial signal-containing spectra for synthetic
1660 signals of varying powers and frequencies. With a limit on dark photon power extracted,
1661 Sec. 4.3 works back through the system to determine a limit on ϵ above which we have some
1662 confidence we would have observed a signal. This produces the exclusion limit, which is

1663 ultimately the deliverable of this experiment. This limit is shown in Sec. ??.

1664 4.1 Data Acquisition

1665 Data were collected during a 9-day run from May 10 to May 19, 2023. This data run is
1666 referred to Run 1.4 in the code base since it was the fourth attempt at taking this data. It
1667 was used for to publish the limit of Run 1A, so it is referred to as Run 1A throughout this
1668 thesis. its details are shown in Table ??.

Specification	Value
Analysis span	50-300 MHz
Antenna	AB-900A biconical antenna
RTSA	Teledyne GPU system (Sec. 2.5.7)
Frequency resolution ($\Delta\nu_{RF}$)	47.7 Hz
Length of record	2^{24} samples
Sample rate	800 MHz
Window type	None (rectangular)
Acquisition time per spectrum	20.96 ms
Run start time	2023-05-10 11:29:48
Total time of run	8 days, 21.13 hours
Efficiency (Time spent scanning antenna/total time)	92.03%

Table 4.1: Run 1.4 Details. Many specifications are related and can be computed from each other but are listed for reference. The efficiency differs from that calculated in Fig. 3.16 mainly because of switching to a terminator and brief daily pauses to move the antenna.

1669 Each day was subdivided into data-collection (23 hours 15 minutes) and setup (45 min-
1670 utes) periods. The setup period includes moving the antenna, changing a 12 V battery for
1671 the LNA (Sec. 2.5.6), file management and documentation. In order to reduce the data
1672 rate and storage requirements, all data were pre-averaged into 3-minute chunks and then

1673 saved. This pre-averaging is shown in Fig. 2.45. Additionally, an RF switch (see Fig. 2.37)
1674 is actuated for a 3-minute scan for every 15 antenna scans in order to monitor the status
1675 of the amplifier chain. For the data analysis, all 9 days of data were averaged together to
1676 create a single spectrum S_o (Fig. 4.1). If candidates are found, their time dependence are
1677 observed by looking at the 3-minute pre-averages. All further analysis is performed on the
1678 full 9-day S_o spectrum and is described below (Sec. 4.2).

1679 4.1.1 Raw data, S_o

1680 All 9 days of pre-averaged data from the run are averaged together. The stability of the
1681 sample clock (Sec. 3.3.3) ensures that this is a simple process. Frequency bins ($\Delta\nu_{RF} =$
1682 47.7 Hz) corresponding to a given frequency are added and normalized by the total number
1683 of pre-averaged spectra. This process produces the raw spectrum, S_o (Fig. 4.1), on which
1684 we will perform a search for power excess.

1685 Inspection of S_o reveals small power variations over spans of tens of kHz. The origin of
1686 these variations is explored in Sec. 2.3, but it is summarized here. Given an antenna in a
1687 cavity in thermal equilibrium with the input of an amplifier, whose input is assumed to be real
1688 and matched, one would expect an output PSD which is constant with respect to frequency
1689 up to small variations in system gain. The theory for this is outlined by Dicke in [77]. These
1690 variations are not noise; for a given antenna position, we repeatedly measure the same shape
1691 (though the noise riding on these variations *is* random). The origin of the observed small
1692 variations lies in the effective temperature difference between the room and LNA causing a

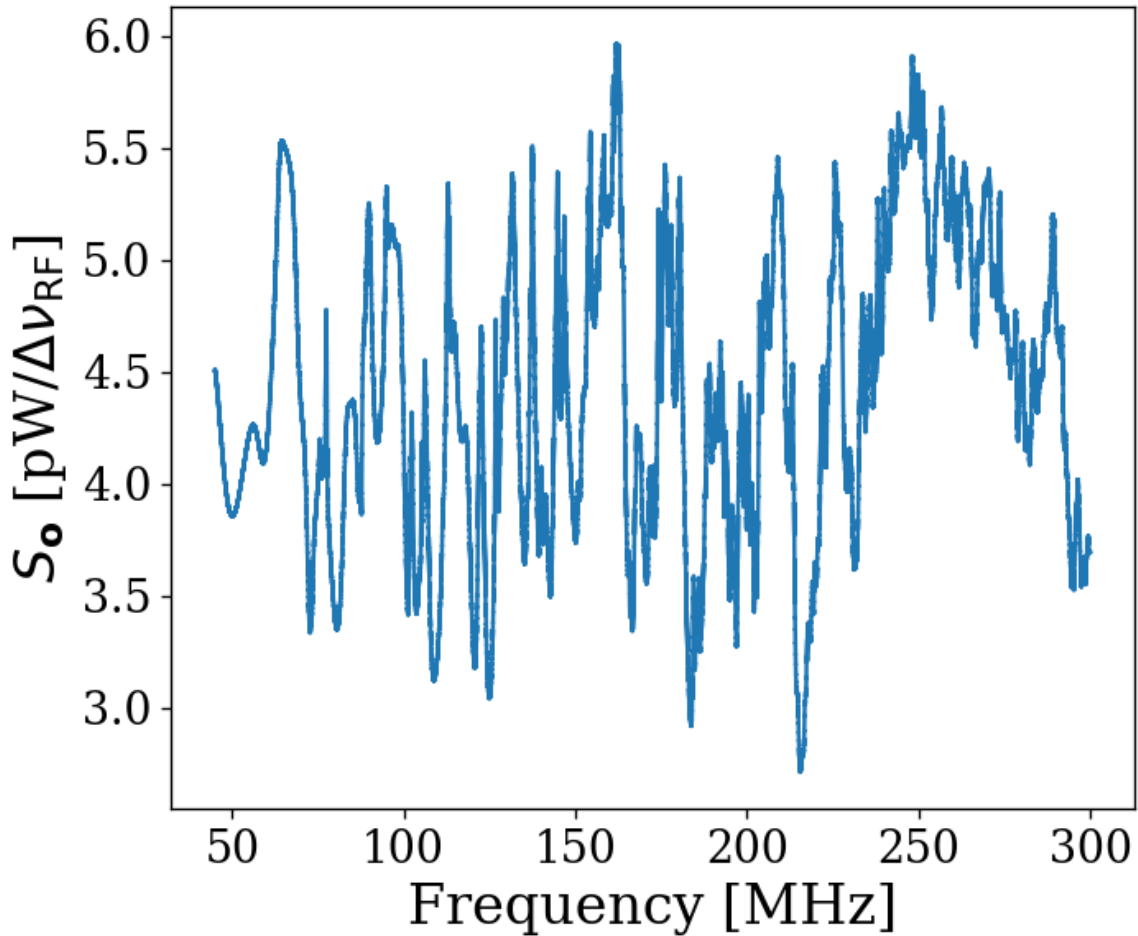


Figure 4.1: Run 1A averaged, output-referred antenna power spectrum S_o . Data were taken over a 9-day period at 9 antenna positions. For context, Fig. 4.2 shows these data plotted alongside the power spectrum of the terminator. The narrow variations are mainly due to the effective temperature difference between the room and LNA (Sec. 2.3), though there is a small contribution due to amplifier gain and noise temperature variations (Sec. 4.1.1). The variations seen here are not noise; their shape is repeatable for a given antenna position. The noise on this background is not visible at this level of zoom, but is seen in Fig. 4.4, which shows a zoomed-in view of the spectrum at 240 MHz. The noise is also seen nicely in Fig. 4.17

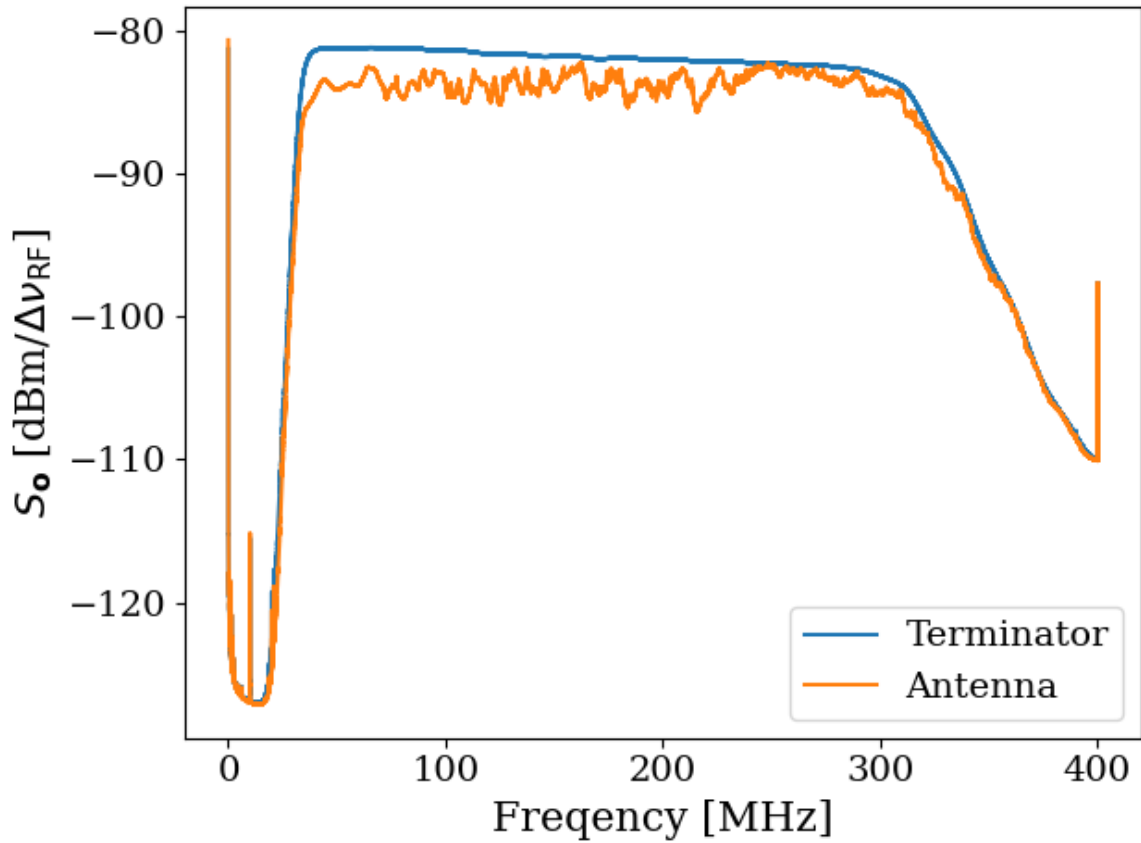


Figure 4.2: Logarithmic scaled Run 1A averaged, output-referred, antenna and terminator power spectra. Bandwidth is defined by hardware band-pass filters (Fig. 2.37). Spurious signals at 10 MHz, as well as low and high-frequency behavior, are ADC effects and are visible in Fig. 3.15.

1693 net power flow from the antenna into the LNA. This effective temperature difference partially
 1694 excites modes of the antenna/cavity system, causing the observed variations. We suspect this
 1695 effect originates from a small reactive component of the LNA's input causing the electronic
 1696 cooling described originally by Radeka [19]. This effect can be eliminated by adding an
 1697 isolator between the antenna and LNA [32, 78] though for our experiment, it is impractical
 1698 to get an isolator that covers such a wide band at relatively low frequency. Furthermore, the

1699 relatively wide (tens of kHz) variations are handled by fitting to them, which is discussed in
1700 Sec. 4.1.

1701 **4.2 Data Analysis**

1702 At this point, we have compiled a single, averaged, output-referred power spectrum, S_o
1703 (Fig. 4.1). The task of *analysis* is to extract a dark photon signal from this spectrum if
1704 it is present. Otherwise, in its absence, we would like to set a limit on the amount of
1705 output-referred power we would be able to detect *most of the time* were a narrow signal
1706 to be present in this averaged dataset. We quantify the meaning of “most of the time”
1707 by conducting a series of Monte Carlo “pseudo-experiments” on artificial, signal-containing
1708 spectra for synthetic signals of varying powers and frequencies. The following subsections
1709 are organized as follows:

1710 4.2.1: Fit S_o to extract an estimate of the background B (which we call \hat{B}) whose origin was
1711 discussed in Sec. 4.1.1. See Fig. 4.4.

1712 4.2.2 Divide the spectrum by \hat{B} to generate the *normalized spectrum*, which very nearly
1713 follows a Gaussian distribution. Discuss statistics of the normalized spectrum and
1714 choose a global significance level and its associated *significance threshold*. See Fig. 4.5.
1715 Also note this was derived in Sec. 2.2.

1716 4.2.3 Apply a matched filter to the normalized spectrum and establish a significance thresh-
1717 old on its output using the same method defined in the previous section. See Fig. 4.6.

1718 The previous three steps comprise our *detection algorithm* which is shown in Fig. 4.3.

1719 4.2.4 Perform a Monte Carlo analysis to simulate the required power of a signal that can be
1720 detected above the significance threshold 95% of the time. We use this to recover a
1721 95% exclusion limit on the output referred power spectrum.

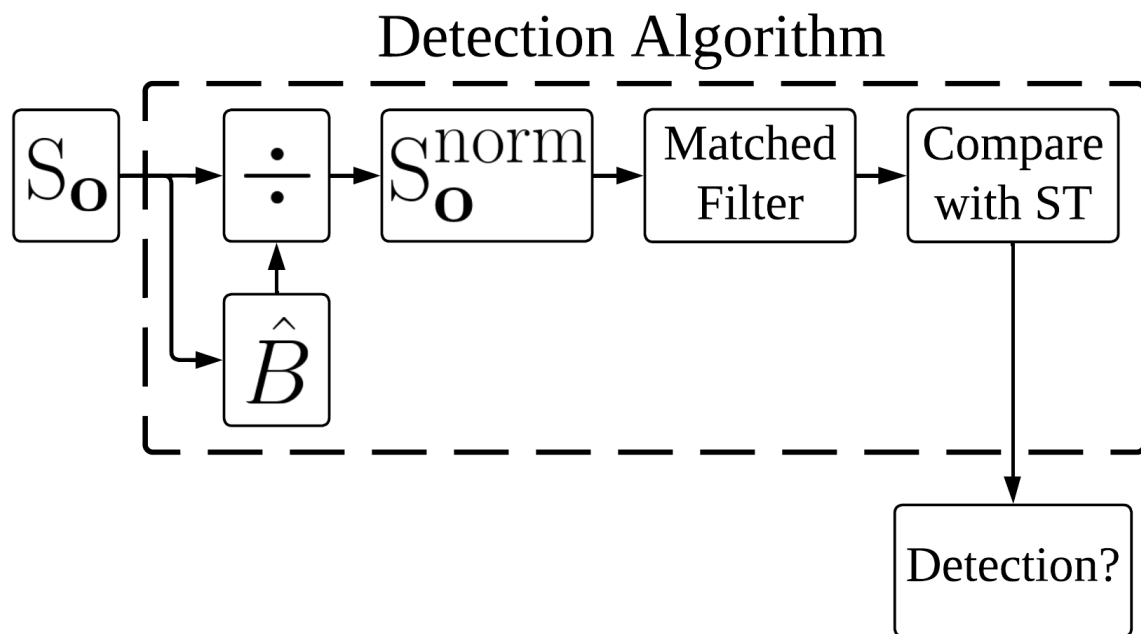


Figure 4.3: Flow chart outlining the logic of signal processing in the detection algorithm of sections 4.2.1 through 4.2.3. \hat{B} is the smoothed fit to S_o generated by low pass filtering. The output, *Detection?*, is a Boolean array which signifies a detection or lack thereof at each frequency bin. We detect a candidate if a bin contains more power than a significance threshold (ST) (Sec. 4.2.2).

1722 In Sec. 4.3 we convert this threshold on S_o into an actual limit on ϵ .

1723 Throughout the figures of this section we will follow a relatively large (40 fW, output-
1724 referred) software-injected, synthetic dark photon signal at 240 MHz to illustrate what a
1725 candidate would look like as it passes through the analysis procedure. This signal is added

1726 to S_o . For clarity, a single interfering candidate has been removed. This is discussed in
1727 Sec. 4.2.5.

1728 As a final note, at this point if you are unfamiliar with the data analysis, it would be
1729 advantageous to spend a few minutes looking through Figs. 4.17 through 4.19 to get a sense
1730 of the task at hand. It can be disorienting to deal with a spectrum that contains 8 million
1731 frequency points. Zooming in on a signal is very informative.

1732 4.2.1 Fit background, $\hat{B}(\nu)$ ¹

1733 As shown in Fig. 4.1, the measured power spectrum looks like flat thermal noise *multiplied* by
1734 some frequency-dependent background, $B(\nu)$ ². However, for this section we will not concern
1735 ourselves with the origin of B or any details of the experiment aside from two assumptions:

1736 1. The measured background is the product of a normally distributed spectrum and some
1737 background. This is enforced by the central limit theorem due to the large number of
1738 averaged spectra, independent of any experimental specifics.

1739 2. The line shape of the signal is known and the width of this signal is much narrower
1740 than the width of features on the background, viz. $\Delta\nu_{DP} \ll \Delta\nu_B$

1741 The first assumption (1) implies that if we were able to extract the background, dividing
1742 S_o by this extracted background would yield a *dimensionless*, normally distributed power

¹Code for this section can be found at: https://github.com/josephmlev/darkRadio/tree/master/daqAnalysisAndExperiments/run1p4/run1p4_analysis/analysisClass.ipynb

²When I was first working on this, I used $H(\nu)$ to represent this background. This naming convention persists in the analysis code.

1743 spectral density on which a search for a dimensionless signal is performed. The second
1744 assumption (2) will be critical in both performing the fit to the background (this section),
1745 and performing matched filtering (Sec. 4.2.3).

1746 In light of these assumptions, we attempt to fit the background power spectrum. Since
1747 this fit estimates B , we use the symbol \hat{B} to refer to it. As discussed in [20], a particularly
1748 effective fitting technique that can discriminate between the wide bumps of S_o and a narrow
1749 signal is to use a low pass filter. We implement this filter in two stages:

- 1750 1. A median pre-filter (51 bins or about 2.4 kHz wide) attenuates any very narrow, very
1751 large excursions which would interfere with any following filters, causing them to
1752 “ring”³
- 1753 2. A 6th-order Butterworth low pass filter (corner frequency of 210 bins or 10 kHz)

1754 These bin widths/frequencies should be interpreted as the width of spectral features on
1755 S_o that are attenuated and will, therefore, not show up in the background fit. A narrow
1756 zoom of this fit with a synthetic signal is shown in orange in Fig. 4.4.

³I recommend that this pre-filtering step is omitted if the spectrum analyzer in use does not produce large spurs. It is the slowest part of the analysis chain. It also causes the filtered spectrum to deviate slightly from Gaussian.

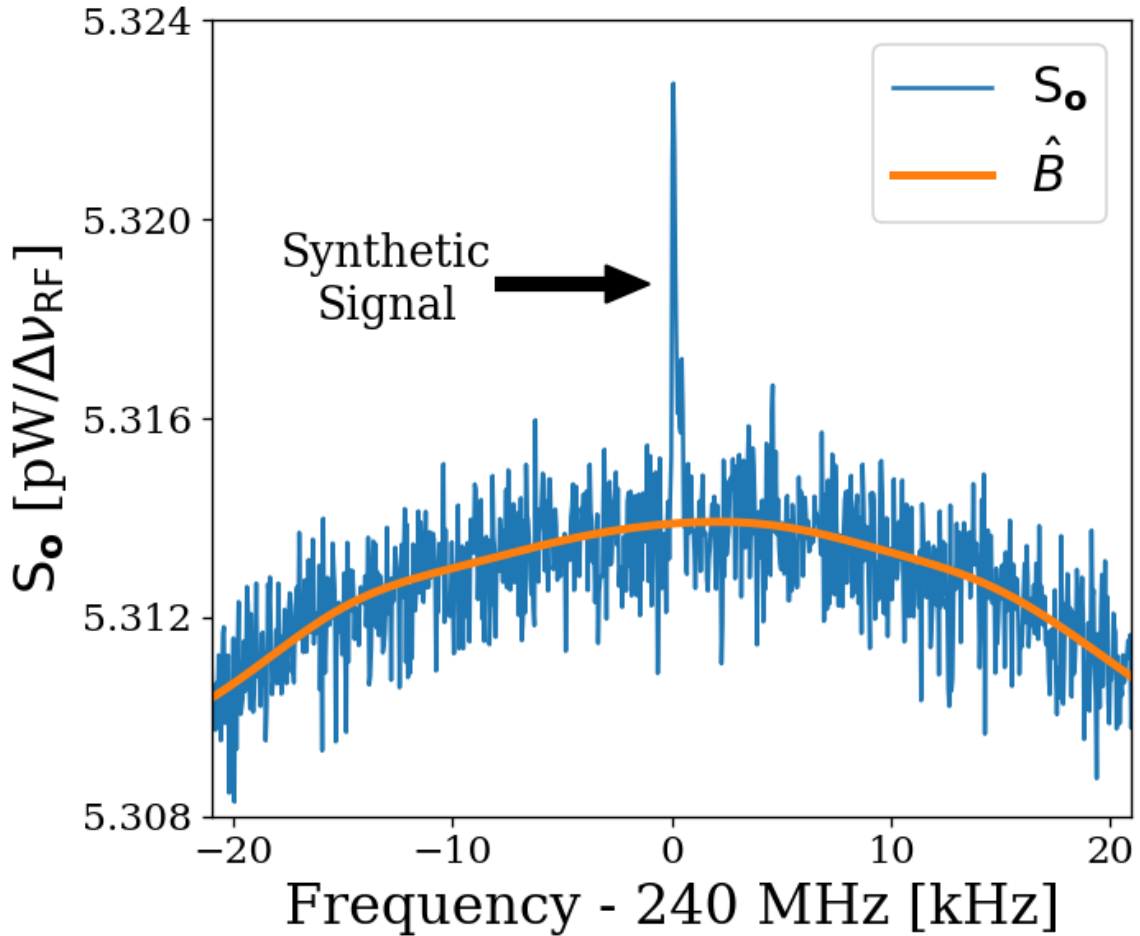


Figure 4.4: Fitting background \hat{B} in the presence of a synthetic signal injected at 240 MHz. Starting from the averaged, output-referred spectrum (S_o), we fit the background using a series of filters (section 4.2.1, and Fig. 4.3). This figure is a highly zoomed-in view (240 MHz \pm 20 kHz) in order to show the noisy Rayleigh signal shape.

¹⁷⁵⁷ **4.2.2 Normalized spectrum, S_o^{norm}**

¹⁷⁵⁸ Once we have a fit to the background, \hat{B} , division of S_o by this fit yields a dimensionless,

¹⁷⁵⁹ Gaussian distributed spectrum

$$S_o^{\text{norm}} \equiv \frac{S_o}{\hat{B}}. \quad (4.1)$$

1760 As discussed in Sec. 2.1.1.3, this normalized spectrum (Fig. 4.5) should have a mean $\mu_{\text{norm}} = 1$
 1761 and a standard deviation given by the Dicke radiometer equation $\sigma_{\text{norm}} = (\tau \Delta\nu_{\text{RF}})^{-1/2}$ where
 1762 τ is the total integration time (≈ 9 days) and $\Delta\nu_{\text{RF}}$ is the width of a bin (47.7 Hz). This
 1763 works out to a predicted σ_{norm} of 1.727×10^{-4} . μ_{norm} and σ_{norm} calculated from the data
 1764 are $1 - 1.2 \times 10^{-5}$ and 1.741×10^{-4} respectively, which agree with the predicted values
 1765 to better than 1%. Knowing the statistics of the background allow us to set a threshold
 1766 above which we have some confidence that a candidate is not a random fluctuation. This
 1767 significance threshold was derived in Sec. 2.2.1. As a reminder, the probability that all N
 1768 bins are less than z standard deviations, $z\sigma$, for a standard normal distribution is given
 1769 by $\left\{ \frac{1}{2} [1 + \text{erf}(z/\sqrt{2})] \right\}^N$, where $\text{erf}(z)$ is the standard error function and z is real. A 5%
 1770 ST for 5.2×10^6 bins (our 50-300 MHz analysis span) works out to 5.6σ . This is shown in
 1771 Fig. 4.5.

1772 It is possible to set a simple limit using this significance threshold on the normalized
 1773 spectrum, which was our method in [4]. However, knowing the line shape of the dark photon
 1774 signal provides additional information that improves sensitivity (up to a factor of ≈ 2) at
 1775 the higher frequency end of the spectrum, as shown in Fig. 4.8.

1776 4.2.3 Signal-matched filter

1777 As discussed in 4.2.2, one simple method to set a limit is to look for single-bin excursions
 1778 above some threshold. However, galactic dynamics impart a dark photon candidate with
 1779 a Rayleigh-distributed, spectral signature, which has a dimensionless width $Q_{\text{DP}} \approx 10^6$

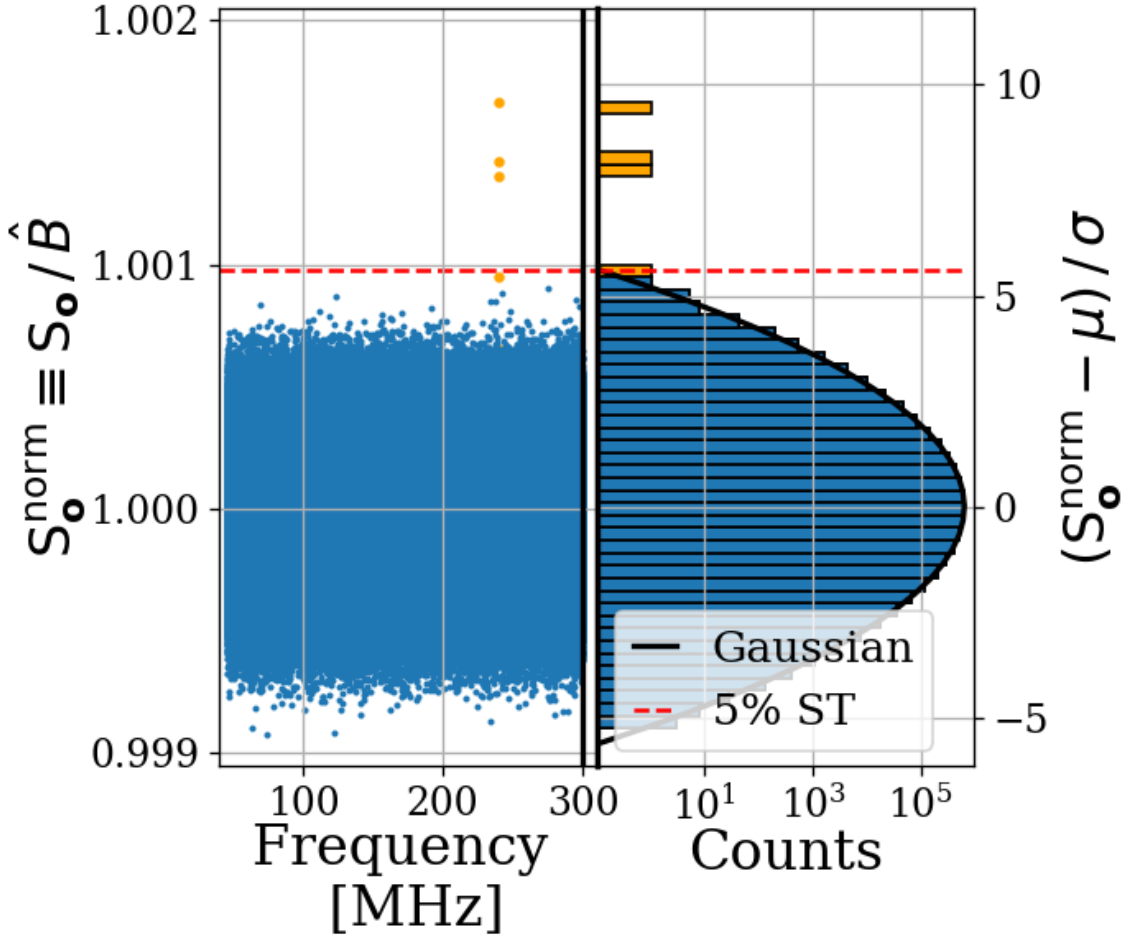


Figure 4.5: Dividing S_o by \hat{B} yields a dimensionless, normally distributed power spectrum that we define as S_o^{norm} . We show S_o^{norm} in two ways: a normalized power/frequency spectrum (*left*) and rescaled into Z-score units and collapsed into a histogram (*right*). The histogram shows power excess and Gaussian fit, but frequency information is lost. We compute a 5% significance threshold ST (*dashed red*), above which we will detect a candidate by chance 5% of the time. Bins adjacent to the 240 MHz synthetic signal show up in orange on both plots. A single interfering signal has been removed for clarity. We discuss this further in Sec. 4.2.5

1780 [33]. This means that the expected width of a candidate signal over our analysis span (50-
 1781 300 MHz) varies between 50-300 Hz. We set $\Delta\nu_{\text{RF}} = 47.7 \text{ Hz}$ to maximize SNR for the lowest
 1782 expected signal width. However, this divides signal power between adjacent bins, an effect

1783 that becomes more pronounced at higher frequencies, leading to a decrease in sensitivity.
1784 By using a signal processing technique known as *signal-matched filtering* [79, 80], we restore
1785 some of the sensitivity lost due to the splitting of signal between the fixed-width frequency
1786 bins of the FFT. A similar “optimal weighting” procedure has been well established in axion
1787 haloscope experiments, notably by [20, 81]. Below, the signal-matched filter is referred to
1788 simply as a *matched filter*.

1789 For a known signal shape, the detection technique that optimizes SNR is the matched
1790 filter. This is implemented on the normalized power spectrum using the Rayleigh-distributed
1791 spectral line shape of [33] as a template. Since we have a constant $\Delta\nu_{\text{RF}}$ and expect the
1792 width of the signal to vary across our span, we must calculate several templates of varying
1793 width to match the expected line shape. Every 10% of fractional frequency change, a new
1794 template is generated and used to search that small subspan of the normalized spectrum,
1795 each of which is also normally distributed though with its own standard deviation. This
1796 results in 20 subspans (50-55 MHz, 55-60.5 MHz etc.). The normalized spectra of all 20
1797 subspans and the histogram of the 227-250 MHz subspan are shown in Fig. 4.6.

1798 As the width of the templates increase, the standard deviation of the output decreases,
1799 resulting in the $\nu^{-1/2}$ shape of the 5% significance threshold shown in Fig. 4.6. It should be
1800 noted that since the total number of bins remains 5.2 million, the 5% significance threshold
1801 still corresponds to 5.6σ ; the shaping in Fig. 4.6 is due to the variation in σ for different
1802 templates, not a change in the $z = 5.6$ pre-factor.

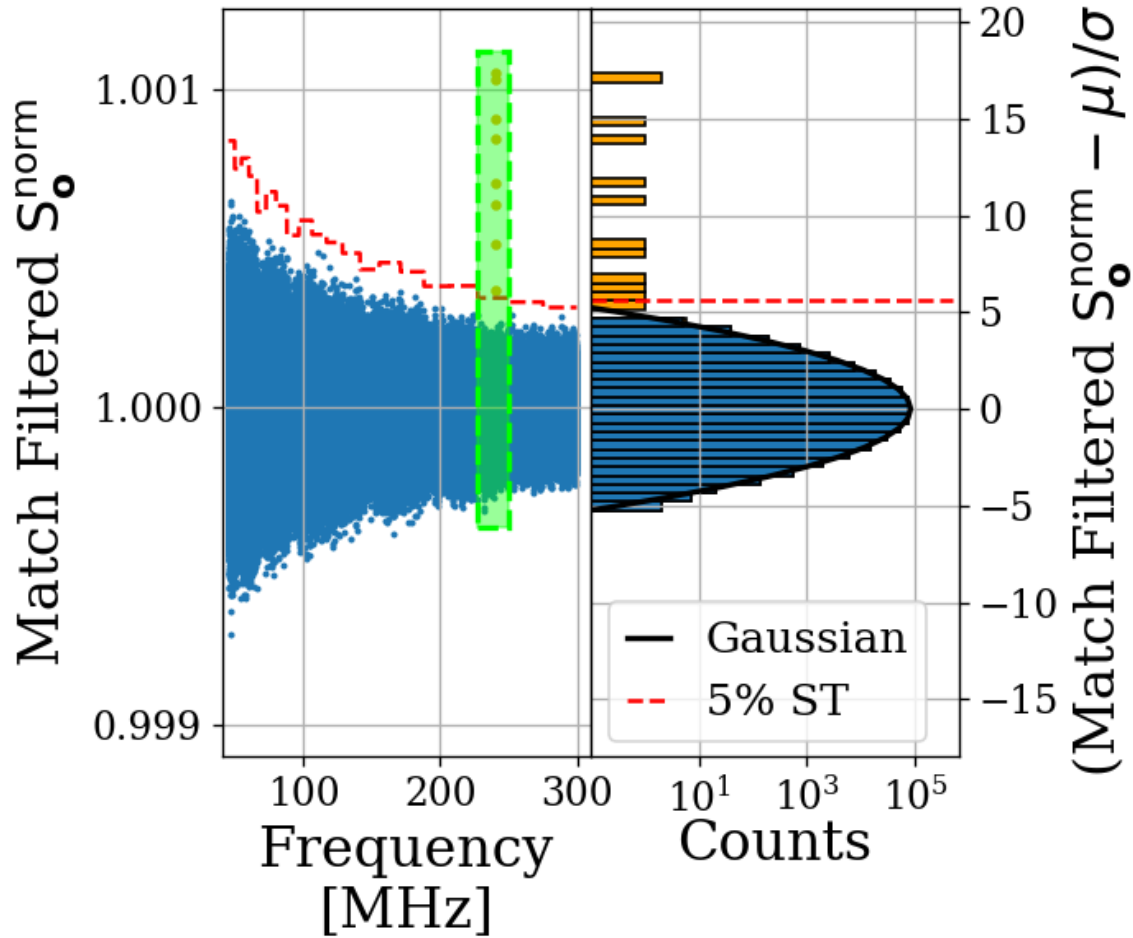


Figure 4.6: S_o^{norm} after it has been passed through a matched filter. The template varies in width throughout the frequency span resulting in 20 subspans, each with a constant 5% significance threshold ST (*dashed red*). This is discussed in the text of this section. The histogram only includes 227-250 MHz subspan (enclosed in the green box). The signal-to-threshold ratio of the synthetic signal (orange) improves by a factor of about 1.8 as compared to Fig. 4.5 without a matched filter. The frequency dependence of this effect is shown in Fig. 4.8. A single interfering signal has been removed for clarity.

1803 4.2.4 Monte Carlo: pseudo experiments

1804 The previous three sub-sections outline the procedure for detecting the presence of a signal

1805 of known spectral line shape embedded in wide-band noise. We refer to this procedure as a

1806 *detection algorithm* (see Fig. 4.3), which we now calibrate through a Monte Carlo method.
1807 Synthetic background spectra are generated, and known signals are added to this background
1808 to create a *test spectrum*. This test spectrum is passed to the detection algorithm, which
1809 attempts to detect the signal. This process is repeated many thousands of times, and the
1810 statistics of the detectability of a signal (as a function of its frequency and power) provide
1811 insight into how much power could have been detected in the experiment.

1812 A synthetic, background spectrum is constructed by multiplying some background $B(\nu)$
1813 by randomly generated Gaussian white noise characterized by μ_{norm} and σ_{norm} , as discussed
1814 in section 4.2.2. A Rayleigh-distributed signal of known, total integrated, output-referred
1815 power and frequency, $\lambda(p, \nu)$, can now be added to this spectrum to create a *test spectrum*
1816 that can be passed through the detection algorithm (see Sec. 2.1.2 for a discussion of signal
1817 line-shape). The frequencies of the synthetic signals are evenly spaced (approximately every
1818 10 MHz). However, because the signal spans a small number of bins (one to six), the shape
1819 of the discretized signal is very sensitive to the frequency at which its peak lands relative to
1820 the bins. To compensate for the unknown dark photon frequency relative to a given bin, the
1821 frequency of the synthetic signal is randomly jittered by $\pm\Delta\nu_{\text{RF}}/2$, which is drawn from a
1822 uniform probability distribution at each iteration of the Monte Carlo. By repeatedly running
1823 these synthetic, signal-containing, test spectra through the detection algorithm, statistics are
1824 built up about how much total integrated power is required to detect a signal as a function
1825 of frequency *most of the time*. We quantify this as the statistical power of the detection
1826 algorithm and denote it $100\% - Y = 95\%$ following the standard convention of hypothesis
1827 testing.

	Only Noise	Noise + Signal
Detection	X	100% – Y
No Detection	100% – X	Y

Table 4.2: Threshold parameters that are part of the detection algorithm and Monte Carlo. X is the significance of the analysis. It is a parameter passed to the detection algorithm which specifies the significance threshold. The quantity 100% – Y is the statistical power of the analysis. It is a parameter in the MC, which specifies a threshold on signal power where a given signal is detected in 100% – Y of the MC iterations. We choose both X and Y = 5%.

1828 This Monte Carlo allows us to treat the detection algorithm as a black box that can
 1829 be calibrated by passing it a known input (a test spectrum, i.e. a synthetic S_o containing
 1830 a synthetic signal, both software-generated) and looking at its output; a Boolean array of
 1831 frequency bins representing signal detection. These data, along with a simple linear fit to
 1832 the 95% confidence interval, are shown in Fig. 4.7.

1833 The Monte Carlo's output $MC_{lim}(\nu, Y)$, is a normalized limit on signal power required
 1834 for detection. It is a function of frequency ν and statistical power $1-Y$. MC_{lim} can simply be
 1835 converted back to the limit on the total output-referred power contained in injected signals
 1836 which can be detected 95% of the time,

$$P_o^{lim} = MC_{lim}\sigma_{norm}\hat{B}. \quad (4.2)$$

1837 P_o^{lim} is shown in Fig. 4.8 in blue. Also shown in Fig. 4.8 is a limit that does not include
 1838 any matched filtering (orange) to highlight the frequency-dependent improvement of the
 1839 matched filter. This limit is only for illustration and not used in the following sections.

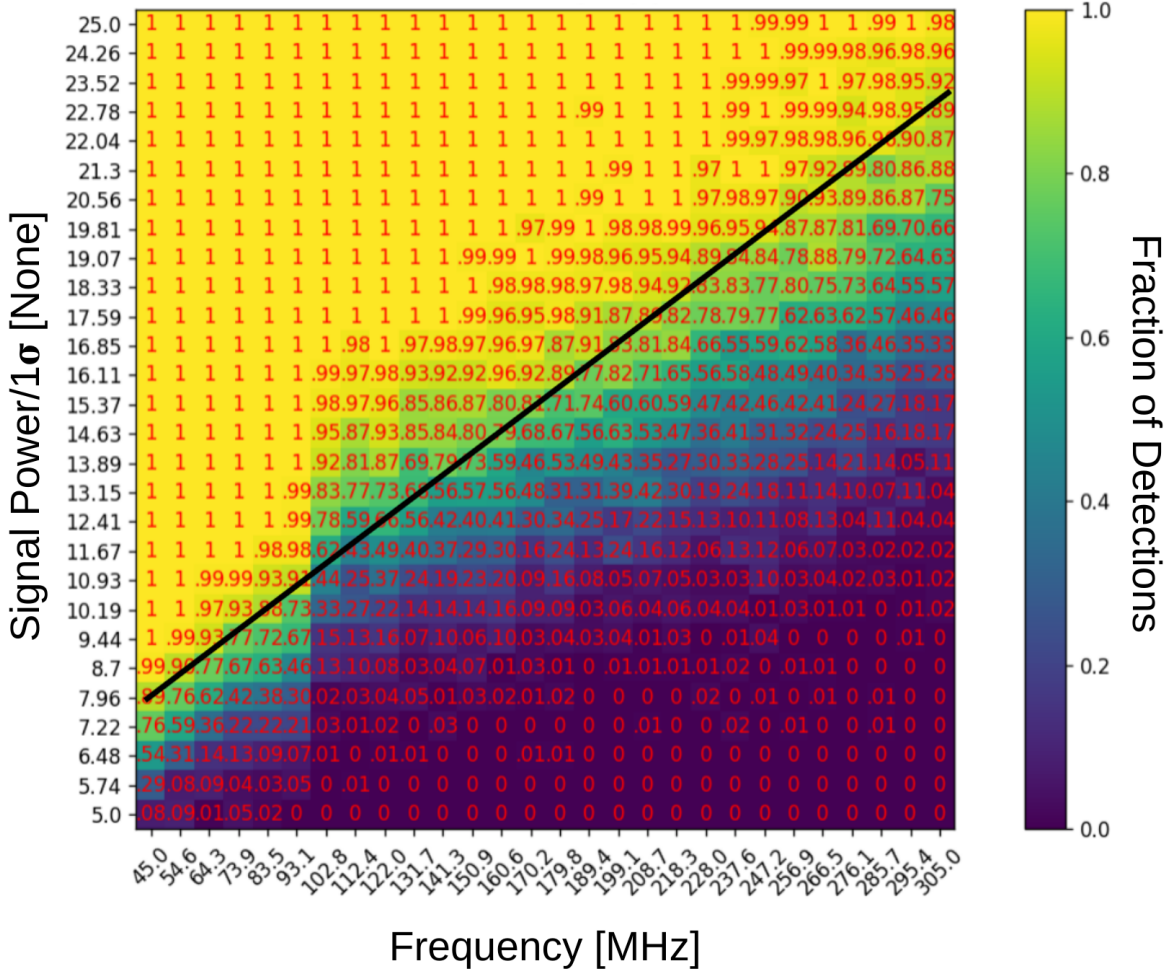


Figure 4.7: Result of Monte Carlo pseudo experiments on signal detection. Color and red numbering show the fraction of detections for each frequency/injected signal power of the 784 combinations tested. The signal power is shown in units of noise standard deviation σ . MC_{lim} is shown as a black line. This line was inserted by eye and gives an approximate fit to the frequency vs. injected signal power which results in a detection 95% of the time. The approximate form of this line is MC_{lim}(ν , Y = 5%) = 0.0686[P_{norm}/MHz] + 2.411[P_{norm}] where P_{norm} is the normalized injected signal power shown on the Y-axis.

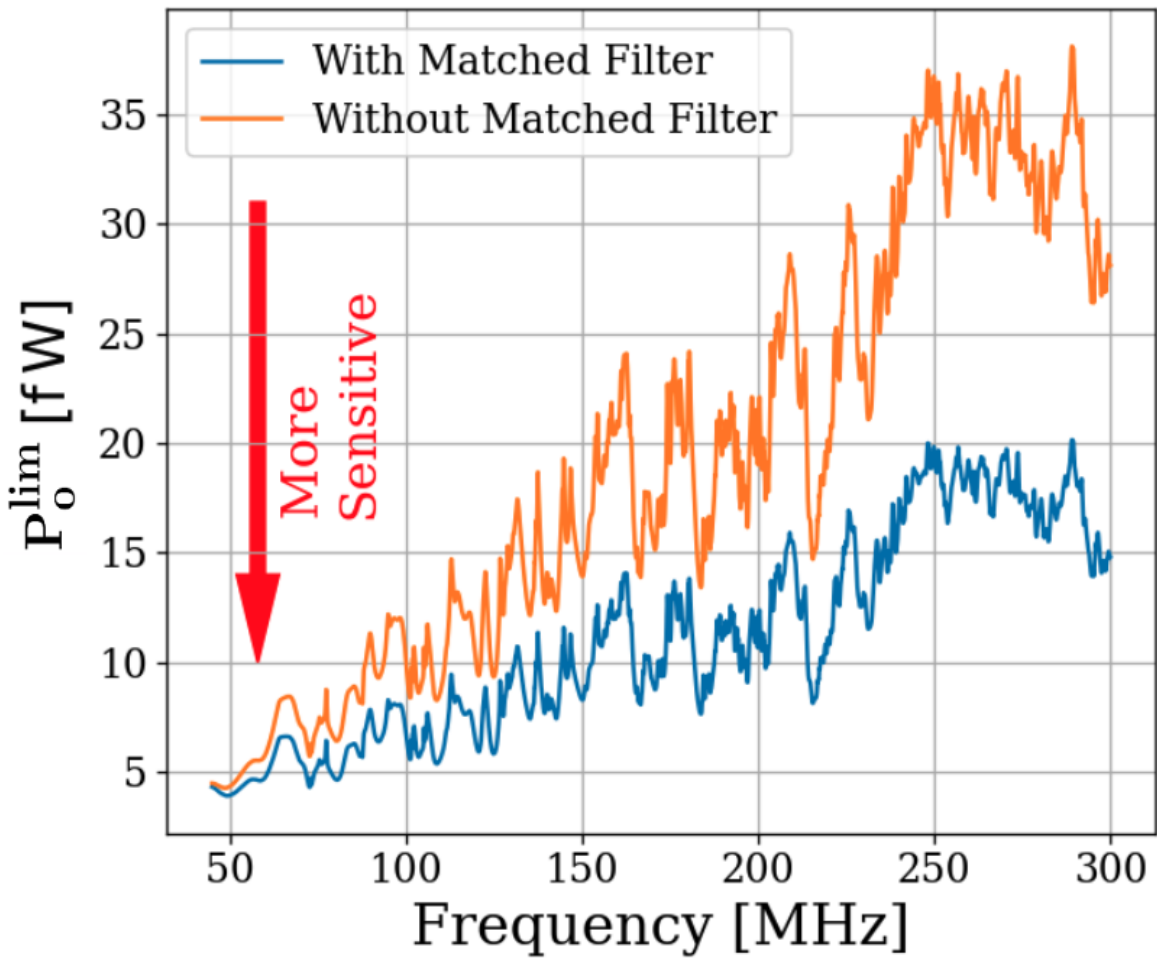


Figure 4.8: Limit on output-referred total integrated signal power, P_o^{lim} . Limits computed with (blue) and without (orange) a matched filter (Sec. 4.2.3). The limits are similar at lower frequencies, but the matched filter improves sensitivity at higher frequencies where the signal power is split among more bins. The blue curve is used in the following sections.

1840 4.2.5 Rejection of a single candidate

1841 Passing S_o through the detection algorithm diagrammed in Fig. 4.3 yields a single candidate
1842 at 299.97 MHz which is approximately 1 kHz wide. This candidate first became detectable
1843 above the noise after about 4 days of averaging, indicating it is just on the threshold of
1844 detectability. Four factors allow for the conclusion that the candidate is an interfering signal
1845 originating from within the PC or ADC, and not a signal in the shielded room (either a dark
1846 photon or RFI):

1847 • The candidate is present not only in the main spectrum, but also in the veto and
1848 terminator spectrum.

1849 • Inspection of the time evolution of this signal shows a narrow signal (about two bins,
1850 or \sim 100 Hz wide) which seems to wander in frequency periodically over the course of a
1851 day and, therefore, with temperature. This is expected behavior for a quartz oscillator.

1852 • Reducing the gain of the system causes the SNR of the candidate to *increase*, indicating
1853 it enters the signal path after the gain stages.

1854 • Changing the clock rate causes the frequency of the candidate to change.

1855 The limit set in this section is referred to the output of the amplifier chain. A single
1856 significant candidate was found, but the method of determining that it was not due to a
1857 dark photon was outlined above. The topic of the next section will be to work back through
1858 the amplifier chain, to an E-field limit in the cavity and ultimately to a limit on ϵ .

1859 4.3 Calibration

1860 In this section, we describe the calibration of the experiment and estimate its uncertainty.

1861 The previous section concluded with a frequency-dependent limit on the output-referred

1862 power P_o^{\lim} (Fig. 4.8), which we now must convert into a frequency-dependent limit on ϵ .

1863 We begin by inverting Eq. 1.7,

$$\epsilon(\nu) < \sqrt{\frac{|\mathbf{E}_{\text{ant}}^{\lim}|^2 \varepsilon_0}{2 \rho_{DM}}}, \quad (4.3)$$

1864 where the *lim* superscript indicates a limit, below which a detectable electric field may be

1865 hiding. The $<$ should be taken to mean that in setting a limit on $|\mathbf{E}_{\text{ant}}^{\lim}|$, ϵ is constrained to

1866 be less than the right-hand side (if it exists at all).

1867 The first step of calibration is to convert from output-referred power to *antenna-referred*

1868 *power*. This represents the signal power presented to the LNA by the antenna via a matched

1869 transmission line and is given by

$$P_{\text{ant}}(\nu) = \frac{P_o}{G} - T_{\text{amp}} k_B \Delta\nu_{\text{RF}}, \quad (4.4)$$

1870 where G and T_{amp} are the frequency-dependent system gain and noise temperature (74–75 dB

1871 and 100–120 K respectively, measured via the Y-factor method, see Sec. 3.1.1) and k_B is

1872 Boltzmann’s constant.

1873 Ultimately, the exclusion limit is set by fluctuations on this baseline described by

$$\begin{aligned}
P_{\text{ant}}^{\lim}(\nu) &= \frac{P_{\text{o}}^{\lim}}{G} - \left(\frac{2}{n} \right)^{1/2} T_{\text{amp}} k_B \Delta\nu_{\text{RF}} \\
&= \frac{P_{\text{o}}^{\lim}}{G} - \left(\frac{2 \Delta\nu_{\text{RF}}}{\tau} \right)^{1/2} T_{\text{amp}} k_B,
\end{aligned} \tag{4.5}$$

where the *lim* superscript indicates an exclusion limit, n is the total number of spectra averaged together, and τ is the total integration time. In the second line, we have used $n = \Delta\nu_{\text{RF}} \tau$. In practice, the LNA correction is small; the first term divided by the second varies with frequency between 7 and 50. The $\tau^{-1/2}$ dependence of P_{o}^{\lim} is implicit because it was calculated from S_{o} which is itself an averaged spectrum. As mentioned above, this $\tau^{-1/2}$ dependence implies that the limit on ϵ scales as $\tau^{-1/4}$.

In the remainder of this section we explore the relationship between P_{ant}^{\lim} and $|\mathbf{E}_{\text{ant}}^{\lim}|$ so that we can use our experimental data to set a constraining limit on ϵ by employing Eq. 4.3.

4.3.1 Average effective aperture, $\langle A_e(\nu) \rangle$

An antenna's effective aperture, A_e [m^2], represents the effective area that it has to collect power density or irradiance [W/m^2] from an incident Poynting vector. It was defined in Eq. 2.9. Notably, it assumes a polarization match between the wave and the antenna (see Sec 2.1.1.2).

A_e is useful for an antenna in free space, however some modifications must be made to construct an analogous quantity for an antenna in a cavity.

The first modification is to average over many configurations of the system. The background for this is given in Sec. 2.4. As discussed, we denote this averaging with $\langle \rangle$ so that the

1891 average, effective aperture is denoted $\langle A_e \rangle$. It is interesting to note that by averaging over
 1892 configurations (namely antenna direction), $\langle A_e \rangle$ simplifies since $\langle D(\Omega) \rangle = 1$ by construction
 1893 [23].

1894 The second modification is to introduce a resonant enhancement factor that corresponds
 1895 to the system's tendency to "ring up" in the same way any resonator will. We refer to
 1896 this as *composite Q* and represent it as \tilde{Q} . It is analogous to the standard quality factor
 1897 of a resonator with one important modification; we operate our experiment across a wide
 1898 frequency range so we define \tilde{Q} across the continuum of these resonances, not only on classical
 1899 eigenmodes of the system.

1900 These modifications provide a relationship between an observable E-field (\mathbf{E}_{ant} in Eq.
 1901 4.3) and the power available at the port of an antenna for a given aperture

$$\langle P_{\text{ant}} \rangle = \frac{|\mathbf{E}_{\text{ant}}|^2}{\eta_0} \langle \tilde{Q} A_e \rangle, \quad (4.6)$$

1902 where η_0 is the impedance of free space. With this in mind, we perform an RF simulation
 1903 to compute $\langle \tilde{Q} A_e \rangle$.

1904 4.3.2 Simulation of $\langle \tilde{Q} A_e \rangle$

1905 It is difficult to make claims about statistical uniformity in the "undermoded" regime where
 1906 modes are not sufficiently mixed [82], so we have employed a commercial, electromagnetic,
 1907 finite-element modeling software package (COMSOL Multiphysics RF module [60]). Within
 1908 the simulation, a model of the antenna (with a 50Ω feed) is placed in a simplified room with

1909 wall features removed. Spot testing at various frequencies has shown that averaging results
1910 from various antenna positions using this simplified simulation behaves very similarly to one
1911 with the room features included at a fraction of computational complexity.

1912 Two similar simulations are run; driving an E-field while measuring the antenna's re-
1913 sponse and driving a second small monopole antenna and measuring the response of the
1914 primary antenna.

1915 In the first simulation, we drive currents on the walls which correspond to a surface E-
1916 field magnitude of 1 V/m (made up of equal components in the x, y and z directions) using
1917 COMSOL's source electric field option. This field takes the place of \mathbf{E}_{ant} in Eq. 4.6. The
1918 antenna/cavity system resonates and causes an enhancement by \tilde{Q} . The power received at
1919 the antenna's port is measured, allowing the calculation of $\tilde{Q} A_e$, again from Eq. 4.6. By
1920 repeating this simulation for several positions, averaging allows us to compute $\langle \tilde{Q} A_e \rangle$.

1921 The second simulation shares the same geometry, but is used to compute a correction
1922 factor to account for differences between simulation and measurement and to estimate un-
1923 certainty on the first simulation through comparison to physical measurement. Rather than
1924 driving the system through currents on the walls, power is injected into the system with a
1925 40 cm monopole. From this simulation, two-port scattering parameters (S-parameters, de-
1926 fined in 4.3.3) are computed. A similar test is performed on the physical system using a
1927 vector network analyzer (VNA) which provides a physical measurement of the S-parameters
1928 to compare with the simulation. The processing of the simulated and measured S-parameter
1929 datasets is discussed in the following sub-section. A screenshot of the COMSOL model GUI
1930 is shown in Fig. 4.9. The resulting S-parameters from the simulation are plotted against the

1931 measured S-parameters in Fig. 4.10

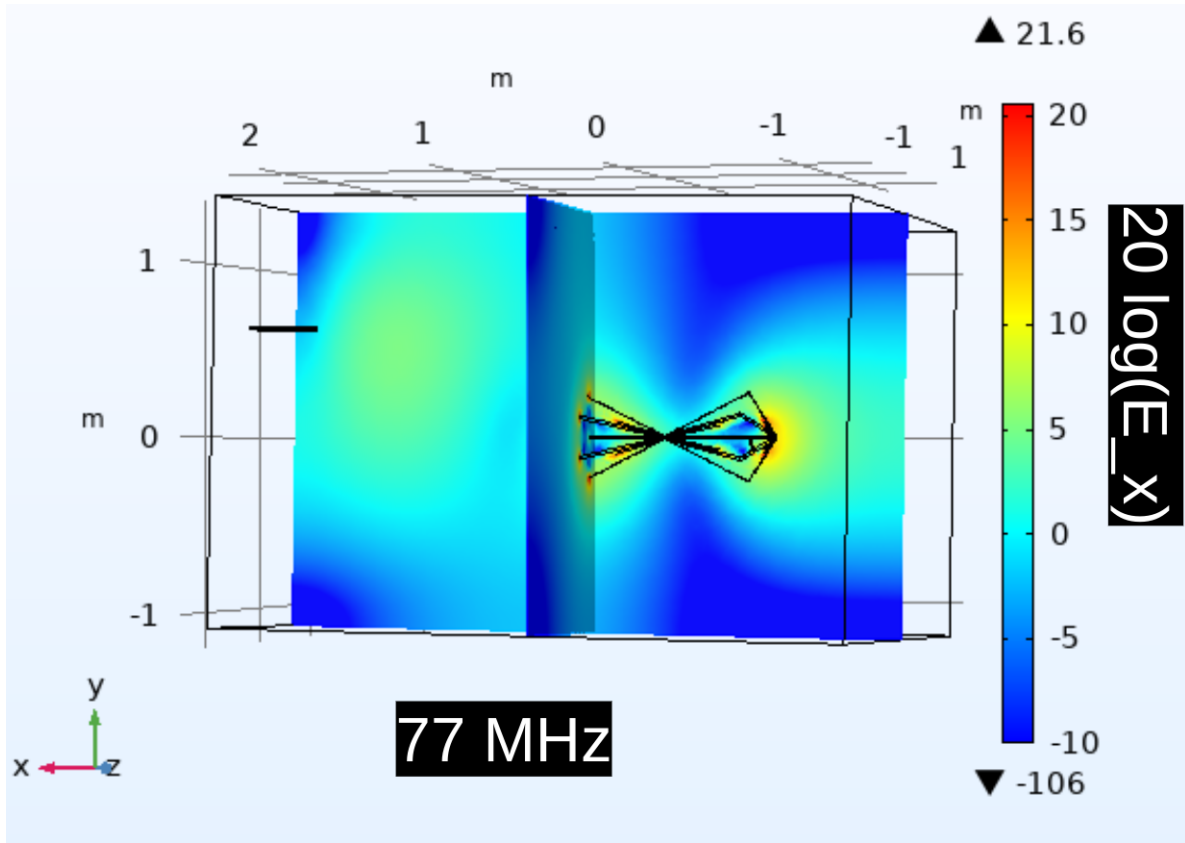


Figure 4.9: Screenshot of COMSOL simulation GUI for two-antenna validation. Shown only at a single position and single frequency (77 MHz). There are 18 antenna positions, 3 E-field components, and ~ 1000 frequency points, so there are many similar figures to this one. The x-component of the electric field is shown in color compared to 1 V/m.

1932 Both simulations are run at the same 18 positions; 9 of which are approximately equivalent to the physical antenna positions while the other 9 are different in order to estimate how
1933 many positions are required for decent convergence of $\langle \tilde{Q} A_e \rangle$. Repeatedly averaging 9 different,
1934 random positions (with replacement) results in about 20% variation on their averaged
1935 $\langle S_{21} \rangle$ coefficients at each frequency, allowing us to conclude 9 positions and polarizations
1936 provide acceptable convergence. This is a bootstrap method[83].
1937

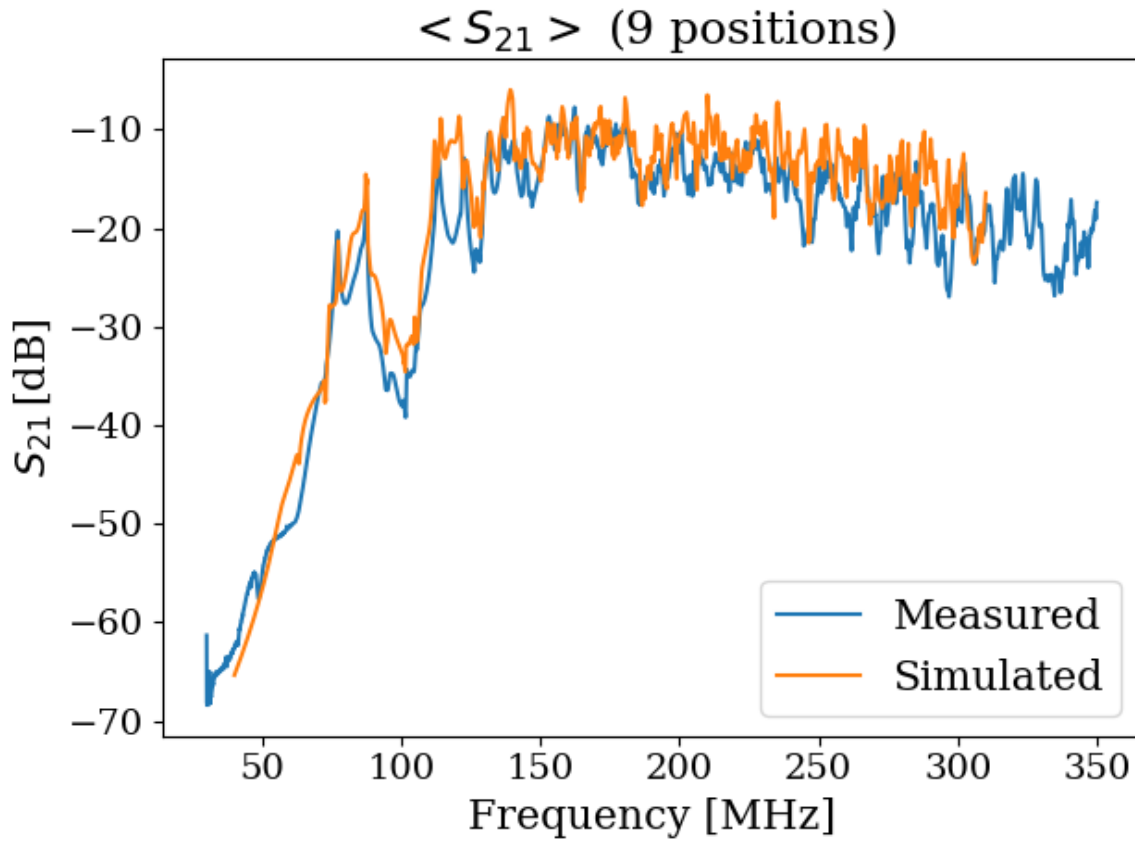


Figure 4.10: Simulated vs. measured $\langle S_{21} \rangle$. Averaged over 9 antenna positions. The procedures for generating these data are described in the text of this section.

1938 **4.3.3 Correction and uncertainty of $\langle \tilde{Q} A_e \rangle$**

1939 As outlined above, we approximate the uncertainty of the simulation by injecting power into

1940 the system via a second antenna and comparing the results to simulation.

1941 For a two-port microwave device, the ratio between the voltage presented at port one and

1942 the voltage measured at port two is known as S_{21} [43, 44]. For our system, S_{21} is a measurable

1943 quantity that is similar to a dark photon detection in that it requires the antenna to convert

1944 an electric field (which has interacted with the room) into a port voltage. Having frequency-

1945 dependent measurements of S_{21} for simulation and measurement gives us a correction to
 1946 the simulation (to account for discrepancies in geometry) and estimate the uncertainty on
 1947 $\langle \tilde{Q} A_e \rangle$.

1948 The difference between the measured and simulated values of $\langle |S_{21}| \rangle$ is described by

$$\langle |S_{21}^{\text{meas}}|^2 \rangle = \alpha \langle |S_{21}^{\text{sim}}|^2 \rangle, \quad (4.7)$$

1949 where meas/sim indicates measured/simulated and the average is over all 18 measured/sim-
 1950 ulated positions and orientations of the antenna. We have taken the square since we are
 1951 interested in the aperture, which is proportional to the square of the voltage. This equa-
 1952 tion implies α is a frequency-dependent, multiplicative correction factor which results in a
 1953 corrected $\langle |S_{21}^{\text{sim}}|^2 \rangle$. We find α to have a mean of 0.6, a minimum of 0.1 and a maximum of
 1954 2.

1955 To determine uncertainty on effective aperture, we define the following test statistic

$$\Delta = \frac{\langle |S_{21,n}^{\text{meas}}|^2 \rangle - \alpha \langle |S_{21,n}^{\text{sim}}|^2 \rangle}{\langle |S_{21}^{\text{meas}}|^2 \rangle}, \quad (4.8)$$

1956 where n refers to the subset of n measured/simulated positions sampled randomly with re-
 1957 placement. Δ defines the fractional difference between corrected, simulated S_{21} and measured
 1958 S_{21} . The test statistic, Δ , is calculated 1000 times, providing a distribution of frequency
 1959 dependent Δ s. The curves bounding 63% of these curves are taken to be the uncertainty
 1960 on Δ . Thus we calculate the corrected $\langle \tilde{Q} A_e \rangle$ as well as its uncertainty. This is shown as a
 1961 function of frequency in Fig. 4.11. The uncertainty on it is shown in gray and is simply

$$\delta \langle \tilde{Q} A_e \rangle = \langle \tilde{Q} A_e \rangle \delta \Delta. \quad (4.9)$$

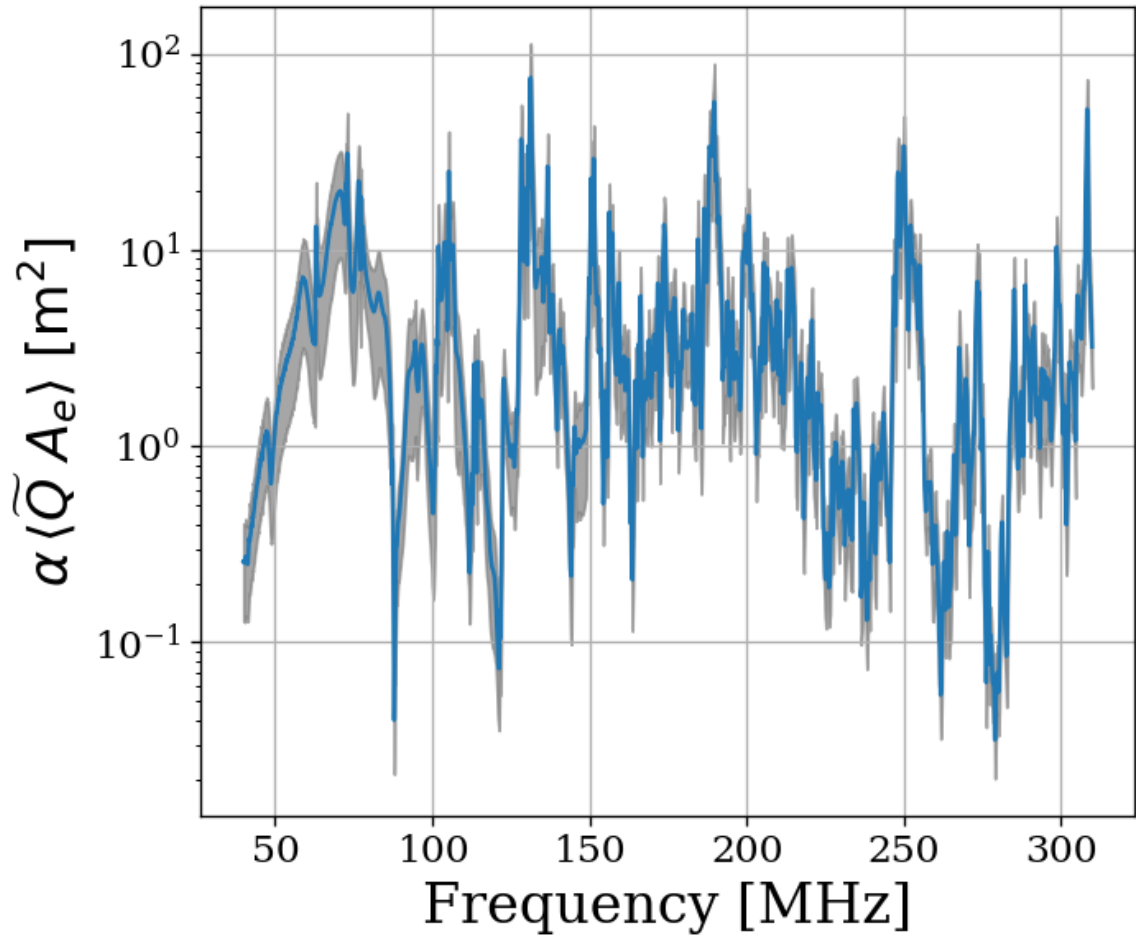


Figure 4.11: Corrected average effective aperture. Calculated with COMSOL RF. The aperture correction α (Eq. 4.7) and its uncertainty (gray) are estimated by comparing simulations to measured S parameters.

1962 A brief summary of the system's aperture is in order. In free space an antenna's ability
 1963 to couple an incoming wave's power density into a transmission line is given by its effective
 1964 aperture, Eq. 2.9. An antenna in a cavity acts as a coupled oscillator that exhibits very

1965 complex resonances above the first few modes (~ 100 MHz for our system). Attempts to
 1966 simulate an aperture for the antenna-cavity system are difficult because of the system's
 1967 extreme dependence on the placement of any conductor in the room, especially the antenna.
 1968 Averaging over system configurations (antenna positions and polarizations in our case) allows
 1969 for a significantly more repeatable *statistical* treatment of the aperture/quality factor, which
 1970 we call $\langle \tilde{Q} A_e \rangle$. Comparison of simulated and measured S_{21} gives a small, dimensionless
 1971 correction factor α , Eq. 4.7.

1972 Armed with $\alpha \langle \tilde{Q} A_e \rangle$ we now compute a limit on ϵ using the measured and simulated
 1973 quantities via Eqs. 4.5 and 4.6,

$$\epsilon(\nu) < \sqrt{\frac{1}{2c\rho_{\text{DM}}} \frac{P_{\text{ant}}^{\text{lim}}}{\alpha \langle \tilde{Q} A_e \rangle}}, \quad (4.10)$$

1974 where c is the speed of light, ρ_{DM} is the local dark matter density and $P_{\text{ant}}^{\text{lim}}$ is defined in
 1975 Eq. 4.5. We have separated the equation into constants (or, in the case of ρ_{DM} , values that
 1976 we fix) and values that we measure or simulate.

1977 In order to validate our entire detection system, we inject sub-threshold signals into the
 1978 shielded room to verify we are able to detect them.

1979 4.4 Hardware Injection Test ⁴

1980 To validate the detection methodology, a separate proof-of-concept run with a proxy dark
 1981 photon signal injected into the shielded room was performed. Apart from the injection

⁴Code for this section can be found at: <https://github.com/josephmlev/darkRadio/tree/master/daqAnalysisAndExperiments/run1p4/injectionTesting/injectionTesting.ipynb>

1982 antenna (a 40 cm monopole, see Sec. 4.3.2), the setup was equivalent to run 1.4, including
1983 the data analysis. The proxy dark photon signal (detailed in Sec. 4.4.1.2) was injected at a
1984 frequency set by a colleague and was unknown to me at the time of analysis, constituting a
1985 blind analysis.

1986 4.4.1 Injection test prerequisites

1987 4.4.1.1 Determination of required injected power

1988 To accomplish the test, a minimum detectable power required for injection P_{inject} must be
1989 computed. P_{inject} should correspond to a signal that can be detected in a predictable amount
1990 of time (with some uncertainty, discussed in detail in Sec. 2.2.2). A simple way to begin
1991 is to read off the detectable, total integrated, power from Fig. 4.8. In other words the
1992 power contained in a dark photon line, integrated over the few bins spanned by the line
1993 ($Q_{\text{DP}} \approx 10^6$, discussed in Sec. 2.1.2). This gives the amount of output-referred power that
1994 would be detectable 95% of the time after 9 days of integration. Since we do not want to
1995 wait 9 days for this test, it is simple to convert this detection limit into one that would be
1996 produced in a shorter time using the Dicke radiometer equation, Eq. 2.16. Namely, the limit
1997 on power scales like the square root of time⁵, so a one-hour integration will require a factor
1998 $\sqrt{9 \text{ days}/1 \text{ hour}} = 14.7$ more power than is shown in Fig. 4.8.

1999 At this point, the simplest way to proceed is to measure the average through-power of the

⁵It is important to point out that one needs to test whether or not the system in question actually behaves as predicted by the Dicke equation for the amount of averaging in question. After lots of averaging, one may encounter non-thermal backgrounds that do not scale properly. It is shown in Fig. 4.16 that the dark radio system follows the Dicke radiometer equation at least for 9 days.

2000 monopole to the bicon in several antenna positions. This power is proportional to $\langle |S_{21}|^2 \rangle$.
2001 This is the same as the set up described in Sec. 4.3.2. The bicon was moved to 9 positions
2002 and the resulting S-parameters were measured at the reference planes shown in Fig. 4.12.
2003 They are shown in Fig. 4.13 after being averaged together.

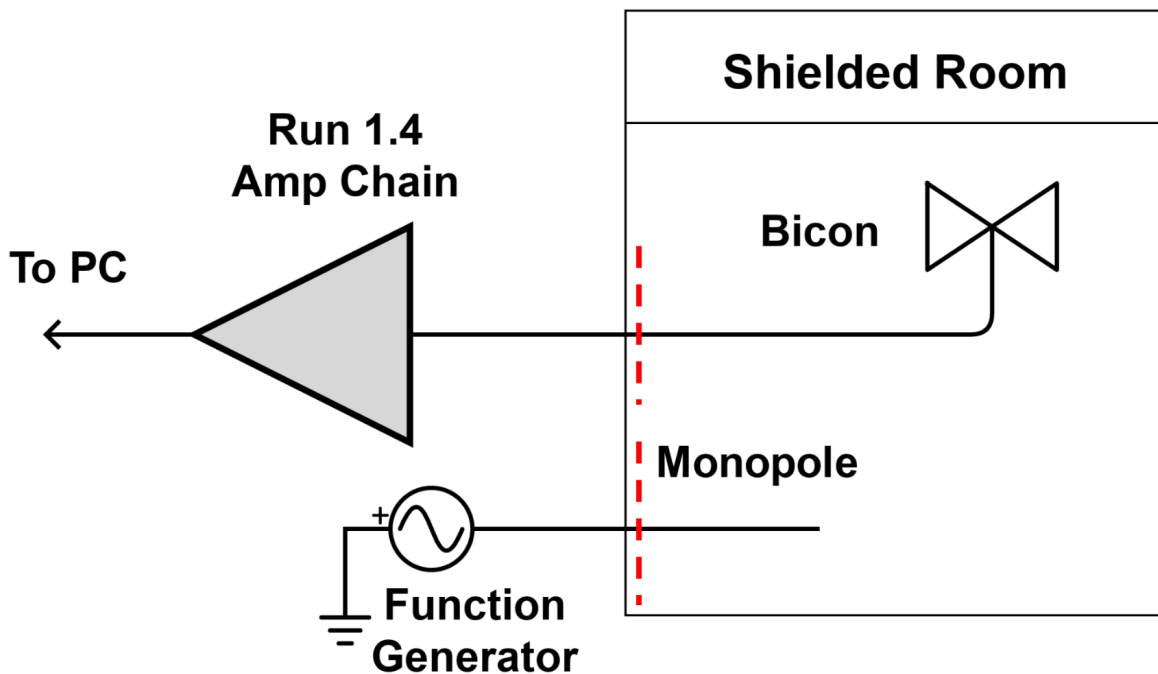


Figure 4.12: Schematic of hardware injection test. Dashed red lines indicate reference planes used to measure S-parameters, shown in Fig. 4.13. “Amp Chain” includes amplifiers, attenuators and filters as described in Sec. 2.5.4.

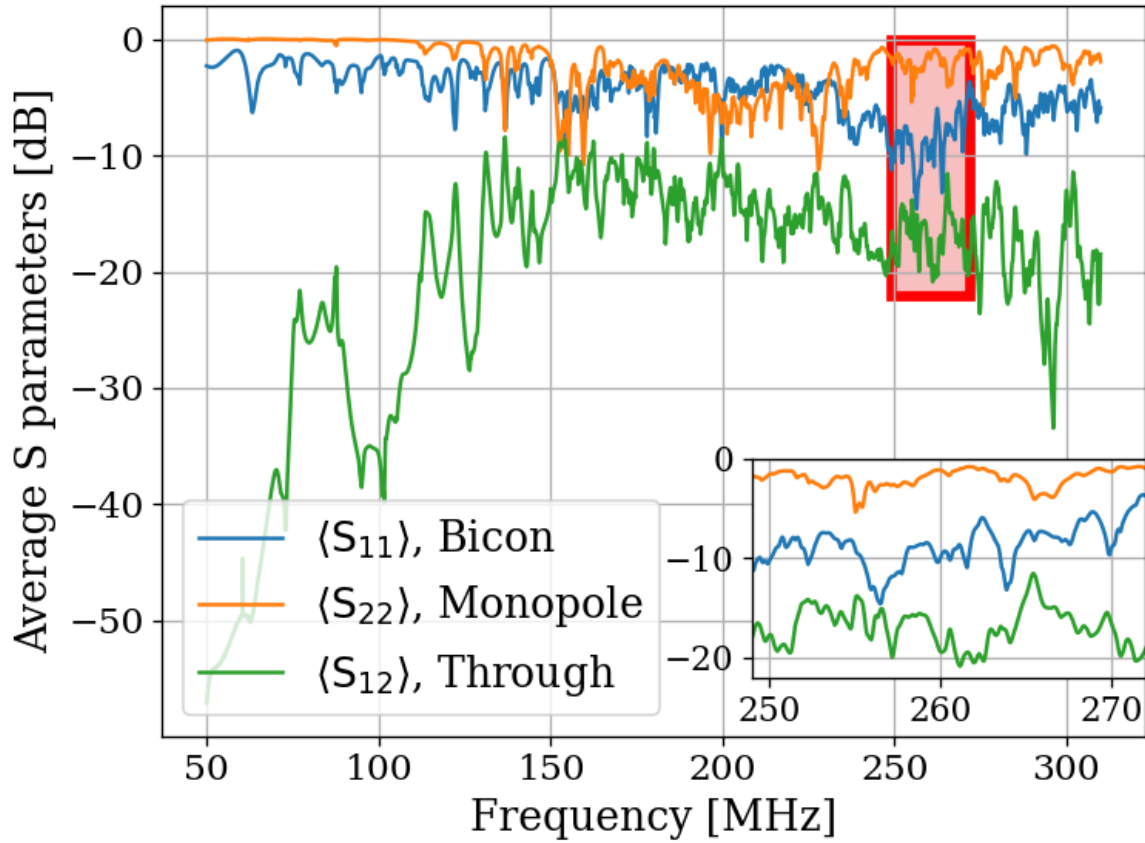


Figure 4.13: Average S-parameters of hardware injection test. Taken at 9 positions of the bicon antenna and averaged together (linearly). Ports 1 and 2 are defined to be for the bicon and monopole respectively. Note that $\langle S_{12} \rangle = \langle S_{21} \rangle$ so only $\langle S_{12} \rangle$ is shown. The inset shows a zoom-in of the area enclosed by the red box. Also note that dB is implicitly proportional to power.

2004 Knowing the output-referred power limit, the system's average $\langle |S_{21}|^2 \rangle$, and the gain G,
 2005 allows for a calculation of the required signal strength (as a function of frequency) which
 2006 will become detectable after a known amount of time. In order to simplify the test, a
 2007 smaller 1 MHz band is chosen between 268 and 269 MHz for the blind injection, where
 2008 $\langle |S_{21}|^2 \rangle$ is constant to about 1 dB. At first glance, this seems like cheating. However, there
 2009 are still $\sim 21,000$ frequency bins in this span, so a detection is very unlikely to be random.

2010 Furthermore, the entire 50-300 MHz span is sent to the detection algorithm (Discussed in
2011 Sec. 4.2 and illustrated in Fig. 4.3), which produces an output without knowing about this
2012 frequency restriction.

With all this in mind, the signal power required is simply

$$P_{\text{inject}} = \frac{P_{\text{o}}^{\text{lim}}}{G \langle |S_{21}|^2 \rangle},$$

2013 where each term is a function of frequency. For the parameters described in this section
2014 (including the increase in the power limit $\sqrt{9 \text{ days}/1 \text{ hour}} = 14.7$), this works out to
2015 $\approx 6 \times 10^{-19} \text{ W}$ or -152.5 dBm. The Rigol DSG830 signal generator is not calibrated
2016 to such low levels, so this was achieved through attenuation⁶.

2017 4.4.1.2 Proxy dark photon signal injection

2018 Now that the power for signal injection has been established, the finite-width proxy-signal
2019 ($Q_{\text{DP}} \approx 10^6$) is generated. The signal's line-shape is discussed in Sec. 2.1.2. An intuitive way
2020 to accomplish this would be with an arbitrary waveform generator injecting a time domain
2021 signal which is the Fourier transform of the the expected Rayleigh line shape, Eq. 2.24. This
2022 is the method employed by the ADMX experiment (see, for example, [84]). Another option
2023 would be to frequency-modulate a sine wave such that it slowly sweeps out the line shape,
2024 spending an amount of time at each frequency weighted by Eq. 2.24. While intuitive, I was
2025 unable to get this to work. Zhu et al.'s method of frequency hopping [85] is the discretized
2026 version of this, and it was very simple to implement. The signal generator is set to change

⁶Experience with this signal generator has shown it exhibits the best performance is when it is set around -30 dBm. Higher than this, large non-harmonic distortions appear, contaminating the run. Smaller, and the signal-to-spurious-noise-floor of the generator is poor, also contaminating the run.

2027 frequencies at some interval (discussed below). The frequency is randomly drawn from the
2028 PDF of Eq. 2.24.

2029 There are three considerations that determine the frequency hop period τ_{FH} that the
2030 frequency is changed⁷. First, τ_{FH} should be much longer than the acquisition time of a single
2031 buffer τ_{FFT} ⁸. On the Rigol signal generator, the power is briefly shut off while the frequency
2032 is changed. $\tau_{\text{FFT}} \ll \tau_{\text{FH}}$ ensures that most FFTs of data do not contain a frequency-hop.
2033 Second, τ_{FH} should be small compared to the total time of integration τ , so that there are
2034 many frequencies represented in the entire run. In the limiting case, $\tau_{\text{FH}} = \tau$ will yield an
2035 averaged spectrum containing a single injected frequency. In this case, the proxy-signal will
2036 be a delta function in the frequency domain. Third, τ_{FFT} should be longer than the ring-up
2037 time of the room, $\tau_{\text{FFT}} \gg Q/\nu$. For $Q = 100$ and $\nu = 260$ MHz, the right-hand side of this
2038 inequality is ≈ 0.3 μ s.

2039 Testing has shown that $\tau_{\text{FH}}/\tau_{\text{FFT}} \approx 10$ is more than adequate to address the first con-
2040 sideration. For Run 1A (and therefore, this test, which shares settings with Run 1A),
2041 $\tau_{\text{FFT}} = 2^{24}/800$ MHz = 21 ms, so τ_{FH} was set to 250 ms. This means that over 1 hour, the
2042 frequency will be set to $\approx 1.4 \times 10^4$ values, which addresses the second and third concerns.
2043 A histogram of this signal is shown in Fig. 4.14.

⁷Zhu et al. randomized this period to prevent any unintentional periodic signals entering. I did not find this to be necessary.

⁸One can likely bypass this restriction by coordinating the signal generator and ADC such that there is some dead time between collection of buffers, in which the frequency is set. Testing has shown that this restriction is adequate to avoid this extra programming step

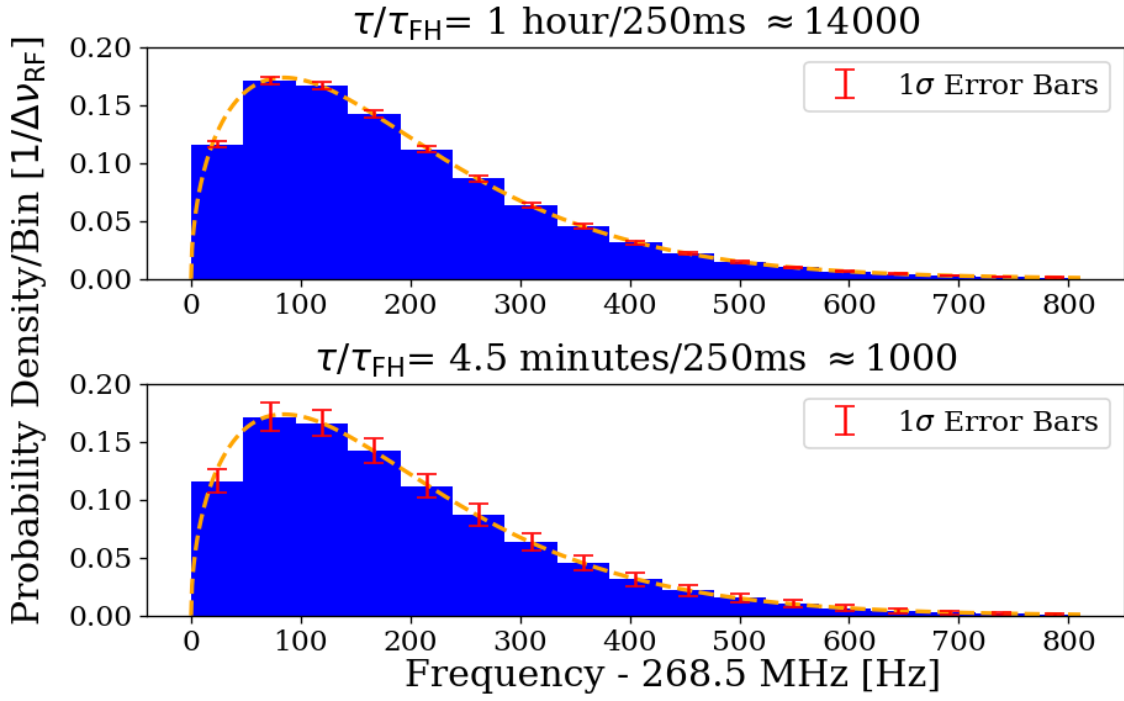


Figure 4.14: Histogram of frequencies used for hardware injection test, with realistic $\Delta\nu_{\text{RF}} = 47.7 \text{ Hz}$. The Orange dashed curve is the expected line shape from 2.24, and is the PDF frequencies are drawn from. The blue histogram and error bars are generated from the Monte Carlo simulation. They show the mean value per bin, with 1σ error bars in red. This involves generating 1000 lists of random frequencies (each of length τ/τ_{FH}), binning the data and calculating the standard deviation of each bin. τ is the total acquisition time and τ_{FH} is the amount of time spent on each frequency before “hopping” to the next. Their ratio, τ/τ_{FH} , is the number of frequencies that are injected in a given injection test, and was approximately 1.4×10^4 for the one-hour test outlined in this section. Two plots give an idea of how error scales with τ/τ_{FH} .

2044 4.4.2 Performing the injection test

2045 Due to the uncertainties involved, more data were taken than the required 1 hour. This also
 2046 helped produce the pretty plot in Fig. 4 of Levine et al. [39]. 3.6 hr of data were collected
 2047 and saved in 30 s pre-averages so that progressively more data could be averaged if the signal
 2048 was not detected at the predicted time. As mentioned above, the signal was injected at a

2049 relatively high frequency within the span so that it would be split up into 5 or 6 bins, testing
2050 the matched filter's effectiveness. The bicon was moved to 9 positions. Spectra resulting from
2051 9 antenna positions and 30 seconds of pre-averaging at each position were averaged together
2052 giving 4.5 m time resolution. Three of these spectra are shown in Fig. 4.15. The standard
2053 deviation of these spectra average down with the square root of time, closely following the
2054 Dicke radiometer equation (discussed in Sec. 2.1.1.3). This scaling is shown in Fig. 4.16.

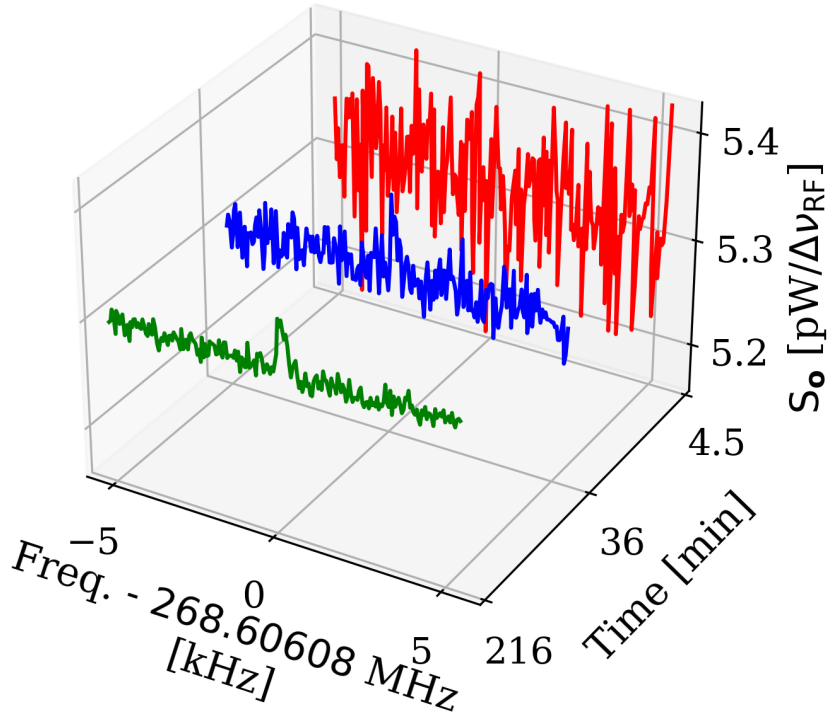


Figure 4.15: Output-referred power spectral density from the hardware injection test illustrating noise averaging down to reveal a persistent, hardware-injected, dark photon proxy signal. Spectra shown are highly zoomed around the injected frequency, 268.60608 MHz. The red, blue and green spectra represent 4.5, 36 and 216 minutes of integration time, respectively. The standard deviation of these spectra (excluding the bins containing the injected signal) averages down with the square root of time as expected. The blue spectrum shows the amount of averaging required for the signal to be detected by the detection algorithm (including the matched filter) at 5% significance. The tight zoom shown here is less than 1 part in 10^4 of the full 50-300 MHz spectrum analyzed.

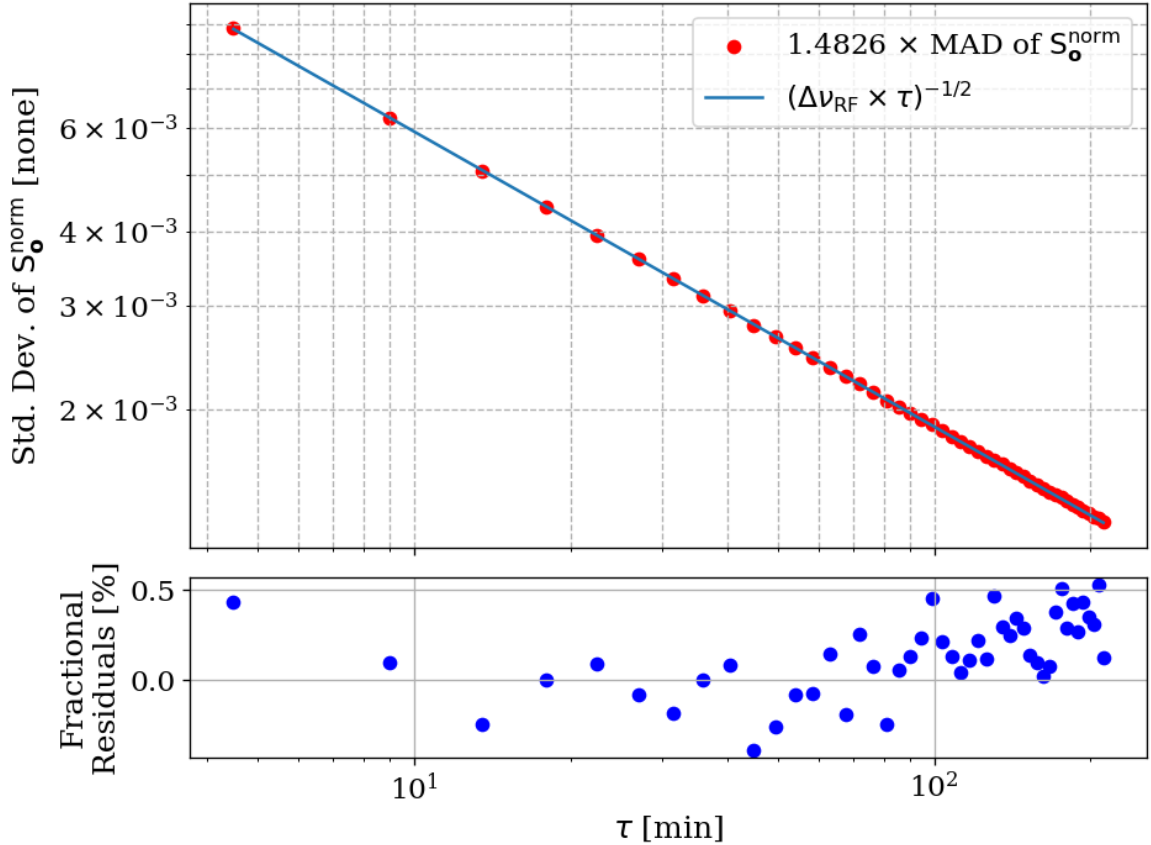


Figure 4.16: Standard deviation of output-referred power spectral density from the hardware injection test, computed with median absolute deviation (MAD). The blue curve represents the predicted standard deviation from the Dicke radiometer equation, Eq. 2.16. Each point corresponds to 9 antenna positions with an additional 4.5 minutes of data averaged (see Sec. 4.4.2). MAD provides a more robust measure of variability, reducing the influence of outliers and offering a better fit than direct standard deviation calculations. Note that the factor of 1.4826 is required to convert between MAD and standard deviation and assumes normally distributed data. It is derived in Sec. 2.3 of [86].

2055 These spectra were generated one at a time and passed through the detection algorithm.
2056 The first spectrum where a signal was detected was at 36 minutes, shown in blue in Fig. 4.15.
2057 Although hardly detectable to the eye, the matched filter detects the signal with 5% signifi-
2058 cance. At the point the signal was detected (i.e. before all data were averaged together), the
2059 injection frequency was confirmed to have been correctly identified, resulting in a success-
2060 ful, blind, hardware injection test. Only after this confirmation were all the data averaged
2061 together to make Fig. 4.15.

2062 **4.4.3 Inspection of Data**

2063 This final subsection simply contains some full-page figures which show data from the injec-
2064 tion test. They are all from the same 34 minutes of data but at different stages of processing,
2065 closely following the three main steps of Analysis, Sec. 4.2. They are meant to simulate the
2066 experience of inspecting a 2^{24} -point FFT's power spectrum in a matplotlib widget window.
2067 The zoom is seemingly unending, a feature that is difficult to appreciate in a printed docu-
2068 ment. These figures should provide some context for how futile a manual search of unfiltered
2069 data would be. Try and pick out the signal in the top left panel of Fig. 4.17!

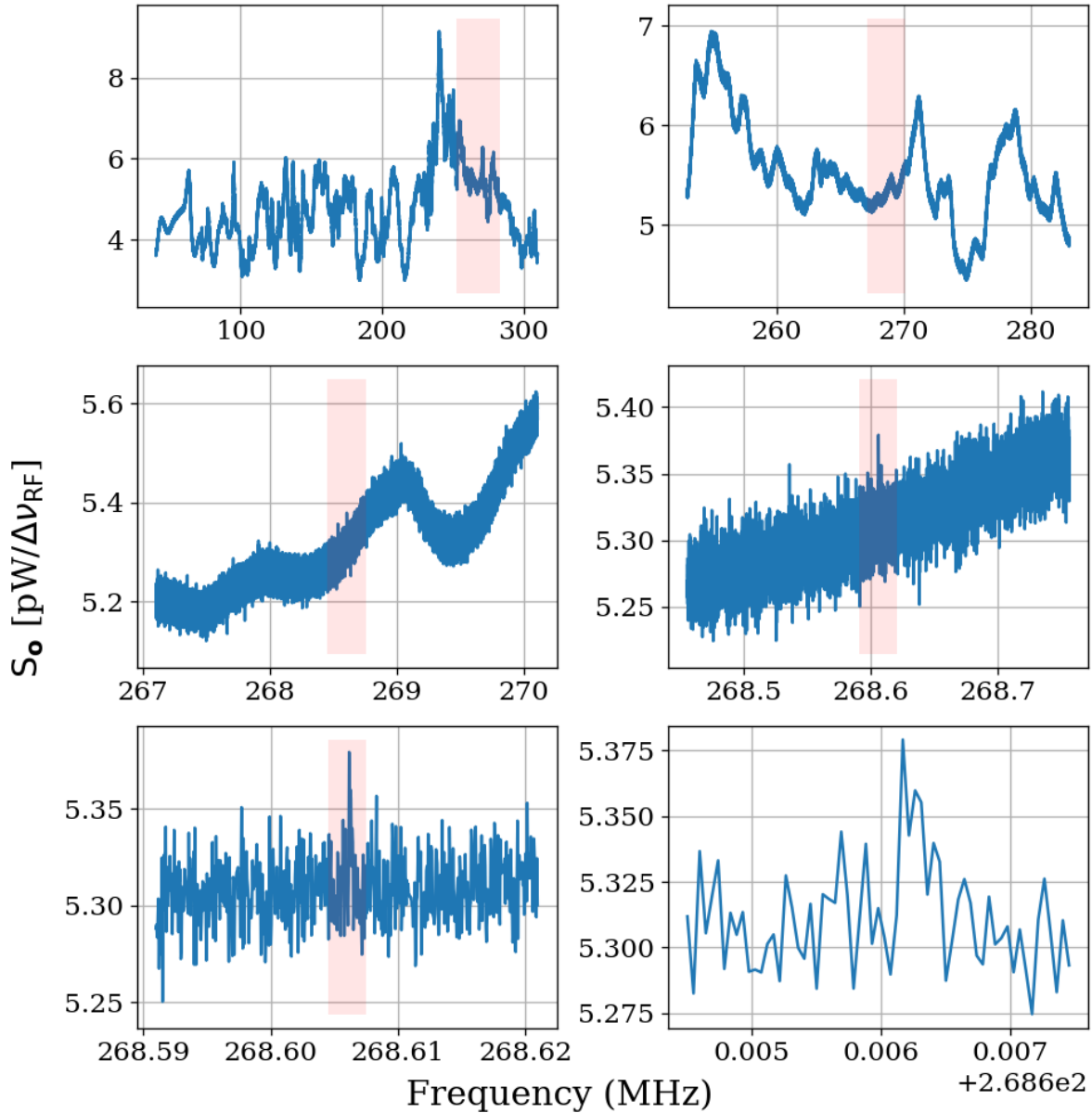


Figure 4.17: Output-referred power spectrum from hardware injection test. Injected signal at 268.60608 MHz. All spectra correspond to a total of 36 minutes of averaging, split evenly between 9 antenna positions. The full 50-300 MHz span contains $\approx 5.2 \times 10^6$ bins. Light pink boxes show the zoom level on the following plot.

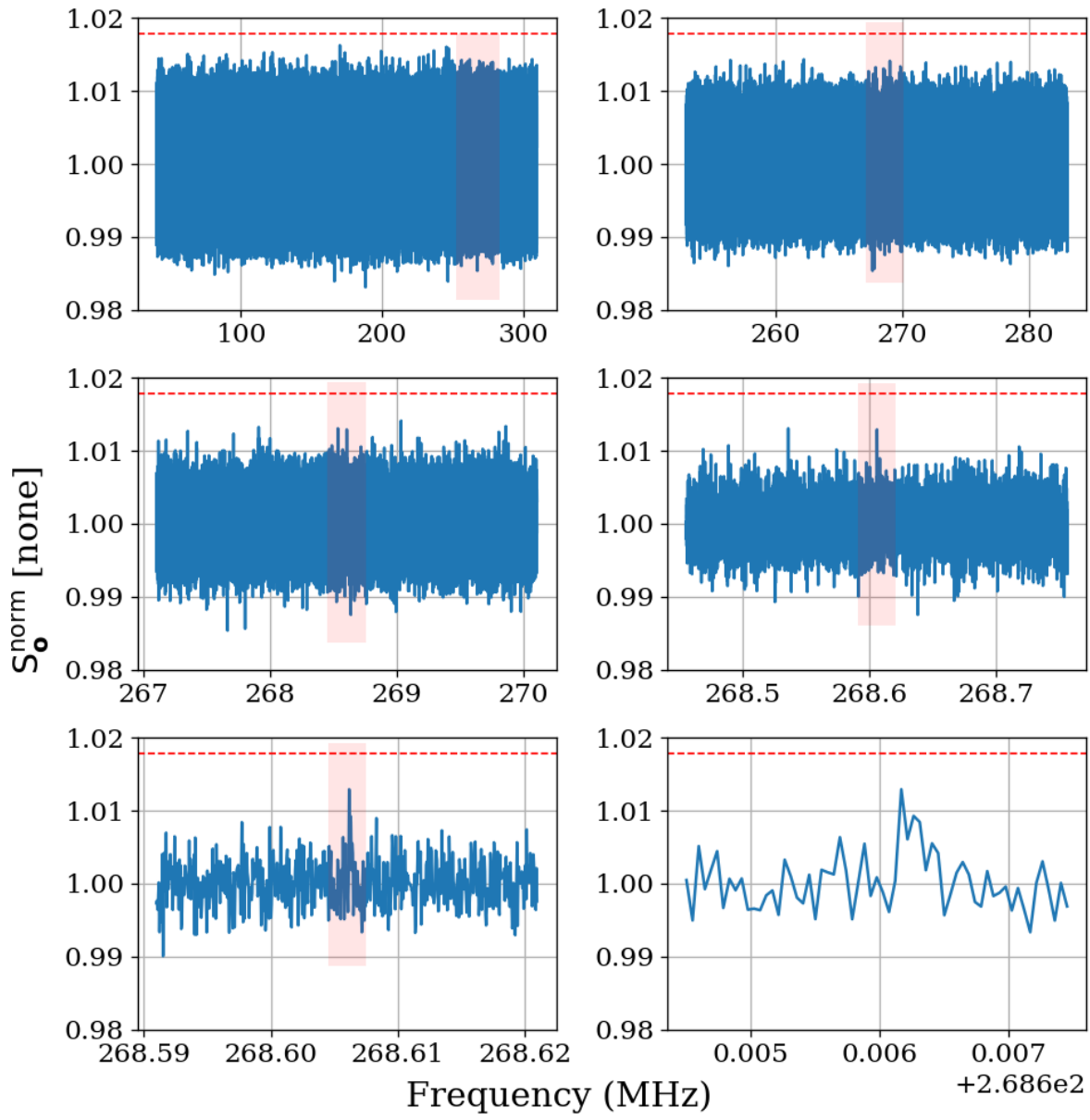


Figure 4.18: Normalized, output-referred power spectrum from hardware injection test. Injected signal at 268.60608MHz. Light pink boxes show the zoom level on the following plot. The red dashed line indicates the 5% significance threshold, derived in Sec. 2.2.1. A signal was not detectable above this threshold.

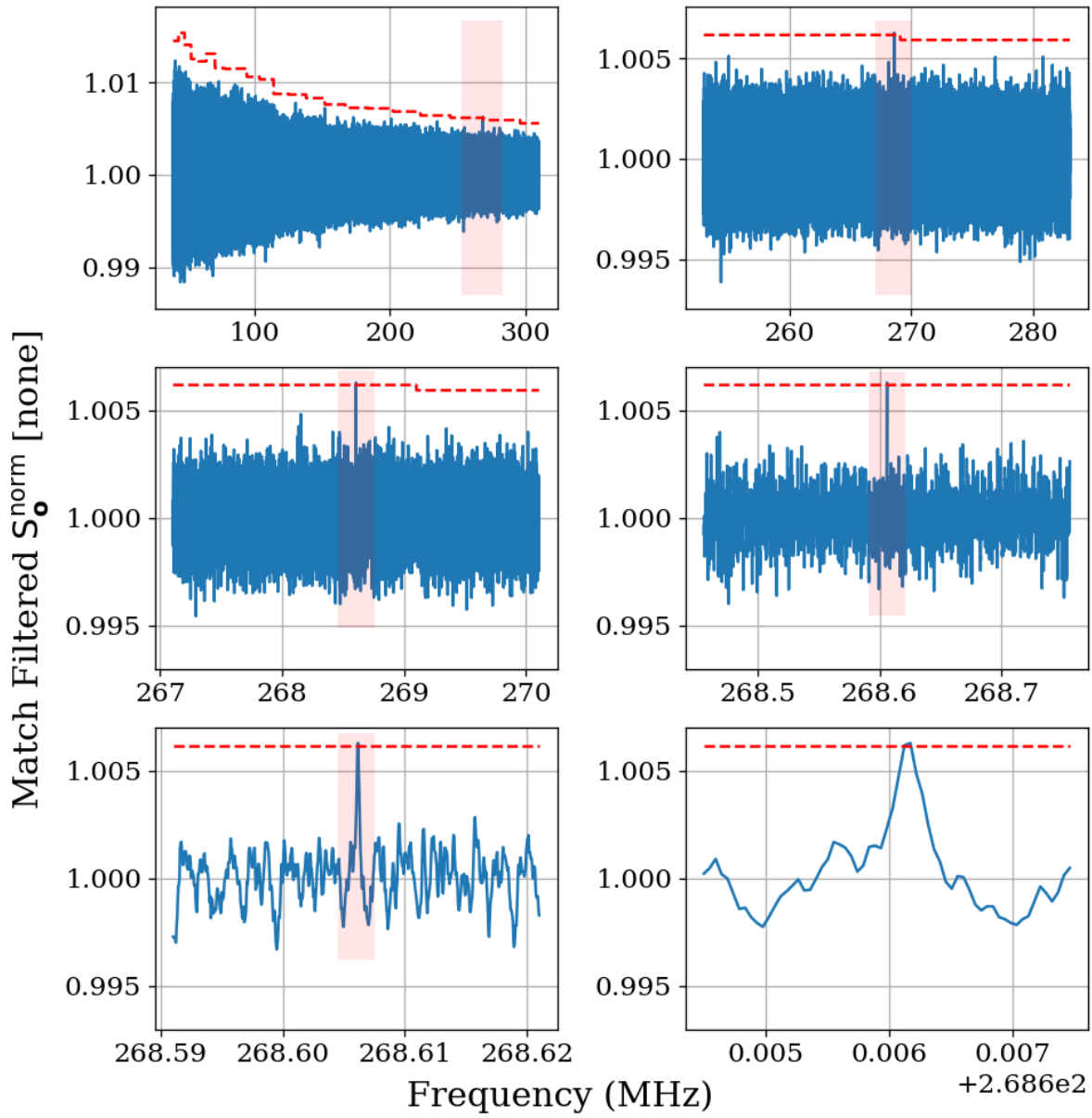


Figure 4.19: Matched filtered, output-referred power spectrum from hardware injection test. Injected signal at 268.60608MHz. Light pink boxes show zoom level on following plot. Red dashed line indicates the 5% significance threshold, derived in Sec. 2.2.1. Introducing the matched filter pushed signal above detectable above threshold compared to Fig. 4.18.

₂₀₇₀ Chapter 5

₂₀₇₁ Results

XXXXXX

₂₀₇₂

XXXXXX

2073 In this chapter, we report a 95%, frequency-dependent, exclusion limit on the kinetic
2074 mixing strength ϵ of the dark photon (Fig. 5.1). We discuss uncertainties in measured data,
2075 the identification of a candidate signal and our process of excluding it. Finally, we display
2076 our results in context by plotting these new limits on top of an aggregation of existing limits
2077 in Fig. 5.2. Future runs of this experiment from 0.3-14 GHz in similar room-temperature
2078 RF enclosures and using 100 K noise temperature LNAs are indicated (the foundation for
2079 such a system is outlined in Sec. 6.2). We have only indicated planned runs, however at
2080 microwave frequencies, highly resonant cryogenic cavities and cryogenic LNAs as well as sub-
2081 THz instrumentation are feasible and could result in an order of magnitude improvement in
2082 the limit over the indicated frequency range and beyond. The design principles of such a
2083 system are outlined in Sec. 6.3.

2084 **5.1 Discussion of uncertainties**

2085 The systematic uncertainty in this experiment comes primarily from three sources, listed in
2086 order of their contribution from greatest to least:

- 2087 1. Fractional uncertainty on the simulated antenna aperture, which is discussed in Sec. 4.3.3,
2088 $\approx 60\%$
- 2089 2. Fractional uncertainty on the first-stage amplifier noise temperature, $\approx 10\%$
- 2090 3. Fractional uncertainty on the gain of the amplifier chain, $\approx 5\%$

2091 The uncertainty on the simulated antenna aperture is significantly larger than the other
2092 two, and so we neglect them in the reported uncertainty on the ϵ limit.

2093 We follow the convention of similar experiments where we fix the value of ρ_{DM} and
2094 solve for an ϵ limit given this value. Therefore, we treat ρ_{DM} as a known constant with no
2095 uncertainty.

2096 **5.2 Exclusion Limit¹**

2097 This section incorporates the exclusion limit on output-referred power (Fig. 4.8) and Eq. 4.10
2098 to report a 95%, frequency-dependent, exclusion limit on the kinetic mixing strength ϵ of
2099 the dark photon. This limit is presented in Fig. 5.1, as well as in context by plotting it with
2100 other, similar experiments in Fig. 5.2.

¹Code for this section can be found at: <https://github.com/josephmlev/darkRadio/tree/master/Computelimit>

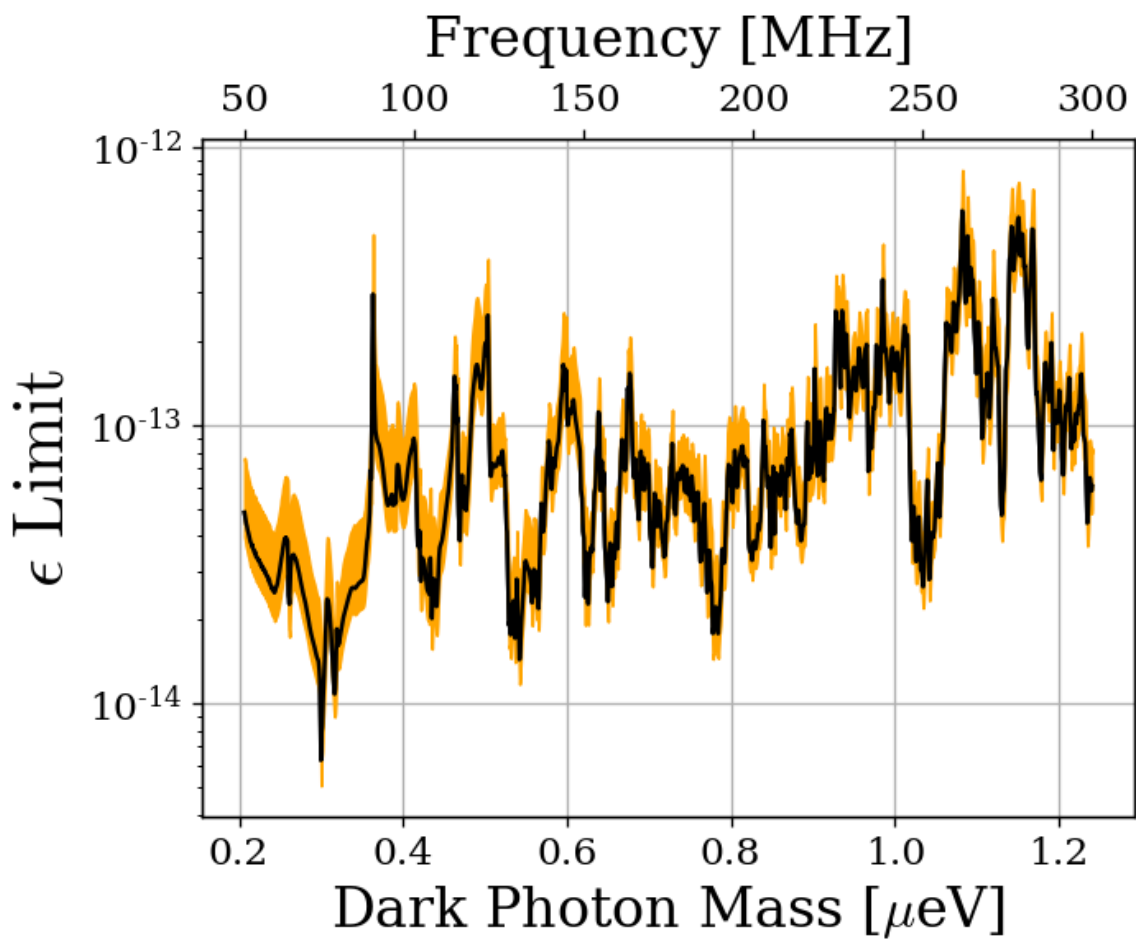


Figure 5.1: 95% exclusion limit on ϵ with uncertainty shown in the orange shaded region. This is based on a local dark matter density of $\rho_{\text{DM}} = 0.45 \text{ GeV/cm}^3$. The error estimate does not take the comparatively small gain and amplifier noise temperature errors into account.

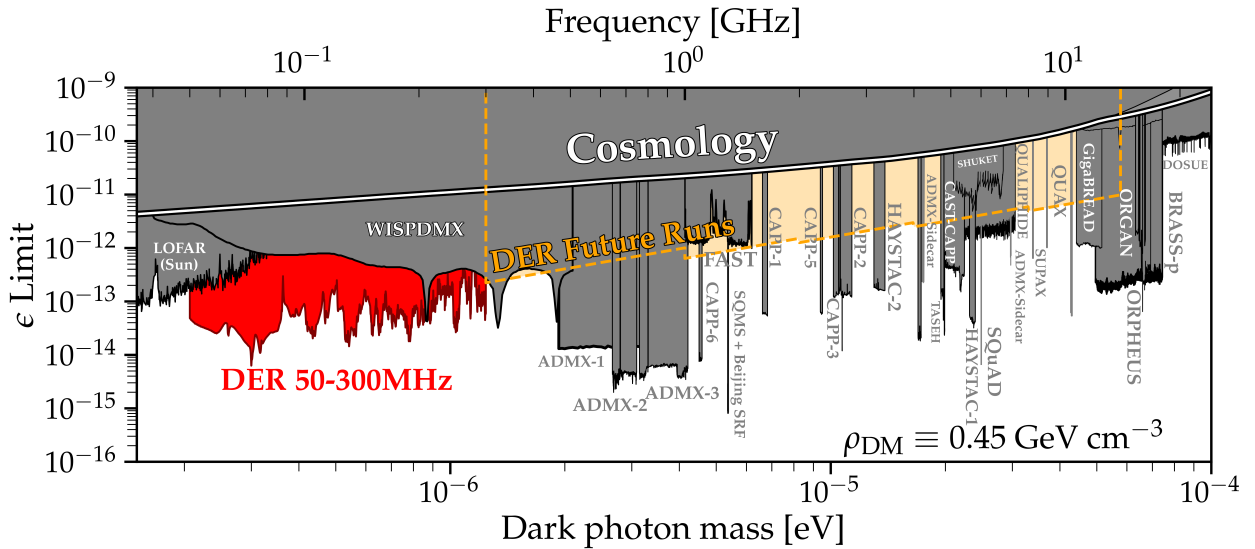


Figure 5.2: Dark photon limits of various experiments circa August 2024, with this work shown in red. The ragged lower bound is due to the complex structure of the resonant modes of the shielded room. Plot adapted by Ben Godfrey from [87] using code found at [88] and includes limit projections of various axion experiments. Astrophysical limits such as CMB interactions with the dark photon are in the region labeled *Cosmology*. Planned wideband extensions of our experiment searching from 0.3-14 GHz in similar room temperature RF enclosures are indicated (*orange*). These planned runs are summarized in Table 6.1.

2101 Chapter 6

2102 Beyond 300 MHz

To infinity and beyond!

2103

Buzz Lightyear

2104 As discussed in previous chapters, there is a wide parameter space available for explo-
2105 ration. This chapter details how the Dark E-Field Radio Experiment is poised to clear out
2106 additional parameter space.

2107 Since the parameter space consists of two variables (namely mass, AKA frequency ν and
2108 kinetic mixing ϵ), the “area” of this space must be considered. The advantage of this exper-
2109 iment is not absolute sensitivity; many experiments are orders of magnitude more sensitive
2110 due to extremely high Q superconducting cavities or lumped-element circuits. Rather, the
2111 advantage lies in the ability to clear out large frequency spans efficiently. The aforemen-
2112 tioned high-Q experiments are only capable of searching a single, narrow frequency span at
2113 a given time and must slowly step through the total required frequency span, waiting for
2114 $\approx Q/\nu$ at each step for the system to ring up. Limitations on tuning require swapping out
2115 hardware, slowing down the process. See, for example, DMRadio m³[89].

2116 The four completed or planned phases are outlined in Table 6.1. These phases are
2117 projected to exclude the orange shaded region shown in Fig. 5.2.

2118 The remainder of this chapter is arranged XXXXXXXXXXXXXXXX

Run Name	Frequency Range	Antenna	LNA	Mixer	Status	Statistical Uniformity	Comments
1A	50-300 MHz	Compower Bicon, 50-300 MHz	Pasternack PE15A-1012	N/A	Complete, published	Below lowest usable frequency.	N/A
1B	300-1000 MHz	RF Space UWB-5 Vivaldi, 0.3-6 GHz	Pasternack PE15A-1012	N/A	Preliminary run complete by moving antenna. 21 candidates detected.	Mode stirrer	50% dead time to allow for 2 GHz sampling rate on Teledyne
2A	1-8 GHz	Small Vivaldi, model TBD	Low noise factory LNC0.3_14B	Miteq TB0440LW1	Waiting on mode stirrer and mixer system commissioning	Use mode stirrer to ensure uniformity	N/A
2B	8-14 GHz	TBD	Low noise factory LNC0.3_14B	Miteq TB0440LW1	Waiting on mode stirrer and mixer system commissioning	Mode stirrer	N/A

Table 6.1: Overview of future runs including hardware (antenna, LNA, mixer), status, how/if statistical uniformity will be ensured, and any comments

2119 **6.1 A first attempt at Run 1B¹**

2120 A preliminary attempt at Run 1B (300-1000 MHz) has been completed. This attempt had
2121 a few issues which are discussed here and will be addressed in the future, but are beyond
2122 the scope of this thesis. In this section, upgrades and data acquisition are discussed. The
2123 projected ϵ limit from this run (along with Runs 2A and 2B) is shown in Yellow in Fig. 5.2,
2124 however this projection is independent of the data shown here.

2125 **6.1.1 Run 1B upgrades**

2126 There are three main upgrades to consider before beginning Run 1B: software upgrades of
2127 the GPU-based spectrum analyzer, modifying the current antenna stand to accept a Vivaldi
2128 antenna, and building a mode stirrer to ensure statistical uniformity. The remainder of this
2129 subsection will detail these upgrades.

2130 **6.1.1.1 Run 1B spectrum analyzer**

2131 The GPU-based spectrum analyzer (Sec. 2.5.7) is capable of sampling at up to 2.5 GHz,
2132 easily allowing for a run up to 1 GHz. However, the PCIe-based ADC has a maximum data
2133 transfer rate of 7GB/s. To accommodate two channels (main experiment and veto), the
2134 system was set up with 50% dead time to allow for data to transfer. The limit on ϵ scales
2135 with the quarter root of time, so this is only a 16% reduction in sensitivity. This is purely a
2136 software upgrade and has been completed

¹Code for this section can be found at: <https://github.com/josephmlev/darkRadio/tree/master/daqAnalysisAndExperiments/run1B/analysis>

2137 **6.1.1.2 Vivaldi antenna stand**

2138 The COMPOWER bicon antenna stand was modified to accommodate the RFSpace UWB-5
2139 Vivaldi antenna. This was completed and pictures of the modifications are shown in Figs. 6.1
2140 and 6.2.



Figure 6.1: Picture of modified COMPOWER antenna stand holding Vivaldi antenna for Run 1B.

2141 **6.1.1.3 Mode stirrer and statistical uniformity**

2142 Run 1A relied on moving the antenna to improve the statistical uniformity (Sec.2.4) but still
2143 required simulation to calibrate it (Sec.4.3.2). Run 1B, however, benefits from its frequency

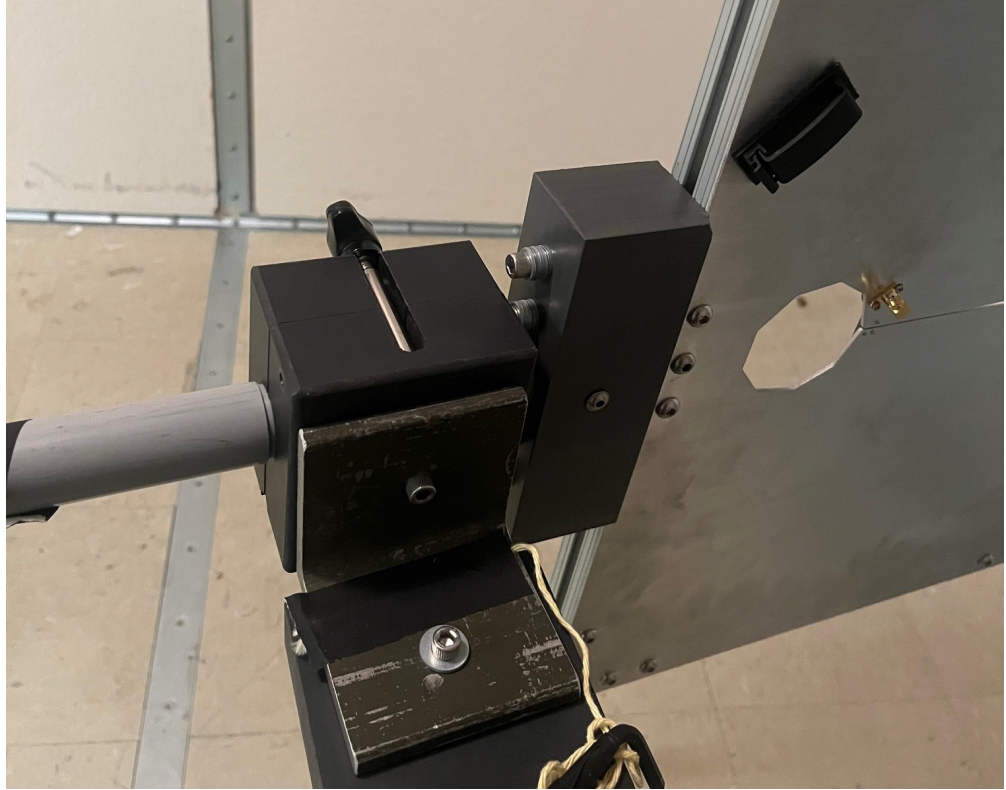


Figure 6.2: Closeup of modified COMPOWER antenna stand holding Vivaldi antenna for Run 1B

2144 range beginning above the lowest usable frequency of the shielded room (~ 200 MHz, see
2145 Sec. 2.34). To take advantage of this, a proper mode stirrer (Sec. 2.4) must be employed. A
2146 lack of mode stirrer is the main limitation of this attempt at Run 1B. At the time of writing,
2147 work is ongoing to construct a mode stirrer. **comment:** Since this is ongoing, I will circle
2148 back and add photos with current progress right before submitting a final draft

2149 **6.1.2 Run 1B data run and analysis**

2150 The first attempt at Run 1B, (Run 1B.1) was taken between September 13 and 22, 2023.
2151 At the time of writing, this has been the only attempt at this run. The raw data are shown
2152 in Fig. 6.3. The normalized standard deviation σ_{norm} (defined in Sec. 4.2.2 from the Dicke
2153 radiometer equation) is predicted to be 0.9885×10^{-3} , and is calculated from the data to be
2154 1.001×10^{-3} .

2155 Processing this data through the detection algorithm (Fig. 4.3) of Run 1A, yields the
2156 normalized, signal-matched-filtered spectrum and 5% significance threshold which are shown
2157 in Fig. 6.4.

2158 Comparison of the spectrum and threshold pictured in Fig. 6.4 reveal 21 candidates².
2159 Furthermore, 13 of these are clustered between 758 and 768 MHz. This frequency span is
2160 reserved for the First Responder Network Authority (FirstNet) and is likely in use locally
2161 by emergency services.

2162 All of these candidates are almost certainly RFI with enough energy (i.e. signal power
2163 integrated over the 9-day run) to overcome the isolation of the shielded room (Fig. 3.13).
2164 These signals are visible in the veto spectrum (Fig. 6.5), but further investigation is required
2165 to conclusively exclude them as dark photons.

2166 Since simulations of this run are extremely difficult to calculate (wavelength at 1GHz <<
2167 room dimensions), it will have to be revisited when statistical uniformity can be established,
2168 i.e. with a mode stirrer. For this reason, further time domain analysis of these candidates is

²There are a total of 60 bins over the threshold, but many bins are adjacent. Combining adjacent bins results in 21 independent candidates

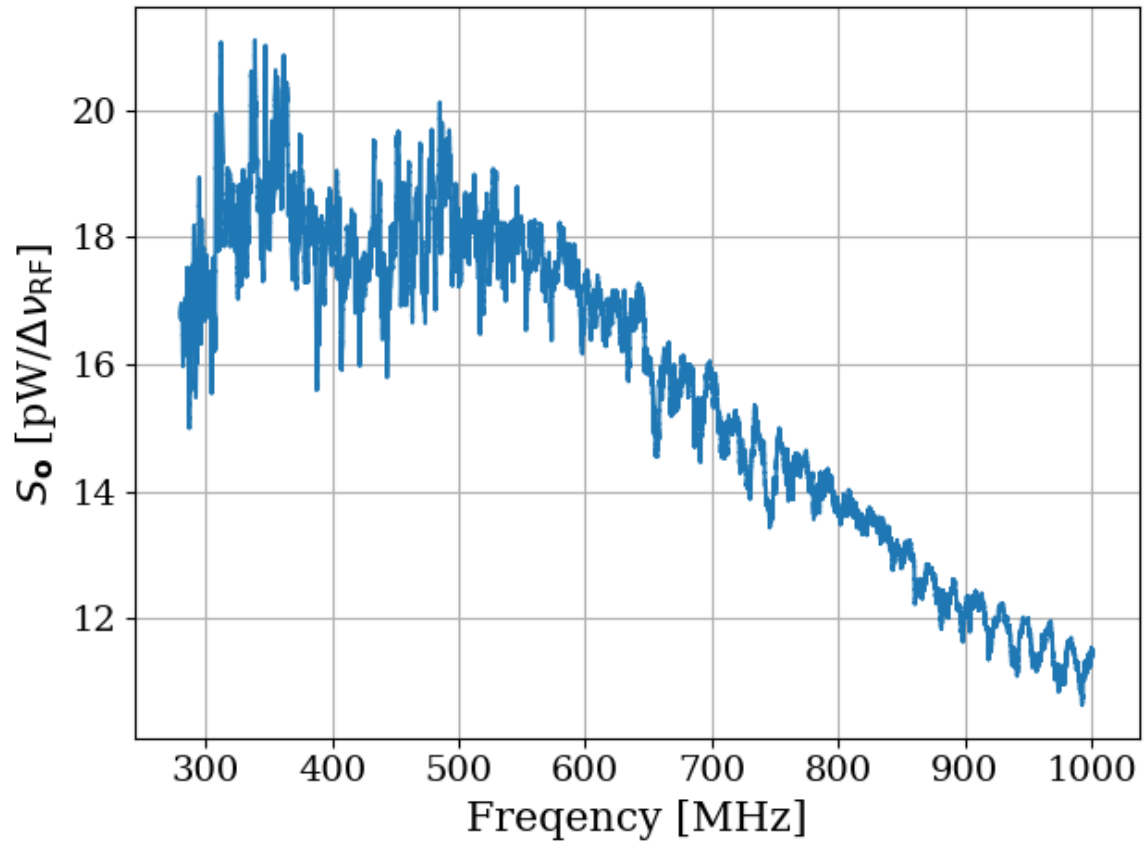


Figure 6.3: Run 1B averaged, output-referred antenna power spectrum S_o . Data were taken over a 9-day period at 9 antenna positions. The narrow variations are mainly due to the effective temperature difference between the room and LNA (Sec. 2.3), though there is a contribution due to amplifier gain and noise temperature variations (Sec. 4.1.1). The variations seen here are not noise; their shape is repeatable for a given antenna position. The noise on this background is not visible at this level of zoom.

2169 not explored here.

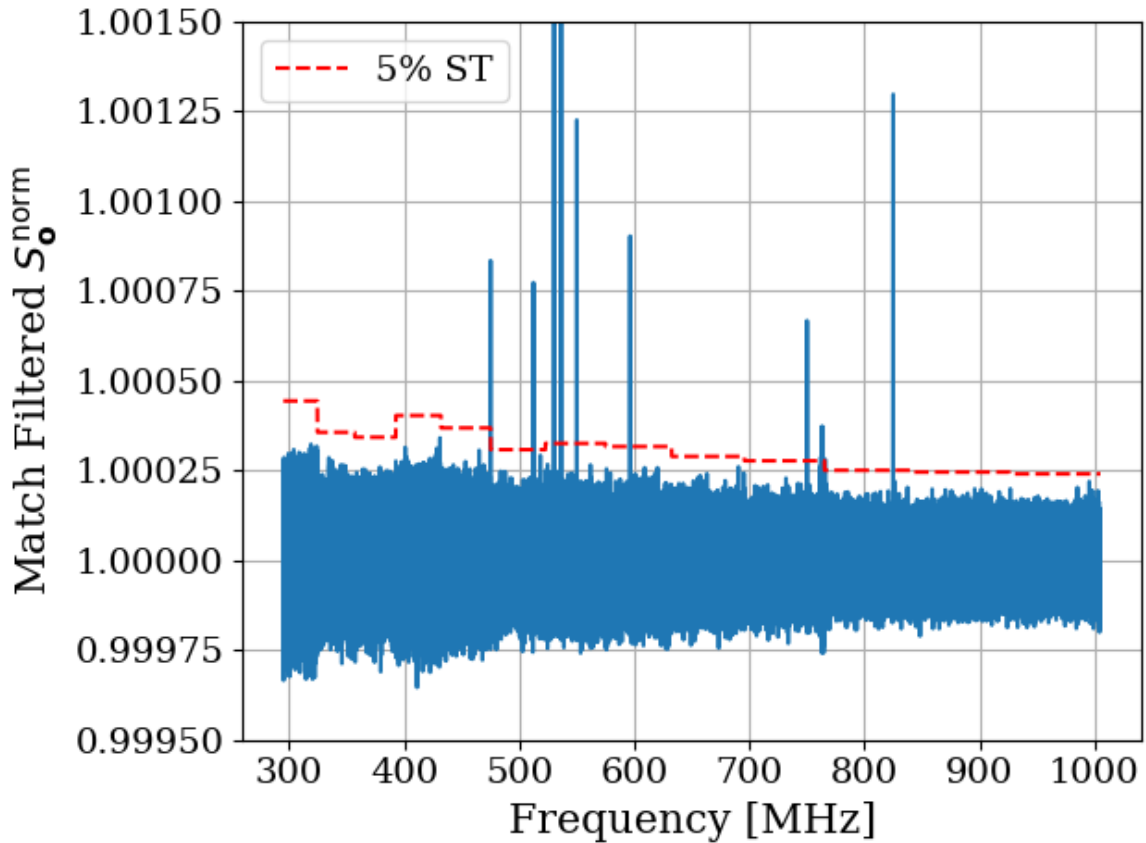


Figure 6.4: Run 1B S_o^{norm} after it has been passed through a matched filter. The template varies in width throughout the frequency span resulting in 13 subspans, each with a constant 5% significance threshold ST (*dashed red*), see Secs. 2.2.1 and 4.2.3. This plot is to Run 1B as Fig. 4.6 was to Run 1A. In contrast to Fig. 4.6, however, the narrow signals are not injected. They are almost certainly RFI with enough power to overcome the isolation of the shielded room (Fig. 3.13). These signals are visible in the veto spectrum, but further investigation is required to conclusively exclude them as dark photons. The vertical scale has been set such that the tops of some of the signals are cut off.

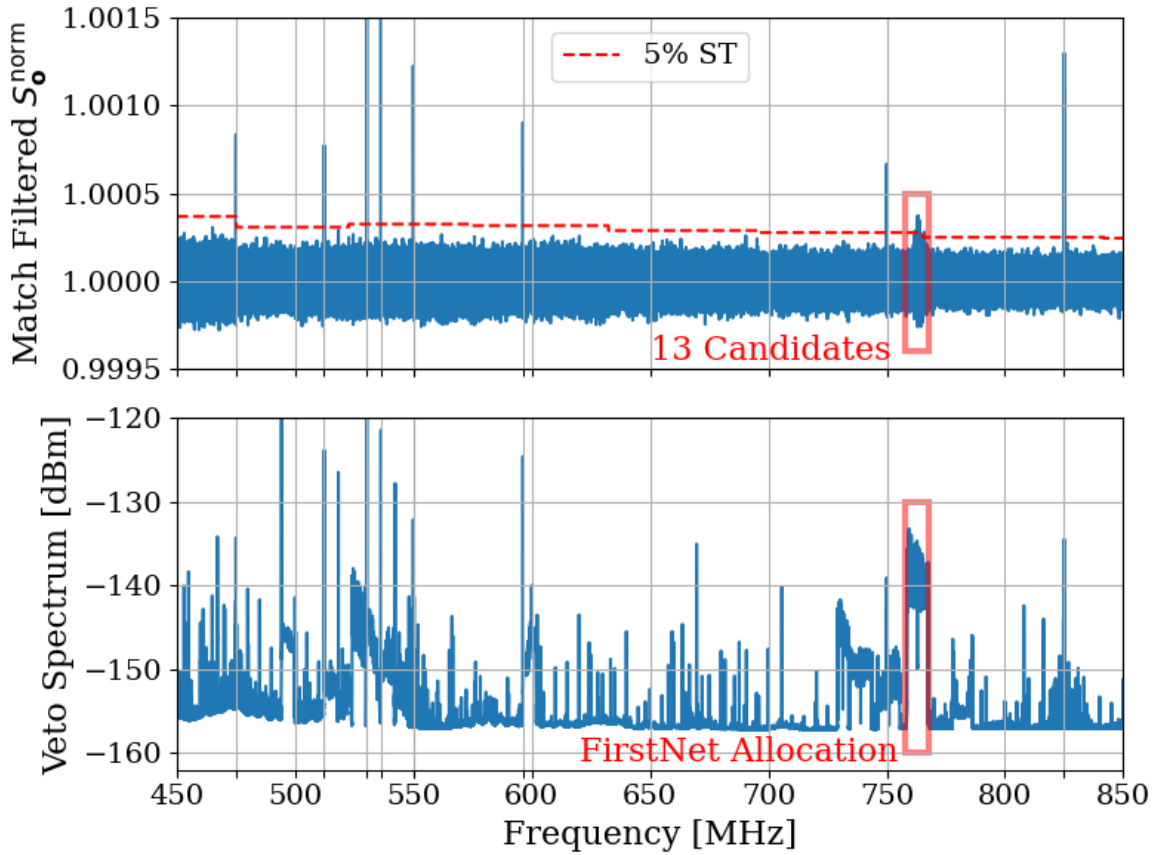


Figure 6.5: 9-day averaged veto spectrum and Run 1B S_0^{norm} after it has been passed through a matched filter. The 5% significance threshold ST (Sects. 2.2.1 and 4.2.3) is shown as a dashed red line. There are 21 independent candidates, however 13 of them are found in the FirstNet frequency span (758–768 MHz) which is discussed in the text of this subsection. This frequency span is shown in both the veto and experimental spectra with a red box. The remaining 8 candidates have ticks added to the x-axis to guide the eye between candidates in the upper panel and RFI in the lower panel. The vertical scale has been set such that the tops of some of the signals are cut off.

2170 6.2 Mixer System: Run 2

2171 Run 1 relied on an ADC with a sample rate of up to 2.5 GHz, allowing for direct RF sampling
2172 of Run 1A/B. This system is a flexible platform, allowing for future upgrades to extend its
2173 maximum frequency through the use of a mixer system which is described in this chapter.

2174 6.2.1 Frequency mixing

2175 Frequency mixing is a technique in RF and microwave systems used to shift the frequency
2176 of a signal to another frequency range which is more useful for a given task. For example,
2177 electronics are simpler to design at kHz frequencies, but antennas operate at MHz. After
2178 processing a kHz signal for transmission, it can be mixed up to MHz for transmission over
2179 the air. Once it is received, it can be mixed back down to kHz. Mixer engineering is a
2180 rather complex topic, and many details will be omitted here. The reader is encouraged to
2181 reference the Marki Microwave mixer primer [90] for a tutorial on mixers and Ch. 13 Pozar's
2182 *Microwave Engineering* [91] for a more thorough treatment.

2183 In a mixer system, an input signal (RF) is combined with another signal, typically from
2184 a local oscillator (LO), such that the two frequencies multiply or "mix", producing an inter-
2185 mediate frequency (IF). In other words, the RF signal $\cos(2\pi f_{\text{signal}}t)$ is multiplied by a local
2186 oscillator signal $\cos(2\pi f_{\text{LO}}t)$ ³. Using the trigonometric identity

³The multiplication of CW signals outlined here is a simplification. In reality, the LO should have higher harmonics and approximate a square wave to overcome the transition region of the voltage-current curve of a real diode. See the Marki Microwave mixer primer for more details [90].

$$\cos(A)\cos(B) = \frac{1}{2}(\cos(A+B) + \cos(A-B)), \quad (6.1)$$

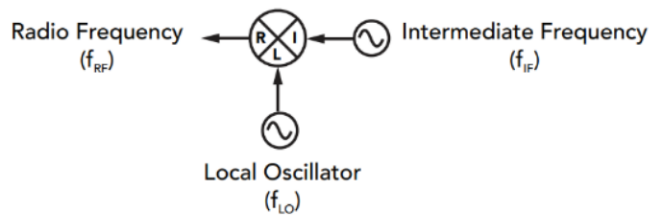
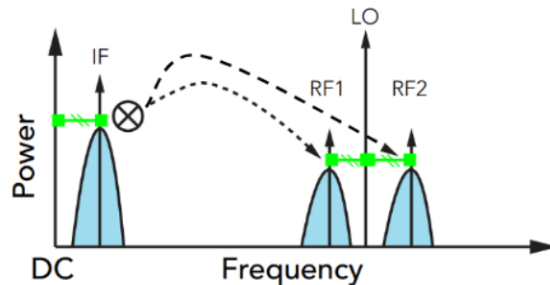
2187 it can be seen that this multiplication produces two new components: one at the sum
2188 frequency $f_{\text{signal}} + f_{\text{LO}}$ and one at the difference frequency $|f_{\text{signal}} - f_{\text{LO}}|$.

2189 A mixer is a 3-port device that has two inputs and one output. The LO port is almost
2190 always an input, while the RF and IF ports can be used as either an input or an output (as
2191 long as they are opposite)⁴. Such a system can be used for upconversion (downconversion),
2192 where the RF is shifted to a higher (lower) frequency, as shown in Fig. 6.6. The remainder
2193 of this subsection will focus on downconversion, but both downconversion and upconversion
2194 are important in the system that is presented later in this section.

⁴Again, this is simplified. All three ports actually behave as a load and a source. See the first footnote of the Marki Microwave mixer primer [90].

UPCONVERSION

$$f_{RF1} = f_{LO} - f_{IF} \quad f_{RF2} = f_{LO} + f_{IF}$$



DOWNCONVERSION

$$f_{IF} = |f_{LO} - f_{RF}|$$

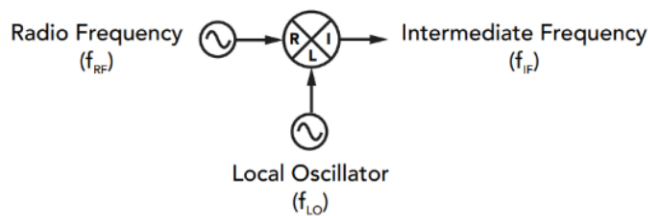
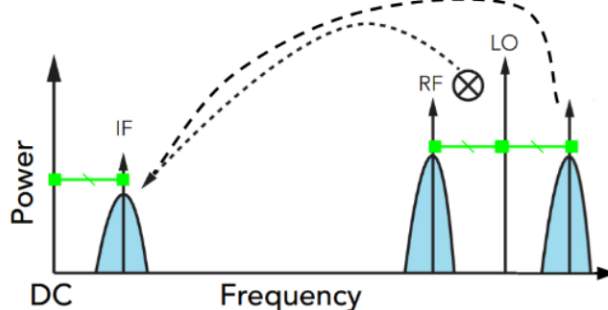


Figure 6.6: Overview of basic mixer operation in both upconversion and downconversion mode. The green lines with hash marks represent the IF frequency. Image modified from Marki Microwave's mixer primer [90].

2195 6.2.1.1 The superheterodyne receiver

2196 The presence of both a sum and difference frequency in Eq. 6.1 creates a challenge when
 2197 employing mixers. A mixer performing downconversion will present both the sum-frequency
 2198 and difference-frequency at its IF port (see Eq. 6.1). Usually, one of these signals will be
 2199 desirable and will not. The latter is known as an image. This situation is shown in frequency
 2200 space in Fig. 6.7.

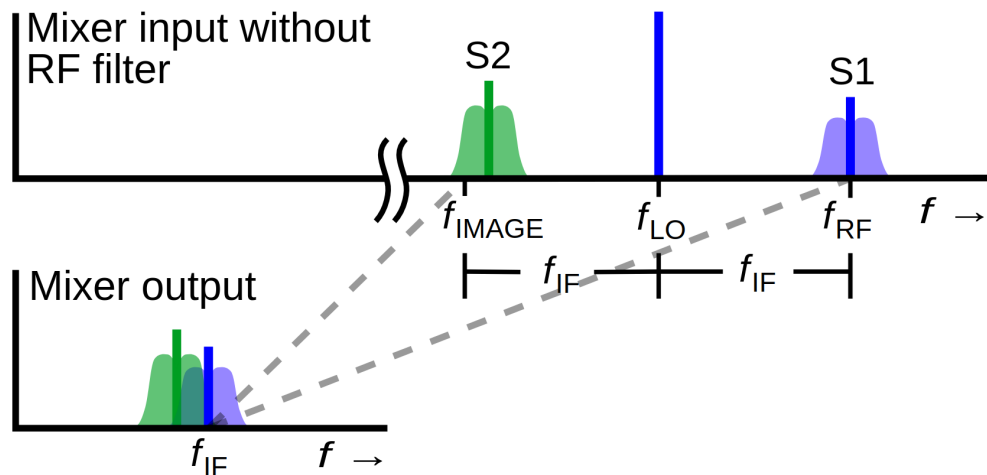


Figure 6.7: Illustration of the problem of images in frequency mixing. Both S1 and S2 are overlapping at the mixer's output as predicted by Eq. 6.1. The image must be filtered before mixing to avoid this problem. Image from Wikipedia[92, 93]

2201 The situation when the signal above the LO is desired and the signal below the LO is the
 2202 image is known as low-side injection downconversion. To rephrase the previous sentence,

Low-Side Injection: $f_{LO} < f_{RF}$ (desired signal is above the LO)

High-Side Injection: $f_{LO} > f_{RF}$ (desired signal is below the LO).

2203 The solution to this image problem is to filter the image out of the RF before mixing.

2204 Furthermore, in a realistic mixer, the LO will bleed through to the IF port and will also

2205 need to be filtered. These points motivate including both an RF and IF filter in the design

2206 of a mixer-based receiver system (sometimes known as a superheterodyne receiver). The

2207 schematic of this type of system is shown in Fig. 6.8. Figure 6.9 shows the result of filtering

2208 the RF and IF in frequency space; the signal S1 is available for further processing at the

2209 desired frequency.

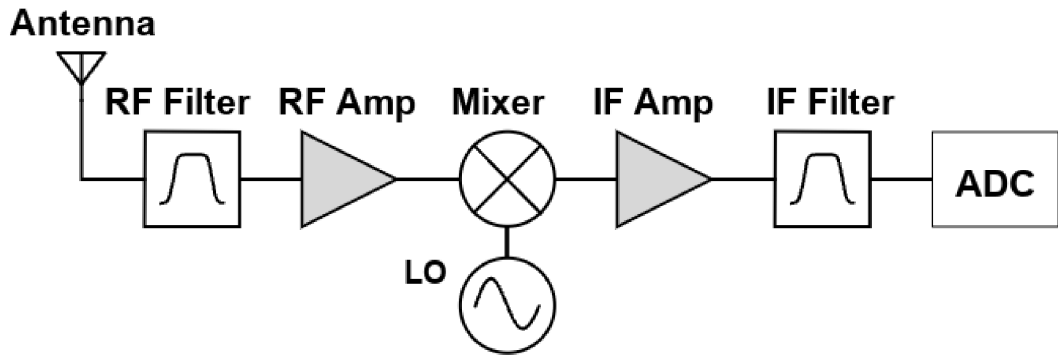


Figure 6.8: Schematic of a basic superheterodyne receiver system. The introduction of the RF filter before the mixer removes the image. The IF filter separates interfering signals that were near S1. This is an example of low-side injection down conversion, as described in the text of this subsection. Image based on one from Wikipedia[92]

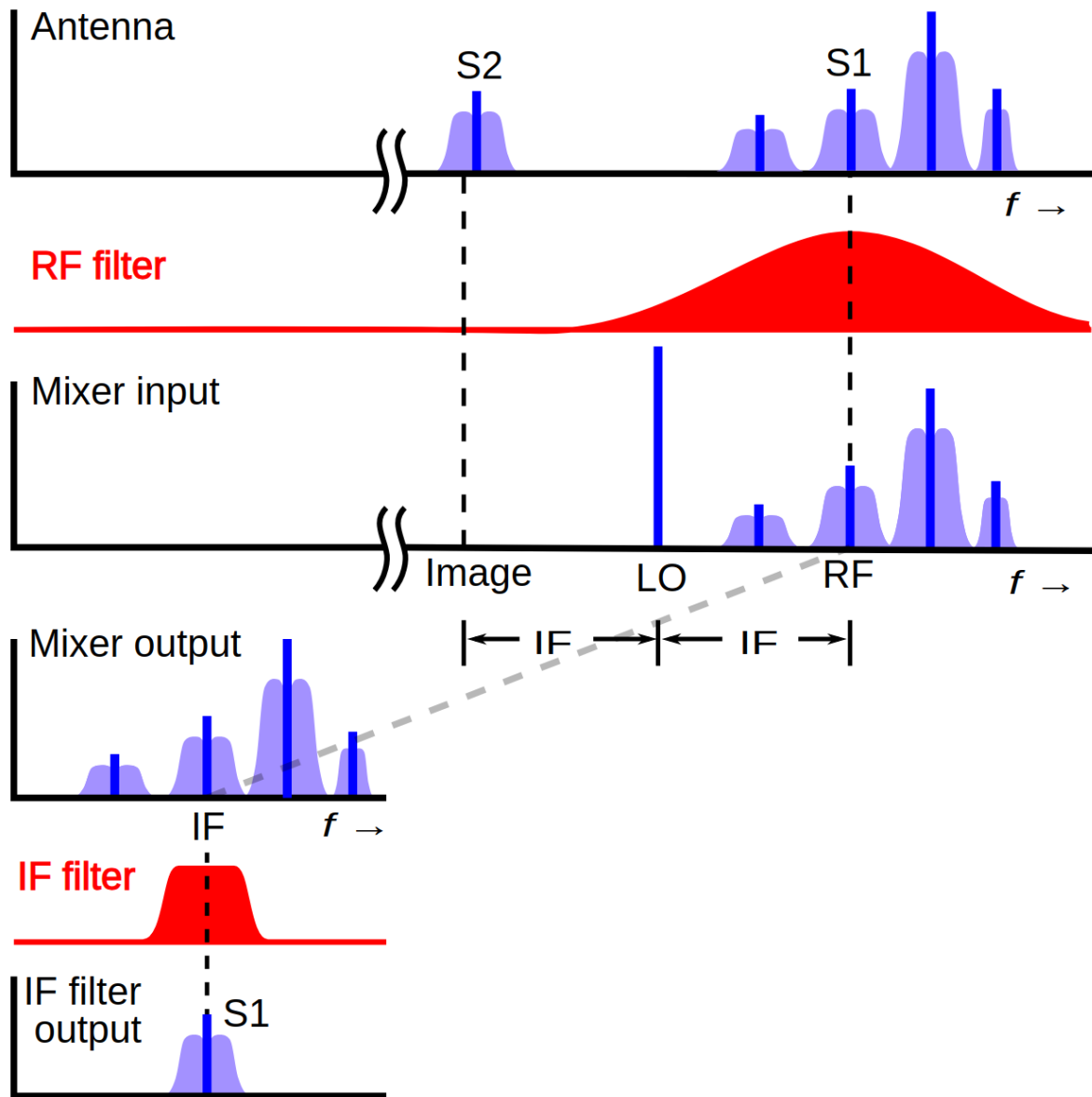


Figure 6.9: Image from Wikipedia[92, 94]

2210 6.2.1.2 Beyond the ideal mixer

2211 This sub-subsection outlines a few issues that were considered in the design of the mixer

2212 system. It is by no means an exhaustive list, but will hopefully provide some guidance into

2213 which specifications are relevant. Again, the Marki mixer primer is an excellent resource
2214 [90].

2215 mixer loss

2216 intermodulation spurs

2217 LO bleed

2218 6.2.2 Design requirements

2219 The maximum sampling rate of the ADC (2.5 GHz) sets a limit as to how high of frequencies
2220 it can directly sample. Introducing a mixer system between the front end of the experiment
2221 (antenna/LNA) and the DAQ (ADC/GPU/PC) allows for previously inaccessible frequencies
2222 to be mixed down into the so-called *baseband* of the ADC, $\lesssim 1$ GHz. The block diagram of
2223 such a system is shown in Fig. 6.10.

2224 The ability to control the mixer system via software greatly boosts efficiency since it
2225 means the experiment can be set up and stepped through a large frequency span (several
2226 GHz) without human intervention. The span of a given step will be limited by the hardware
2227 of the front end, e.g. antenna, LNA. The bandwidth of the baseband (1.25 GHz) sets the
2228 maximum span that may be scanned at each step, though to reduce the data transfer rate,
2229 a smaller span closer to 500 MHz will likely be used for Run 2.

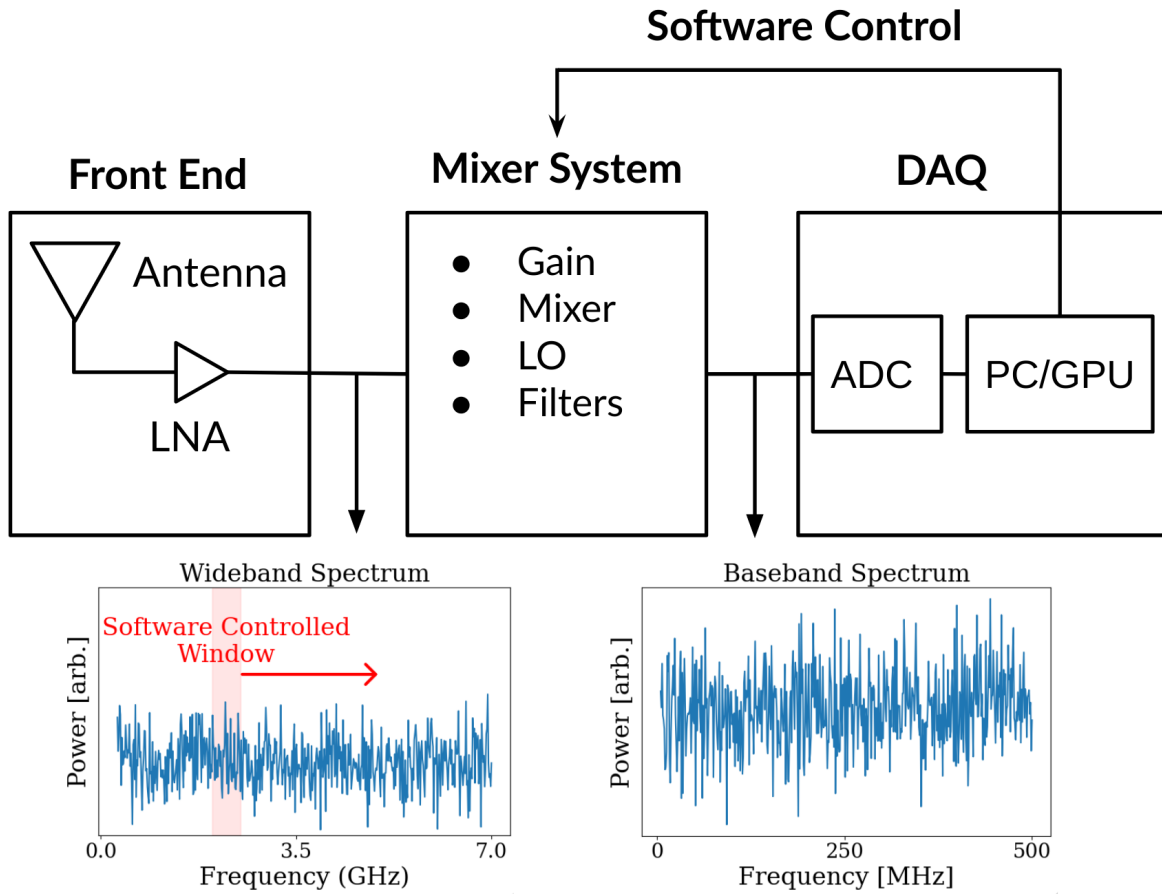


Figure 6.10: Block diagram of the mixer system to be used in Run 2. The PC provides control of the mixer system to sweep the frequency span (shown as a red box on the wideband spectrum) that is mixed down to the baseband and digitized. Frequencies are based on Run 2A, but are nominal and shown only for illustration.

2230 6.2.3 The Dual-conversion superheterodyne receiver ⁵

2231 Allowing wideband (~ 6 GHz) RF into the mixer means the IF will be a sum of two frequency
 2232 bands (see Eq. 6.1 and Fig. 6.7). This could be avoided with the use of an RF filter, however,
 2233 this filter would need to be changed at each ~ 500 MHz span. The requirement that the

⁵Code for this section can be found at: <https://github.com/josephmlev/darkRadio/tree/master/daqAnalysisAndExperiments/mixerSystem/simFreqResponse/simFreqResponse.ipynb>

2234 system be software-controlled is non-trivial in light of the image problem.

2235 One simple solution that was explored is to use a bank of RF filters and a pair of coax
2236 RF switches. This was deemed impractical due to the high cost of a pair of high channel
2237 count switches and the limited frequency span of these switches. A 16-channel switch is
2238 $\sim \$3,000$, and has a maximum frequency of 8 GHz. Additionally, filters would need to be
2239 custom further adding to the cost.

2240 An elegant solution is the dual conversion superheterodyne receiver⁶. In this configura-
2241 tion, the RF band is mixed twice before being output as a final intermediate frequency to be
2242 digitized (IF2). The first mixer (M1) mixes the RF to a fixed IF frequency span (IF1), set
2243 by a fixed IF1 filter⁷. This mixer is controlled by an LO (LO1) with a software-controllable
2244 frequency. LO1 is set such that the desired RF1 frequency will be mixed to IF1. After this,
2245 the rest of the system looks just like the superheterodyne receiver of Sec. 6.2.1.1. The fixed,
2246 band-limited IF1 is simply mixed to IF2, also known as baseband. In this case, $\sim 30\text{-}500$ MHz,
2247 set by the ADC.

2248 A schematic of a dual conversion superheterodyne receiver is shown in Fig. 6.11. Simula-
2249 tions of the system response at various points along the signal path are shown in Figs. 6.12
2250 and 6.13. These simulations do not show the signal after M2 since it is relatively simple after
2251 the first conversion.

⁶Thank you to Greg Wright for suggesting this.

⁷This first mixing stage can be either an upconverter, a downconverter, or even a nonconverter. The only requirement is to mix RF1 such it lands in the span of the IF1 band-pass filter. A useful way to think about the first mixer stage is that it simply moves where the IF1 filter's span lands on RF1.

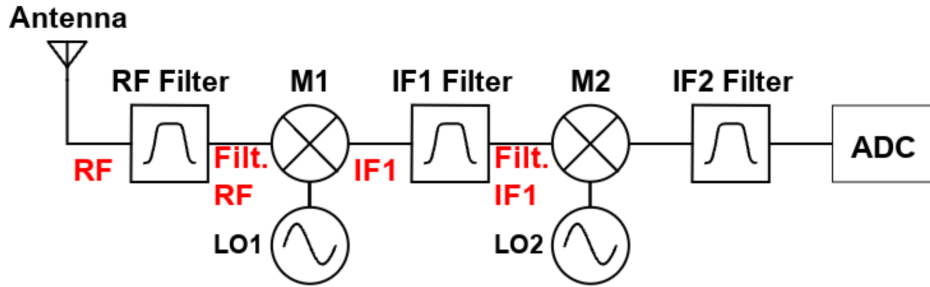


Figure 6.11: Schematic of simplified dual conversion superheterodyne receiver. Text in red indicates the location of each subplot in Fig. 6.12.

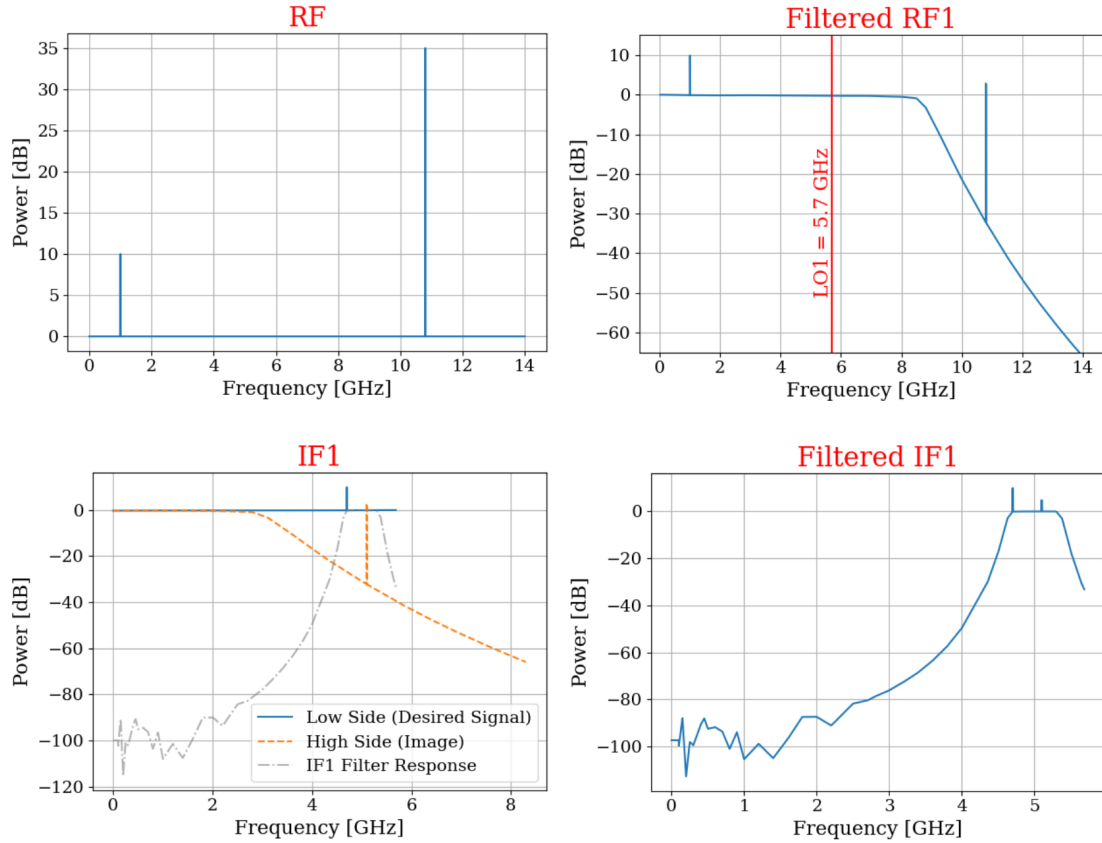


Figure 6.12: Simulated frequency response of dual conversion superheterodyne receiver. The input RF is the mean of broadband noise, plus two coherent signals at 1 and 10.8 GHz. All of these components have been normalized to the mean of the noise. Each panel shows the spectrum at the points indicated in red text along Fig. 6.11. LO1 is set to 5.7 GHz, the lowest setting that will be used in Run 2A. The RF and IF filter response functions are taken from manufacturer data sheets from the filters in the system described in Sec. 6.2.3.1. Note the for

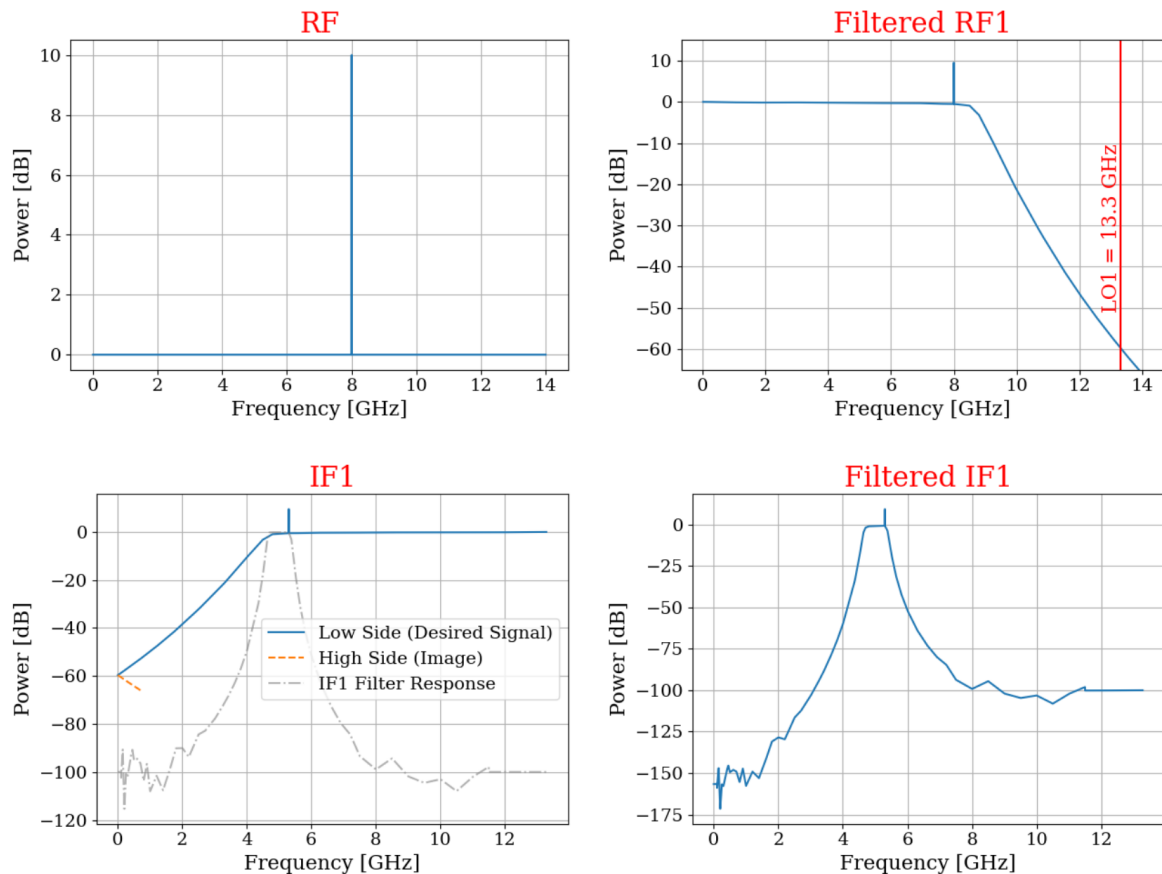


Figure 6.13: XXXX

2252 6.2.3.1 Run 2A mixer system design



Figure 6.14: Schematic of Run 2A dual conversion superheterodyne receiver.

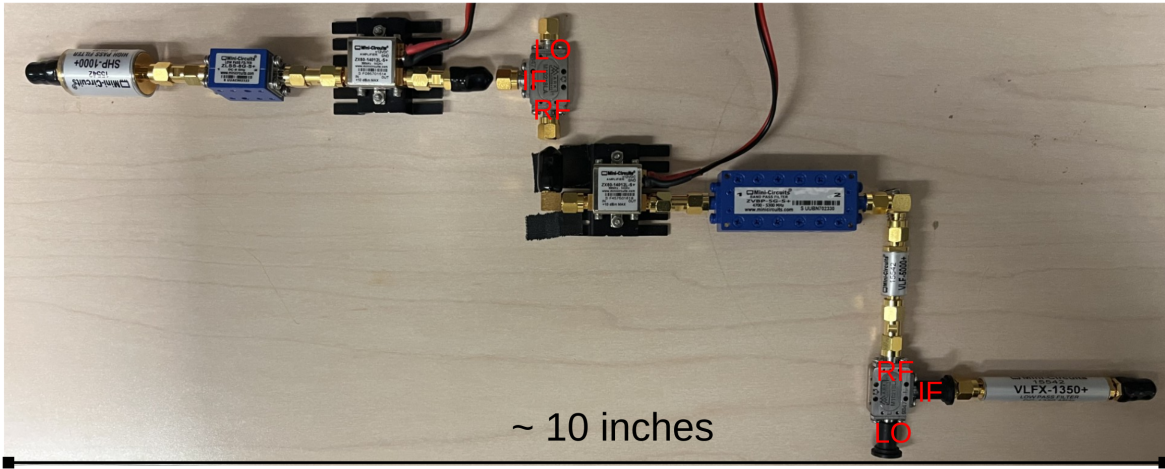


Figure 6.15: Picture of the (partially assembled) dual-conversion mixer system. Mixer 1 is a Miteq TB0440LW1, but is on loan from Paul Stucky in the UCD Chemistry department, so an extra Marki M1-0218LP is used as a placeholder. Note that Mixer 1 is connected “backwards”; the RF goes into the IF port and the IF emerges from the RF port. This configuration allows for the Miteq mixer to accept frequencies as low as 500 MHz for the first conversion step. **comment: retake, 2 amps are missing**

2253 6.2.3.2 Additional considerations

2254 This sub-subsection lists a few design points considered during the design phase of the mixer
 2255 system. Hopefully it clarifies some design choices.

2256 The Marki mixer primer [90] raises the point that the RF port of a real mixer will source
 2257 a $2L \times 1R$ image spur. If this spur is out of the pass band of the RF filter, it will reflect off
 2258 the filer, mix with the LO and downconvert to the desired difference frequency. To mitigate
 2259 this, amplifiers were placed on either side of both mixers. This spur was not measured.

2260 When dealing with wideband noise, the total power in a given bandwidth must be con-
 2261 sidered to prevent clipping at each stage of a signal chain (see Sec. 2.5.4.4). On the other
 2262 hand, the finite LO-IF isolation of M1 means that a healthy signal level is required to keep

2263 the signal-to-noise ratio high.⁸ This motivates adding gain throughout the system.⁹ The
2264 amount of required gain changes drastically when going through the IF1 filter since the
2265 bandwidth is reduced from $\sim 7\text{ GHz}$ to $\sim 0.6\text{ GHz}$. Assuming a flat power spectral den-
2266 sity, this requires $10\log_{10}(7\text{ GHz}/0.6\text{ GHz}) \sim 10.7\text{ dB}$ of make-up gain to achieve the same
2267 total-integrated power as before the filter.

2268 There is a secondary low-pass filter in the IF1 filer section. This can likely be omitted.
2269 It is only there because the IF1 band-pass filter is not rated above 12GHz and testing it
2270 requires borrowed gear.

2271 **6.3 Possible Future Upgrades**

2272 The previous sections in this chapter addressed the progress towards the planned Run 1B
2273 (Sec. 6.1) and Runs 2A/B (Sec. 6.2). This section gives an outline for experiments beyond
2274 this. This section will be rather vague compared to the previous sections of this chapter. If
2275 those sections were a road map, this section is verbal instructions providing general direc-
2276 tions.

⁸If we are being literal, we actually want a high noise-to-signal ratio. The experiment gives noise (which may contain a small, burred signal), and the coherent LO is contaminating this noise. One man's noise is another's signal.

⁹In practice, gain comes quantized in 12 dB amplifiers, so attenuators may be needed to get precisely the correct amount.

2277 **6.3.1 Detector design principles to maximize the signal-to-noise
2278 ratio**

2279 Chapter 2 began with a quote by Veljko Radeka [19] that claimed an optimal detector must
2280 have three components:

- 2281 1. The detector design must maximize the signal
2282 2. Noise must be reduced at its physical source
2283 3. The signal and noise must be optimally filtered.

2284 The common thread is the improvement of the signal-to-noise ratio. The considerations
2285 are as true today as they were in 1974.

2286 **6.3.1.1 Maximize the signal**

2287 There are a few ways to ensure that the signal emerging from the detector is maximized. The
2288 traditional approach has been to use a highly resonant cavity. See, for example ADMX [21],
2289 HAYSTAC [47]. To push to lower masses with wavelengths larger than practical cavities,
2290 lumped element detectors use electronic resonant circuits in place of resonant cavities to
2291 achieve a similar effect. See DMRadio [22, 89, 95] and ABRACADABRA [96].

2292 While these experiments have very high Q, they are only sensitive at a single frequency
2293 which must be scanned. The dark E-field radio (DER) technique differs in that it is broad-
2294 band; many frequencies are scanned simultaneously by taking a Fourier transform. At higher

2295 mass, a smaller reverb chamber can be employed, as long as the frequency of interest remains
2296 above the lowest usable frequency (defined in Sec. 2.4.2).

2297 A careful analysis of scan rates to reach a given sensitivity of ϵ for the DER technique
2298 compared to single-resonance experiments should be performed before attempting to over-
2299 come the difficulties of a DER-like experiment above ~ 20 GHz.

2300 **6.3.1.2 Reduce noise**

2301 The DER experiment operates at room temperature, using a low noise amplifier (LNA).
2302 Compared to cryogenic experiments, this represents an advantage in terms of reduced ex-
2303 perimental complexity, but it means the dominant background is classical thermal noise
2304 (~ 300 K, Sec. 2.1.1), followed closely by amplifier noise (~ 100 K, Sec. 2.1.4). These noises
2305 add to form the total system temperature $T_s \approx 400$ K. However, the limit in sensitivity scales
2306 with $T_s^{-1/2}$ (at least in the classical regime, $h\nu \ll k_b T$). For this reason, most haloscope
2307 experiments choose to forgo experimental simplicity and operate at extremely cold temper-
2308 atures (100s of mK, sometimes lower). At these temperatures, quantum effects begin to
2309 dominate the noise budget and simple linear amplifiers must be replaced by read-out tech-
2310 nologies such as superconducting quantum interference devices (SQUIDs) or single photon
2311 counting.

2312 **6.3.1.3 Filtering**

2313 Section 4.2.3 introduced signal-matched filtering as the optimal filtering for a dark photon
2314 of known lineshape, discussed in Sec. 2.1.2. This will be an important consideration going

2315 forward, but will not change much.

2316 However, there is an additional filter that has the potential to improve the sensitivity
2317 of Run 1A as well as any future runs. Assuming that the dark photons are uniformly
2318 polarized, the power received by a linearly polarized antenna will be modulated by the
2319 rotation of the earth. The time series of each frequency bin can be searched for modulation
2320 by $\alpha \cos^2(12\text{hr} \times t)$, where α is a dimensionless parameter that depends on the geometry
2321 of the antenna relative to the rotation of the earth. Many useful ideas for this calculation
2322 are presented in [87], however, the idea in this paper is simply to set up the experiment to
2323 maximize the signal, not search for modulations on existing data. As far as I know, this
2324 analysis idea was independently arrived at by both myself and Brian Kolner (a co-author
2325 on[39]).

2326 **6.3.2 Leveraging Axion experiments for Dark Photon searches**

2327 Axions (introduced in Sec. 1.3.1.1), are an ultra-light dark matter candidate similar to dark
2328 photons. They require a magnetic field to convert into standard photons, but they are
2329 detected using techniques very similar to dark photons. Axion experiments represent a sig-
2330 nificant investment of resources and frequently do not take full advantage of their sensitivity
2331 to dark photons. This subsection lists a few methods that can leverage this investment to
2332 probe the dark photon parameter space.

2333 **6.3.2.1 Reanalysis of Axion data**

2334 A highly efficient dark photon search can be conducted by recognizing that many axion
2335 searches would have been sensitive to dark photons if not for vetos which rely on the state of
2336 an applied magnetic field. SHAFT[97], for example, has two toroids that can generate fields
2337 in opposite directions¹⁰. While the magnetic flux through the pick-up coil from an axion
2338 would flip polarity as the magnetic fields are reversed, the flux from a dark photon would not
2339 (see Fig. 1 of [97]). This differential technique gives a convenient way to veto radio frequency
2340 interference. However, careful inspection of the time dependence of candidates may allow
2341 these signals to be reduced without relying on the magnetic field veto and ruling out dark
2342 photons¹¹.

2343 An attempt to perform this analysis was performed in 2021 [98], but was limited by the

2344 **6.3.2.2 Design and operation of Axion experiments with Dark Photons in**

2345 **mind**

2346 By recognizing that an axion experiment is almost a dark photon experiment, the experiment
2347 can be designed from the beginning to maximize its sensitivity to dark photons. The main
2348 modification is to not veto based on the state of the magnetic field, as pointed out in
2349 Sec. 6.3.2.1. This comes with the caveat that interfering signals must be mitigated, likely
2350 harder than it sounds. One possible solution is to simply conduct the experiment in a

¹⁰Actually, the field directions flip to all four possible combinations and they have a clever analysis chain to maximize sensitivity.

¹¹This is just an example, as DMRadio will not rely on a veto and have much better sensitivity to dark photons in the SHAFT frequency range.

2351 shielded room, similar to the Dark E-Field Radio Experiment.

2352 Appendix A

2353 Overview of RTSA code base

2354 A basic overview of the code which are used to acquire and process data are outlined here.

2355 The version control is very simple and each experiment has it's own directory containing

2356 several key files. The general usage template from which other experiments can be developed

2357 is in the `teledyneTemplate` directory. The important files, in order of importance, are

2358 • `settings.py`: Settings are controlled from this file. If the DAQ code isn't to be

2359 modified, this is all the user must interact with in normal usage. While it is a python

2360 script, it functions more like a text file. Descriptions and notes about allowed values

2361 are included as comments. Read them carefully, settings can conflict.

2362 • `drDaq*.py`: Main script which calls all the helper functions. To take data, run this

2363 script after modifying (and saving) `settings.py`. There is usually a suffix indicating

2364 the date and information about version.

2365 • `avgFftModule.py`: This is modified code from teledyne. It handles all the heavy

2366 lifting: Interfacing with the C++ API, pinning GPU memory, transfer of data from
2367 PCIE card to the GPU, computation of the FFT on the GPU. This is all wrapped in
2368 a class called `avgFft`. An instance of this class is called `avgSpec` and is the workhorse
2369 of `drDaq.py`

2370 • `daqHelpers.py`: Lots of helper functions which are separated here to keep other code
2371 clean. It is imported as a module in other files. Lots of useful code lives in here,
2372 including the code that converts time series to power spectra (normalization is non-
2373 trivial, see Eq. 2.15), writes info to `database.txt`, saves the pre-averaged spectra
2374 including metadata in an HDF5 file.

2375 • `plotTesting.py`: This uses `dash` to host a web app which allows interactive `plotly`
2376 graphs for simple visualisation of run data. This is extremely useful as it can tell you
2377 if amplifiers die. Without this, all data would have to be averaged and more fully
2378 analyzed, but this is a good light-weight option. There is some creative use of data
2379 down sampling so it runs quickly while not removing any candidates. An example
2380 window is shown in Fig. A.1.

2381 • `backup.sh`: Simple shell script which backs up run data to locations of your choosing.
2382 In the `teledyneTemplate` directory, it is set up to back up to the secondary hard disk
2383 drive in the DR2 machine, and to peloton, but this can be easily modified. When taking
2384 real data, this script should not be run at the same time as `drDaq.py`. `backup.sh`
2385 should be run first, so it completes while the antenna is moved and batteries changed.
2386 This ensures there is not a heavy load on the hard drive due to back ups while data

2387 acquisition is ongoing. `valonInit.py`: sets up the valon signal generator to work as a
2388 clock. This should probably be a function inside of `daqHelpers.py`, but there may have
2389 been a reason I kept it separate.

2390 • `gdrapi.py` Comes from Teledyne. Defines functions for the api. I have not modified
2391 it at all.

2392 • `helperCupy.py` Comes from Teledyne. Defines functions for the GPU. I have not
2393 modified it at all.

2394 • `streamingHelpers.py` comes from Teledyne. Defines functions for streaming from
2395 PCIE card to GPU. I have not modified it at all.

2396 A Tips for using the RTSA system

2397 • As of September 2024, you must boot into kernel version 5.15.

2398 • Make sure to run `insmod.sh` in the `teledyneInstall/gdrcopy` directory after restart-
2399 ing the machine.

2400 – look at `teledyneInstall/installGuide.txt` on how to handle common errors
2401 involving this process.

2402 • Read through the `settings.txt` file carefully! Some settings will conflict with others,
2403 but they are mostly noted. There are also some notes about possible upgrades which
2404 could be made, some of which without much effort.

2405 **B Data structure and processing**

2406 Figure 2.45 shows the handling of data as it comes in as an RF time series and is converted
2407 to pre-averaged spectra. While significantly less cumbersome than the raw data, processing
2408 these spectra still represents a challenge. This subsection outlines how I have attempted to
2409 handle it. While it is a little convoluted, this is the third iteration of how to handle this
2410 data processing and is likely simpler than it seems on first blush. In other words, there is
2411 probably a better way to do this, but don't knock it til you try it.

2412 **B.1 Writing data**

2413 Once a pre-averaged spectrum is computed by dividing the running sum by `NOF_BUFFERS_TO_RECEIVE`,
2414 this can be written to an HDF5 file. Whether or not it is, can be controlled by the `SAVE_H5`
2415 boolean variable¹. Each pre-averaged spectrum is uniquely specified by `ACQ_NUM` in a given
2416 data run. In order to simplify backups and avoid placing all our eggs in one HDF5 basket,
2417 `NUM_SPEC_PER_FILE`² pre-averaged spectra are saved into a single HDF5 file, before starting
2418 a new file. These files are simply named as a zero-indexed number followed by their `.hdf5`
2419 extension. These files are saved in `SAVE_DIRECTORY`³. I usually make this save directory in
2420 a secondary SSD named `drBiggerBoy` in order to preserve the main drive. I think the stress

¹This variable exists because when testing things or taking miscellaneous measurements, you will frequently want to acquire a single spectrum without engaging the complex machinery of the HDF5 saving procedure.

²I have kept this around 16 and not experimented much outside of this range, but it's probably fine. This keeps the files around 1 GB. For run 1.4, this is about 45 minutes of antenna data and 3 minutes of terminator data per file, so if a file is corrupted it's not a big deal. I have never had a problem, this is paranoia inherited from Ben.

³A reminder that this is specified, like all other variables, in `settings.py`. Note you must create this directory ahead of time and include a sub-directory called `data`. It says this in the comments of `settings.py` which you are reading, right?

2421 of continuous reads and writes will probably kill this drive, so I prefer to keep it separate
2422 from the main boot drive, drBigBoy.

2423 When `SAVE_H5 == 1`, a `database.txt` file is created in `SAVE_DIRECTORY`, shown in Table
2424 A.1.

Attribute	Pre-averaged spectrum 0	Pre-averaged spectrum 1
ACQ_NUM	0	1
DATETIME	2023-05-10 11:32:48.365	2023-05-10 11:35:49.193
SWITCH POS	0	1
ANT POS IDX	0	0
TEMP	295.64	295.54
LEN FFT LOG2	24	24
SAMPLE RATE MHZ	800.0	800.0
NOF BUFFERS	8600	8600
AMP1	1012_E_PbAcid	1012_E_PbAcid
AMP2	ZKL_9p05VReg	ZKL_9p05VReg
LPF	HSP50+	HSP50+
HPF	288S+	288S+
ATTENUATOR	4dB_FIXED	4dB_FIXED
ADC	ADQ32	ADQ32
CLOCK	SRS_VIA_VALON	SRS_VIA_VALON
File Number	0	0

Table A.1: Example database file from run 1.4. In this run, `ACQ_NUM` counts up to 4175, and these spectra are saved between 261 HDF5 files. Some of the values are auto-generated (`temp`, `DATETIME`, etc.) while others are manually entered into `settings.txt` (`AMP1`, `LPF`, etc.) Note that this table has been transposed in order to fit on the page.

2425 When setting up a data run, you must test that the data are saved how you expect. I have
2426 had success by reducing `NOF_BUFFERS_TO_RECEIVE` to a small number⁴, and taking a simu-
2427 lated data run. The process of switching is hacked together and can give you unpredictable

⁴`NOF_BUFFERS_TO_RECEIVE` times the time per buffer must be larger than around 2 seconds or it will crash

2428 results. Did I mention to read the comments in `settings.py`?

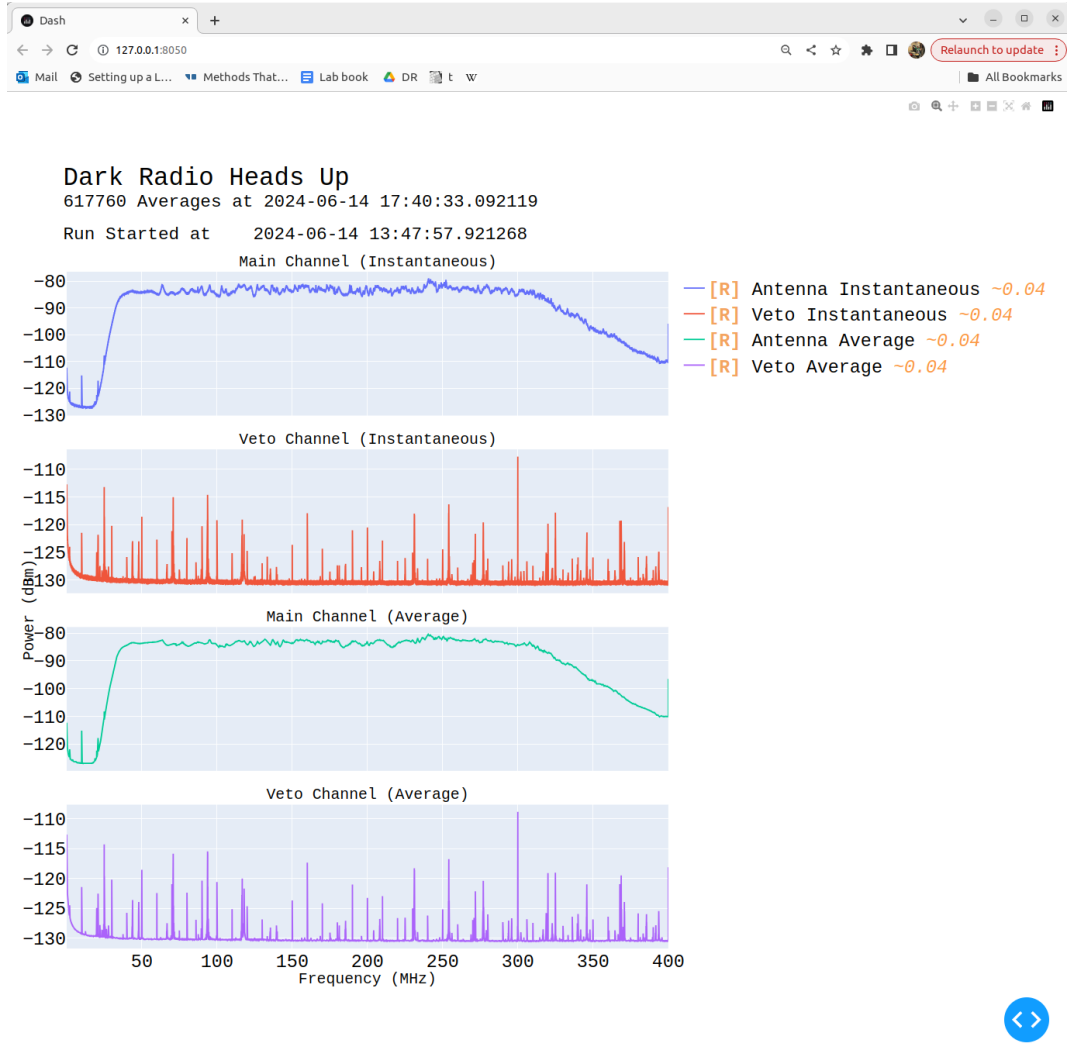


Figure A.1: Real time heads up window for data acquisition. Built with Plotly and Dash, and displays in web browser, in this case Google Chrome. Spectra contain 2^{23} frequency bins, so are down-sampled so as to display 10^4 bins at any given level of zoom. This allows for interaction with the plot in real time with very little lag. The resolution currently displayed (in MHz) is shown in yellow next to the legend (right of first plot). This down-sampling is "smart" in that it will show any excursions, and is implemented with the `plotlyResampler` package in `MinMaxAggregator` mode. Mousing over a curve causes a "Tooltip" to appear, indicating the frequency and power at that point in the curve. The frequency axes are all linked, so zooming on one plot will cause all plots to display the same frequency range. Icons on upper right allow for navigation of plot. Frustratingly there is no back button, so be careful when zooming on a very narrow feature; a wrong move means you have to go all the way back out and start over.

2429 **B.2 Reading and averaging data**⁵

2430 After taking a data run, you should have a `SAVE_DIRECTORY` containing a directory full of
2431 many HDF5 files and a `database.txt` file (and possibly a directory of plotting spectra if
2432 that is chosen in `settings.txt`. The basic idea is to “pre-process” the HDF5 files into a
2433 single, large HDF5 file which can be more quickly accessed to compute a single, averaged
2434 S_o spectrum for further analysis (see next chapter). The `database.txt` file is loaded into
2435 python as a pandas dataframe in order to find specific spectra in this large data structure.

2436 I tried (for a while) to keep the files separate to allow for multi-processing to speed up
2437 the averaging, but I ran into issues. The most serious issue is that all the files live on the
2438 same drive, so you can’t get much of a speed up since the drive is read-limited to around
2439 500 MB/s. I found multiprocessing is more effort than it’s worth. It takes about 20 minutes
2440 to pre-average run 1.4 (9 days of data, 3 minute pre-averages yields 4175 spectra which take
2441 about 280 GB), and you only have to do this once after a run.

2442 Following the example of `run1p4_packAvgAllAnalysis.ipynb`, the first step is to load
2443 `database.txt` as a pandas dataframe which can be used to index the pre-processed file.
2444 Next, a list of which `ACQ_NUMs` correspond to an antenna and terminator must be computed,
2445 after removing any which are known to be contaminated⁶. The list of indices which are
2446 to be averaged together is called either `antIdx` or `termIdx`. Note that you can devise any
2447 number of ways to generate these lists, or even hard code them. The code given is just an

⁵Code for this section can be found at: https://github.com/josephmlev/darkRadio/tree/master/daqAnalysisAndExperiments/run1p4/run1p4_analysis/run1p4_packAvgAllAnalysis.ipynb

⁶In run 1.4, the first antenna and terminator spectra are thrown out, since the computer monitor was on to verify the run started successfully. This was out of paranoia and probably didn’t do anything.

2448 example.

2449 Next, info in the dataframe (no power spectra data yet) are analyzed as a sanity check.

2450 These are not super important but a good check.

2451 The cell beginning with the comment `#pack pre proc dataset` is where the heavy lifting
2452 happens. A large HDF5 file is initialized. It contains two datasets, one for each channel
2453 (main experiment and veto in run 1.4). Note that in this example, it is hard coded to expect
2454 8388609 frequency bins ($2^{23} + 1$), and this must be changed if doing something other than a
2455 2^{24} -point FFT. The HDF5 sub-files are iterated over, their data is read, and written into the
2456 pre-processed HDF5 file. Make sure not to remove the error handling for closing the HDF5
2457 file, or you will corrupt it and have to rerun the pre-processing.

2458 Now that the pre-processed HDF5 file has been packed with data and a list of indices
2459 to be averaged has been generated, averaging is trivial (though still takes a few minutes, so
2460 maybe test it with a sub set of `avgIdxs`. The code is provided below:

```
2461
2462 def avgSpecFromPacked(avgIdxs, specStr):
2463     sum = np.zeros(2**23+1)
2464     for i in avgIdxs:
2465         sum += f[specStr][:,i]
2466     avgSpec = sum/(len(avgIdxs))
2467     return avgSpec
2468
```

Listing A.1: Python function for averaging spectra from pre-processed data

2469 Note that this assumes a single HDF5 file, `f`, is in scope. `specStr` is a string which
2470 specifies which channel to average, for example `spec_W_chA`.

2471 The output of this function is S_o which can be passed to following functions for further

2472 analysis.

²⁴⁷³ Bibliography

- 2474 [1] Fritz Zwicky. “The Redshift of Extragalactic Nebulae”. In: (1933).
- 2475 [2] Vera C. Rubin and Jr. Ford W. Kent. “Rotation of the Andromeda Nebula from a
2476 Spectroscopic Survey of Emission Regions”. In: (1970).
- 2477 [3] Marco Battaglieri *et al.* *US Cosmic Visions: New Ideas in Dark Matter 2017: Com-*
2478 *munity Report*. 2017. DOI: 10.48550/ARXIV.1707.04591. URL: <https://arxiv.org/abs/1707.04591>.
- 2479
- 2480 [4] Benjamin Godfrey et al. “Search for dark photon dark matter: Dark E field radio pilot
2481 experiment”. In: *Phys. Rev. D* 104 (1 July 2021), p. 012013. DOI: 10.1103/PhysRevD.
2482 104.012013. URL: <https://link.aps.org/doi/10.1103/PhysRevD.104.012013>.
- 2483 [5] E. E. Barnard and A. C. Ranyard. “Structure of the Milky Way”. In: *Knowledge: An*
2484 *Illustrated Magazine of Science* 17 (Nov. 1894), p. 253.
- 2485 [6] Kelvin, William Thomson, Baron. *Baltimore Lectures on Molecular Dynamics and the*
2486 *Wave Theory of Light*. English. Collection: University of California Libraries. London,
2487 Baltimore: C. J. Clay and sons; Publication agency of the Johns Hopkins University,
2488 1904, pp. xxi, 703. URL: <https://archive.org/details/baltimorelecture00kelvrich>.

- 2489 [7] Richard H. Maurer. “The Idea Man”. In: *SLAC Beam Line* 31.1 (2001). Accessed:
2490 2024-06-23. URL: <https://www.slac.stanford.edu/pubs/beamline/31/1/31-1-maurer.pdf>.
- 2492 [8] Anthony Tyson. “Mapping Dark Matter with Gravitational Lenses”. In: *Physics Today*
2493 45.6 (June 1992), pp. 24–32. ISSN: 0031-9228. DOI: 10.1063/1.881309. eprint: <https://pubs.aip.org/physicstoday/article/45/6/24/407200/Mapping-Dark-Matter-with-Gravitational-LensesMost>. URL: <https://doi.org/10.1063/1.881309>.
- 2497 [9] R. Clausius. “XVI. On a mechanical theorem applicable to heat”. In: *The London, Edinburgh, and Dublin Philosophical Magazine and Journal of Science* 40.265 (1870),
2498 pp. 122–127. DOI: 10.1080/14786447008640370. eprint: <https://doi.org/10.1080/14786447008640370>. URL: <https://doi.org/10.1080/14786447008640370>.
- 2501 [10] Herbert Goldstein, Charles P. Poole, and John L. Safko. *Classical Mechanics*. 3rd. San
2502 Francisco: Addison-Wesley, 2002. ISBN: 9780201657029.
- 2503 [11] A. S. Eddington. “The Kinetic Energy of a Star Clusters”. In: *Monthly Notices of the Royal Astronomical Society* 76.6 (Apr. 1916), pp. 525–528. ISSN: 0035-8711. DOI:
2504 10.1093/mnras/76.6.525. eprint: <https://academic.oup.com/mnras/article-pdf/76/6/525/18494199/mnras76-0525.pdf>. URL: <https://doi.org/10.1093/mnras/76.6.525>.
- 2508 [12] Gianfranco Bertone and Dan Hooper. “History of dark matter”. In: *Reviews of Modern Physics* 90.4 (2018), p. 045002.

- 2510 [13] F. D. Kahn and L. Woltjer. “Intergalactic Matter and the Galaxy.” In: *American*
2511 *Journal of Physics* 130 (Nov. 1959), p. 705. DOI: 10.1086/146762.
- 2512 [14] Hugo van Woerden and Richard G. Strom. “The beginnings of radio astronomy in
2513 the Netherlands”. In: *Journal of Astronomical History and Heritage* 9.1 (June 2006),
2514 pp. 3–20.
- 2515 [15] J.I. Read. “The Local Dark Matter Density”. In: *J. Phys.* G41 (2014), p. 063101. URL:
2516 <https://arxiv.org/abs/1404.1938>.
- 2517 [16] S Sivertsson et al. “Estimating the local dark matter density in a non-axisymmetric
2518 wobbling disc”. In: *Monthly Notices of the Royal Astronomical Society* 511.2 (Apr.
2519 2022), pp. 1977–1991. ISSN: 0035-8711. DOI: 10.1093/mnras/stac094.
- 2520 [17] Sung Hak Lim et al. *Mapping Dark Matter in the Milky Way using Normalizing Flows*
2521 and *Gaia DR3*. 2023. arXiv: 2305.13358 [astro-ph.GA]. URL: <https://arxiv.org/>
2522 abs/2305.13358.
- 2523 [18] Virginia Trimble. “History of Dark Matter in Galaxies”. In: *Planets, Stars and Stel-*
2524 *lar Systems: Volume 5: Galactic Structure*. Ed. by Gerard Gilmore. New York, NY:
2525 Springer, 2013, pp. 1093–1116.
- 2526 [19] V. Radeka. “Signal, Noise and Resolution in Position-Sensitive Detectors”. In: *IEEE*
2527 *Transactions on Nuclear Science* 21.1 (1974), pp. 51–64. DOI: 10.1109/TNS.1974.
2528 4327444.

- 2529 [20] B. M. Brubaker et al. “HAYSTAC axion search analysis procedure”. In: *Physical Re-*
2530 *view D* 96.12 (Dec. 2017). DOI: 10.1103/physrevd.96.123008. URL: <https://doi.org/10.1103%2Fphysrevd.96.123008>.
- 2531
- 2532 [21] C. Boutan et al. *Axion Dark Matter eXperiment: Run 1A Analysis Details*. 2023. arXiv:
2533 2312.16668.
- 2534 [22] Maximiliano Silva-Feaver et al. “Design Overview of DM Radio Pathfinder Experi-
2535 *ment*”. In: *IEEE Transactions on Applied Superconductivity* 27.4, 2631425 (June 2017),
2536 p. 2631425. DOI: 10.1109/TASC.2016.2631425.
- 2537 [23] David Hill. “Plane Wave Integral Representation for Fields in Reverberation Cham-
2538 bers”. en. In: 40 (1998-08-01 00:08:00 1998).
- 2539 [24] W. L. Stutzman and G. A. Thiele. *Antenna Theory and Design*. John Wiley Sons,
2540 1998.
- 2541 [25] J.D. Kraus. *Antennas*. McGraw-Hill, 1950. ISBN: 07-035410-3.
- 2542 [26] H. Nyquist. “Thermal Agitation of Electric Charge in Conductors”. In: *Phys. Rev.* 32
2543 (1 July 1928), pp. 110–113. DOI: 10.1103/PhysRev.32.110. URL: <https://link.aps.org/doi/10.1103/PhysRev.32.110>.
- 2544
- 2545 [27] J. B. Johnson. “Thermal Agitation of Electricity in Conductors”. In: *Phys. Rev.* 32 (1
2546 July 1928), pp. 97–109. DOI: 10.1103/PhysRev.32.97. URL: <https://link.aps.org/doi/10.1103/PhysRev.32.97>.
- 2547

- 2548 [28] Robert H Dicke. “The measurement of thermal radiation at microwave frequencies”.
2549 In: *Review of Scientific Instruments* 17.7 (1946), pp. 268–275.
- 2550 [29] Albert Einstein. “Über die von der molekularkinetischen Theorie der Wärme geforderte
2551 Bewegung von in ruhenden Flüssigkeiten suspendierten Teilchen”. In: *Annalen der
2552 Physik* 322.8 (1905), pp. 549–560.
- 2553 [30] Herbert B. Callen and Theodore A. Welton. “Irreversibility and Generalized Noise”.
2554 In: *Phys. Rev.* 83 (1 July 1951), pp. 34–40. DOI: 10.1103/PhysRev.83.34. URL:
2555 <https://link.aps.org/doi/10.1103/PhysRev.83.34>.
- 2556 [31] C. L. Mehta. “Coherence-time and effective bandwidth of blackbody radiation”. In:
2557 *Il Nuovo Cimento (1955-1965)* 28.2 (1963), pp. 401–408. DOI: 10.1007/BF02828589.
2558 URL: <https://doi.org/10.1007/BF02828589>.
- 2559 [32] Raphael Cervantes et al. *Deepest Sensitivity to Wavelike Dark Photon Dark Matter
2560 with SRF Cavities*. 2022. arXiv: 2208.03183 [hep-ex].
- 2561 [33] Alexander V. Gramolin et al. “Spectral signatures of axionlike dark matter”. In: *Physi-
2562 cal Review D* 105.3 (Feb. 2022). ISSN: 2470-0029. DOI: 10.1103/physrevd.105.035029.
2563 URL: <http://dx.doi.org/10.1103/PhysRevD.105.035029>.
- 2564 [34] Michael S. Turner. “Periodic signatures for the detection of cosmic axions”. In: *Phys.
2565 Rev. D* 42 (10 Nov. 1990), pp. 3572–3575. DOI: 10.1103/PhysRevD.42.3572. URL:
2566 <https://link.aps.org/doi/10.1103/PhysRevD.42.3572>.
- 2567 [35] Greg Durgin. *Lecture on Noise Figure*. Accessed: 2024-06-23. 2017. URL: https://www.youtube.com/watch?v=M_SRUF4TQgA.

- 2569 [36] Pasternack Enterprises. *PE15A1012: 1 Watt Amplifier Operating From 0.01 GHz to*
- 2570 6 GHz. Accessed: 2024-05-17. 2024. URL: <https://www.pasternack.com/images/ProductPDF/PE15A1012.pdf>.
- 2571
- 2572 [37] SP Devices. *ADQ32 Datasheet*. Accessed: 2024-06-23. 2024. URL: https://www.spdevices.com/en-us/Products_/Documents/ADQ32/20-2378%20ADQ32%20datasheet.pdf.
- 2573
- 2574
- 2575 [38] Benjamin Godfrey. “A Novel Search for Dark Photons”. Ph.D. dissertation. UC Davis,
- 2576 2022. URL: <https://escholarship.org/uc/item/72b776v4>.
- 2577 [39] Joseph Levine et al. *New Limit on Dark Photon Kinetic Mixing in the 0.2-1.2 μeV*
- 2578 *Mass Range From the Dark E-Field Radio Experiment*. 2024. arXiv: 2405.20444
- 2579 [hep-ex]. URL: <https://arxiv.org/abs/2405.20444>.
- 2580 [40] L.A. Wainstein and V.D. Zubakov. *Extraction of Signals from Noise*. Englewood Cliffs,
- 2581 NJ: Prentice-Hall, 1962. ISBN: 9780132981330.
- 2582 [41] Andy Marvin and Simon Jonathan Bale. “Thermal Noise Measurements in a Rever-
- 2583 beration Chamber”. English. In: *IEEE Transactions on Electromagnetic Compatibility*
- 2584 64.3 (June 2022). © 2022 IEEE. This is an author-produced version of the published
- 2585 paper. Uploaded in accordance with the publisher’s self-archiving policy. Further copy-
- 2586 ing may not be permitted; contact the publisher for details, pp. 893–896. ISSN: 0018-
- 2587 9375. DOI: [10.1109/TEMC.2022.3142937](https://doi.org/10.1109/TEMC.2022.3142937).
- 2588 [42] F. Reif. *Fundamentals of Statistical and Thermal Physics*. Long Grove, IL: Waveland
- 2589 Press, 2009. ISBN: 9781577666127.

- 2590 [43] R. H. Dicke. “A Computational Method Applicable to Microwave Networks”. In: *Journal*
2591 *of Applied Physics* 18.10 (Oct. 1947), pp. 873–878. ISSN: 0021-8979. DOI: 10.1063/
2592 1.1697561. eprint: <https://pubs.aip.org/aip/jap/article-pdf/18/10/873/18307533/873\1\online.pdf>. URL: <https://doi.org/10.1063/1.1697561>.
- 2593
- 2594 [44] Hewlett-Packard. *S-Parameter Design*. Application Note 154. 1990. URL: https://www.hpmemoryproject.org/an/pdf/an_154.pdf.
- 2595
- 2596 [45] NoiseWave. *NoiseWave FAQ Document*. Accessed: 2024-06-23. 2024. URL: <https://noisewave.com/faq.pdf>.
- 2597
- 2598 [46] Whitham D. Reeve. *Noise Tutorial Part III: Attenuator and Amplifier Noise*. Revision
2599 0.1, Updated: July 7, 2014. Reeve Engineers. 2014. URL: https://www.reeve.com/Documents/Noise/Reeve_Noise_3_AttenAmpNoise.pdf.
- 2600
- 2601 [47] S. Al Kenany et al. “Design and operational experience of a microwave cavity axion
2602 detector for the 20-100 μ eV range”. In: *Nuclear Instruments and Methods in Physics*
2603 *Research Section A: Accelerators, Spectrometers, Detectors and Associated Equipment*
2604 854 (May 2017), pp. 11–24. ISSN: 0168-9002. DOI: 10.1016/j.nima.2017.02.012.
2605 URL: <http://dx.doi.org/10.1016/j.nima.2017.02.012>.
- 2606 [48] Raphael Cervantes et al. *Deepest Sensitivity to Wavelike Dark Photon Dark Matter*
2607 *with SRF Cavities*. 2022. arXiv: 2208.03183 [hep-ex].
- 2608 [49] Maurio B. Grando, Christian R. Boutan, and Jihee Yang. *A Multiport Approach to*
2609 *Thermal Noise and Scattering Parameter Simulation of Cryogenic Experiments*. 2022.
2610 arXiv: 2209.04008 [physics.ins-det]. URL: <https://arxiv.org/abs/2209.04008>.

- 2611 [50] G.H. Bryant. *Principles of Microwave Measurements*. London, United Kingdom: Pe-
2612 ter Peregrinus Ltd., on behalf of the Institution of Electrical Engineers, 1993. ISBN:
2613 0863412963.
- 2614 [51] David A. Hill. “Wall Losses and Cavity Q”. In: *Electromagnetic fields in cavities: De-*
2615 *terministic and statistical theories*. John Wiley & Sons Inc., 2009, pp. 31–33.
- 2616 [52] R.H. Price, H.T. Davis, and E.P. Wenaas. “Determination of the statistical distribution
2617 of electromagnetic-field amplitudes in complex cavities”. In: *Physical Review E* 48
2618 (1993), pp. 4716–4729. DOI: 10.1103/PhysRevE.48.4716.
- 2619 [53] John David Jackson. *Classical Electrodynamics*. 3rd. New York: Wiley, 1998. ISBN:
2620 9780471309321.
- 2621 [54] Bing-Hope Liu, David C. Chang, and Mark T. Ma. *Eigenmodes and the Composite Q*
2622 *Factor of a Reverberating Chamber*. Tech. rep. Aug. 1983.
- 2623 [55] *Series 83 RF Shielded Enclosure*. Lindgren R.F. Enclosures, Inc. 2021. URL: <https://www.ets-lindgren.com/datasheet/shielding/rf-shielding-and-accessories/11003/1100307>.
- 2626 [56] David A. Hill. *Electromagnetic Theory of Reverberation Chambers*. Technical Note
2627 1506. Gaithersburg, MD: National Institute of Standards and Technology, 1998. URL:
2628 https://tsapps.nist.gov/publication/get_pdf.cfm?pub_id=24427.
- 2629 [57] D.A. Hill. “A reflection coefficient derivation for the Q of a reverberation chamber”. In:
2630 *IEEE Transactions on Electromagnetic Compatibility* 38.4 (1996), pp. 591–592. DOI:
2631 10.1109/15.544314.

- 2632 [58] Lawrence Krauss et al. “Calculations for cosmic axion detection”. In: *Physical Review*
2633 *Letters* 55.17 (1985), pp. 1797–1800. DOI: 10.1103/PhysRevLett.55.1797. URL:
2634 <https://doi.org/10.1103/PhysRevLett.55.1797>.
- 2635 [59] *Biconical Antenna AB-900A*. Rev. D05.19. Com-Power Corporation. May 2019. URL:
2636 <https://documentation.com-power.com/pdf/AB-900A-1.pdf>.
- 2637 [60] *COMSOL Multiphysics*. 5.4. Available at <https://www.comsol.com/>. COMSOL, Inc.
2638 One First Street, Suite 4 Los Altos, CA 94022.
- 2639 [61] Zhong Chen and Michael D. Foegelle. “A numeric investigation of ground plane effects
2640 on biconical antenna factor”. In: *Electromagnetic Compatibility, 1998. 1998 IEEE In-*
2641 *ternational Symposium on*. Vol. 2. IEEE. IEEE, 1998, pp. 802–806. DOI: 10.1109/I
- 2642 ISEMC.1998.750302. URL: <https://ieeexplore.ieee.org/document/750302>.
- 2643 [62] John D. Kraus. *Antennas*. 2nd. New York: McGraw-Hill, 1988, p. 892. ISBN: 9780070354227.
- 2644 [63] Mini-Circuits. *ZKL-1R5: 50 Ω Gain Block Amplifier*. Accessed: 2024-06-23. 2024. URL:
2645 <https://www.minicircuits.com/pdfs/ZKL-1R5.pdf>.
- 2646 [64] Texas Instruments. *LM317: 3-Terminal Adjustable Regulator*. Accessed: 2024-06-23.
2647 2024. URL: <https://www.ti.com/lit/ds/symlink/lm317.pdf?ts=1720749307506>.
- 2648 [65] Alan V. Oppenheim, Alan S. Willsky, and S. Hamid Nawab. *Signals and Systems*. 2nd.
2649 Upper Saddle River, NJ: Prentice Hall, 1996. ISBN: 978-0138147570.
- 2650 [66] Mini-Circuits. *ZX75LP-288-S+: Low Pass Filter*. Accessed: 2024-06-23. 2024. URL:
2651 <https://www.minicircuits.com/pdfs/ZX75LP-288-S+.pdf>.

- 2652 [67] Mini-Circuits. *SHP-50+: High Pass Filter*. Accessed: 2024-06-23. 2024. URL: <https://www.minicircuits.com/pdfs/SHP-50+.pdf>.
- 2653
- 2654 [68] *Biconical Antenna*. AB-900A. Rev. D. Com-Power Corporation. May 2019.
- 2655 [69] *The Y Factor Technique For Noise Figure Measurements*. 1MA178. Version 5e. Rhode
- 2656 & Schwarz. Oct. 2021.
- 2657 [70] *Noise Figure Measurement Accuracy: The Y-Factor Method*. 1MA178. Version 5e.
- 2658 Keysight Technologies. Oct. 2021.
- 2659 [71] Wikipedia contributors. *Y-factor Sketch*. Accessed: 2024-06-23. 2024. URL: https://en.wikipedia.org/wiki/Y-factor#/media/File:Y-factor_sketch.jpg.
- 2660
- 2661 [72] Rigol Technologies. *RSA5000 Series: Real-Time Spectrum Analyzer Datasheet*. Ac-
- 2662 cessed: 2024-06-23. 2024. URL: https://beyondmeasure.rigoltech.com/acton/attachment/1579/f-0816/1/-/-/-/RSA5_datasheet.pdf.
- 2663
- 2664 [73] “IEEE Standard Method for Measuring the Effectiveness of Electromagnetic Shielding
- 2665 Enclosures”. In: *IEEE Std 299-1997* (1998), pp. 1–48. DOI: [10.1109/IEEESTD.1998.88115](https://doi.org/10.1109/IEEESTD.1998.88115).
- 2666
- 2667 [74] David W. Allan. “Statistics of atomic frequency standards”. In: *Proceedings of the*
- 2668 *IEEE 54.2* (1966), pp. 221–230.
- 2669 [75] Keysight Technologies. *Analyzing Frequency Stability in the Frequency and Time Do-*
- 2670 *mains*. Tech. rep. 5991-4797EN, August 11, 2014. USA: Keysight Technologies, 2014.

- 2671 [76] Stanford Research Systems. *FS725 Rubidium Frequency Standard Manual*. Accessed:
2672 2024-06-23. 2024. URL: <https://www.thinksrs.com/downloads/PDFs/Manuals/FS725m.pdf>.
- 2673
- 2674 [77] R. H. Dicke. “The Measurement of Thermal Radiation at Microwave Frequencies”.
2675 In: *Rev. Sci. Instrum.* 17 (1946), p. 268. DOI: 10.1063/1.1770483. URL: <https://aip.scitation.org/doi/10.1063/1.1770483>.
- 2676
- 2677 [78] S. Al Kenany et al. “Design and operational experience of a microwave cavity axion de-
2678 tector for the 20-100 micro-eV Range”. In: *Nuclear Instruments and Methods in Physics*
2679 *Research Section A: Accelerators, Spectrometers, Detectors and Associated Equipment*
2680 854 (May 2017), pp. 11–24. ISSN: 0168-9002. DOI: 10.1016/j.nima.2017.02.012.
2681 URL: <http://dx.doi.org/10.1016/j.nima.2017.02.012>.
- 2682 [79] G. Turin. “An introduction to matched filters”. In: *IRE Transactions on Information*
2683 *Theory* 6.3 (1960), pp. 311–329. DOI: 10.1109/TIT.1960.1057571.
- 2684 [80] Robert N McDonough and Anthony D Whalen. *Detection of signals in noise*. Academic
2685 Press, 1995.
- 2686 [81] S. Asztalos et al. “Large-scale microwave cavity search for dark-matter axions”. In:
2687 *Phys. Rev. D* 64 (9 Oct. 2001), p. 092003. DOI: 10.1103/PhysRevD.64.092003. URL:
2688 <https://link.aps.org/doi/10.1103/PhysRevD.64.092003>.
- 2689 [82] G. Orjubin et al. “Statistical model of an undermoded reverberation chamber”. In:
2690 *IEEE Transactions on Electromagnetic Compatibility* 48.1 (2006), pp. 248–251. DOI:
2691 10.1109/TEMC.2006.870705.

- 2692 [83] B. Efron. “Bootstrap Methods: Another Look at the Jackknife”. In: *The Annals of*
2693 *Statistics* 7.1 (1979), pp. 1–26. DOI: 10.1214/aos/1176344552. URL: <https://doi.org/10.1214/aos/1176344552>.
- 2694
- 2695 [84] R. Khatiwada et al. “Axion Dark Matter Experiment: Detailed design and operations”.
2696 In: *Review of Scientific Instruments* 92.12 (Dec. 2021), p. 124502. ISSN: 0034-6748.
2697 DOI: 10.1063/5.0037857. eprint: https://pubs.aip.org/aip/rsi/article-pdf/doi/10.1063/5.0037857/16136265/124502/_1/_online.pdf. URL: <https://doi.org/10.1063/5.0037857>.
- 2698
- 2699
- 2700 [85] Yuqi Zhu et al. “An improved synthetic signal injection routine for the Haloscope
2701 At Yale Sensitive To Axion Cold dark matter (HAYSTAC)”. In: *Review of Scientific*
2702 *Instruments* 94.5 (May 2023). ISSN: 1089-7623. DOI: 10.1063/5.0137870. URL: <http://dx.doi.org/10.1063/5.0137870>.
- 2703
- 2704 [86] Frank Hampel et al. *Robust Statistics: The Approach Based on Influence Functions*.
2705 John Wiley & Sons, Mar. 1986. ISBN: 9780471735779. DOI: 10.1002/9781118186435.
- 2706 [87] Andrea Caputo et al. “Dark photon limits: A handbook”. In: *Phys. Rev. D* 104 (9
2707 Nov. 2021), p. 095029. DOI: 10.1103/PhysRevD.104.095029. URL: <https://link.aps.org/doi/10.1103/PhysRevD.104.095029>.
- 2708
- 2709 [88] Ciaran O’Hare. *cajohare/AxionLimits: AxionLimits*. <https://cajohare.github.io/AxionLimits/>. Version v1.0. July 2020. DOI: 10.5281/zenodo.3932430.
- 2710
- 2711 [89] DM Radio Collaboration et al. *Electromagnetic modeling and science reach of DM Radio-*
2712 *m³*. 2023. arXiv: 2302.14084 [hep-ex]. URL: <https://arxiv.org/abs/2302.14084>.

- 2713 [90] Ferenc Marki and Christopher Marki. *Mixer Basics Primer: A Tutorial for RF &*
- 2714 *Microwave Mixers*. Marki Microwave, Inc. Morgan Hill, CA, 2010. URL: https://markimicrowave.com/assets/c2c4688b-15c7-4421-a703-254cb238f9fb/Mixer_Basics_Primer.pdf.
- 2715
- 2716
- 2717 [91] David M. Pozar. *Microwave Engineering*. 4th ed. Hoboken, NJ: Wiley, 2011. ISBN:
- 2718 978-0470631553.
- 2719 [92] Wikipedia contributors. *Superheterodyne receiver*. Accessed: 2024-06-23. 2024. URL:
- 2720 https://en.wikipedia.org/wiki/Superheterodyne_receiver.
- 2721 [93] Chetvorno. *Superheterodyne image problem*. Accessed: 2024-11-14. 2024. URL: https://commons.wikimedia.org/wiki/File:Superheterodyne_image_problem.svg.
- 2722
- 2723 [94] Chetvorno. *How superheterodyne receiver works*. Accessed: 2024-11-14. 2024. URL:
- 2724 https://commons.wikimedia.org/wiki/File:How_superheterodyne_receiver_works.svg.
- 2725
- 2726 [95] Arran Phipps et al. “Exclusion limits on hidden-photon dark matter near 2 nev from
- 2727 a fixed-frequency superconducting lumped-element resonator”. In: *Microwave Cavities*
- 2728 and Detectors for Axion Research. Springer, 2020, pp. 139–145.
- 2729 [96] Jonathan L. Ouellet et al. “Design and implementation of the ABRACADABRA-10
- 2730 cm axion dark matter search”. In: *Phys. Rev. D* 99 (5 Mar. 2019), p. 052012. DOI:
- 2731 [10.1103/PhysRevD.99.052012](https://doi.org/10.1103/PhysRevD.99.052012). URL: <https://link.aps.org/doi/10.1103/PhysRevD.99.052012>.
- 2732

- 2733 [97] Alexander V. Gramolin et al. “Search for axion-like dark matter with ferromagnets”.
2734 en. In: *Nature Physics* 17.1 (Jan. 2021), pp. 79–84. ISSN: 1745-2473, 1745-2481. DOI:
2735 [10.1038/s41567-020-1006-6](https://doi.org/10.1038/s41567-020-1006-6).
- 2736 [98] Sumita Ghosh et al. “Searching for dark photons with existing haloscope data”. In:
2737 *Physical Review D* 104.9 (Nov. 2021), p. 092016. DOI: [10.1103/PhysRevD.104.092016](https://doi.org/10.1103/PhysRevD.104.092016).